

DNA 4212F

EVALUATION OF THE VIRGIN MECHANICAL AND THERMAL ✓ PROPERTIES OF AVCO 3DCC **HEATSHIELD MATERIALS**

Southern Research Institute 2000 Ninth Avenue South Birmingham, Alabama 35205

March 1977

Final Report for Period October 1974-July 1975

CONTRACT No. DNA 001-75-C-0037

APPROYED FOR PUBLIC RELEASE; DISTRIBUTION UNLIMITED.

THIS WORK SPONSORED BY THE DEFENSE NUCLEAR AGENCY UNDER RDT&E RMSS CODE B342076464 N99QAXAC31323 H2590D.

CEPY AVAILABLE TO THE BUES WAS PERMIT FULLY LEGISLE PRODUCTION

Prepared for

Director

DEFENSE NUCLEAR AGENCY

Washington, D. C. 20305

Destroy this report when it is no longer needed. Do not return to sender.

UNCLASSIFIED SECURITY CLASSIFICATION OF THIS PAGE (When Data Entered) READ INSTRUCTIONS BEFORE COMPLETING FORM REPORT DOCUMENTATION PAGE REPORTINUMBER 2. GOVT ACCESSION NO. 3. RECIPIENT'S CATALOG NUMBER DNA 4212F 1 TYPE OF REPORT & PERIOD COVERED EVALUATION OF THE YIRGIN MECHANICAL AND Final Report for Period Oct 4 74-July 475 THERMAL PROPERTIES OF AVCO 3DCC HEAT-SHIELD MATERIALS. 6. PERFORMING ORG. REPORT NUMBER EAS-77-657-3406-5-1-F AUTHOR(s) CONTRACT OR GRANT NUMBER(S John R./Koenig DNA_001-75-C-0037, DNADTI-73-6-0016 PROGRAM ELEMENT, PROJECT, AREA & WORK UNIT NUMBERS PERFORMING ORGANIZATION NAME AND ADDRESS Southern Research Institute 2000 Ninth Avenue South Subtask N99QAXAC313-23 Birmingham, Alabama 35205 -11. CONTROLLING OFFICE NAME AND ADDRESS 12. REPORT DATE Director Defense Nuclear Agency IS. NUMBER OF PAGES Washington, D.C. 20305 528 14. MONITORING AGENCY NAME & ADDRESS(If different from Controlling Office) 15. SECURITY CLASS (of this report) UNCLASSIFIED 15a. DECLASSIFICATION/DOWNGRADING 16 DISTRIBUTION STATEMENT (of this Report) Approved for public release; distribution unlimited. 17. DISTRIBUTION STATEMENT (of the abstract entered in Block 20, if different from Report) 18. SUPPLEMENTARY NOTES This work sponsored by the Defense Nuclear Agency under RDT&E RMSS Code B342076464 N99QAXAC31323 H2590D. 19. KEY WORDS (Continue on reverse sign if necessary and identify by block number) Composites Mechanical Properties Carbon-Carbon Nondestructive Evaluations Heatshields Thermal Properties 20. ABSTRACT (Continue on reverse side if necessary and identify by block number) The mechanical and thermal properties of a state-of-the-art carbon-carbon heatshield material was determined for both cylindrical and conical forms of the material. Nondestructive evaluations were performed to characterize the nature of the material and define variability between and within pieces of the material.

DD 1 JAN 73 1473 EDITION OF 1 NOV 65 IS ORSOLETE

Recommended values for analysis are provided.

UNCLASSIFIED

SEC JRITY CLASSIFICATION OF THIS PAGE (When Data Entered)

328 1 ma

UNCLASSIFIED	
SECURITY CLASSIFICATION OF THIS PAGE(When Data Entered) ,	
1	
1	
1	
]	
· ·	
•	
ĺ	
}	
•	
·	
ļ	
1	
į	
İ	
	·

UNCLASSIFIED
SECURITY CLASSIFICATION OF THIS PAGE(When Data Entered)

PREFACE

This final report documents the results of research performed by Southern Research Institute on The Mechanical and Thermal Properties of AVCO 3DCC Cylinders and Cones under Contract Number DNA001-75-C-0037 and DNA001-73-C-0076. Major T. Swartz was the initial DNA project engineer with the responsibility subsequently assumed by Mr. D. Kohler and Major W. Mercer. The Southern Research Institute project leader was Mr. J. R. Koenig, Research Engineer. Mechanical evaluations were performed under the supervision of Mr. N. A. Kheir, Associate Engineer, thermal evaluations were under the supervision of Dr. J. R. McDonald, Head, Applied Thermal Section and nondestructive characterizations were under the supervision of Mr. H. E. Littleton, Head, Nondestructive Characterization Section. Overall supervision and guidance was provided by Mr. C. D. Pears, Director, Mechanical Engineering Research Department.

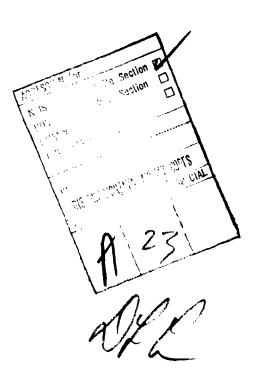


TABLE OF CONTENTS

	Page
PREFACE	1
INTRODUCTION	15
MATERIAL	16
MATRICES	18
TEST PROCEDURES AND SPECIMEN DESIGN	19
Tension	19
Compression	22
Torsion	23
Thermal Expansion	23
Thermal Conductivity	23
Heat Capacity	24
Nondestructive Characterization	24
Visual and Light Microscopy	25
Radiography	
Madiography	25
Ultrasonics (Velocity, Pulse-Echo, and	
Attenuation)	26
Eddy Curren'	26
Gravimetric Bulk Density	27
Radiometric Density Gaging	27
Electrical Resistivity	27
Electrical Resistivity	21
CUTTING PLANS	27
NONDESTRUCTIVE CHARACTERIZATION OF CYLINDERS	28
WALE TO BE SEED TO THE TOTAL OF	
NONDESTRUCTIVE CHARACTERIZATION OF 3DCC CONES	33
MECHANICAL AND THERMAL PROPERTIES OF 3DCC CYLINDERS	34
Circumferential Tensile Results	35
Axial Tensile Results	38
Radial Tensile Results	39
Circumferential Compressive Results	39
Axial Compressive Results	41
Torsional Shear Results	42
Thermal Expansion	42
Thermal Conductivity Results	
Charific track	44
Specific Heat	44
Recommended Design Data for 3DCC Cylinders	44

TABLE OF CONTENTS - CONTINUED

	Page
MECHANICAL AND THERMAL DATA ON THE 3DCC CONE	46
Circumferential Tensile Results	47
Axial Tensile Results	47
Radial Tensile Results	49
Circumferential Compressive Results	49
Axial Compressive Results	50
Torsional Shear Results	51
Thermal Expansion Results	52
Axial Thermal Expansion	53
	53
Radial Thermal Expansion	
Thermal Conductivity Results	53
Specific Heat	53
Variation of Properties Along the Cone	54
CONCLUSIONS	55
ADDENDICES	222

LIST OF ILLUSTRATIONS

Figure		Page
1	Schematic of Material Structure for AVCO 3DCC .	57
2	Tensile Specimen for Axial Evaluations of Cylindrical 3DCC	58
3	Tensile Specimen for Axial Evaluations on Conical 3DCC	59
4	Radial Tensile Specimen for AVCO 3DCC	60
5	Schematic of High Temperature Hoop Facility	61
6	Circumferential Compressive Specimen for AVCO 3DCC Cylinder and Cone	62
7	Axial Compressive Specimen and Torsional Shear Specimen for AVCO 3DCC Cone	63
8	Curved Specimen Compressive Test Fixture	64
9	Thermal Expansion Specimen for AVCO 3DCC	65
10	Drawing of Specimen for Thermal Conductivity Measurements in Comparative Rod Apparatus	66
11	Radial Inflow Strip Specimen	67
12	Cutting Plan for AVCO 3DCC Cylinder R327-1	68
13	Cutting Plan for AVCO 3DCC Cylinder CC-5 (131-1)	69
14	Cutting Plan for AVCO 3DCC Cone K357-2	70
15	Top and Bottom of CC-3	71
16	Structure of CC-3	72
17	Radiometric Density Map of CC-3 (129-1)	73
18	Radial Velocity Map of CC-3 (129-1)	74
19	Radiometric Density Map of CC-3 (129-2)	75

Figure		Page
20	Radial Velocity Map of CC-3 (127-2)	76
21	Typical Structure of CC-4	77
22	0.75 Inch Discontinuity in Outer Surface of Cylinder 131-1 (CC-5)	78
23	Radiometric Density Map of CC-5	79
24	Radial Velocity Map of CC-5	80
25	Low Absorptive Striation in Cylinder 131-1 (CC-5) also Typical in Other Cylinders	81
26	Structure of CC-5 as Seen in Bl-1-QC-3	82
27	Radiometric Density Map of CC-6 (132-1&2)	83
28	Radial Velocity Map of CC-6 (132-1&2)	84
29	Debond Areas in CC-6 (132-1) (2X)	85
30	Debond Areas in CC-6 (132-1)	86
31	Cracking Along Circumferential Bundles and Loose Circumferential Bundles in CC-6 (132-1)	87
32	Debond Areas in 132-1-SoRI-R3	88
33	Zones of Cracking Around Circumferentials in 132-1-SoRI-R3	68
34	End Views of CC-6 (132-2)	90
35	Close Up of External Surface of CC-6 (132-2) .	91
36	Radiometric Density Map of CC-7 (131-1)	92
37	Radial Velocity Map of CC-7 (133-1)	93
38	Eddy Current Map of CC-7 (133-1)	94
39	Cracking Around Radials in CC-7 (133-1)	95

Figure		Page
40	Edge of CC-7 (133-1)	96
41	Debonds in CC-7 (133-1)	97
42	3DCC Cylinder CC-7 Debond Locations	98
43	3DCC Cylinder CC-7 Debonds versus Radials	99
44	Bottom Edge of Cylinder 133-2 (CC-7) at 2X	100
45	Radiometric Density Map for CC-9 (134-2)	101
46	Radial Velocity Map for CC-8 (134-2)	102
47	Debond Area in 3DCC Cylinder CC-8 at 0°	103
48	Debond Area in 3DCC Cylinder CC-8 at 90°	104
49	Rough Area on External Surface of CC-8 After Reimpregnation	105
50	Pushed Radials in CC-8	106
51	Radiometric Density Map of R327-1	107
52	Radial Velocity Map of R327-1	108
53	Anomaly on End of Cylinder K327-1	109
54	Circumferential Velocity Map of R327-1	110
55	Radiometric Density Map of R327-2	111
56	Structure of R327-2	112
57	Radial Velocity Map of R327-2	113
58	Porous Region in 327-2 on the ID at 225°	114
59	Structure of Forward Section of K357-1	115
60	Toose Padials on AFT of K357-1	116

Figure		Page
61	Porous Matrix Areas of Cone K357-1 (2X)	117
62	Circumferential Velocity at Top on Virgin 3DCC Cone K357-1	118
63	Circumferential Velocity Ten Inches from Bottom on Virgin 3DCC Cone K357-1	119
64	Circumferential Velocity One Inch from Bottom on Virgin 3DCC Cone K357-1	120
65	Eddy Current Traces for Virgin 3DCC Cone K357-1 100 KHz 0° Lift-Off	121
66	Radiometric Density Map of K357-2	122
67	Radial Velocity Map of K357-2	123
68	Eddy Current Traces for Cone K357-2	124
69	Structure of Ends of K357-2	125
70	Porous Areas in Cone K357-2	126
71	Cylinder 131-1 (CC-5) Hoop Tensile Stress-Strain Curves at 70°F	127
72	Cylinder 132-1 (CC-6) Hoop Tensile Stress-Strain Curves	128
73	Cylinder 133-2 (CC-7) Hoop Tensile Stress-Strain Curves	129
74	Cylinder 133-2 (CC-7) Hoop Tensile Stress-Strain Curves at 70°F	130
75	Cylinder 134-2 (CC-8) Hoop Tensile Stress-Strain Curves at 70°F	131
76	Cylinder R327 Hoop Tensile Stress-Strain Curves at 70°F	132

the second second control of the second cont

Figure		Page
77	Cylinder K366 (Dining Car) Hoop Tensile Stress-Strain Curves at 70°F	133
78	Composite Plot of Probable Values for Circumferential Tensile Tests by Cylinder at 70°F	134
79	Hoop Tensile Stress-Strain Curves for 129-2- TC-3 at 2000°F	135
80	Hoop Tensile Stress-Strain Curves for 132-1- TC-4 at 3000°F	136
81	Probable Value Curves for Hoop Tensile at 70°F, 2000°F and 3000°F	137
82	Composite Axial Tensile Stress-Strain Curves of 131-1 (CC-5) at 70°F	138
83	Composite Axial Tensile Stress-Strain Curves of 131-1 (CC-5) at 2000°F	139
84	Composite Axial Tensile Stress-Strain Curves of 131-1 (CC-5) at 3000°F	140
85	Composite Axial Tensile Stress-Strain Curves of 131-1 (CC-5) at 3500°F	141
86	Composite of Axial Tensile Probable Value Curves at 70°F, 2000°F and 3000°F	142
87	Comparison of Clip-on versus Strain Data in Compressive Curved 3DCC Specimen-Unsupported .	143
88	Compressive Ring Segment for fCC Ring 8-R1 With and Without Side Support	144
89	Circumferential Compressive 3DCC Curved Specimen - No Lateral Support	145
90	Composite Stress-Strain Curves for Straight Circumferential Compressive Specimens of 3DCC at 70°F	146

Figure		Page
91	Composites of Curved Coupon Compressive Stress-Strain Curves for CC-5 and CC-4	
92	Comparison of PV Curves for Circumferential Compressive at 70°F	148
93	Composite Axial Compressive Stress-Strain Curves of 3DCC at 70°F	149
94	Composite Axial Compressive Stress-Strain Curves of 3DCC at 3000°F	150
95	Composite Axial Compressive Stress-Strain Curves of 3DCC at 4000°F	151
96	Composite Axial Compressive Stress-Strain Curves of 3DCC at 5000°F	152
97	Composite Axial Compressive Stress-Strain Curves of 3DCC at 5500°F	153
98	Composite Axial Compressive Probable Value Stress-Strain Curves of 3DCC Cylindrical Material	154
99	Composite Torsional Shear Stress-Strain Curves at 70°F	155
100	Composite Torsional Shear Stress-Strain Curves at 3000°F	156
101	Circumferential Thermal Expansion Data of Cylindrical AVCO 3DCC	157
102	Axial Thermal Expansion Data of Cylindrical AVCO 3DCC	158
103	Radial Thermal Expansion Data of Cylindrical AVCO 3DCC	159
104	Axial Thermal Conductivity of Cylindrical AVCO 3DCC	160
105	Radial Thermal Conductivity of Cylindrical	161

Figure		Page
106	Heat Capacity of Cylinder R327-1	162
107	Enthalpy versus Temperature for Cylinder R327-1.	163
108	Circumferential Tensile Moduli versus Temperature	164
109	Axial Tensile Moduli versus Temperature	165
110	Circumferential Compressive Moduli versus Temperature	166
111	Axial Compressive Moduli versus Temperature	167
112	Recommended Moduli for Cylindrical 3DCC	168
113	Recommended Thermal Expansion for Cylindric 1. AVCO 3DCC $A_r/A_t = 0.49 \dots \dots$.	169
114	Recommended Thermal Conductivity for Cylindrical AVCO 3DCC $A_r/A_t = 0.49 \dots \dots$	170
1.15	Tensile Strength Data for 3DCC Cylinders	171
1.16	Tensile Strain Data for 3DCC Cylinders	172
117	Circumferential Stress-Strain Curves for K357-2-TC-1-C (Bottom Ring from Cone)	173
118	Circumferential Stress-Strain Curves for K357-2-T-2-C (Middle Ring from Cone)	174
119	Circumferential Stress-Strain Curves for K357-2-T-3-C (Top Ring from Cone)	175
120	Probable Value Curves for Conical Ring Tensile Tests	176
121	Composite Axial Tensile Stress-Strain Plot of 3DCC at 70°F	177
122	Composite Axial Tensile Stress-Strain Plot of 3DCC at 2000°F	178
123	Composite Axial Tensile Stress-Strain Plot of 3DCC at 3000°F	179

Figure		Pa ge
124	Composite Axial Tensile Stress-Strain Plot of 3DCC at 3500°F	180
125	Composite Plot of Axial Tensile Specimens from Cone K357-2	181
126	Fracture Locations from Axial Tensile Specimens	182
127	Composite Circumferential Compressive Plot for 3DCC at 70°F	183
128	Composite Circumferential Compressive Plot for 3DCC at 3000°F	184
129	Composite Circumferential Compressive Plot for 3DCC at 5000°F	185
130	Composite Axial Compressive Stress-Strain Plot for 3DCC at 70°F	186
131	Composite Axial Compressive Stress-Strain Plot for 3DCC at 3000°F	187
132	Composite Axial Compressive Stress-Strain Plot for 3DCC at 4000°F	188
133	Composite Axial Compressive Stress-Strain Plot for 3DCC at 5000°F	189
134	Composite Axial Compressive Stress-Strain Plot for 3DCC at 5500°F	190
135	Axial Compressive Probable Value Curves for Conical 3DCC	191
136	Thermal Expansion of Cone 357-2 in the Circum- ferential Direction	192
137	Thermal Expansion of 3DCC Cone K357-2 in the Axial Direction	193

Figure		Page
138	Thermal Expansion of 3DCC Cone K357-2 in the Radial Direction	194
139	Thermal Conductivity of 3DCC Cone K357-2 in the Axial Direction	195
140	Thermal Conductivity of 3DCC Cone K357-2 in the Radial Direction	196
141	Heat Capacity of Cone K357-2	197
142	Enthalpy of Cone K357-2	198
143	Tensile Data for 3DCC Cone K357-2	199
144	Tensile Data for 3DCC Cone K357-2	200
145	Individual Compressive Data Points for 3DCC Cone K357-2	201
146	Individual Compressive Data Points for 3DCC Cone K357-2	202
147	Comparison of Moduli by A_r/A_t	203
148	Comparison of Strengths by A_r/A_t	204
149	Variation of Moduli and Strengths with A_r/A_t - General Trend	205

LIST OF TABLES

Table		Page
1	Engineering Test Matrix for 3DCC Composite Cylinder (25 Inches of Material Available)	206
2	AVCO 3DCC Engineering Test Matrix for 3DCC Cylinders	207
3	AVCO 3DCC Enigneering Test Matrix for 3DCC Cones	208
4	NDC of 3DCC Cylinders	209
5 /	NDC of 3DCC Cylinders	210
6	Nondestructive Characterization of 3DCC Cylinders	211
7	Radial Pushout for Various 3DCC Materials	212
8	Nondestructive Characterization Summary Table .	213
9	Nondestructive Characterization of 3DCC Cones .	214
10	Ring Circumferential Tensile Data for 3DCC Cylinders	215
11	Axial Tensile Data for 3DCC Cylinders	216
12	Radial Tensile Data for 3DCC Cylinders	217
13	Circumferential Compressive Data for 3DCC Cylinders	218
14	Hydrostatic Compressive Ring Data for 3DCC Cylinders	219
15	Ring Flexural (2-Point Load) Data for 3DCC Cylinders	220
16	Axial Compressive Data for 3DCC Cylinders	221
17	Torsional Shear Data for 3DCC Cylinders	222
18	Design Modulus for 3DCC	223

ままる全角を開発を通過を100mのでは100mのでは、

LIST OF TABLES - CONTINUED

Table		Page
19	Ring Circumferential Tensile Data for 3DCC Cone .	224
20	Axial Tensile Data for 3DCC Cone K357-2	225
21	Radial Tensile Data for 3DCC Cone	226
22	Circumferential Compressive Data for 3DCC Cone	. 227
23	Axial Compressive Data for 3DCC Cone	
24	Axial Torsional Shear Data for 3DCC Cone	

EVALUATION OF THE VIRGIN MECHANICAL AND THERMAL PROPERTIES OF AVCO 3DCC HEATSHIELD MATERIALS

INTRODUCTION

This is the final report on the evaluation of the virgin properties of AVCO 3DCC heatshield materials and the generation of an engineering data package on both cylindrical and conical forms of that material. The current effort, which included most of the evaluations and testing, was performed under Prime Contract Number DNA001-75-C-0037. The effort was begun under Contract Number DNA001-73-C-0076. The latter contract had, as one of its objectives, support for the Carbon-Carbon Design Program (CCDP) in which two carbon-carbon heatshield materials, selected from the results of the AFML Advanced Heatshield Program (AHP) and Subsequent Advanced Composite Heatshield Assessment (ACHA), were being evaluated for heatshield application. The two materials were the Sandia developed CVD - felt carbon-carbon (FCC) and the AVCO 3DCC material evaluated here.

This report will discuss the nature of the 3DCC material, briefly discuss the processing of the material and discuss the different pieces of the material received for evaluation. It will then show the test matrices used, define the specific test techniques used and show the design of the specimens used. A detailed discussion of the different apparatuses and procedures used is included as an appendix to the report. The results of the nondestructive evaluations of each of the cylinders and cones used will be given and then the mechanical and thermal data will be provided, first for the cylinders and then the cones. A set of probable values for design purposes had been generated for both the cylinders and the cones. The raw data are provided as appendices to the report.

神・ 編 の の

This report is one of a series of reports being generated under the current contract, DNA001-75-C-0037. Other reports include:

- 1. The Combined Response Study
- 2. Above Ground/Underground Response of 3DQP
- 3. Above Ground/Underground Response of 3DCC
- 4. Thermal Insulation Studies

- 5. Special Compressive Testing of 3DQP
- 6. Advanced Integrated Heatshield Materials Evaluation

MATERIAL

These evaluations were performed on cylinders and cones of AVCO 3DCC. Briefly, this material is constructed by laying up carbon fibers (WYB) in unidirectional resin filled plates. The plates are cut into slats which are placed into longitudinal grooves in a mandrel then cut circumferentially to form the radials. Thornel 50 tape is used to form the axial and circumferential fibers. The unit cell structure formed is shown in Figure 1. The dimensions shown are typical for the cylindrical form.

The material is then impregnated with SC1008 resin at 150°F and 2000 psi, pyrolyzed at 1200°F for 72 hours and graphitized at 4900°F for 72 hours. These latter steps are repeated until a minimum density of 1.60 is obtained, at which time a final impregnation with furfuryl alcohol is performed and heat the timents repeated.

This brief description is not definitive and the process has varied over the period of time in which the materials discussed in this report are processed. More detailed descriptions of this process are included in AFML-TR-75-195 and AVCO CCDP final report.

The sizes of the relative constituents in this structure are defined by the area of the radials (in the R-Z plane) over the total area (A_r/A_t) . The A_r/A_t on all the cylinders discussed here is 0.49 and the A_r/A_t of the cone ranges from 0.52 (top) to 0.76 (bottom). For the cylindrical material the ratio of circumferential yarns/unit area to axial yarns/unit area is approximately 1.55.

The cylinders used for this study were those produced for use in ACHA and, later, for use in CCDP. Most of the engineering data package reported here were generated on cylinders CC-5, CC-8 and R327 with supporting data from several other cylinders. The nomenclature, CC(N), was established for identification in the CCDP program. The corresponding ID numbers for the cylinders used in this program are:

CC-3	129-1
CC-3	129-2
CC-4	130-1
CC-5	131-1
CC-6	132-1
CC-6	132-2
CC-7	133-1
CC-7	133-2
CC-8	134-2
New Properties Cylinder	R327-7-1

All of the cylinders were nominally 9 inches in diameter and 0.75 inches thick. For convenience, the CCDP numbers will be used to identify cylinders with the exception of the new properties cylinder, which was not assigned a CCDP number and will be referred to as R327.

A large portion of the engineering data were originally scheduled to be generated on specimens from CC-8 which at that time was referred to as the properties cylinder. This cylinder was of subpar density and the radials were easily pushed out during routine machining. While the cylinder was later redensified, it was atypical of most of the other cylinders and not used for this program except for some limited thermal data. This problem was discussed in more detail in DNA 3487 F-3 and will be discussed further in the Nondestructive Characterization (NDC) Section of this report. The cutting plans were changed to utilize a portion of CC-5 and the new properties cylinder, R327. A. least one hoop tensile ring was scheduled from each of the cylinders listed above and other supporting data, some developed for other purposes, is reported here from these cylinders. The nondestructive evaluations for all the cylinders are reported here to develop a source of comparison.

The conical data came from cone K357-2 which was referred to as the "properties cone". It had a 7° half angle and was nominally 0.5 inches thick.

MATRICES

· 是 我一

The different cylinders used in generating the cylindrical data reported here were evaluated under the CCDP program using NDC techniques. These included gravimetric bulk density, radiometric density gaging, radial velocity maps, eddy current, visual examination and X-rays. Typical specimens were evaluated using sonic velocity in the direction of test, gravimetric density, electrical resistivity (where appropriate) and X-rays. Eddy current response was measured on the circumferential tensile rings.

The mechanical and thermal matrix originally scheduled during CCDP in evaluating the cylinders is shown in Table 1. This matrix was altered during the course of the program to provide additional data required to define the response of this material. In particular, for curved coupon compressive runs, two hydrostatic compressive runs and a ring flex test were added to aid in the interpretation of the circumferential compressive modulus, additional thermal expansion runs were added to check out anomalous behavior seen in specimens from CC-8 and the QC ring were added to the ring tensile matrix to define variation from material to material. The final matrix is shown in Table 2.

The matrix for evaluating the 3DCC cone is shown in Table 3. It is essentially the same as defined under CCDP and parallels the cylinder matrix, with care taken in the cutting plan, to be discussed later, to sort variations along the cone by key properties.

TEST PROCEDURES AND SPECIMEN DESIGN

The design process being attempted in CCDP and as commonly used now requires that the intrinsic material properties be determined in a materials test as opposed to, or in addition to, values obtained from "use" type tests. This philosophy was maintained through the current program and has implications on each of the test techniques used.

Tension

The main criteria which must be met in a tensile test is proper failure mode. The evaluation technique and specimen design employed for a particular strength property are based on the failure mode. The failure mode becomes particularly important in applying specimen data to actual use situations.

In use situations the decision must be made as to the representation of the stress profiles and the failure criteria; that is, whether the principal stresses would be used or whether the stresses obtained by orienting the axes along the primary material axes would be used.

True loading, as opposed to loading with parasitic stresses (or strains), is another criterion. The goal was to obtain homogeneous stress (or strain) fields from the loadings. This is important for proper failure modes and for meaningful strain measurements.

Another criterion that must be met is that the specimen design must provide sufficient cross-sectional area and/or volume such that data obtained are representative of the material. In most cases, a 5-unit cell width was chosen as a minimum gage dimension based on Southern Research Institute (SORI) prior experience with 3D composite materials. However, in a few cases a 3-cell width dimension was the maximum that could be obtained within the material or test facility constraints. This gage section design rationale proved accepable for some of the materials, but for others resulted in significant data scatter due to the fact that the gage sections were not representative when background weave geometry variations were considered. For instance, weave wrinkles of the order of approximately 0.1 to 0.5 inch were observed in some of the materials. A tensile specimen with gage dimensions of 0.2 inch by 0.3 inch by 0.500 inch long located in a wrinkle site naturally, when tested, produced different stress-strain data than a specimen with the regular weave geometry. In lieu of larger specimens with gage dimensions much larger than background weave irregularities and more data, judgements must be carefully made as to the real material response.

The uniqueness of most composites creates additional testing problems other than the specimen design problems discussed up to this point. Strict attention in machining the specimens is required so that the specimen gage sections contain the required number of unit cells located symetrically with respect to the specimen axis and that the material geometry axes are at the proper angles with the specimen axes (either orthogonal or off-axis). Many of the tensile and compressive specimens contained gage sections that can best be described as arc segments from the cylinders. necessary in order that the gage section contain only an integral number of unit cells with no fractions. only created some Machining difficulties but also testing difficulties. In order to apply loadings to these type of gage sections with a minimum of parasitic bending stresses, the centroid of the specimen was calculated and the specimen shifted laterally in the load train of the test facility to align the specimen centroid with the center of loading in the test facility. The axial tensile runs made on the 3DCC cylindrical and conical specimens were performed in a gas-bearing tensile facility. This facility is described in detail in Appendix Al. Averaging clip-on extensometers were used in most of the test to minimize the effect of internally induced bending in the specimen gage on the strain data. Specially designed water-cooled clip-ons were used in the elevated temperature evaluations. The specimens used in conducting the cylindrical axial tensile evaluations is shown in Figure 2. The speicmens used for the conical materials were variations of the specimen shown in Figure 3. On all of the cylindrical material specimens (Figure 2) and on the conical material

specimens from the top and mid-sections of the cone, five cell widths were maintained in the gage section with the specimen centered on an axial bundle and the cut lines passing through radials. For the specimens from the bottom of the cone, only three cell widths were possible. The radial tensile specimen is shown in Figure 4 and was bonded to steel face plates as shown. Circumferential tensile specimens were typically 0.5 inches high by 0.5 inches thick with the radii set by the cylinder or the cone location.

The elevated temperature ring tensile evaluations were made in the recently developed high temperature ring apparatus shown schematically in Figure 5. Essentially, a hydrostatic pressure is transferred to the ring by wedge shapes made up of water cooled steel, pyrolytic graphite and POCO graphite. The best strain measurement results were obtained using a graphite yarn wrapped around the specimen and connected to LVDT's. A more detailed description of this facility is contained in AFML-TR-74-254 "The Development and Demonstration of a High Temperature Ring Test Facility".

Compression

はい

- -

The compressive evaluations were made in a gas-bearing compressive facility very similar to the gas-bearing tensile facility. A description of this facility is included in Appendix A2. The typical specimen used for the axial specimen in Figure 7 (variations of this specimen was also used as described in the results section). The curved coupon compressive test fixture is shown in Figure 8. It essentially, adds a compensating load set to balance the ID and OD strains. It will be described in more detail in the forthcoming Combined Response Study report and has been described in Volume I of DNA report 3487F.

The hydrostatic ring compressive test was similar to the hydrostatic ring tensile test except that the fixture was designed to permit the hydraulically loaded bladder to be placed around the outside of the ring.

Torsion

The torsional specimen used was similar to the compressive specimen shown in Figure 7. A discussion of the torsional technique used is provided in Appendix A3 and in DNA 3487F-1.

Thermal Expansion

The thermal expansion was measured using both quartz and graphite tube dilatometers. The quartz dilatometer measurements are used for confirmation of the graphite dilatometer measurements and for further definition of the curve up to 1500°F. Descriptions of the facilities are contained in Appendices A4 and A5. The specimen used is shown in Figure 9.

Thermal Conductivity

In 3DCC, the reinforcement exhibits significantly different properties than the surrounding matrix. This can be quite critical when monitoring temperatures for a thermal conductivity evaluation. Significant local temperature discontinuities can exist if, for example, a material is composed of widely spaced fiber bundles, such as the radial bundles in many of the cylinders we have previously evaluated, and these bundles provide a direct conduction path by virtue of their conductivity being much higher than the surrounding matrix. We have avoided difficulties here by judicious location of thermocouples (being careful not to end in a radial bundle) and comparison of the temperature gradient measured between the internal walls (local) to that measured between the surfaces (average) monitored by extrapolation m the reference temperatures. The locations of the thermocouples were checked using radiography.

A description of the two facilities used to measure the thermal conductivity, the comparative rod apparatus (CRA) and the radial inflow apparatus (RIA) are provided in Appendices A6 and A7. The specimen used for the comparative rod evaluations is shown in Figure 10 and for the adial inflow evaluations in Figure 11.

Heat Capacity

は、一個の

To determine heat capacity to 5000°F, both the adiabatic and ice calorimeters were employed. The adiabatic calorimeter will be used from 70°F to 1000°F, and above 1000°F the ice calorimeter was used. Descriptions of these techniques are provided in Appendices A8 and A9.

Nondestructive Characterization (NDC)

Characterization by NDC involved determining the physical, background, and disparate natures of the 3DCC material. The physical nature involved the determination of physical properties such as bulk density, ultrasonic velocity, and electrical resistivity. These evaluations provided insight into bulk effects which correlated with material variability and reproducibility. The background and disparate natures are similar in that they often consist of similar material discontinuities such as voids, cracks, reinforcement placement and misorientations, and delams. However, they differ in that the background variations are frequent and inherent in the process, and the disparate variations which are infrequent and not process inherent usually have an anomalous effect on the performance of the material. An understanding of the nature of the material was essential for selective sampling, determining uniformity, reproducibility,

correlating disparate behavior, keying to past and future batches, and gaining insight on inspectability mode and criteria. Effective characterization was injected into the program starting with bulk shapes, continuing with coupon, specimen blank, and finished configuration. This matrix provided for judicious sampling, quick determination of material variability and reproducibility and loop closing.

Visual and Light Microscopy - Visual inspections from 1X to 10X are made on exposed surfaces of bulk and specimen shapes to determine material typicality and surface anomalies. This inspection was effective for surface variations such as yarn bundle fraction variations, separations, macro-voids, discolorations, matrix-rich and matrix-starved areas, yarn bundle wrinkling and spacing variations, ply spacing variations, and void clusters.

Micro-level assessments are made using about 50X photomicrographs. Here one is concerned primarily in establishing material typicality such as microcracking in yarn bundles, microcracking between matrix and yarn bundles, pore sizes, and pore size distributions.

Radiography - Radiography was performed using state-of-theart X-ray techniques for low-absorptive materials. Descriptions of the equipment and standard operating techniques were provided in DNA 3487F-1.

The radiographic exposure positioning varied depending on specimen shape. For nine-inch OD bulk cylinders, the radial and chordal views were used. The radial view exposure was made using a moving slit device (MSD). The cylinder was rotated beneath a 1/4-inch wide slit located between the cylinder and the X-ray source. The film which was attached to the inner

surface of the cylinder records a distortion-free image of the single wall. Double exposure of the film was prevented by lead shielding placed on a diametrical plane beneath the cylinder wall being exposed. For the chordal view positioning involved placing the film under the cylinder and exposing for a chordal view of the cylinder wall. Thic technique was particularly sensitive for circumferentially aligned anomalies such as ply separations. For specimen configurations, at least two views 90° apart are used.

Ultrasonics (Velocity, Pulse-Echo, and Attenuation) - Ultrasonics NDC uses sound energy at frequencies from 11 KHz to 25 MHz. The sound energy is picked up by a transducer which converts sound to electrical energy as it is transmitted through the specimen. Ultrasonic techniques lend themselves particularly to flaws having large interfaces normal to the direction of transmission such as those offered by delaminations and large voids. Ultrasonic velocity is effective for evaluating material background from the standpoint of comparing different batches of the same material and in correlating locations of flaw collections resulting in inherent variability for a given sample of material. Velocity is also useful in evaluating material anisotropy. Attenuation measurements are effective for showing the presence of porosity, cracks and delaminations. These techniques are discussed in Appendices Al0 through Al2.

Eddy Current - The eddy current test indicates differences in electrical impedance between parts to be tested and a reference sample. It is effective for revealing variations such as cracks and variations in fiber volume fractions. It is also a measure of the degree of graphitization variations within a part and between parts. A description of the technique was presented in DNA 3487F-1.

with the same to t

Gravimetric Bulk Density - Bulk density measurements for specimens having a regular configuration are calculated from direct measurements of weight and length. An analytical balance having a sensitivity ± 0.001 gram is used for weighing. Micrometers read to the nearest 0.0005 inch are used for measuring lengths, and a travelling microscope accurate to ± 0.001 inch is used for measuring chord lengths.

Radiometric Density Gaging - Radiometric density gaging is a penetrating radiation technique used for determining the density gradients of the bulk shapes. The basis of the measurements is that the transmitted radiation is inversely proportional to the density or thickness of the material. The technique used is described in DNA 3487F-1. Special manipulating equipment has been constructed for handling cylinders and cones.

Electrical Resistivity - The electrical resistivity is a monitor of the bulk nature of the material and, to some extent, of disparate response. A description of the technique used is given in Appendix Al3.

CUTTING PLANS

The cutting plans used to obtain the specimens for the cylindrical 3DCC engineering data package are presented in Figures 12 and 13. They are minor modifications of the cutting plans developed under CCDP. Additional hoop tensile rings were obtained from each of the other cylinders. The cutting plans by which those rings were excised were shown in DNA 3487F-3. That report also shows the location of the thermal specimens obtain from the original properties cylinder, CC-8. The cutting plan used for the conical data program is shown in Figure 14. The specimens were arranged so that key data could be obtained at various heights in the cone. The DQC arcs shown have been machined and have not, as yet, been tested, except for NDC, the results of which are on file.

NONDESTRUCTIVE CHARACTERIZATION OF CYLINDERS

Each of the cylinders and cones received at SoRI as virgin material were characterized using NDC techniques. The selection of the techniques varied over the period of the CCDP program, but included in all cases were density, radial velocity maps, visual examinations, X-ray and radiometric gaging. Eddy current response was measured on some of the material received in the latter portion of the program. Circumferential velocity was measured on the cones and several of the cylinders. Tables 4 through 6 show a summary of the NDC of the 3DCC cylinders.

Cylinder CC-3 was in two parts identified as 129-1 and 129-2. No anomalies were seen in the visual examinations as shown in Figure 15 which shows the bottom and top surfaces of 129-1 and Figure 16 which shows typical structure of the end of the cylinder in zones of circumferential yarns on the surface and zones with radials on the surface. Maps of the radial velocity and density gradients for the two portions of CC-3 are shown in Figures 17 through 20. On some of these maps the cutting plan is shown in the background to facilitate sorting the nature of the material used for any part. A very distinct density gradient can be seen in 129-1 which was from the lower half of the cylinder. The bottom portion, about four inches, is lower density and the density increases till the top end is over 1.8 density. The velocity maps for both show a more even but more random variation. There exists very distinct density spike in 129-2 at 90° with an adjacent low density zone at 45° at the middle of the cylinder. Cylinder 129 was a low attenuator while 129-2 attenuated the signal more typically of the other materials in the program.

Cylinder CC-4 was not evaluated as a cylinder. For comparison, the data on a single ring from that cylinder are provided in Table 6. This cylinder was higher in density than CC-3 and was also relatively clean in visual examination, with some debonded areas typical of the AVCO 3DCC as shown in Figure 21.

Cylinder CC-5 was similar, though slightly more dense, to CC-3 in its appearance. It had a single anomalous damaged area seen in visual examination at 100°, 8.5 inches from the bottom (Figure 22). The damage apparently occurred before final processing. It appears on the density map (Figure 23) as a high density zone and the velocity map (Figure 24) as a low velocity spot. The top portion of the cylinder is lower density than the rest and the cylinder had a high density zone running two thirds the length of the cylinder at 315°. The low density zone coincides with the part of the specimens used in the engineering data program reported here and is reflected in the density values measured on the specimens. The radiographic examination showed light striations (probably delams) running the full length of the cylinder as shown in Figure 25. This is typical of most of the materials studied under this program. Typical structure of the end on view of CC-5 material is shown in Figure 26.

する は 日本 日本

3.

The maps of the radiometric density and radial velocity of both sections of CC-6 (132-1 and 132-2) are shown in Figures 27 and 28. This cylinder was more dense than the other cylinders of 3DCC tested in this program, 1.71 gm/cm³ in the bottom section and 1.66 gm/cm³ in the top section. In the bottom portion (132-1) severe delaminations were seen in both the X-ray and in the visual examination. Examples of these are shown in Figures 29 and 30. Other visual observations included zones of circumferentials pulled away from the matrix and cracking along circumferential bundles (Figure 31). Similar effects were seen in

machined surfaces from CC-6 (132-1) as shown in Ring 132-1-SoRI-R3 in Figures 32 (debonds) and 33 (cracking). The debond area shown in Figure 32 seems to be continuous through the ring. The top portion (132-2) was cleaner in the X-rays and in visual examination with fewer debonds (Figure 34a), but were more evident in the machined surface (Figure 34b), though still less than seen in 132-1. A close up view of the external surface is shown in Figure 35, showing cracks between circumferentials and radials and two damaged circumferentials.

The radiometric density map and radial velocity map for CC-7 (133-1) are shown in Figures 36 and 37. This cylinder had the unusual feature of the gradients running essentially around the cylinder. The zone from about zero to 180° was lower density than the zone from 180° to 0°. The former area also tended to be higher velocity than the latter. Care should be taken in interpreting the lower portion of the velocity plot which was measured on 0.25 inch material. A map of the eddy current response is shown in Figure 38. Us. J this as a measure of the bulk rather than disparate response, the eddy current data would indicate a higher electrical resistivity in the center of the cylinder and lower at either end. This cylinder, more than those previously discussed showed cracking around the radial bundles. This is shown for two typical areas in Figure 39. The radials at the end of the cylinder were also surrounded by cracks and on on the edge would often fall off as seen in Figure 40. Cylin : CC-7 had debonds typical of the other materials seen but the were more numerous (Figure 41). The locations of debonds on CC-7 are plotted in Figure 42 and the variation with radius st wn in Figure 43. Similar debonds are shown for the other seccions of CC-7 (133-2) in Figure 44.

Cylinder CC-8 (134-2) had by far the lowest density of any of the cylinders received, 1.57 gm/cm³. The next lowest was CC-3 at 1.62 gm/cm³. The radiometric density map is shown in Figure 45. The density was very low toward the center of the cylinder. A map of the radial velocity is shown in Figure 46. The velocity tends to be higher toward the center of the cylinder with three small islands of low velocity. The average velocity is typical for the 3DCC material. The radiographs showed a single large delam area running the length of the cylinder. The visual appearance of this debond at the ends are shown in Figures 47 and 48.

This cylinder was shipped back to the manufacturer for reimpregnation and when received the second time the density was 1.64 gm/cm³. The cylinder had several zones of roughness due to missing matrix and pieces of yarn bundles. Examples of this are shown in Figure 49. During machining of this cylinder, the machining process pushed radials through the cylinder. A picture of the pushed out radials is shown in Figure 50. This problem was discussed in DNA 3487F-3. It was determined to be a material rather than a machining problem.

SoRI developed a test for evaluating the pressure required to pushout a radial. The results of that study on several cylinders are shown in Table 7. Notice that CC-8 and CC-7, the two pieces with the most extensive cracking around the radials as seen visually, had by far the lower values.

The radiometric density and radial velocity maps for the new engineering properties cylinder, R327-1, are shown in Figures 51 and 52. This cylinder had a lower velocity and a higher density at the top end, a trend that has been seen in

several other cylinders. Its appearance was similar to any of the better cylinders discussed previously with one strong anomaly at one end of the as-received cylinder shown in Figure 53. This damaged zone was apparently the result of a mechanical load during processing and extended no more than 1/2 inch into the cylinder. This cylinder, and its sister cylinder, R327-2, had the lowest range of density of any of the 3DCC cylinders seen. A map of the circumferential velocity is shown in Figure 54.

The radiometric density map for the sister billet to R327-1, R327-2 is shown in Figure 55. It had a lower density at the top end but, again, had considerably less variation in density than the other CCDP cylinders. The structure of this cylinder was different from, for example, CC-7 or CC-8, in that the debonds did not appear to be as connected. This is shown in Figure 56. The debonds are just as wide as in CC-7 but run only 1, 2 or 3 cells rather than several inches. The radial velocity map for R327-2 is shown in Figure 57. Both R327-2 and R327-1 had a lower average radial velocity than any of the other cylinders. One anomalous zone was visible on the inside surface of R327-2 as shown in Figure 58. It appeared as a region of high porosity.

Density and velocity measurements were made on each of the specimens used both in this program and elsewhere. These data are reported with the mechanical data and used for correlations of the mechanical and thermal data. The averages and ranges of these data are presented in Table 8. In some cases these represent specimens from the entire cylinder and in others only a few specimens. In general, good agreement is found with the bulk NDC information but reasonable care should be used in comparing these data by cylinder, especially the ranges due to the various number of specimens taken from the different cylinders.

NONDESTRUCTIVE CHARACTERIZATION OF 3DCC CONES

Two 3DCC cones were evaluated during the course of the program, one of which was the properties cone, K357-2, and the second (K357-1) was evaluated, then returned to the manufacturer. One fore and one aft ring was also received with K357-1. The matrix was very similar to that performed on the cylinders, consisting of visual examination, density and velocity maps, X-rays, radiometric density gaging and eddy current maps.

A summary of the NDC for the two cones is given in Table 9. The two cones were similar both in appearance and response to NDC monitors, with K357-1 being slightly more dense and lower velocity. The weave in the circumferential direction was uneven in the forward ring of K357-1 but was far less so in the forward end of the cone, as shown in Figure 59. This would raise questions as to whether data from that ring would be typical of the fore section of the cone. The radials in the rear section (large A_r/A_t) tended to come loose when exposed on the rear surface. This was true both on the ring cut from the bottom and the cone (Figure 60). There were several porous (matrix poor) regions in the cone. examples of which are shown in Figure 61. The circumferential velocity of Cone K357-1 are plotted in Figures 62 through 64. Notice the increase in velocity from top to bottom of the cone (increasing A_r/A_t). A plot of the eddy current response is shown in Figure 65. There is a trend towards increasing inches of eddy from the front to the rear (increased "conductivity") which reverses itself in the last inch of the cone and in the aft ring. The zone from 180° to 270° has a lower eddy response in the aft section. The reference material comes from CC-3 and is the standard used for all of the eddy plots. That region

was also lower density by radiometric gaging. The lowest density by radiometric gaging was at the top and the highest was at the center. Radial velocity followed the same trend as circumferential velocity, being lowest at the top and highest at the bottom (highest $A_r/A_{\rm g}$).

Cone K357-2, the "properties cone", followed the same trends as K357-1 except that the highest density was 1/3 of the way up from the bottom. This is shown in Figure 66 which is a map of the radiometric density. Figure 67 shows the radial velocity map of K357-2. The eddy current response is shown in Figure 68. Debonds in K357-2 were more like those seen in CC-6 than in the engineering properties Cylinder R327. Examples are shown in Figure 69. Figure 69 also shows loss of radials at the bottom of the cone similar to K357-1. Examples of porous areas viewed on the OD of the cone are shown in Figure 70.

MECHANICAL AND THERMAL PROPERTIES OF 3DCC CYLINDERS

The mechanical and thermal properties were generated on specimens excised mostly from Cylinders CC-5 and R327 with supporting data gathered from all of the other cylinders. Circumferential tensile data were gathered on these other cylinders (except CC-4) by design to obtain a mechanical Q.C. Other data were gathered from tasks evaluating the impulse response of this material or on a material evailability basis to obtain special data deemed necessary during the course of the program to interpret key properties. For comparison and support, the AHP data on this material, reported in AFML-TR-72-160, will be given. As will be demonstrated, the properties of this material changed over the period of years in which the materials reported here were produced. An attempt will be made later in this report to sort these distinctions.

Circumferential Tensile Results

The circumferential tensile data were generated at 70°F, 2000°F and 3000°F. The largest data package was at 70°F where the Q.C. rings were run. These data were developed using the hydrostatic ring facility described in the apparatus section. The 2000°F and 3000°F data were generated in the hot ring facility. There were problems in obtaining valid strain data at the elevated temperatures and a number of techniques were tried. The technique which was valid for standard materials used to check out the facility (graphite rod dilatometer on chords) did not work for this material probably because the rings deformed not as cylinders. Moly wires around the circumference were tried but would stretch during the test. A successful technique was finally developed using a graphite yarn wrapped around the circumference and connected to LVDT's. Valid ultimate stress data were obtained for all tests.

The ring tensile data are reported in Table 10, which includes the NDC of each ring, the ultimate strength calculated using thin wall formula and also calculated for the inside and outside surfaces (higher stresses are generated on the inside diameter of the ring), the elastic modulus calculated based on outside wall stresses and the ultimate strain. These data are reported by cylinder with averages given when more than one ring come from a given cylinder. For reference, the AHP rings had an average modulus of 12.9 x 106 psi, thin wall strength of 14,000 psi and a strain-to-failure of 0.001 in./in. at 70°F. The single specimen from CC-3, 129-1-QC-6 was similar to the AHP material in that it was linear to failure and had roughly the same modulus (12.2 x 10 psi), but was stronger (20,700 psi) and, hence had higher strain-to-failure. The specimens from CC-5 and, to a lesser extent, CC-6, had a different nature, showing a distinct secondary modulus. These curves are shown

in composite form in Figures 71 (CC-5) and 72 (CC-6). The first two runs on CC-5 both burst the bladder before reaching failure. Retest gave the ultimate stress shown. The strain data for these two runs were obtained with clip-on extensometers on chords. The clip-on at 0° for TC-2 showed a lower yield than the 90° clip-on which showed similar results to TC-1. The "yield" (beginning of the secondary slope) occurred at roughly the average failure level for the AHP material. The composite for CC-6 (Figure 70) shows the stiffer response recorded by the strain gage located at 270° on the ring. The clip-ons, located at 0° and 180° were in good agreement and showed apparent local failures, first occurring at roughly the ultimate seen in the AHP rings. Dashed lines show an interpretation of the bulk response of the material based on the slopes of the clip-on data after the apparent local yarn failures. The 70°F nondestructive mechanical (NDM) run on TC-5, which was a 3000°F ring, is shown for comparison.

The stress-strain curves for the two specimens from CC-7 are shown in Figure 73. This cylinder was only slightly stronger than the AHP material, which is not unsurprisingly as it has been distinguished by its nature and by other tests to be a substandard cylinder. The stress-strain curves shown in Figure 74 are for the other end of that same cylinder. This ring (133-2-QC-4) was the strongest of all the rings tested showing a wide range of properties from one end to the other end of that cylinder (the specimens were about 26 inches apart). Unfortunately, this end was not evaluated in NDC as a cylinder. The other three cylinders tested, CC-8, R327 and K366 were very similar in their response. The stress-strain curves for these three are shown in Figures 75 through 77.

The good strength of CC-8 (Figure 73) is somewhat anomalous as in many respects, radial pushout for example, this was a poor cylinder (though not as bad as CC-7), yet it did utilize the strength of the circumferential yarns as well as any of the cylinders. This would indicate that a single mechanical Q.C. is insufficient criteria in the evaluation of all responses of a material. The new properties cylinder (R327) and the Dining Car cylinder hoop tensile curves (Figures 76 and 77) are very similar, with K366 being somewhat softer. In both cases, as was the case with CC-6, the strain gages show the material to be stiffer than do the clip-ons. The K366 ring was added to the program as a Q.C. on a cylinder used for UGT rings.

Figure 78 is a composite of probable value curves generated on each of the cylinders. Also shown on this figure is the average AHP data, the range of the ring segment moduli developed in degraded property studies and the end points of data generated by AVCO on several of the cylinders. The initial moduli of all these data are fairly tight, considering the wide variety of the appearance and NDC monitors seen for the different cylinders, however, the hoop strength varies from 15,000 to 31,000 psi. There is good agreement between adjacent specimens from one cylinder but the distinction from end to end of a cylinder is as great as from cylinder to cylinder.

The 2000°F strain data suffered from the equipment developmental problems mentioned earlier. The data from 132-1-TC-6 appear uninterpretable and the only valid value from that test is the ultimate stress. The data from Specimen 129-2-TC-3, as measured by both the wire loop and LVDT (dilatometric technique) are in reasonably good agreement as shown in Figure 79. If a 4000 or 5000 psi lag is presumed, as shown in Figure 80, the data shape becomes similar to the shape of the 70°F probable value and the moduli is in the same ratio as the 2000°F and 70°F

axial data. This presumption gives a strain-to-failure of 0.0016 in./in. and a modulus of 16 x 10⁶ psi. In a similar fashion, except now using graphite yarn and eliminating the lag Specimen 132-1-TC-4 gives a valid 3000°F stress-strain curve while the strain data for TC-8 and TC-9 are invalid.

Figure 81 shows probable value curves for 70°F, 2000°F and 3000°F based on these data. Failure data are added to the curves as X's based on stress level.

Axial Tensile Results

The axial tensile data were generated at 70°F, 2000°F, 3000°F and 3500°F. The strain was measured by clip-on extensometers for 70°F, 2000°F and 3000°F and by the optical strain analyzers at 3500°F A summary of all of the axial tensile data are given in Table 11, which also gives the bulk density, axial velocity and radial velocity measured on the specimen blank. All specimens were from Cylinder CC-5.

The composite stress-strain curves for the four temperatures are given in Figures 82 through 85. The clip-on data (70°F-3000°F) are very consistent, at least through the first half of the curve. Some erratic behavior are seen in the latter portion of the curves, especially at 3000°F, due to relative motion of yarn bundles moving the clip-on flags. The data from 131-1-TA-7 are from the first of two runs on the specimen when the pullrod failed. On reloading the specimen failed at a lower stress. The 3500°F moduli and particularly strains-to-failure are somewhat discounted due to suspected internal bending in the specimens which is not balanced out in the optical analyzer as it is in the balanced clip-on extensometer. A composite of the probable value curves generated on the 70°F, 2000°F and 3000°F data is shown in Figure 86.

Radial Tensile Results

Three radial tensile tests were run, all from Cylinder R327. Ultimate strength was measured on each. The data from these three tests are given in Table 12. All three specimens were below the average density of the cylinder, but the lowest strength specimen was the highest density of the three. The average strength for the three was 366 psi. The specimens all failed near the bond line along θZ planes (the plane of the delams) and the radial fiber bundles pulled out rather than failing. Since the radial pushout (or pullout) strength over such a short length would be minimal (see Table 7), the radial strength reported here is an approximation of the bond of the θZ planes

Circumferential Compressive Results

Most of the circumferential compressive data were generated on straight coupon compressive specimens tested with lateral supports. The lateral supports act to partially, but not fully, counteract the bending loads induced by the curvature of the reinforcements in the specimen. The effect of this curvature on the response of a 3DCC circumferential specimen is shown in Figure 87. In that case, using a curved specimen and no supports better than 50 percent of the response is attributable to bending. A further example, using increasing amounts of side support on a ring (FCC) in the ring segment compressive facility shows not only a decrease in the bending but also significant increase in the average moduli with increasing side support (Figure 88). In addition to affecting the stiffness, the bending load also has a drastic effect on yield and ultimate in 3DCC. This is shown in Figure 89 with data generated under the CCDP program in 3DCC debug material. The supported specimen yielded over 12,000 psi while the unsupported specimen was softer and yielded at about 6000 psi. Successive loadings further decreased the yield strength. The supported specimen failed in shear while the unsupported specimen failed by internal buckle. As the delams in the unsupported specimen were extended with successive loadings, the yield (internal buckle) stress decreased.

Despite the partial support provided by the support pieces, this bending occurred, as expected, in the straight circumferential compressive specimens. However, facilities do not exist to properly evaluate the circumferential compressive properties at elevated temperatures. The approach taken was to evaluate straight specimens (with partial support) at 70°F and at elevated temperatures and to properly evaluate the response in several tests designed to remove the bending mode at room temperature. The tests used in this evaluation were the curved coupon compressive facility, the ring segment facility and the hydrostatic compressive facility. By assuming the change in mode at elevated temperatures was negligible, it was thought that the straight coupon data could be used to extrapolate the "good" circumferential compressive data to elevated temperatures.

The coupon compressive data for 3DCC are given in Table 13. The distinction between the straight and supported curved coupon specimens is evident in both the modulus and the ultimate stress reached. Figure 90 shows a composite of the straight specimen data at 70°F and Figure 91 shows a composite of the curved coupon data. Specimen 131-CC-17 was from the inner portion of the cylinder and 131-CC-18 from the outer portion. These data are compared in Figure 92 which shows the probable value curves from the two tests overplotted. The relative performance is

similar to that shown in the previous studies. Additional supportive data were gathered using the hydrostatic compressive test, loading two rings to 3000 psi and, as before, using the average of the rear 180° hit rings from the degraded property studies. The data from the hydrostatic test are shown in Table 14. The average modulus measured from all the hit rings (<2KT-180°) was 13.5×10^6 psi and the average around two virgin rings tested (from K366) was 12.9×10^6 psi.

One ring was tested in ring flexure (RF2) as a check on the moduli. The results of that test are shown in Table 15. The flex component is quite obvious in the results obtained, the stiffness being below that of the straight coupon compressive data.

Axial Compressive Results

The axial compressive data for the 3DCC material are shown in Table 15. The specimens for these evaluations came from both CC-5 and R327 and are separated by cylinder in Table 16. No strong distinctions are seen between the cylinders except at 70°F where the value for Specimen 131-1-CA-1 was much higher. This point is also high with respect to 3000°F data from the same cylinder and high by fiber volume arguments with respect to circumferential data. No explanation has been found for this unusually stiff specimen. The rest of the data look right with, perhaps, the 4000°F average on the low side. There did not appear to be much effect of stress rate at 5000°F but the effect of stress rate at 5500°F was quite distinct. Composite plots of these stress-strain curves are presented in Figures 93 through 97.

The specimen configuration used differed slightly between the two cylinders, that for R327 having straight sides and that for CC-5 having radial sides. Both had the same number of axial yarns in the gage section but the cross-sectional area of the CC-5 specimens was slightly larger giving even numbers of unit cells. The cut, in both cases, was entirely through radial rather than axial yarns. The composite plots are combined by standardizing on the CC-5 specimen (or, said another way, are plotted versus constant yarn volume fraction). The distinction between the two specimens is about 12 percent in area. This shows up in the moduli at 3000°F and 4000°F (the issue is confused at 5000°F by strain rate) and makes the odd data point at 70°F even more out of line. The CC-5 specimen should better reflect the fiber volume in the bulk cylinder.

A composite plot of probable value curves, based on the radial cut specimens response with the square specimen response factored in, is provided in Figure 98.

Torsional Shear Results

Six torsional shear stress-strain curves were generated, three each at 70°F and 3000°F. Four of the specimens were from Cylinder 131 and two from Cylinder R327. The data from these runs are shown in Table 17 and the composite stress-strain curves in Figures 99 and 100. It should be remembered in evaluating these data that the resultant stiffness measured is a function of the shearing stiffness in both the ZR and $Z\theta$ planes.

Thermal Expansion

The state of the s

The thermal expansion was measured on specimens from CC-5, R327 and the loose radials cylinder, CC-8. Each curve shown here represents the results of at least one quartz dilatometer (1500°F) and one graphite dilatometer (5000°F) evaluation and

usually two or three graphite dilatometer runs. Figure 101 shows the circumferential thermal expansion. The AHP material expansion is plotted for comparison. The expansion of the AHP material was lower than any of the current materials due mostly to a larger negative dip from 70°F to 1500°F. The CC-5 and R327 data were intermediate and the value for the loose radial (CC-8) cylinder material (134-2) is highest. The specimens from 131 seemed to "peel off" from the rest of the data at about 4800°F and had a negative return while R327 specimens continued up. CC-8 also tended to peel over, starting at 4500°F. The axial thermal expansion curves, shown in Figure 102 show the same trends as do the circumferential expansion curves. Again, the material from CC-5 bends over at about 4800°F and has a negative return. In the radial direction, Figure 103, the expansions are much higher and have no negative dip. This is expected due to the WYB reinforcements in the radial direction which have a much higher expansion than the Thornel 50 used in the axial and circumferential directions. The specimens from CC-8 (loose radials) had a much higher expansion than did either the AHP material or the R327 specimens, due, apparently, to the lack of bonding of the axial/circumferential "plies" by the radials. While the CC-8 expansion is much higher through the entire temperature range, the rate of radial expansion tends to increase at about 3800°F indicating, perhaps, that the radials let go completely at that point. Extrapolating back using the slope at 3800°F, there is a difference of three mils at that point which, with an approximate one million modulus in the char, would mean a tensile load of 3000 psi which exceeds typical char strength. Thought of another way, the radial pushout strength of CC-8 was about 40 lbs/half inch length, which with 65 radials in a square inch gives 2600 psi to move the radials in half inch thick material (like the radial CTE specimens).

有一种数型数型

Thermal Conductivity Results

The axial thermal conductivity, which should be dominated by the axial yarns, was measured through 5000°F only on CC-8 (134-2). These data are shown in Figure 104. The conductivity of R327-1 was run as a check on these data through 1500°F only. The initial conductivity of R327 was higher than the CC-8 material, as might be expected due to the poorer bonding, but it is almost identical by 1500°F. The radial conductivity results are shown in Figure 105. The conductivity of CC-8 is higher than that of either R327-1 or AHP and the two do not appear to be converging.

Specific Heat

The specific heat was determined on three specimens from R327. The results are shown in Figures 106 (enthalpy) and 107 (heat capacity).

Recommended Design Data for 3DCC Cylinders

A set of recommended design properties for the 3DCC cylindrical material has been generated based on the data generated under this program. Other data, from the AVCO 3DCC hoop tensile tests and the AHP program have been considered in the generation of these values but the values are biased to reflect the more recently produced materials and ignore some of the anomalies shown by CC-8 (loose radials). These values are for cylinders with an A_r/A_t of 0.49 and may not be representative of either cylinders of different A_r/A_t or conical material. Similar recommendations all be presented for conical material in a later section. Some engineering judgements are contained in the selection of these moduli and a discussion of the various elections made is provided in the following.

A plot of the circumferential tensile moduli is shown in Figure 108. Both the CCDP EDP (current effort) data and AHP data are shown in the 70°F column. The average modulus of the ten 70°F rings run under this program is 13.5 x 10° psi. This mean value is supported by the average of the rear 180° values from ring segment tensile (13.9) and the mean of the AHP data (12.9). It is slightly higher than would be anticipated based on the mean of the axial tensile data (8.5)(1.5) = 12.75). Two valid data points exist at 2000°F and 3000°F (one of which was inferred from the data as discussed). These two data points plus the trend of the axial data were used to develop the trend of the circumferential tensile moduli with temperature. After 3500°F the modulus was presumed to fall linearly to one million psi at 6000°F.

The recommended axial tensile moduli are shown in Figure 109. They are based on the mean of the axial data developed under this program. For comparison, the axial compressive and circumferential tensile values are shown. The lack of agreement with the AHP results are not understood but the current data are consistent with fiber volume arguments and with the trend also seen in the circumferential data of the 3DCC slightly stiffer in tension than in compression.

The recommended ci-cumferential compressive modulus curve is shown in Figure 110. The 70°F value was fixed by the curved coupon compressive data and shifted slightly stiffer than the average based on the hydrostatic compressive data (12.7 x 10° psi) and the ring segment data shown. The trend with increasing temperature was based on the trend seen in the axial data rather than the unsupported straight specimens which would have shown a lower value at 3500°F and higher at 5000°F.

The recommended axial compressive moduli are shown in Figure 111. The axial tensile data are shown for comparison. The 70°F modulus is taken from the two R327 specimens, revised down 12 percent per the arguments presented previously then back up to be in line with the relationship to the tensile data seen in the circumferential data. The data point from CC-5 has been discounted as inconsistent based on fiber volume arguments. The trend with temperature is taken from the average of the data with the R327 specimens adjusted for cross-sectional area as shown.

The four curves generated are shown in Figure 112 and in Table 18. The recommended thermal expansion curves are presented in Figure 113 and the recommended thermal conductivity curves in Figure 114. These data do not reflect the somewhat higher expansion and conductivity of CC-8. The ultimate stress data for both the axial and circumferential tensile tests are summarized in Figure 115 and the ultimate strain data in Figure 116.

MECHANICAL AND THERMAL DATA ON THE 3DCC CONE

The matrix and cutting plans established for the 3DCC cone were designed to evaluate the cone with respect to both the distinctions between conical and cylindrical material and also with respect to variation along the length of the cone. Specimens for four key properties, circumferential tensile, axial tensile, torsional shear and thermal expansion, were intentionally excised and from several locations along the length of the cone to monitor the latter. The A_r/A_t of the cone varies from 0.76 at the bottom to 0.52 at the top. (The cylinders were 0.49). One to one comparison with the cylinders will require extrapolation to equivalent A_r/A_t .

· (1) 经汇票

Circumferential Tensile Results

Three hoop tensile rings were taken from the cone, one each from the top $(A_r/A_t = 0.52)$, middle $(A_r/A_t = 0.67)$ and the bottom $(A_r/A_t = 0.76)$. The results of these three runs are summarized in Table 19. The bottom ring was run with strain gages only. The stress-strain curves for the 0° and 90° strain gages are shown in Figure 117. It was very similar in density, velocities and hoop response to the middle ring shown in Figure 118, which was only slightly weaker and softer. Figure 119 shows the top ring, whose response was somewhat different from the other two. The top ring was much less dense (less so than CC-8 which was rejected on the basis of density before the loose radial problem was discovered), lower circumferential and radial velocity, stronger (approximately 40,000 psi versus approximately 25,000 psi) and softer (under the average for the cylinders). A comparison of the response of the three rings is provided in Figure 120 which show probable value curves for each of the three rings. The bottom ring data are approximated based on the strain gage data for that ring and the trend seen in the other two rings between clip-on and strain gage data.

Axial Tensila Results

The axial tensile data on the cone were generated using three different specimens, one for those near the top (specimens 1, 2, 3, 4 and 10) which contained five rows of axial yarns, one for the specimens near the middle (numbers 5, 6, 7, 8 and 9), which also contained five rows of yarns and one from near the bottom which contained three rows of axial yarns (numbers 11, 12, 13, 14 and 15). The mean A_r/A_t of the top

specimens was 0.57, of the middle specimens was 0.64 and of the bottom specimens was 0.72. The three were evenly distributed among the four test temperatures, 70°F, 2000°F, 3000°F and 3500°F. All strain measurements were made using balancing clip-ons to alleviate the effect of internal bending of the data. The ultimate stress was calculated using the area at the failure location. Two specimens, T-9-A and T-14-A were broken in handling.

The summary for axial tension is given in Table 20, which lists the specimens by temperature. The averages given are unbalanced in that there is one additional top of the cone data point in the 70°F data. As is evident from Table 20, and as will be discussed later, the axial properties vary along the cone. Composite plots of the stress-strain behavior are provided in Figures 121 (70°F), 122 (2000°F), 123 (3000°F) and 124 (3500°F). Specimen T-1-A was run twice because the pullrod broke on the first loading at about 18,000 psi. On reloading, the response was softer. The modulus given in Table 20 is from the first loading. If the first curve was extrapolated to the ultimate stress, the strain-to-failure would be 0.0035 in./in. which is more in line with the rest of the data generated.

Figure 125 shows a composite plot of the probable value curves broken down both by temperature and specimen location. Since there is typically just one (in a couple of cases, two) curve for each condition, the probable value is different from that presented earlier in that judgements based on a set of data are not possible. Some guidance has been taken from trends in the data, but these curves are essentially as reported in Figures 121 through 124 with evident internal bending and noise in the data removed.

Figure 126 is a map of the fracture locations for these specimens. Only two broke out of the gage section (both towards the top). Despite the narrowing of the specimen towards the top almost half (5 out of 12) failed in the bottom half of the specimen. This confirms the supposition that the yarns in the direction of loading are the only significant load bearing portions of the material.

Radial Tensile Results

Three radial tensile specimens were manufactured similar to those made from the cylindrical material. Of these, two were damaged prior to test. The value for one specimen tested was slightly higher than the range of the cylinder material. The $A_{\rm T}/A_{\rm t}$ of that specimen was 0.68. The results are shown in Table 21.

Circumferential Compressive Results

The circumferential compressive tests were run at 70°F, 3000°F and 5000°F only. Because of the number of variables involved, the mosts dominant being the use of a straight specimen, it was not deemed useful to complete the matrix. The effect of the straight specimen was discussed in the cylinder data section. The bending was quite evident in these specimens as shown in the composite plots, Figures 127 through 129. At all temperatures the specimen would continue to bear load after peak stress. Both the peak stress and the modulus for these specimens increased dramatically at 3000°F. This is possibly due to the increase in shear modulus over that range as will be presented. The data from these runs are shown in Table 22. The 70°F stress-strain curves, Figure 127, tend to stiffen with increased loading. Choosing the stiffer portion of the

curve for the modulus calculation gives an average value of 6.9×10^6 psi rather than 4.6×10^6 psi as shown in Table 27. All of the specimens came from the lower portion of the cone with specimens 1 through 5 closer to the top, $A_r/A_t = 0.70$, 11 through 15 closer to the bottom $A_r/A_t = 0.72$ and 6 through 10 intermediate.

Axial Compressive Results

7

The axial compressive data are summarized in Table 22. It was generated at 70°F, 3000°F, 4000°F, 5000°F and 5500°F. The 5000°F and 5500°F data were measured at two stress rates, 10,000 psi/min and 100,000 psi/min. The specimens were all from the mid-section of the cone with the Ar/At of the specimens numbered 1 through 7 being approximately 0.62 and the A_r/A_t of specimens numbered 8 through 15 being approximately 0.65. The data generated on these specimens are summarized in Table 23, which gives the density and velocity data generated on the specimen blank, the ultimate strength, the initial elastic modulus and the total strain-to-failure. Four of the specimens were poorly machined, one off center cutting into one row of axial yarns (of three) and the other three centered on a radial row with only two axial rows centered on a radial row with only two axial rows (instead of three). These are labeled in Table 23.

Figure 130 presents the composite axial compressive stress-strain curve at $70^{\circ}F$. The one curve run on the specimen with only 2.5 axial rows is clearly distinguished by its lower modulus and slightly lower ultimate stress. There is good agreement between the other two specimens, both from the same level in the cone. The average modulus without the mismachined specimen was 7.67×10^6 psi. Figure 131 shows the

composite curves for 3000°F. Again, the poorly machined specimen is distinguished by a softer modulus and 'o er ultimate stress. The average modulus without that specimen was 7.17 x 10⁶ psi. The 4000°F data are shown in Figure 132. The two axial specimen were considerably softer than the other two. The average modulus without that curve was 5.06 x 10 psi. The composite curve for 5000°F is shown in Figure 133. Unlike the cylindrical data, the 5000°F, 10,000 psi stress rate data were much softer than the 100,000 psi stress rate data. Unfortunately, the 10,000 psi run was conducted on a radial centered specimen. This, however, may be significant in that if one ratios this modulus by the average ratio of the less than three row specimens at 70°F, 3000°F and 4000°F (0.73), it is still significantly softer than the 100,000 psi/min specimens giving 2.85 versus 4.7 x 106 psi. The 5500°F curves are shown in Figure 134. The effect of stress rate is quite evident as it was in the cylindrical data.

Figure 135 is a composite plot of probable value curves generated on the axial compressive curves at each condition. The curves are based on the full cell specimens only. The $5000^{\circ}F$, 10,000 psi/min curve is modified based on a 1.37 (1/0.73) factor to account for the specimen and is a "best guess" curve. Insufficient data were gathered to sort any distinction in the slight difference ($A_r/A_t = 0.62$ to 0.65) in cone location.

Torsional Shear Results

The torsional shear data desired from conical specimens at 70°F and 3000°F are shown in Table 24. The 70°F data were generated on specimens at three different locations along the cone. The specimens from the middle and top of the cone ($A_r/A_t=0.615$ and 0.555) were nearly identical in response and similar to the average of the torsional shear data from the cylinders (0.209 x 10^6 psi). (The cylinder data showed a distinct difference

between R327 and CC-5). The specimen from the base of the cone $(A_{\rm r}/A_{\rm t}=0.735)$ was much softer than the other two $(0.05\times10^6$ psi). The three specimens run at 3000°F were taken from the same location in the cone $(A_{\rm r}/A_{\rm t}=0.555)$ as Specimen R357-2-TS-2. The average modulus measured on these specimens was much stiffer, 0.396 x 10^6 psi. (The cylindrical value at 70° F is 64 percent of 3000°F value while, with one 70° F data point, the conical 3000° F shear modulus is only 45.5 percent).

Thermal Expansion Results

The results of the thermal expansion measurements in the circumferential direction on the cone (K357-2) are shown in Figure 136. The specimens were taken from three locations in the cone, TE-4-C from the top of the cone $A_r/A_t=0.54$, TE-5-C from one quarter of the way down the cone $A_r/A_t=0.57$ and TE-1-C and TE-2-C from one third of the way up from the bottom $(A_r/A_t=0.68)$. A fifth specimen, TE-3-C, was destroyed during testing.

The response of all four specimens was essentially identical under 2000°F. Above that temperature, the specimen from the top had a higher expansion than the rest until about 4100°F where it began to shrink. The test was discontinued at 4600°F. When run again the specimen began to shrink again at about 4500°F. It shrank 0.6 mils/inch during the first run to 4600°F and over a mil/inch during the second run to 5100°F. Specimen 5, taken from about three inches further down the cone also began to expand less at about 4300°F and after the run (5100°F) had shrunk 1.3 mils/inch. The other two specimens showed the slight residual expansion typical of carbon-carbons. The expansions of Specimens TE-1-C and TE-2-C were more consistant and were higher than the cylindrical data, as shown in Figure 136.

Axial Thermal Expansion - The axial thermal expansion results are shown in Figure 137. The specimens came from three locations of roughly 72, 72 and 65 A_r/A_t . Through 4000°F, the specimen highest in the cone, TE-3-A, had the highest expansion and vice versa. After 4000°F, 3-A did not expand as much as the other two. All three were fairly similar in expansion to the cylindrical material.

Radial Thermal Expansion - The radial thermal expansion results are shown in Figure 138. All of the specimens came from near the bottom of the cone $(A_r/A_t=0.72 \text{ to } 0.75)$. The radial expansion of these specimens was higher than the axial and circumferential directions (WYB) versus T50 yarn).

Thermal Conductivity Results

The thermal conductivity data generated are presented in Figures 139 (axial) and 140 (radial). In both cases the conductivity appears to be a function of the $A_{\rm r}/A_{\rm t}$. In the axial direction the conductivity is lower than for the cylindrical direction. The average $A_{\rm r}/A_{\rm t}$ of the axial specimens from the cone was about 0.72 or about 75 percent of the axial fiber volume fraction of the cylindrical material $A_{\rm r}/A_{\rm t}$. This is almost exactly the ratio maintained between the two curves through 2000°F after which the ratio is slightly lower (0.7 at 4000°F). Similar results, with the order reversed, are seen in the radial data. CR-2R was taken at an intermediate $A_{\rm r}/A_{\rm t}$.

Specific Heat

The specific heat was determined on three specimens from Cone K357-2. The results are shown in Figures 141 (heat capacity), and 142 (enthalpy).

Variation of Properties Along the Cone

As expected, there are variations of the properties along the cone, most of which can be defined by the changing structure (A_r/A_r) * but which also might be associated with the effect of the changing diameter. The properties available with a wide variety of A_r/A_t 's are the circumferential tension, axial tension, and to a much lesser extent, axial compression. The circumferential tensile data were shown in Table 19. The ring is softer but stronger at the top. As the circumferential volume fraction is not changing, this is probably due to differences in the manufacture of smaller diameter pieces. The change in modulus is also monitored in the change in circumferential velocity. Little difference is seen in the circumferential expansion (the top is slightly higher) except for the shrinking problem near the top discussed earlier. The axial direction shows the strongest correlations as would be expected as the axial fiber volume ratio is decreasing with increasing Ar/At. The effect of changing A_r/A_+ on the axial tensile modulus is shown in Figure 143. The data are not always consistent at each temperature (one data point each), but the trend of decreasing stiffness going down the cone is clear. The effect on strength is more distinct as shown in Figure 144. The top specimens are much stronger than the middle ones, which are stronger than for the bottom. The distinction is not clear in the axial compressive data which have only a slight difference in the A_r/A_t (0.62/0.65). However, plots of that data

 $^{^*}A_{\text{T}}/A_{\text{t}}$ is not fully definitive of the structure, since the ratio of yarn areas varies in the R0 plane, but is used as such here.

do indicate the effect of having less than three full cells in the specimen on the data. These are shown for modulus in Figure 145 and strength in Figure 146. The data discussed to this point are summarized in Figures 147 and 148 which over plot the data from several tests in terms of percentage of the highest value obtained for the several A_r/A_t ratios tested. In both figures for strength and modulus, the circumferential data do not appear to sort by A_r/A_t . The axial data, however, are a strong function of A_r/A_t . The axial data sort directly by A_r/A_t with the sole exception of the 3000°F axial modulus which was stiffer in the conical material for equivalent A_r/A_t than in the cylindrical material. After that, it too sorted by A_r/A_t .

Other data which sorted by A_T/A_t were the torsional shear modulus which was much lower at the bottom of the cone, and the thermal conductivities (Figures 139 and 140), which were apparently a direct function of fiber volume fraction.

A first approximation of the variation of 70°F moduli along a cone (changing $A_{\rm r}/A_{\rm t}$) is provided in Figure 149. Other factors aside from $A_{\rm r}/A_{\rm t}$ undoubtedly contribute to these trends which are for Cone K357. Trends of those properties with temperature can be taken from the data presented herein. As the piece to piece variability has been shown to be quite strong, some keying data would be necessary to apply these data to a new piece.

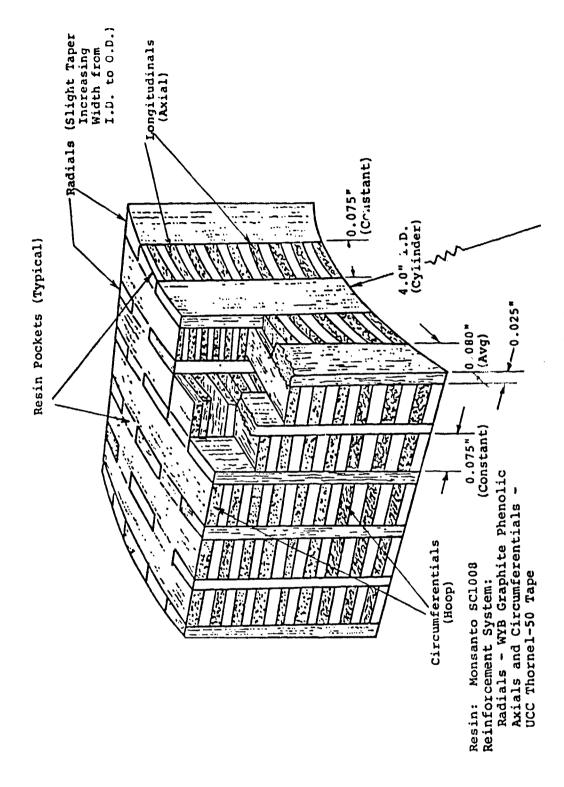
CONCLUSIONS

This report has provided a data package for both the cylinder and conical forms of AVCO 3DCC. The package for the cylinder is more complete in that there was one less variable to be considered. It provides a baseline with

which to interpret the conical data though the trends were not always the same between the two. Variability from piece to piece of these materials has been documented both nondestructively and mechanically. There did not appear to be one test which would characterize the quality of a material by itself. For example, CC-8, which was substandard by a number of criteria, but looked good in circumferential tension.

Several new tests have been qualified under this program, and now form an expanded array of techniques available for evaluating materials for this and similar applications.

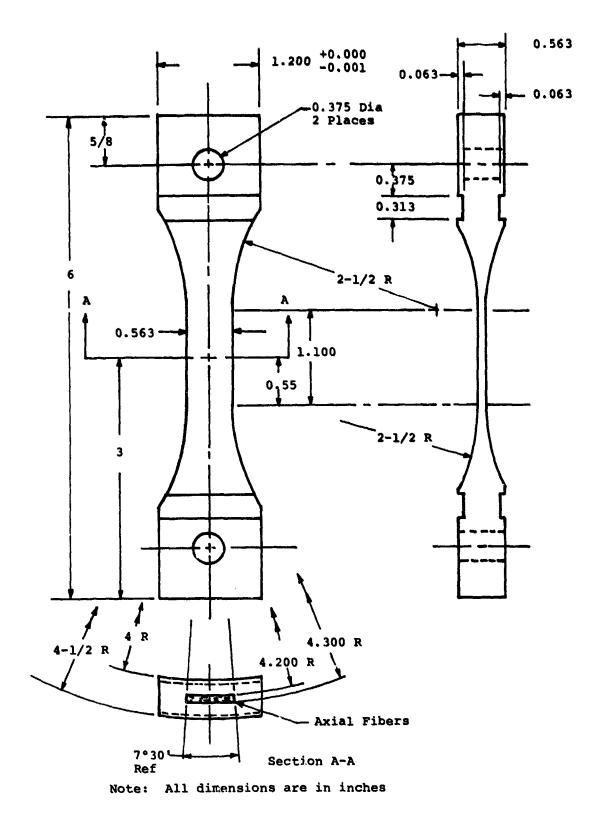
The nature of the background and anomalous structure identified under this program aid the evaluation of damage in these materials and the properties generated provide a virgin baseline for the degraded properties currently under investigation as well as a baseline data package for carboncarbon heatshield design efforts.



は、一個ないのでは、

ì

Figure 1. Schematic of Material Structure for AVCO 3DCC



The second secon

Figure 2. Tensile Specimen for Axial Evaluations of Cylindrical 3DCC

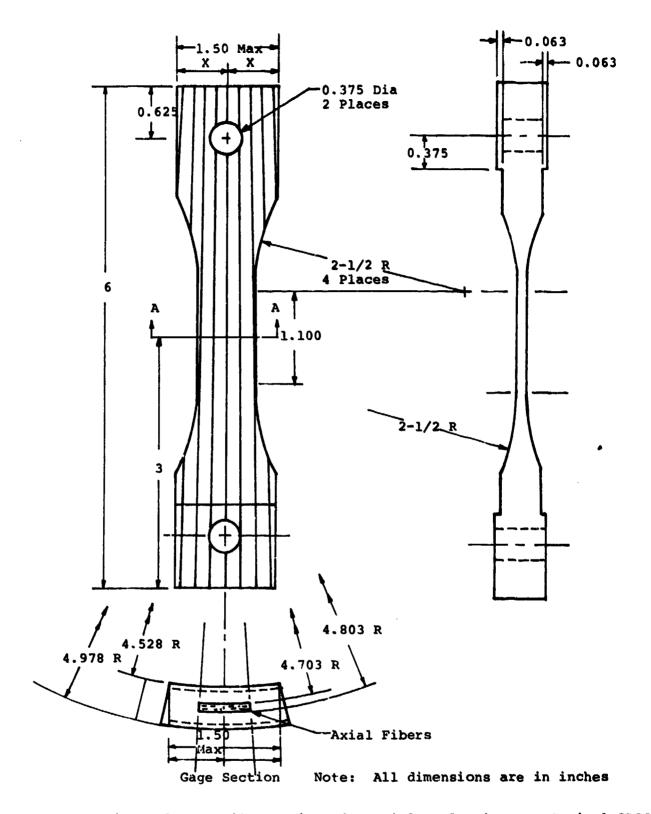
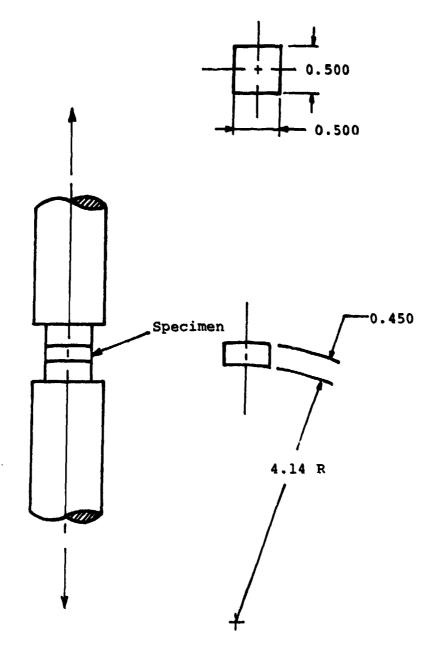


Figure 3. Tensile Specimen for Axial Evaluations on Conical 3DCC



Note: All dimensions are in inches

Figure 4. Radial Tensile Specimen for AVCO 3DCC

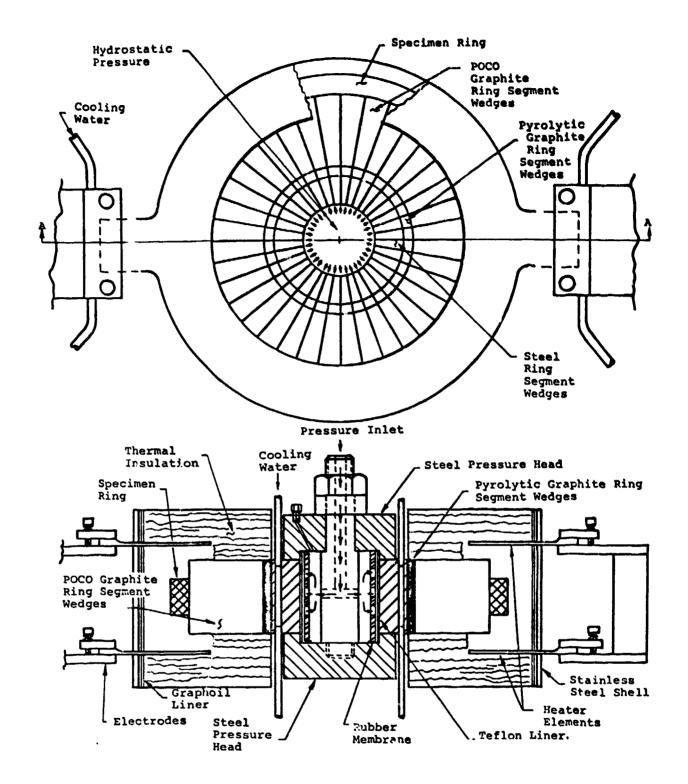
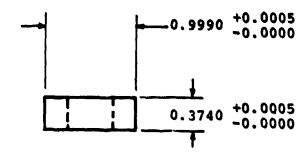
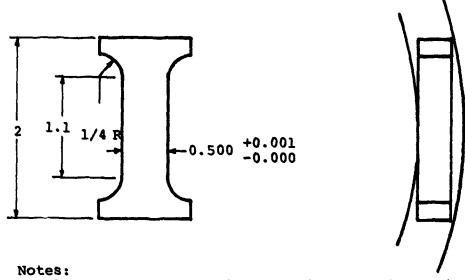


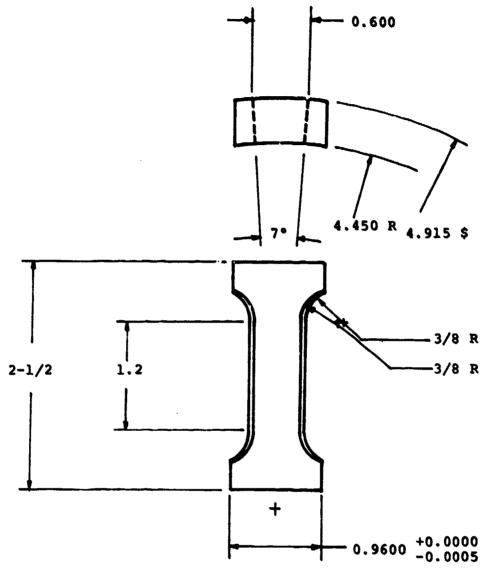
Figure 5. Schematic of High Temperature Hoop Facility





- 1. Tolerances: Decimal ±0.005; Fraction ±1/64
- 2. All dimensions are in inches

Figure 6. Circumferential Compressive Specimen for AVCO 3DCC Cylinder and Cone



Note: All dimensions are in inches

Figure 7. Axial Compressive Specimen and Torsional Shear Specimen for AVCO 3DCC Cone

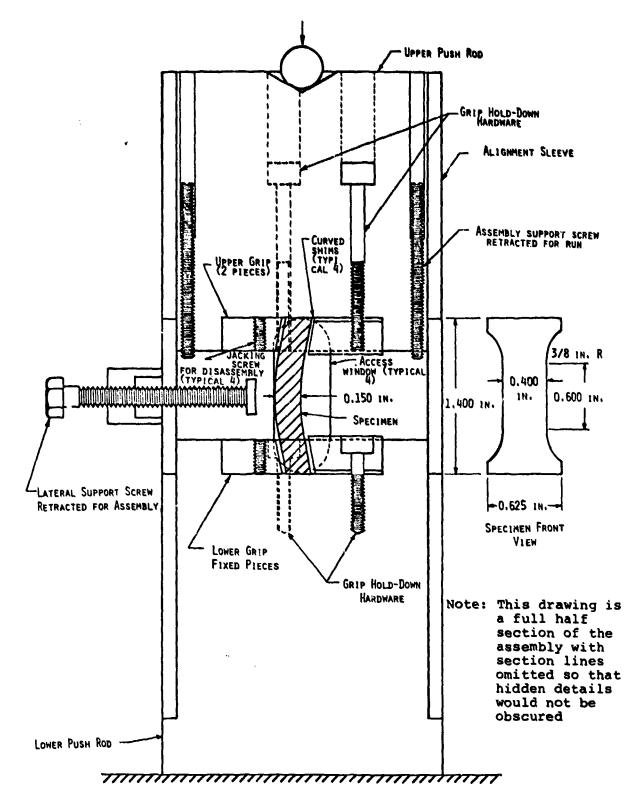
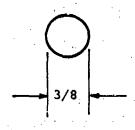


Figure 8. Curved Specimen Compressive Test Fixture



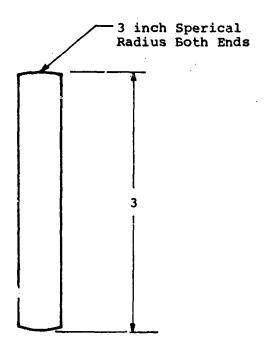
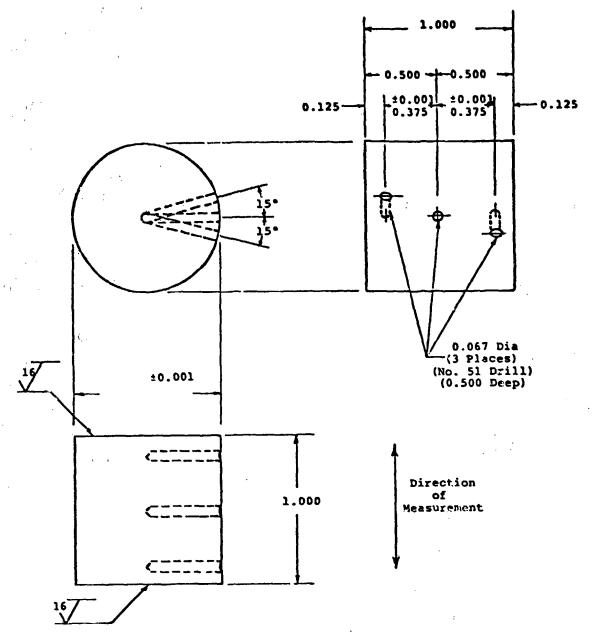
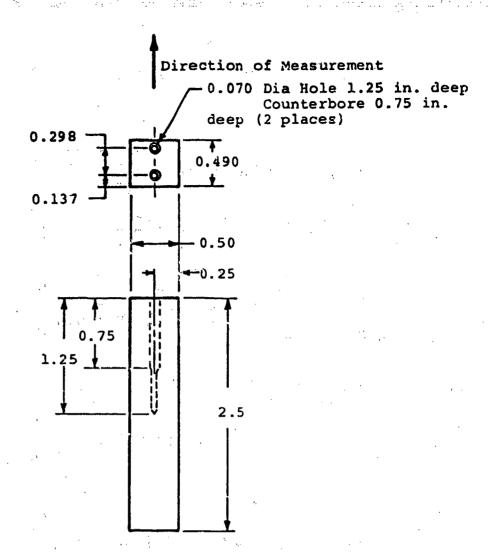


Figure 9. Thermal Expansion Specimen for AVCO 3DCC



Note: All dimensions ±0.005 except where noted

Figure 10. Drawing of Specimen for Thermal Conductivity Measurements in Comparative Rod Apparatus



Notes:

- 1. All dimensions are in inches
- 2. 4 strips = 1 specimen

Figure 11. Radial Inflow Strip Specimen

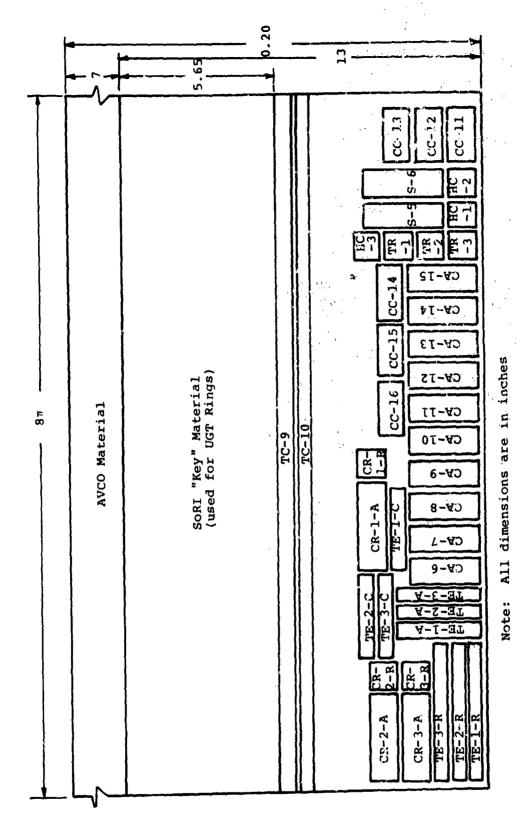
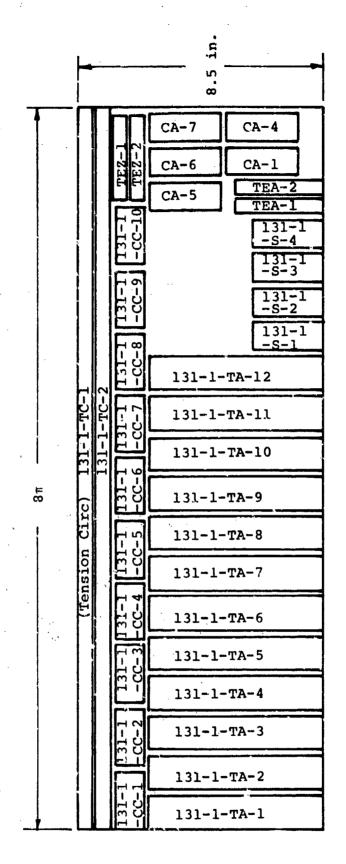
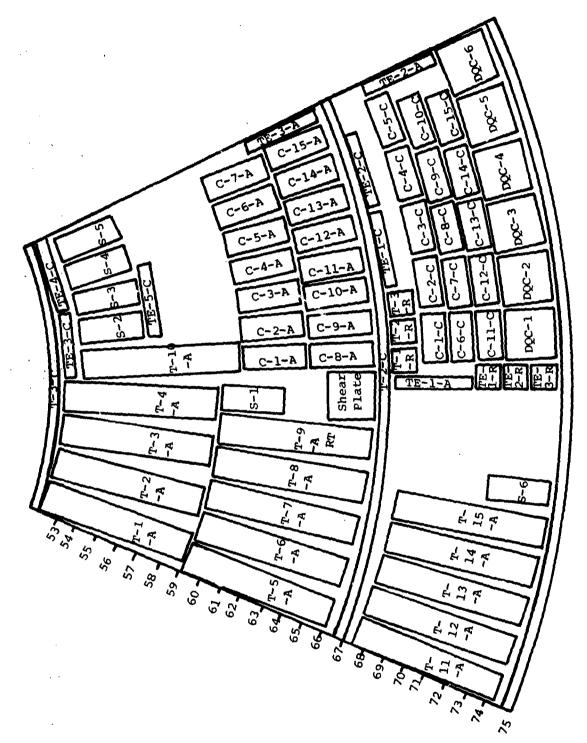


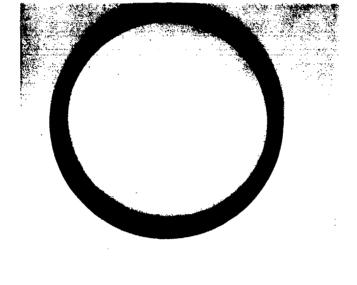
Figure 12. Cutting Plan for AVCO 3DCC Cylinder R327-1



Cutting Plan for AVCO 3DCC Cylinder CC-5 (131-1)

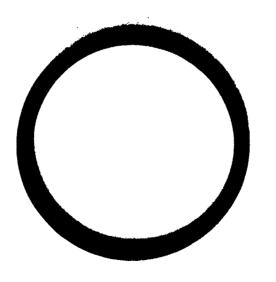


igure 14. Cutting Plan for AVCO 3DCC Cone K357-2





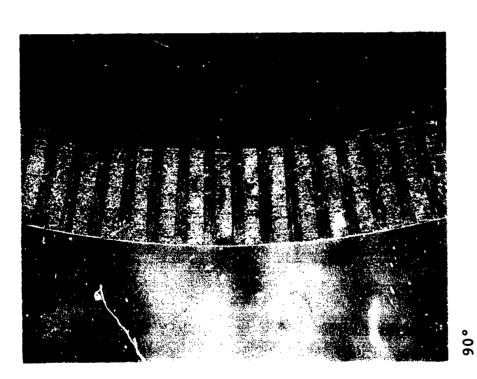
Bottom



The second secon

Figure 15. Top and Bottom of CC-3





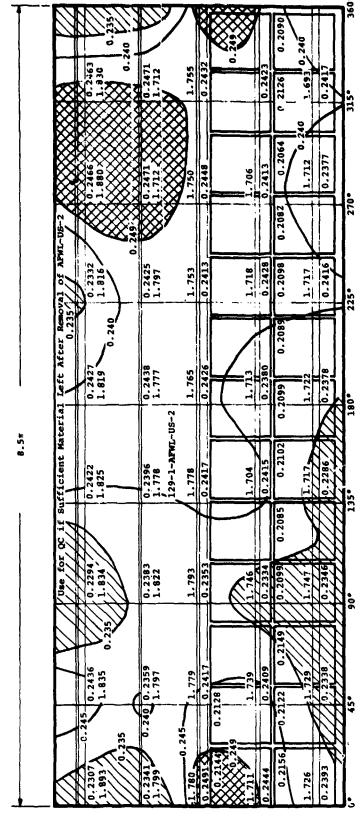
225°

Figure 16. Structure of CC-3

1.80		1.755		+	23	, 0.2126 0.2090 129-1- 129-1- RSA-12 RSA-13	0.2417	315
1.830		1.750	· •	GGA-9	0.2413	0.2064 1.712 1.712	0.2377	270
1.816	1.797	1. 753	腽	1.718 GGA-8	0.2428	0.2098 129-1- 129-1- RSA-9 RSA-9 RSA	0.2416	225°
1.819	1.777		15	.129-1- 129-1- GGA-5 GGA-6	0.2380	0.2099 0.2089 129-1- 129-1- RSA-7 RSA-8	0.2378	180
1.825	1.778	129-1-AFWL-US-2		1- 129-1- 3 GGA-4 1.704	0.2415	5 0.2102 129-1- RSA-6 1.717	0.2286	135•
1.834	1.866	1.7937	1.76	129-1-129-1- GGA-2 GGA-3	1 2	0.2099 0.208 129-1- RSA-4 1.747 RSA-5	0.2346	• 06
1.835	1.82	1.7.9	0.2128	129-1- 129-1- RSA-15 GGA-1- 11.739	0.2409	0.212: 129-1- 158-2 .29-1- 158-2 1.725	0.2338	45.
1.843	762.1	1.780	0.2491	7	0.2444	0.2165 129-1- 129-1 RSA-1 1.726	0.2393	0

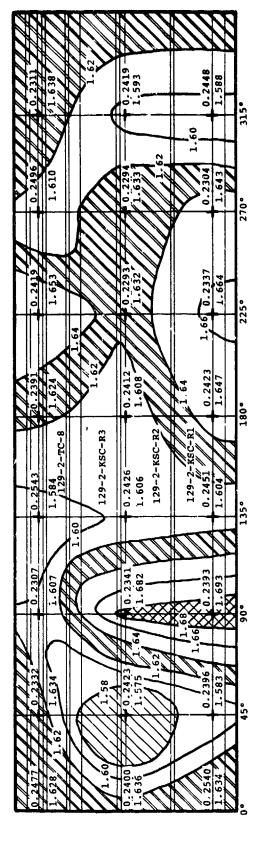
一年 一种 一种

Figure 17. Radiometric Density Map of CC-8 (129-1)



等一 調整器 哲司

Figure 18. Radial Velocity Map of CC-3 (129-1)

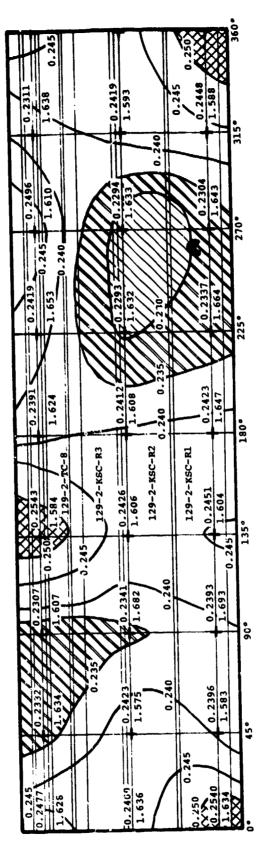


湯を変みない。

Ĭ

は

Figure 19. Radiometric Density Map of CC-3 (129-1)



年一個沙斯三

Figure 20. Radial Velocity Map of CC-3 (127-2)



Top Edge CC4 RI 315°

Bottom Edge CC4 Rl 45°

Figure 21. Typical Structure of CC4

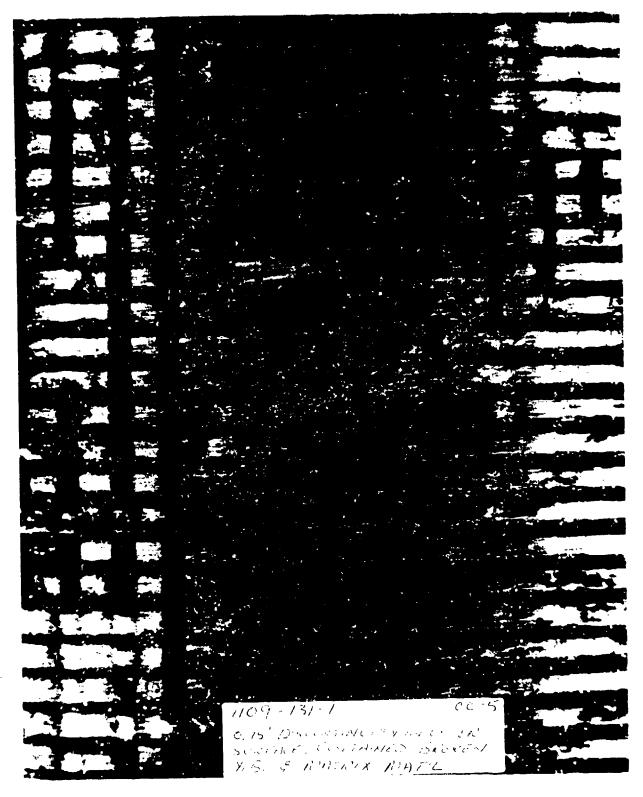
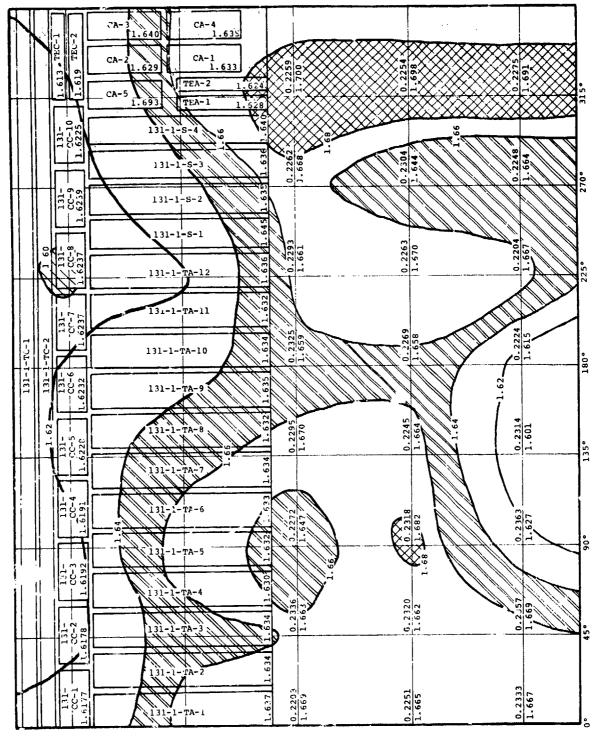


Figure 22. 0.75 Inch Discontinuity in Outer Surface of Cylinder 131-1 (CC-5)



をないない かいまっている

Figure 23. Radiometric Density Map of CC-5

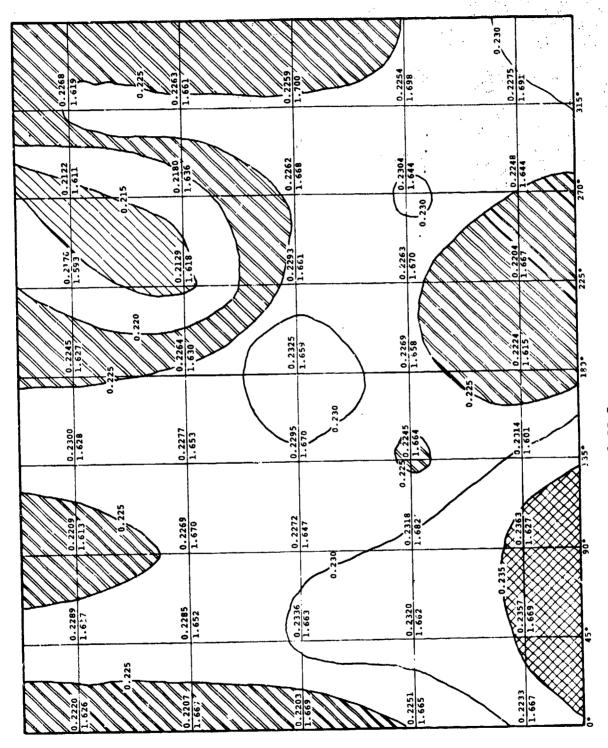


Figure 24. Radial Velocity Map of CC-5

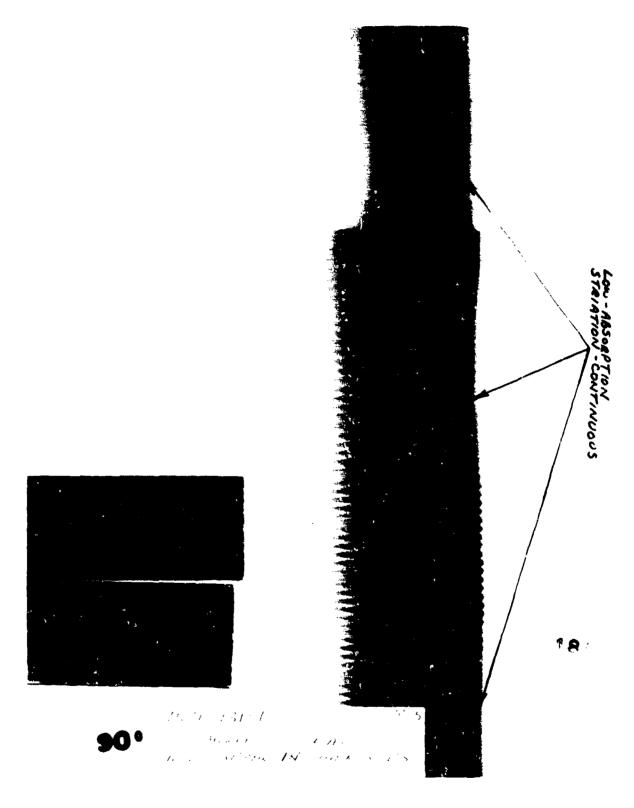
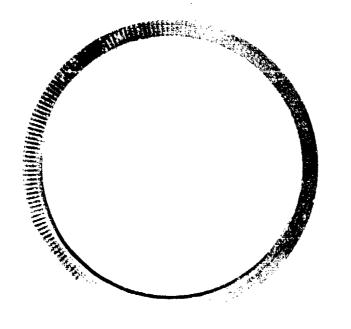


Figure 25. Low Absorptive Striation in Cylinder 131-1 (CC-5) also Typical in Other Cylinders







Top

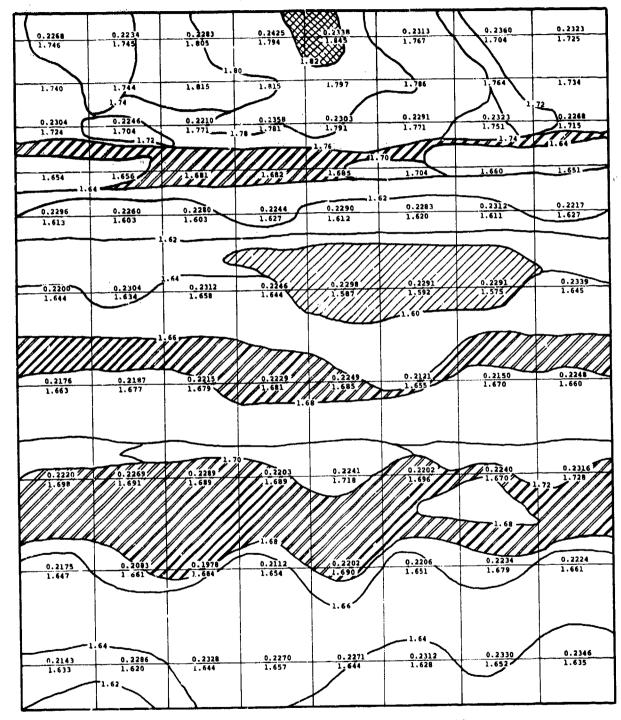


Figure 27. Radiometric Density Map of CC-6 (132-1&2)

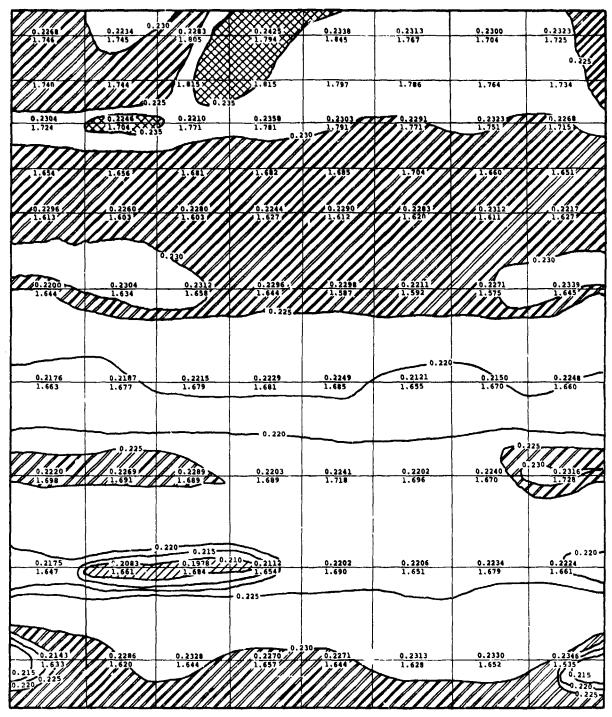
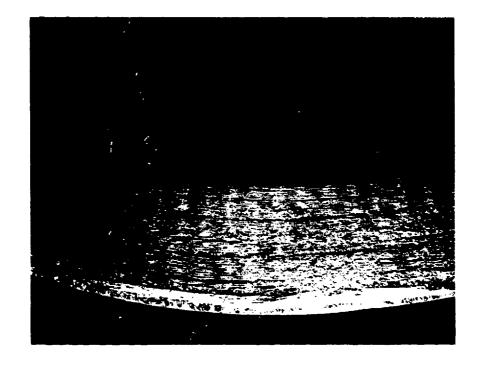
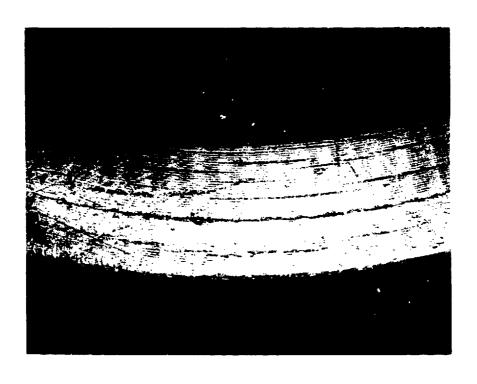


Figure 28. Radial Velocity Map of CC-6 (132-1&2)

から 経過機の





A LK

Figure 29. Debond Areas in CC-6 (132-1) (2X)

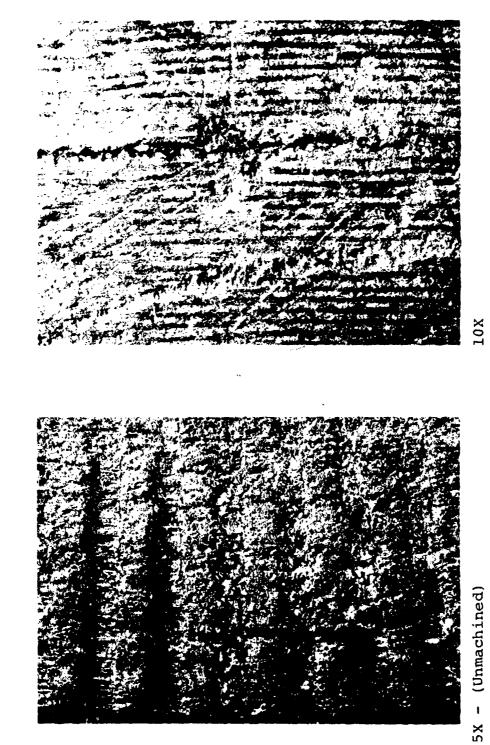
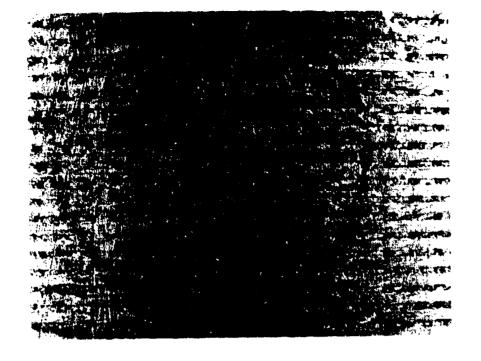
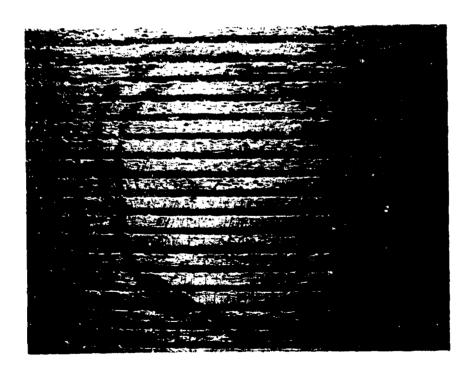
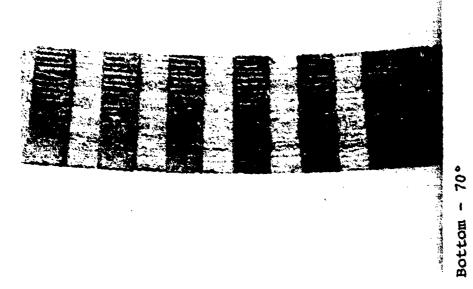
amende de de la company


Figure 30. Debond Areas in CC-6 (132-1)





Cracking Along Circumferential Bundles and Loose Circumferential Bundles in CC-6 (132-1) Figure 31.

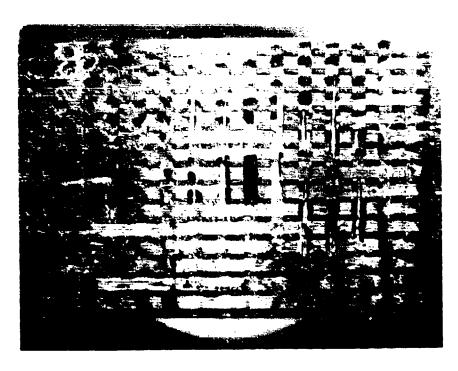






Top - 70°

Debond Areas in 132-1-SoRI-R3 Figure 32.



Zones of Cracking Around Circumferentials in 132-1-SoRI-R3 Figure 33.

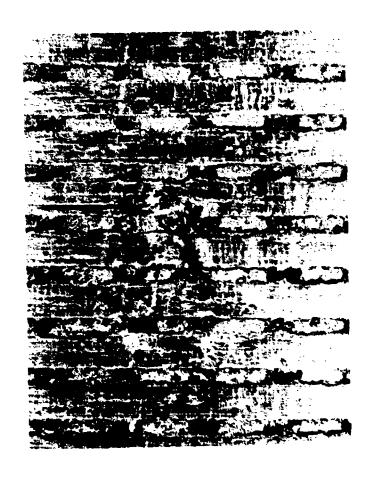
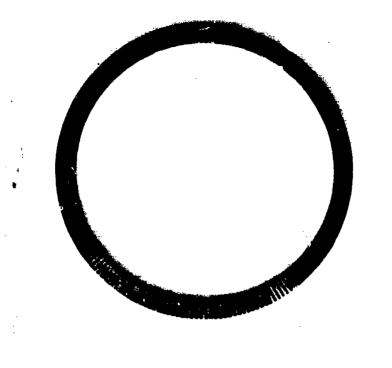
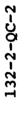
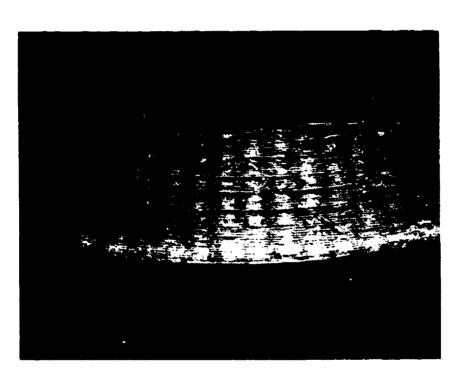


Figure 35. Close Up of External Surface of CC-6 (132-2)



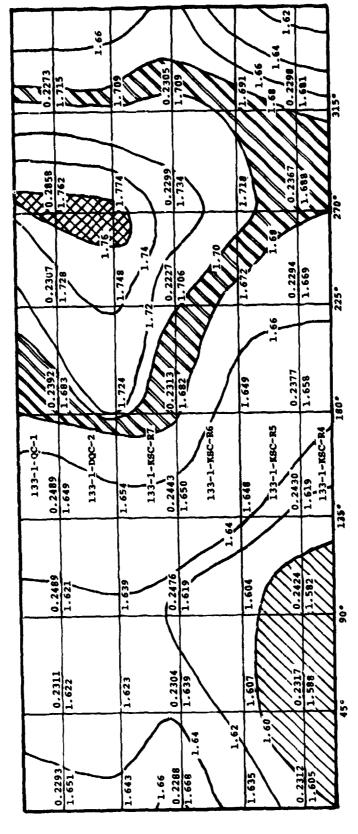




The second second

Unmachined

Figure 34. End Views of KC6 (132-2)

Total Control of the


一 は は ない

Figure 36. Radiometric Density Map of CC-7 (131-1)

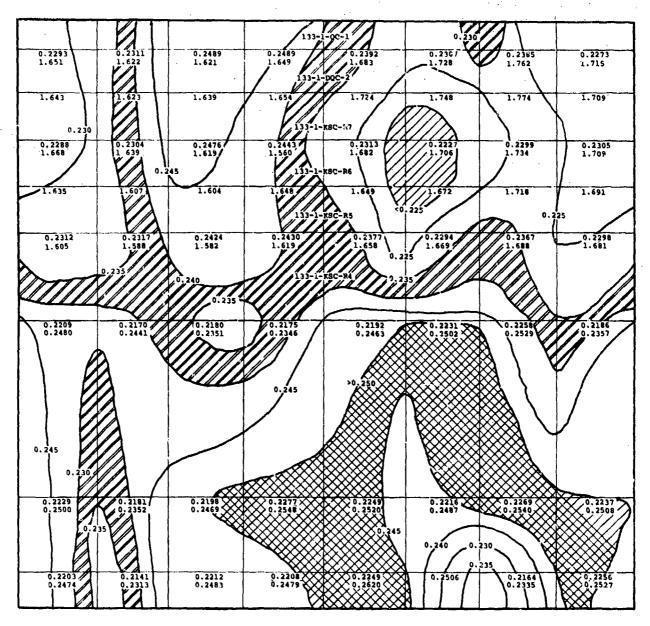


Figure 37. Radial Velocity Map of CC-7 (133-1)

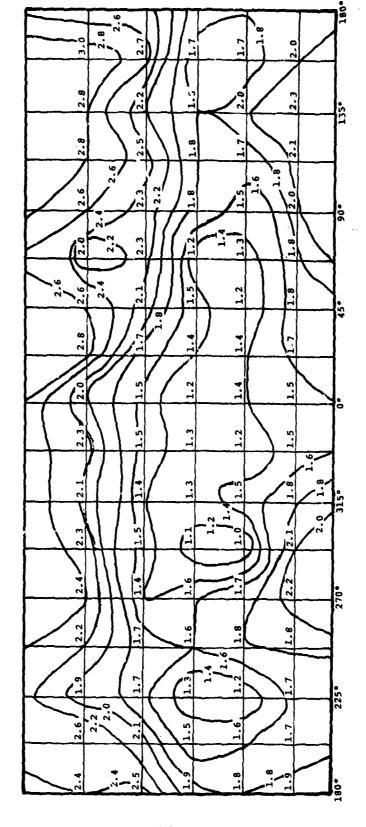
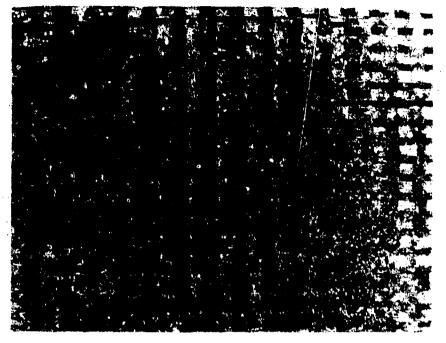
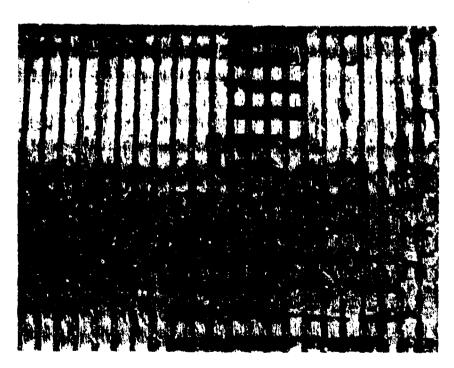


Figure 38. Eddy Current Map of CC-7 (133-1)

Cracking Around Radials in CC7 (133-1)

Figure 39.





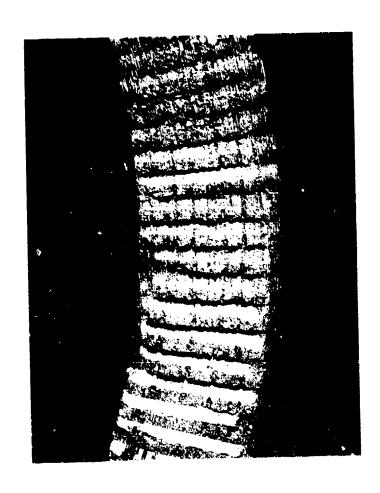
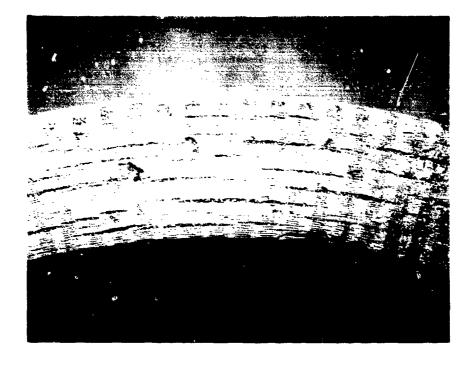


Figure 40. Edge of CC-7 (133-1)



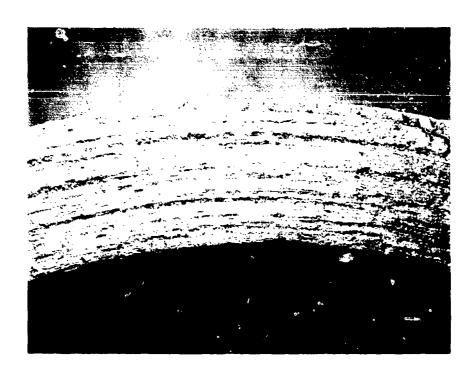
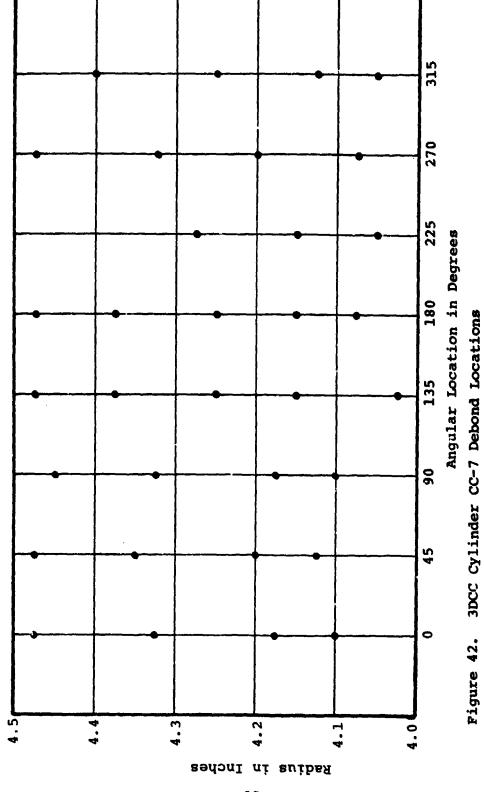
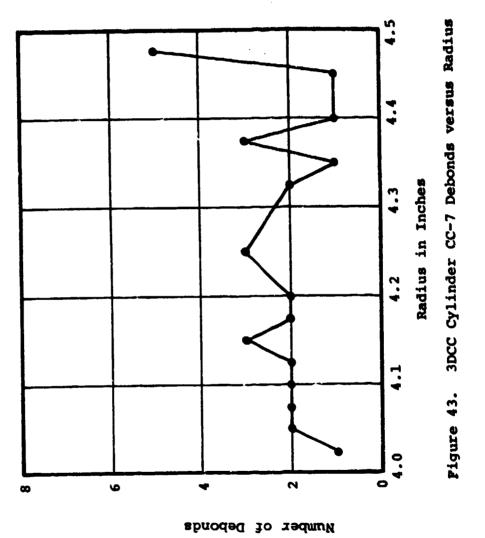


Figure 41. Debonds in CC-7 (133-1)





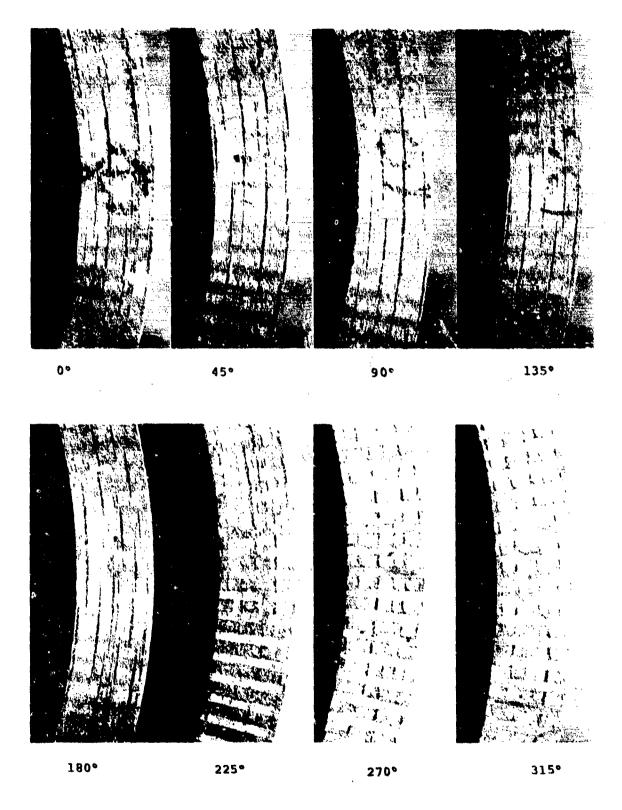
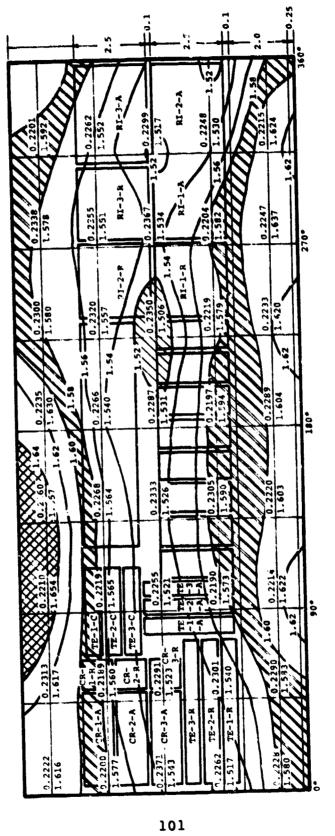


Figure 44. Bottom Edge of Cylinder 133-2 (CC-7) at 2X 100



Radiometric Density Map of CC-8 (134-2) Figure 45.

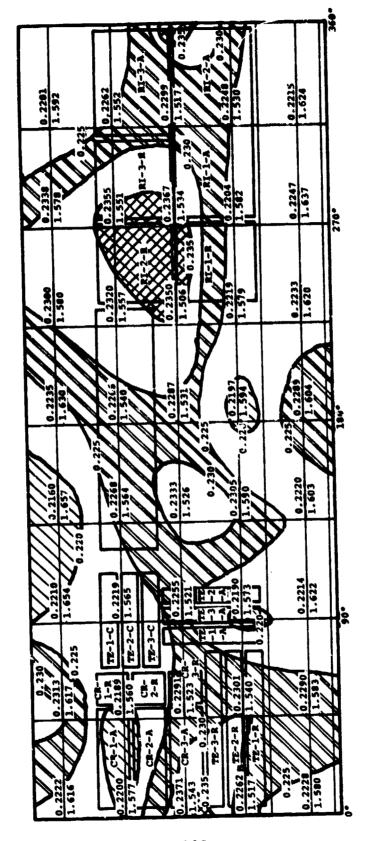


Figure 46. Radial Velocity Map of CC-8 (134-2)

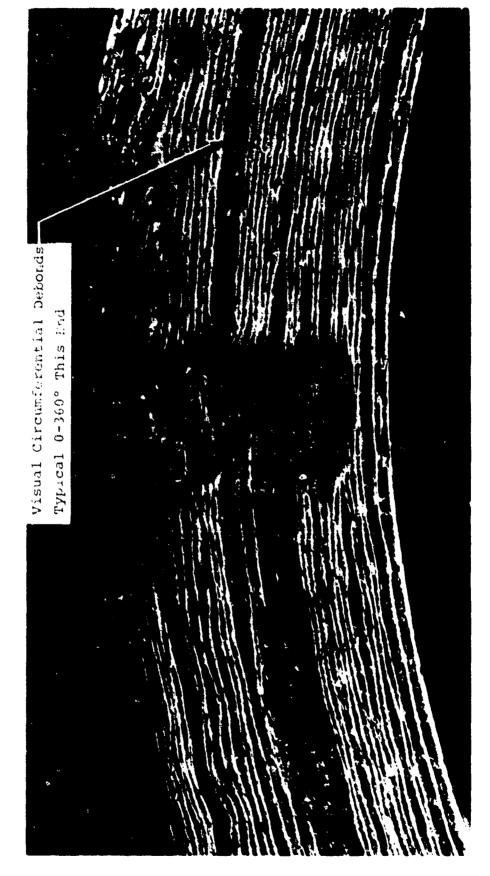


Figure 47. Debond Area in 3DCC Cylinder CC-8 at 0°

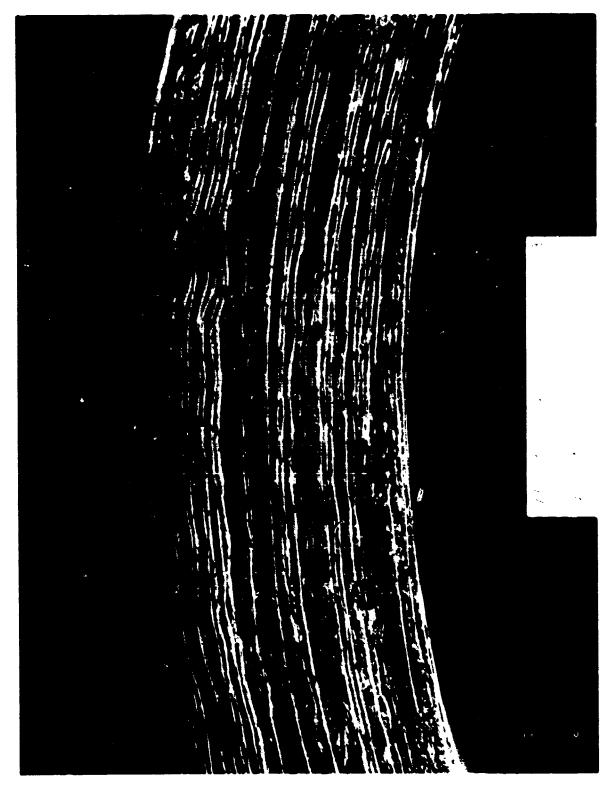
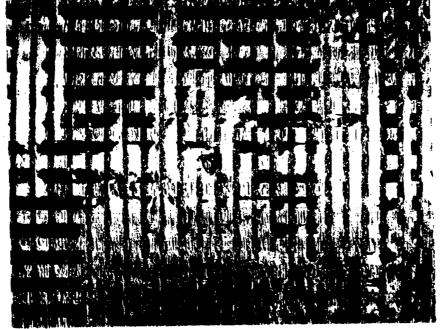
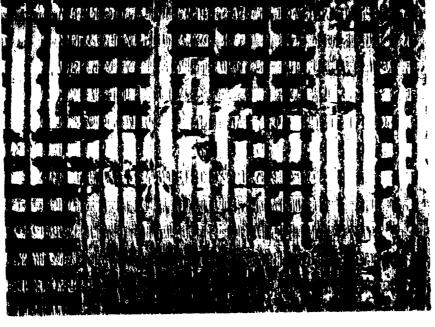


Figure 48. Debond Area in 3DCC Cylinder CC-8 at 90°





Rough Area on External Surface of CC-8 After Reimpregnation

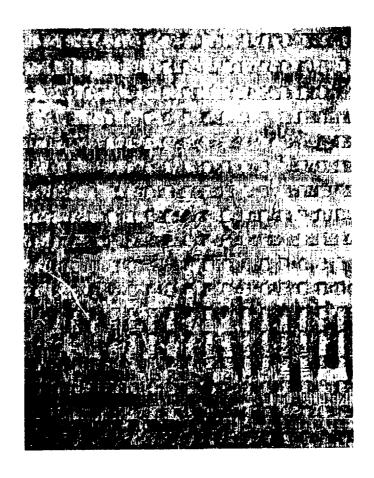
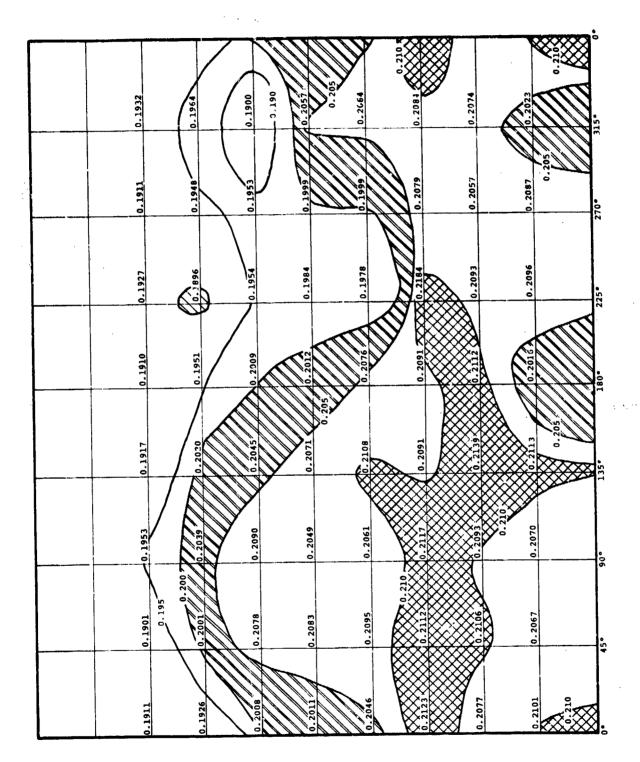


Figure 50. Pushed Radials in CC-8

Figure 51. Radiometric Density Map of R327-1



gure 52. Radial Velocity Map of R327-1

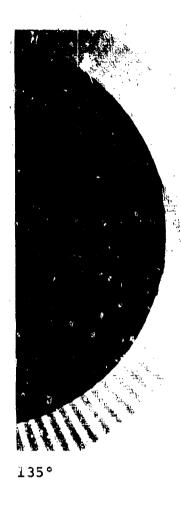


Figure 53. Anomaly on End of Cylinder K327-1

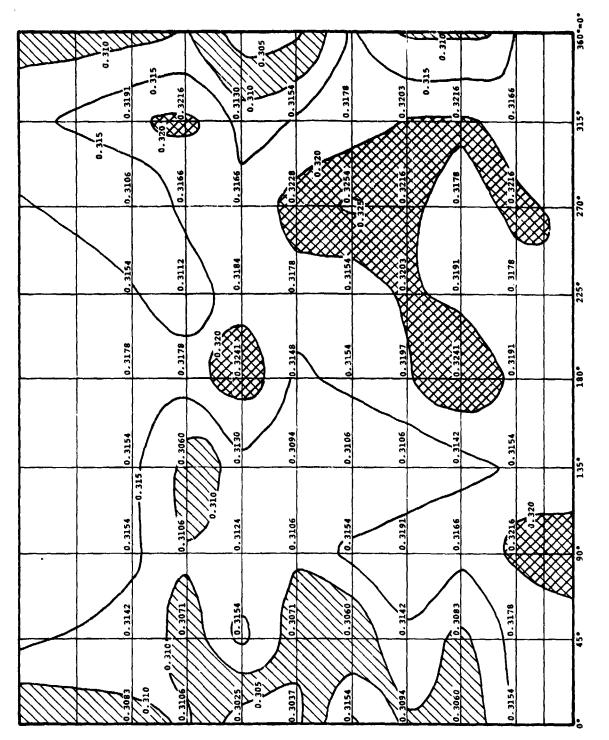


Figure 54. Circumferential Velocity Map of R327-1

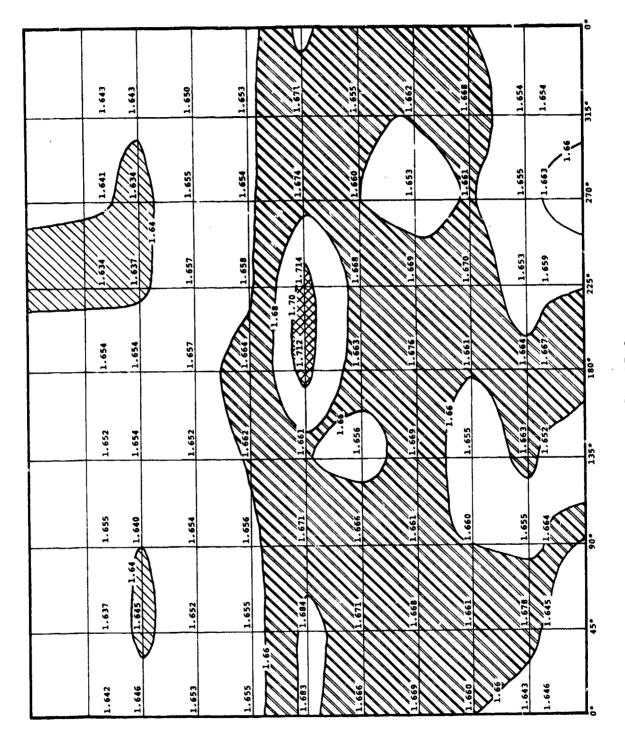
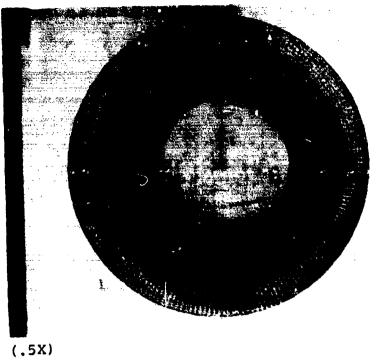


Figure 55. Radiometric Density Map of R327-2



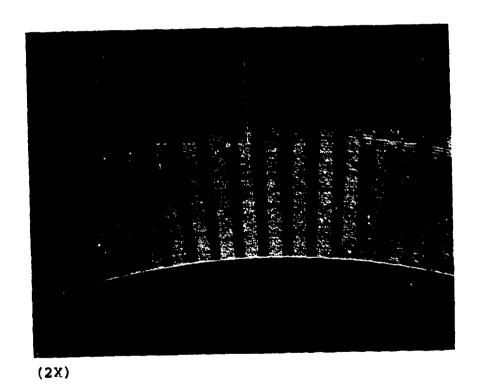


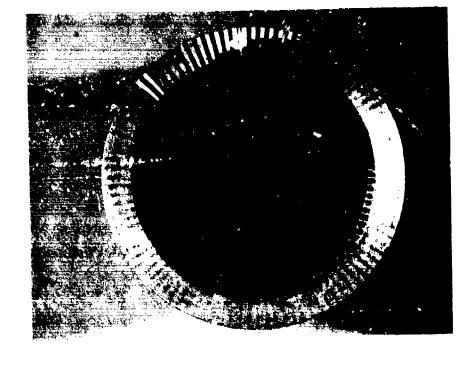
Figure 56. Structure of R327-2

The state of the s

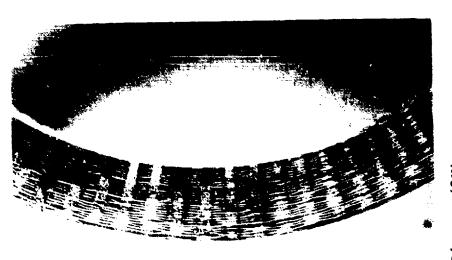
Figure 57. Radial Velocity Map of R327-2



Figure 58. Porous Region in 327-2 on the ID at 225°







Forward Ring - (2X)

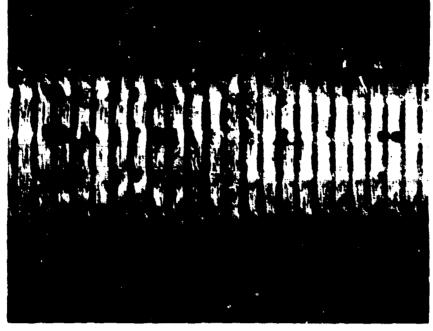
Figure 59. Structure of Forward Section of K357-1



3ottom



Top





A. Bottom 70°

B. Outside 130°

Porous Matrix Areas of Cone K357-1 (2X) Figure 61.

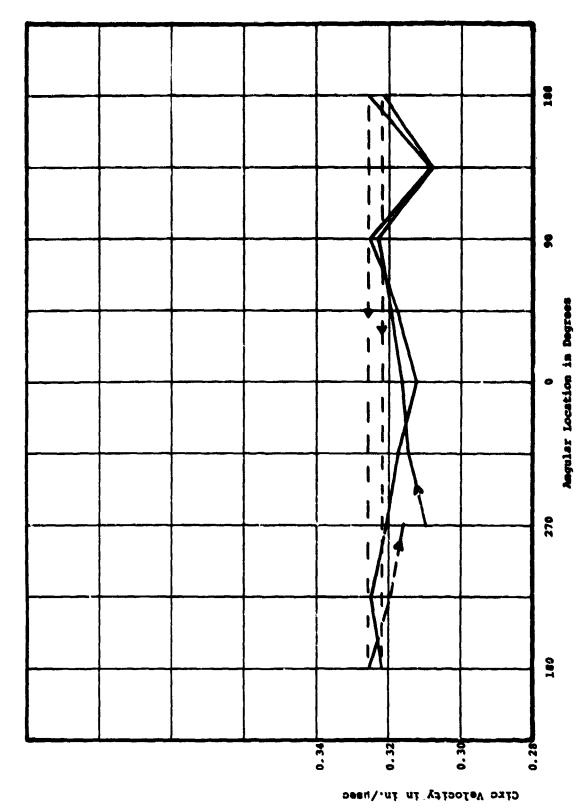
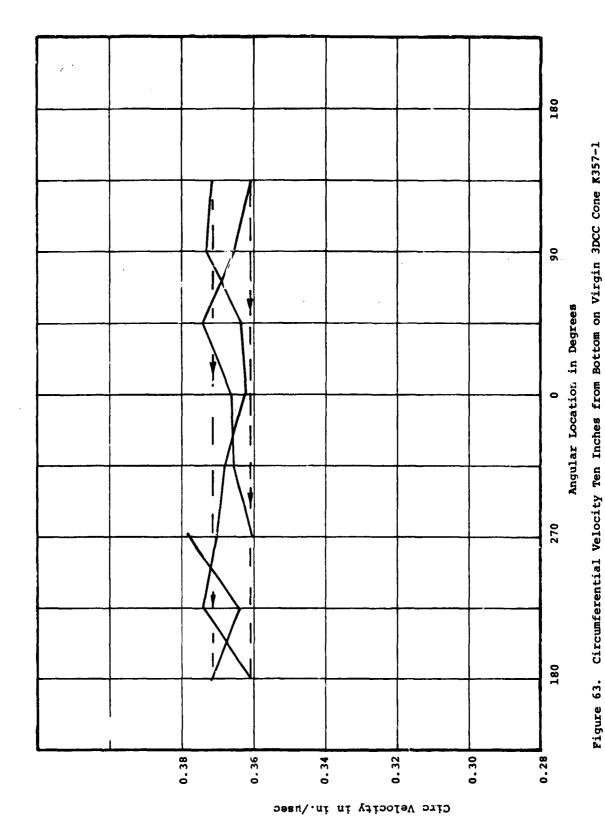
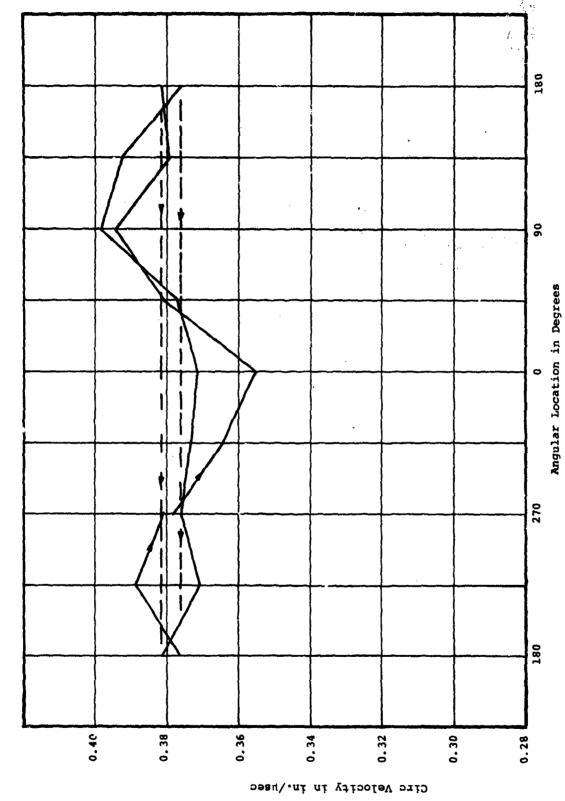


Figure 62. Circumferential Velocity at Top on Virg's 3DCC Cone E357-1



A STATE OF THE PROPERTY OF THE

119



Pigure 64. Circumferential Velocity One Inch from Bottom on Virgin 3DCC Cone K357-1

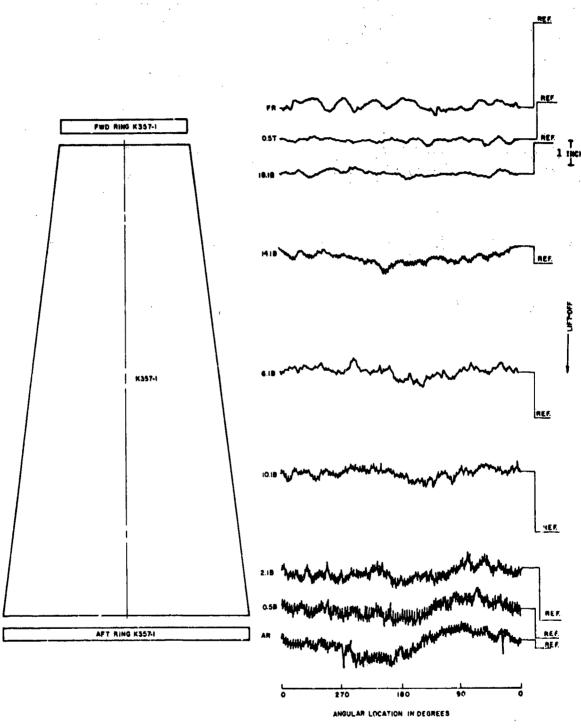


Figure 65. Eddy Current Traces for Virgin 3DCC Cone K357-1 100 KHz 0° Lift-Off

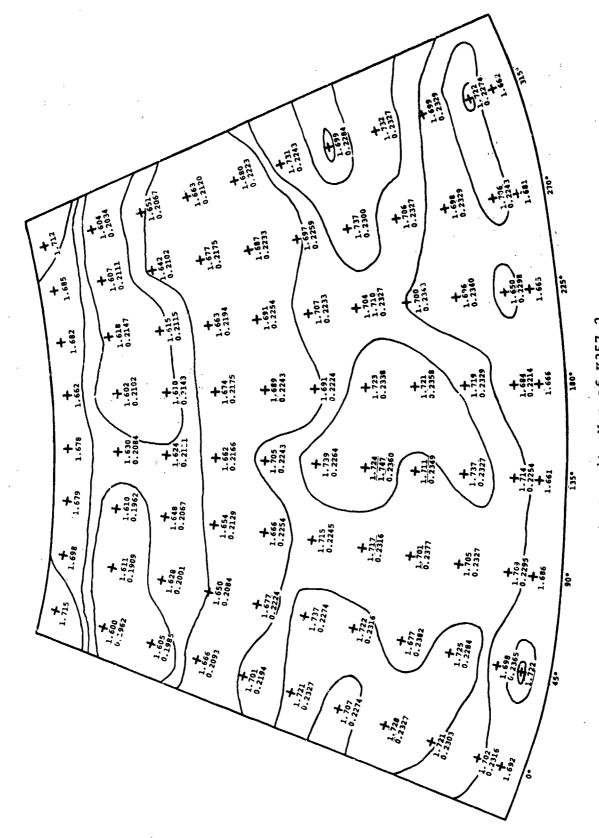


Figure 66. Radiometric Density Map of K357-2

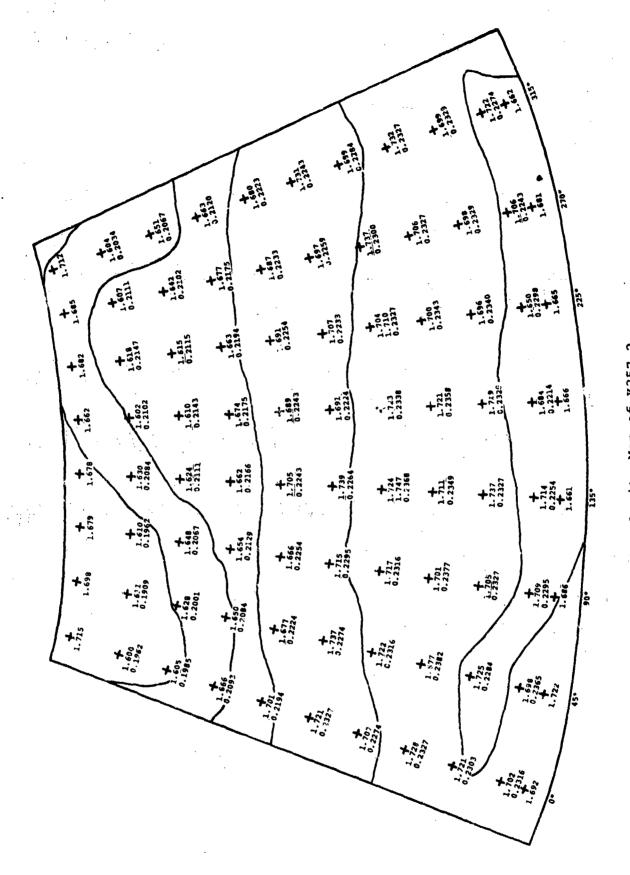
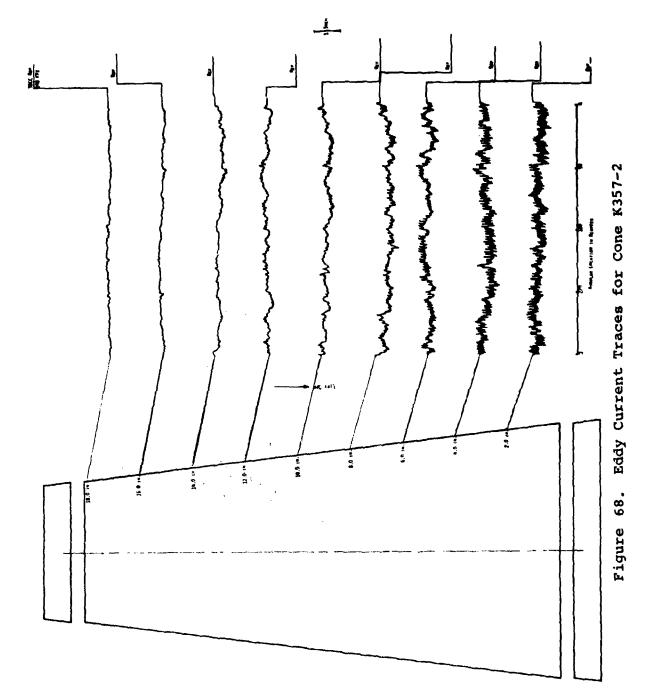


Figure 67. Radial Velocity Map of K357-2



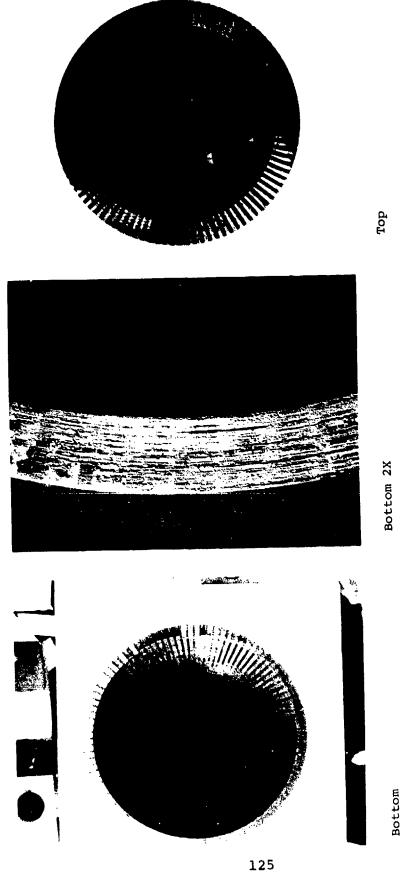
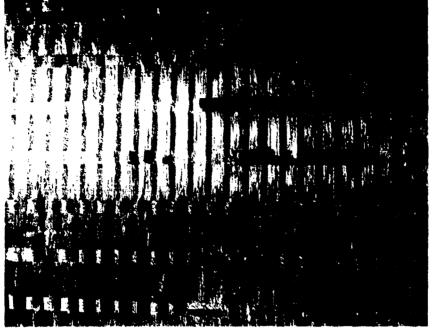
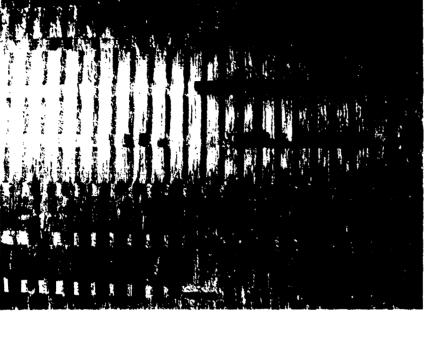
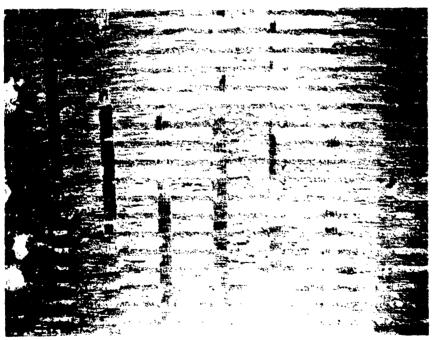


Figure 69. Structure of Ends of K357-2







Porous Areas in Cone K357-2

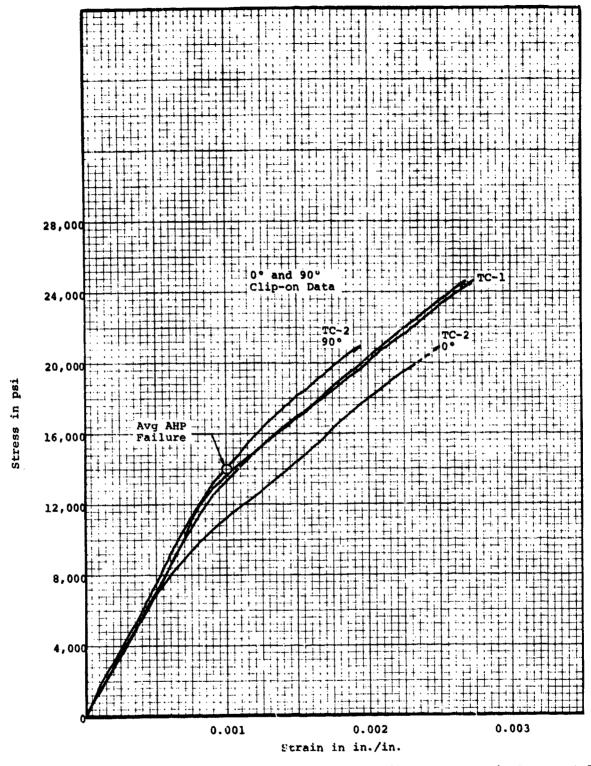


Figure 71. Cylinder 131-1 (CC-5) Hoop Tensile Stress-Strain Curves at 70°F

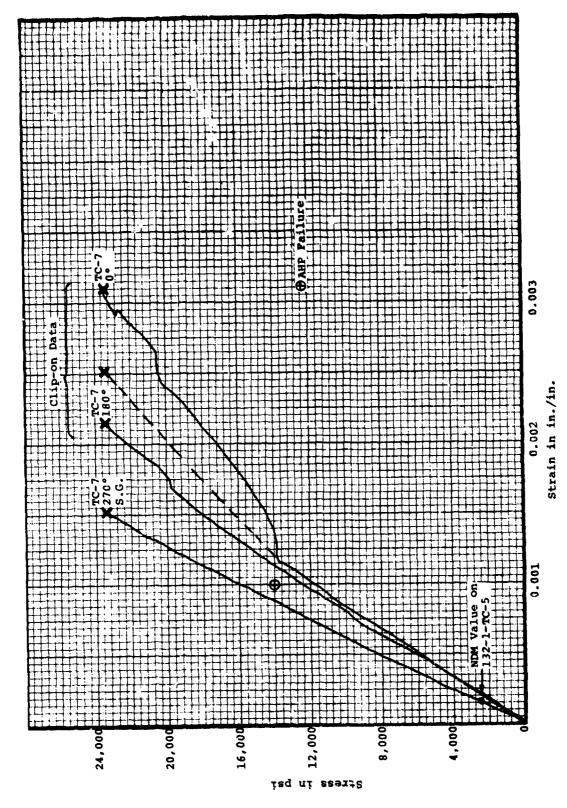
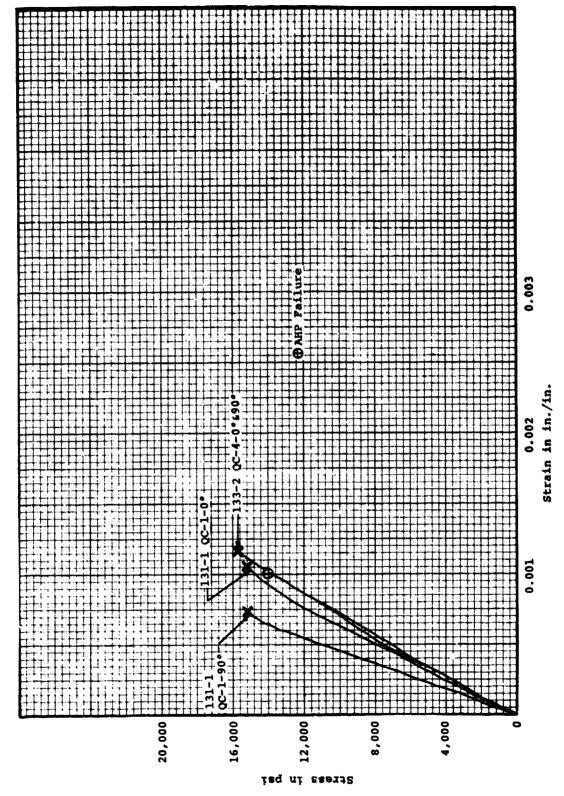


Figure 72. Cylinder 132-1 (CC-6) Hoop Tensile Stress-Strain Curves



re 73. Cylinder 133-2 (CC-7) Hoop Tensile Stress-Strain Curves

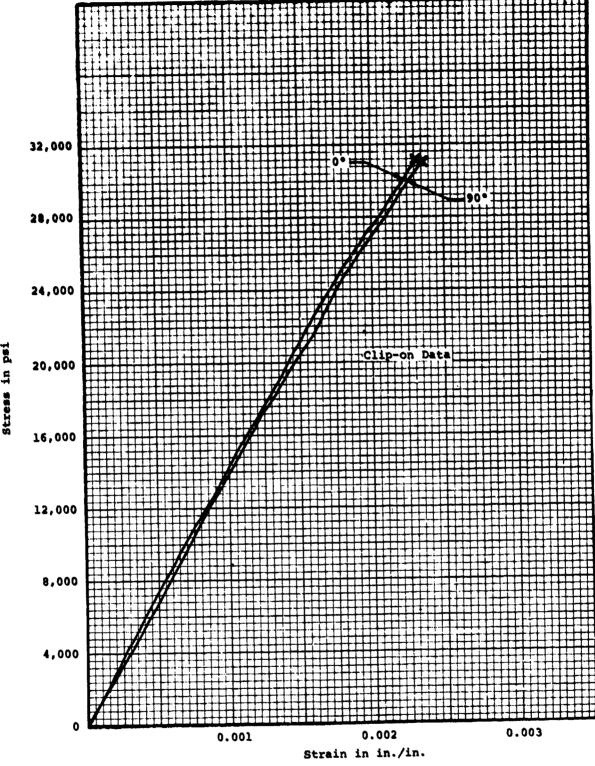


Figure 74. Cylinder 133-2 (CC-7) Hoop Tensile Stress-Strain Curves at 70°F

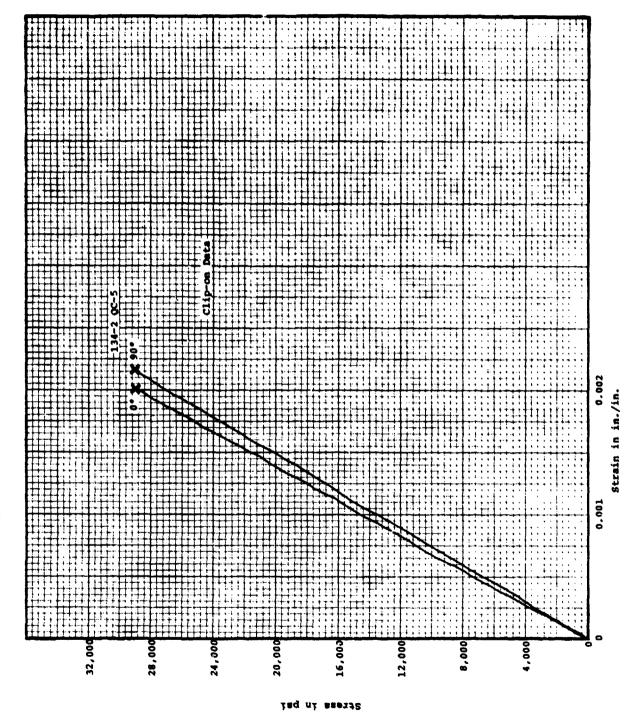
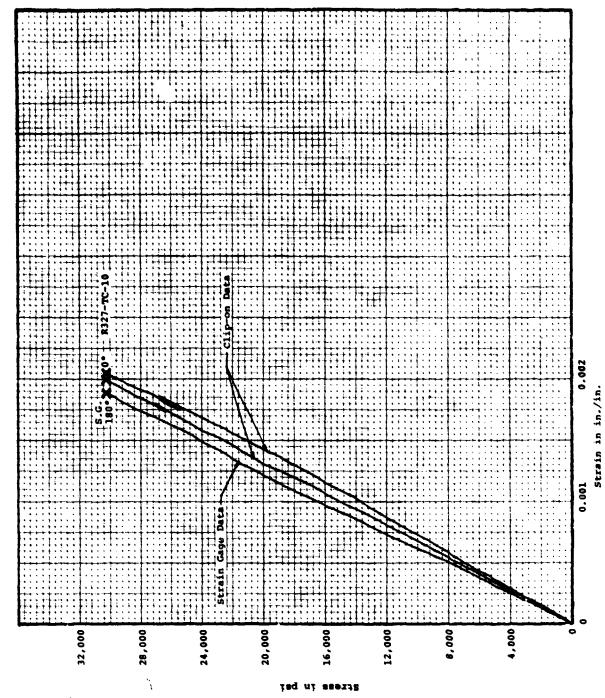


Figure 75. Cylinder 134-2 (CC-8) Hoop Tensile Stress-Strain Curves at



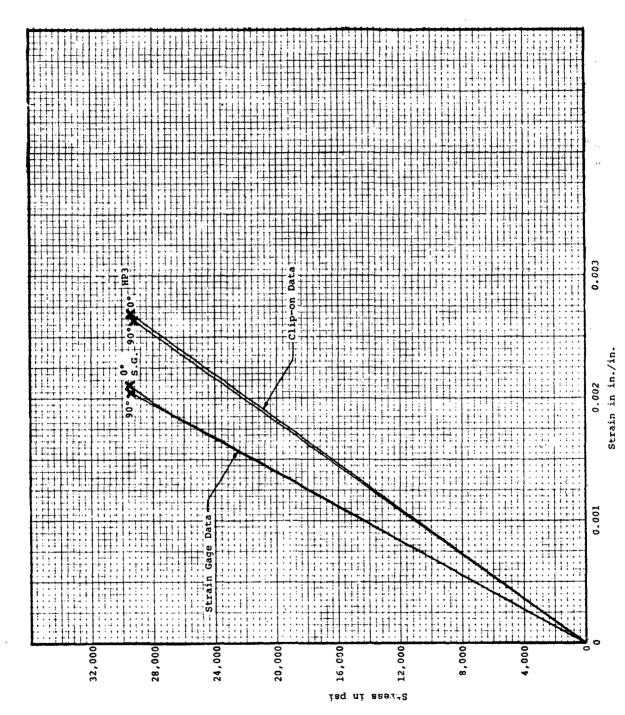


Figure 77. Cylinder K366 (Dining Car) Hoop Tensile Stress-Strain Curves at 70°F

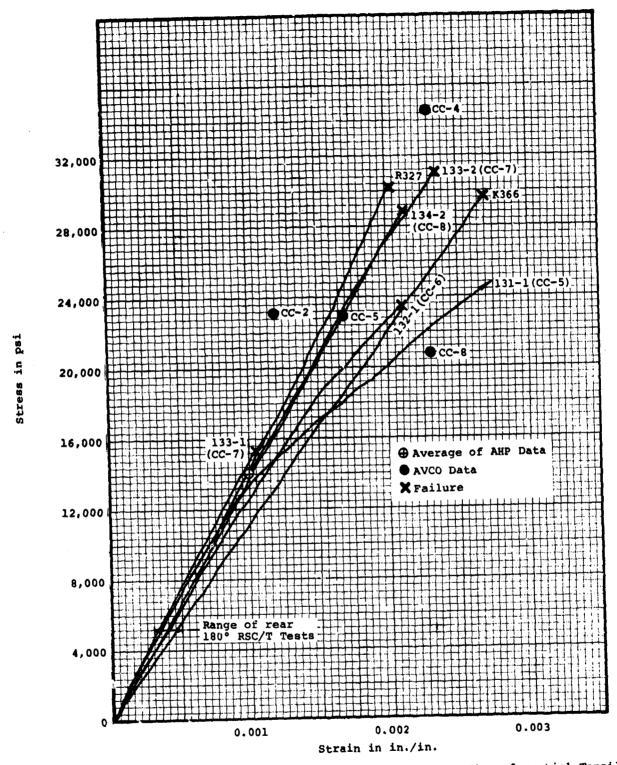


Figure 78. Composite Plot of Probable Values for Circumferential Tensile Tests by Cylinder at 70°F

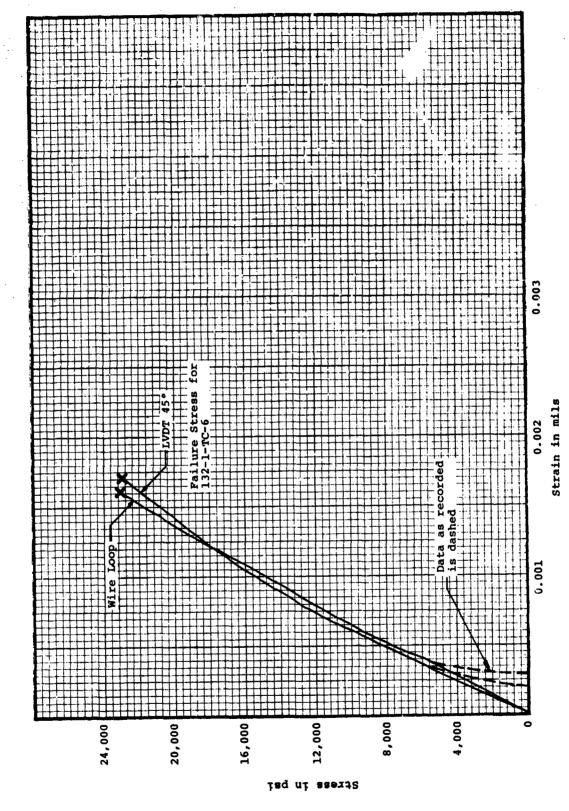


Figure 79. Hoop Tensile Stress-Strain Curves for 129-2-TC-3 at 2000*F

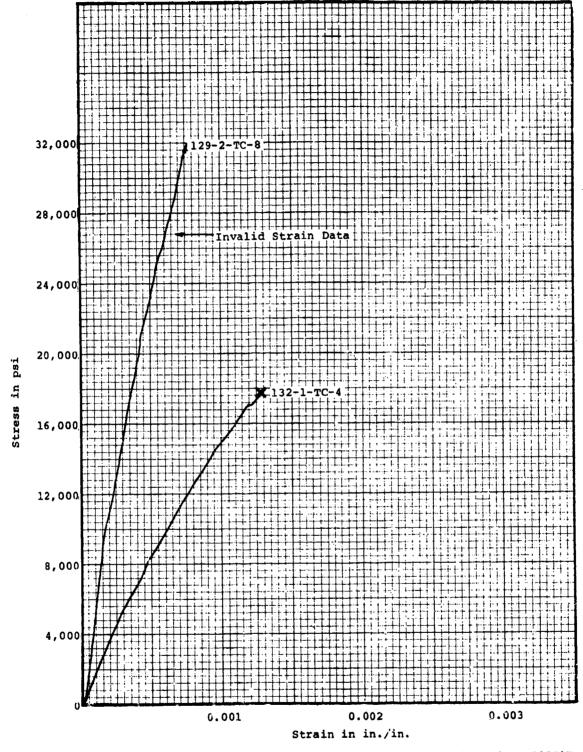


Figure 80. Hoop Tensile Stress-Strain Curves for 132-1-TC-4 at 3000°F

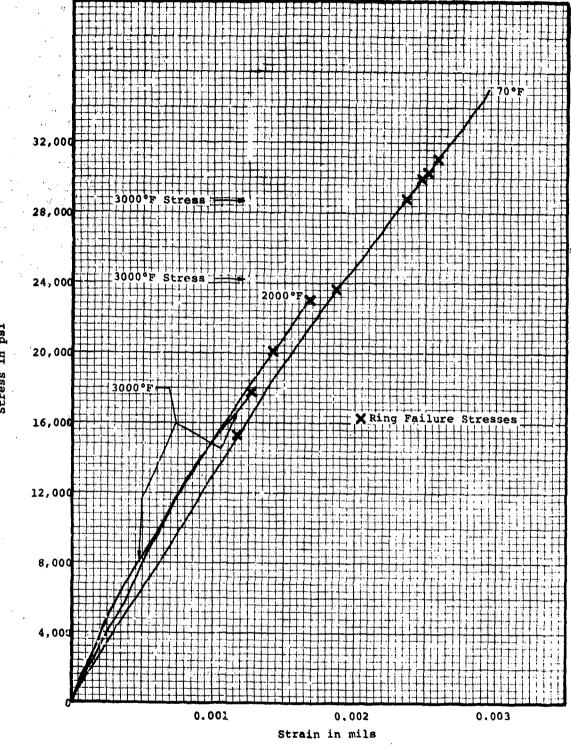


Figure 81. Probable Value Curves for Hoop Tensile at 70°F, 2000°F and 3000°F

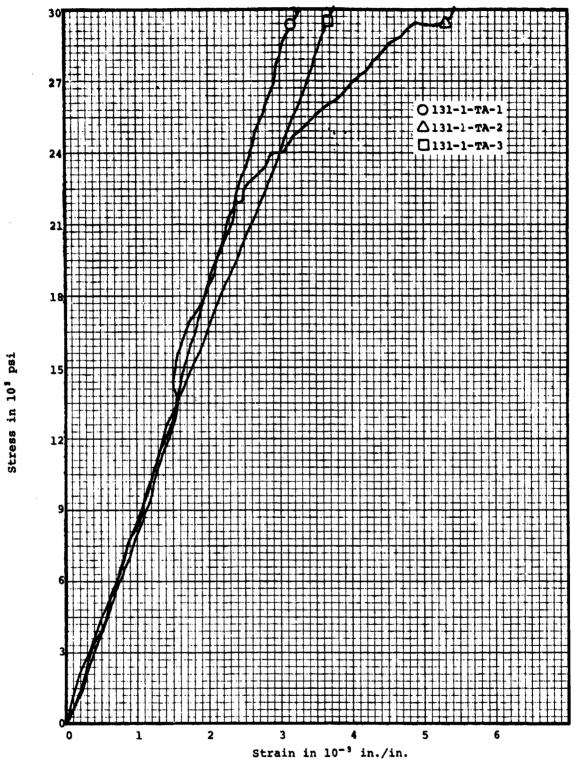


Figure 82. Composite Axial Tensile Stress-Strain Curves of 131-1 (CC-5) at 70°F

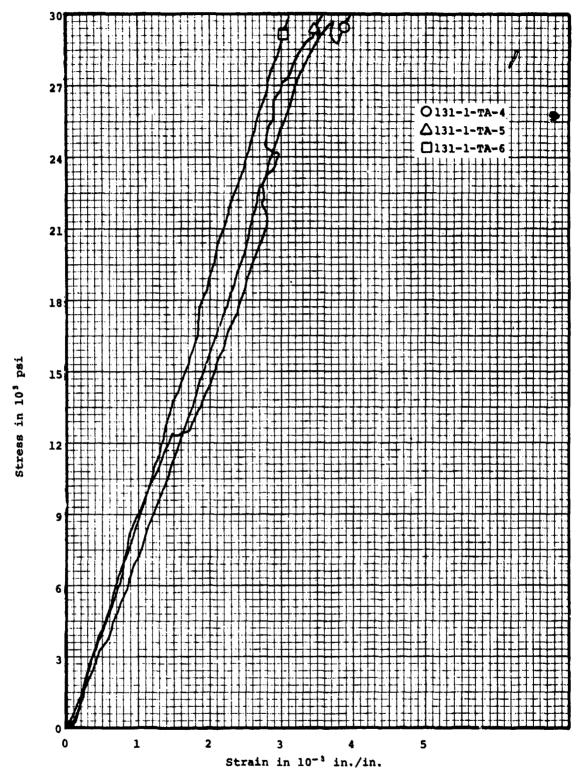


Figure 83. Composite Axial Tensile Stress-Strain Curves of 131-1 (CC-5) at 2000°F

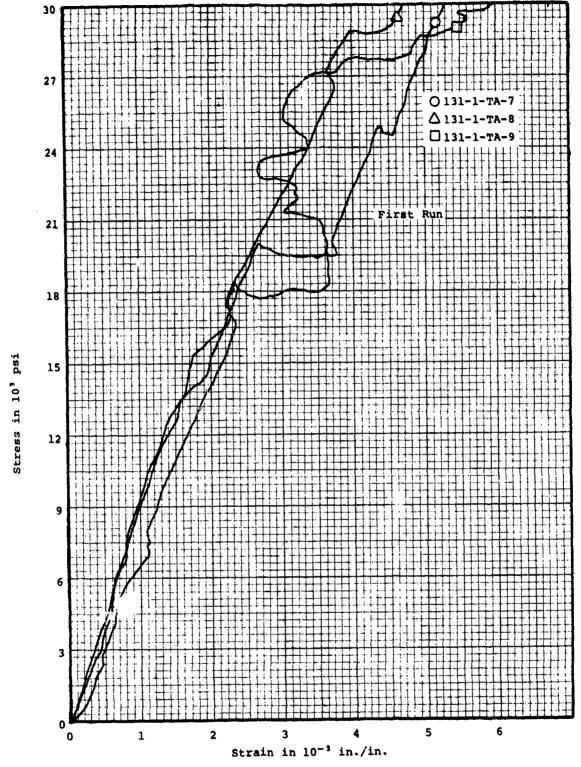


Figure 84. Compare to Axial Tensile Stress-Strain Curves of 131-1 (CC-5) at 3000°F

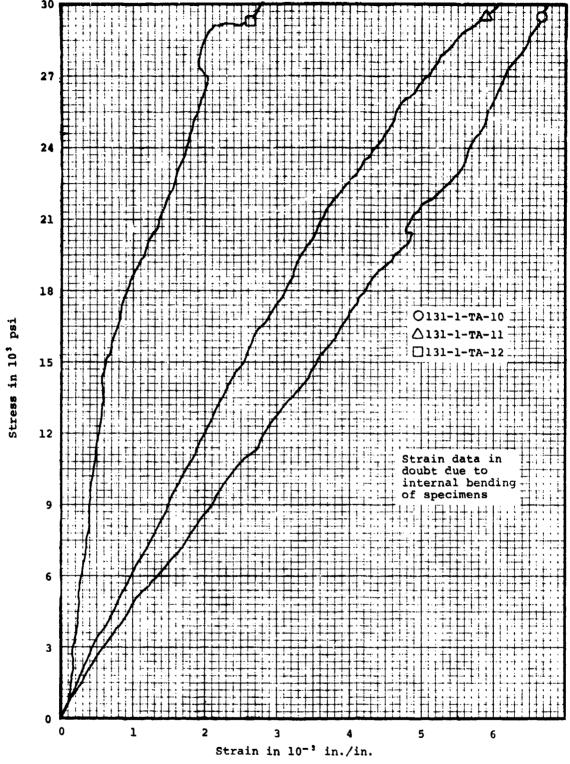


Figure 85. Composite Axial Tensile Stress-Strain Curves of 131-1 (CC-5) at 3500°F

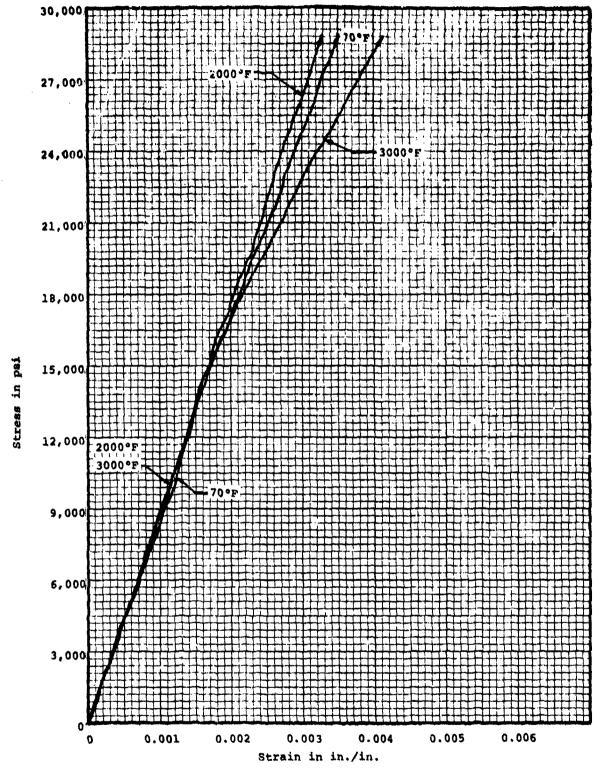


Figure 86. Composite of Axial Tensile Probable Value Curves at 70°F, 2000°F and 3000°F

Strain in pin./in.

Stress psi	Clip-ons	s.G. Convex	S.G. Concave	S.G. Avg	S.G. Bend
0	0	0	0	0	0
2000	-80	-26	-309	-169	131
4000	-160	-43	-620	-331	289
6160	-260	-19	-1116	-568	548
8000	-360	+98	-1800	-851	949

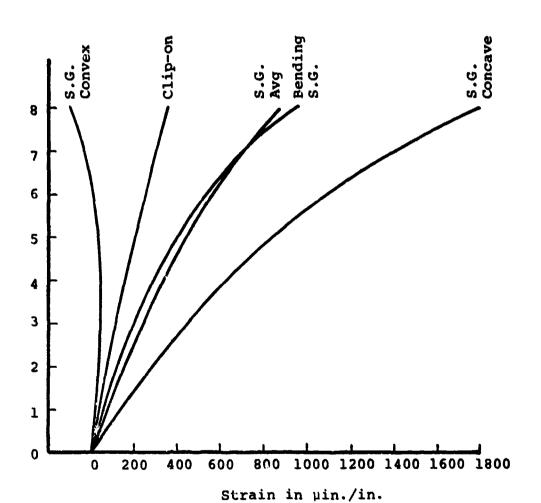
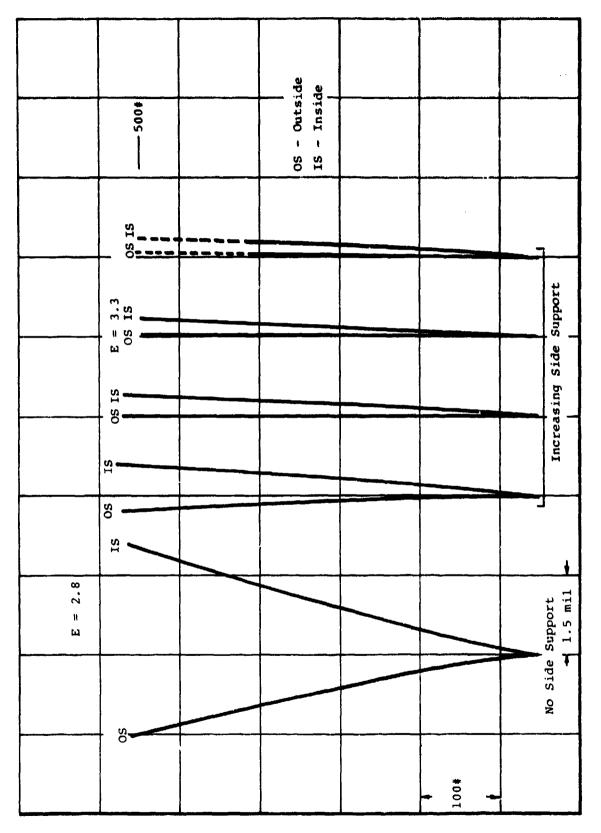


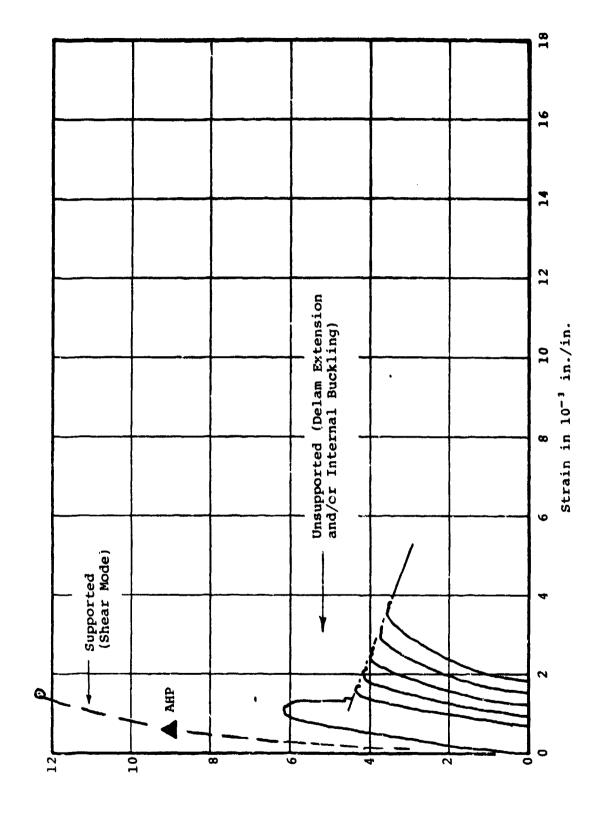
Figure 87. Comparison of Clip-on versus Strain Data in Compressive Curved 3DCC Specimen - Unsupported



Appellon Linear to the

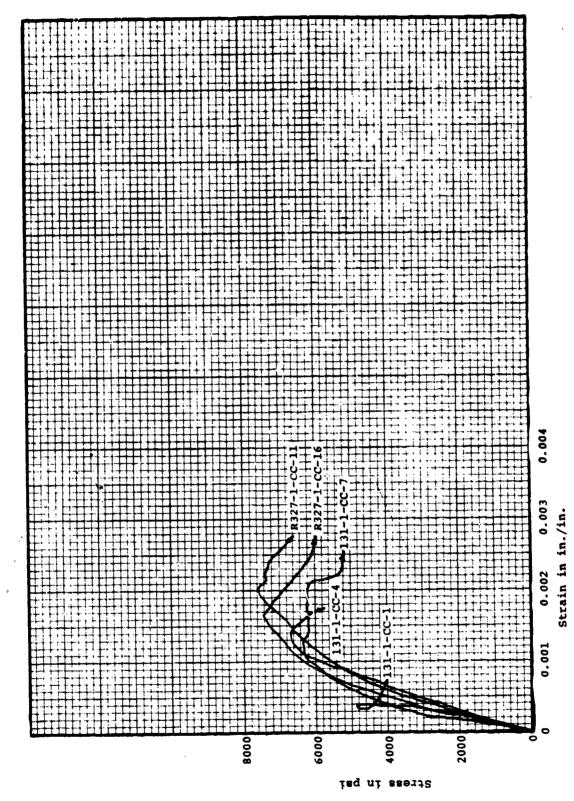
A SECOND CONTROL OF THE SECOND CONTROL OF TH

Figure 88. Compressive Ring Segment for fCC Ring 8-RI With and Without Side Support



Circumferential Compressive 3DCC Curved Specimen - No Lateral Support Figure 89.

THE RESERVE THE PROPERTY OF THE PARTY OF THE



Composite Stress-Strain Curves for Straight Circumferential Compressive Specimens 3DCC at 70°F Figure 90.

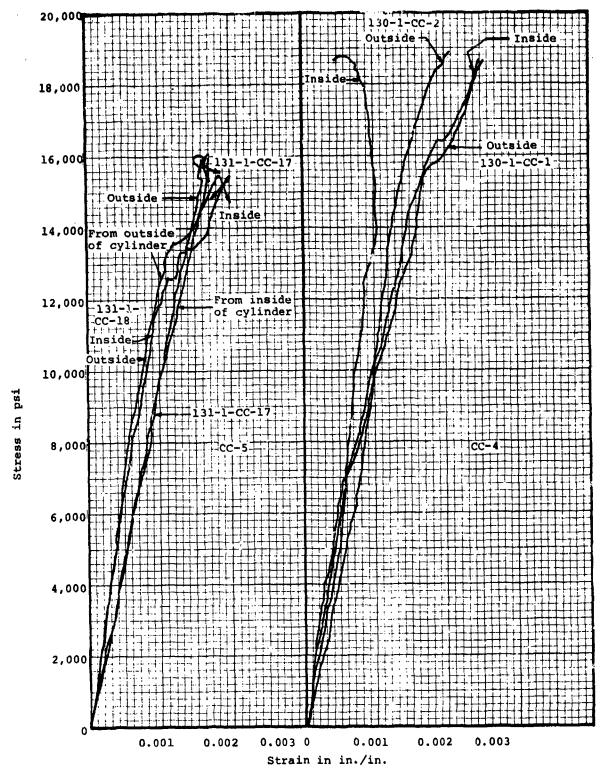


Figure 91. Composites of Curved Coupon Compressive Stress-Strain Curves for CC-5 and CC-4

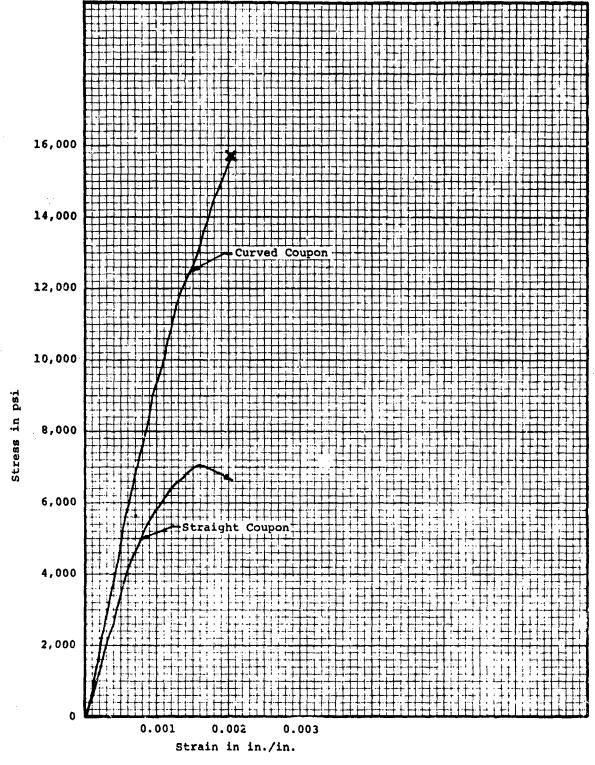


Figure 92. Comparison of PV Curves for Circumferential Compressive at "" "I

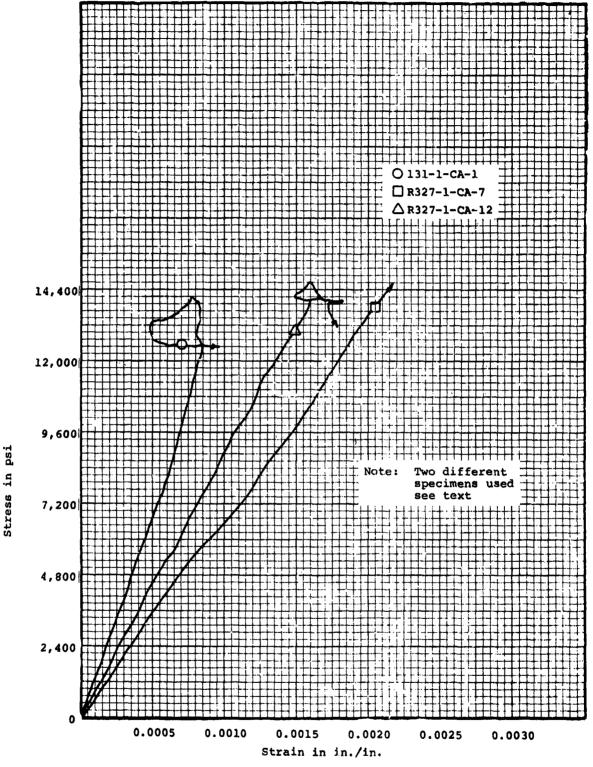


Figure 93. Composite Axial Compressive Stress-Strain Curves of 3DCC at 70°F

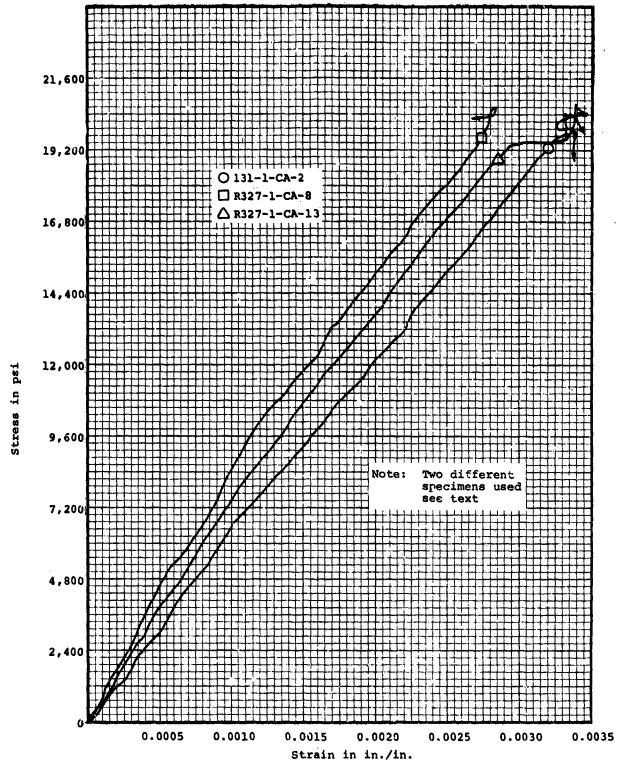
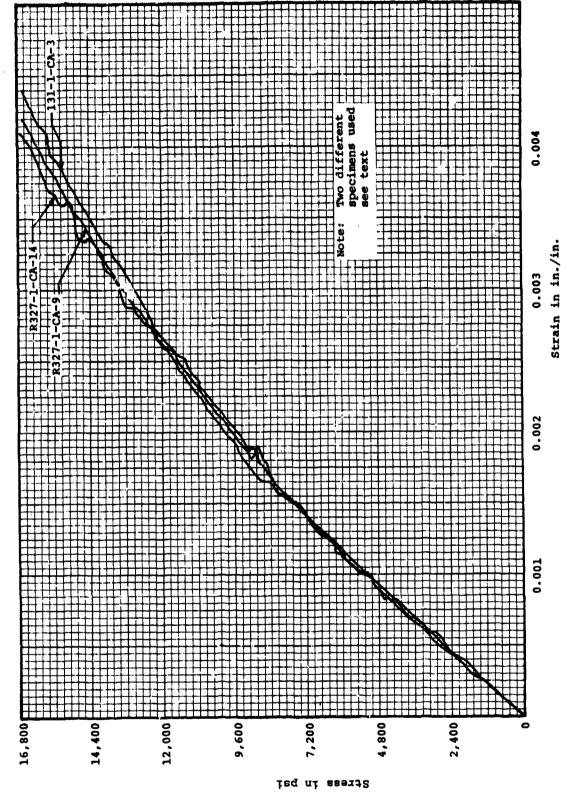


Figure 94. Composite Axial Compressive Stress-Strain Curves of 3DCC at $3000\,^{\circ}\mathrm{F}$



e 95. Composite Axial Compressive Stress-Strain Curves of 3DCC at 4000°F

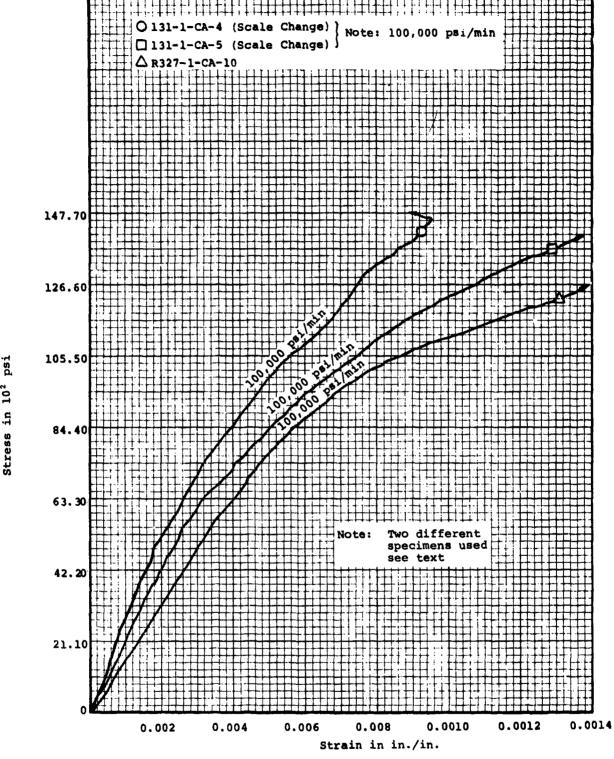


Figure 96. Composite Axial Compressive Stress-Strain Curves of 3DCC at 5000°F

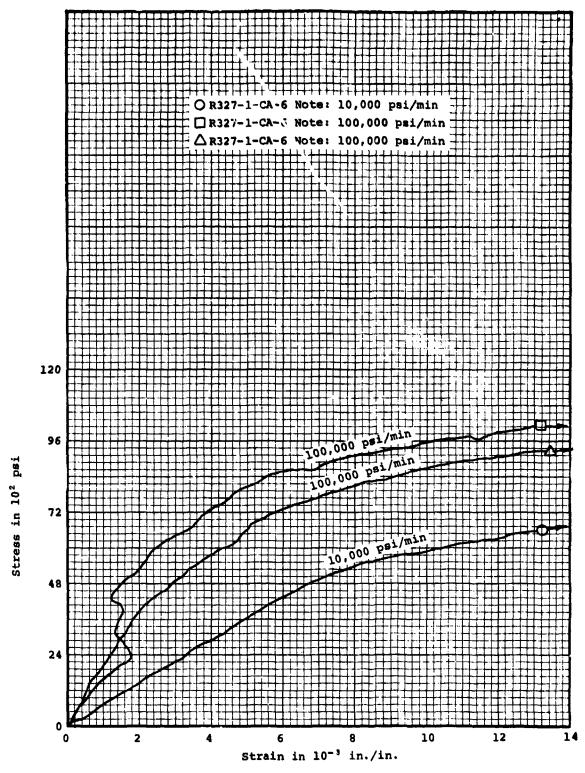
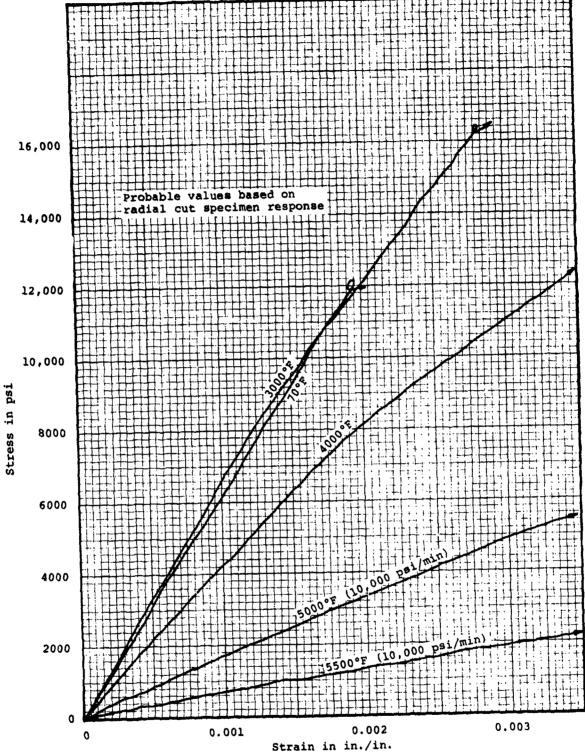
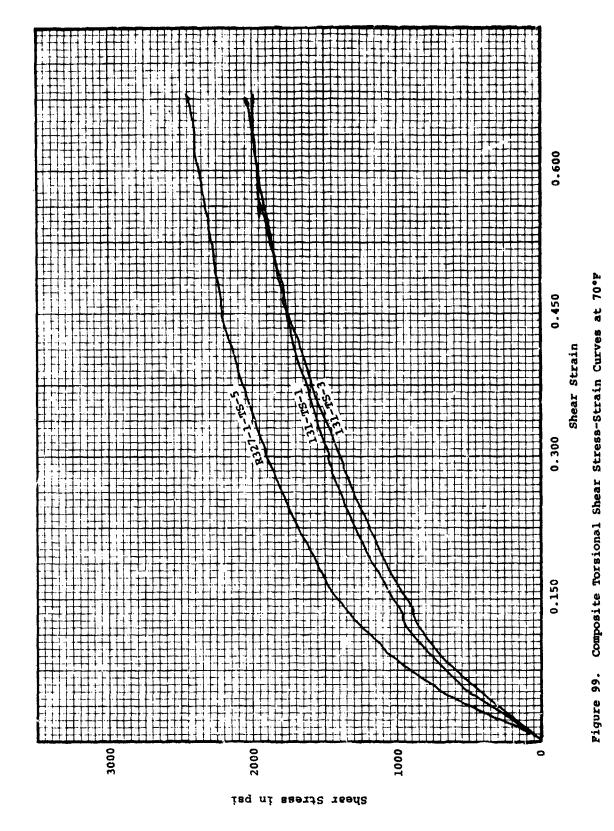


Figure 97. Composite Axial Compressive Stress-Strain Curves of 3DCC at 5500°F



1. A Marine of the control of the co

Figure 98. Composite Axial Compressive Probable Value Stress-Strain Curves of 3DCC Cylindrical Material



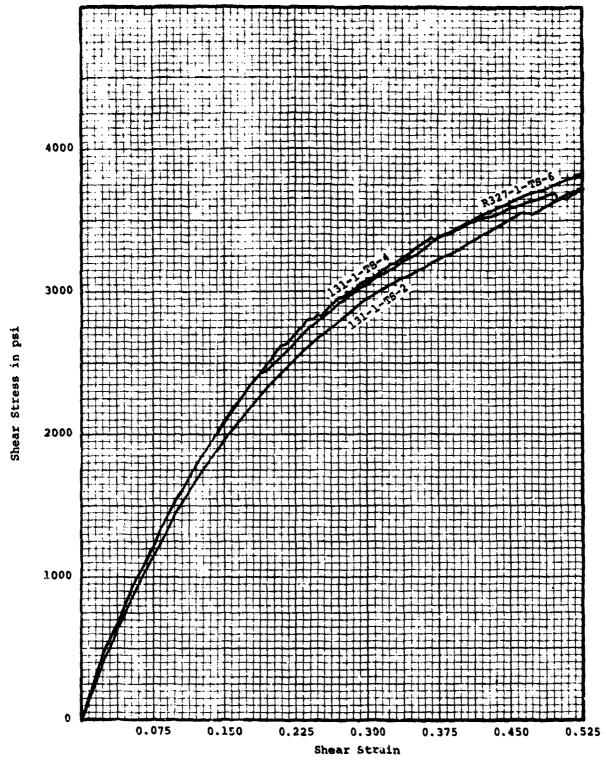


Figure 100. Composite Torsional Shear Stress-Strain Curves at 3000°F

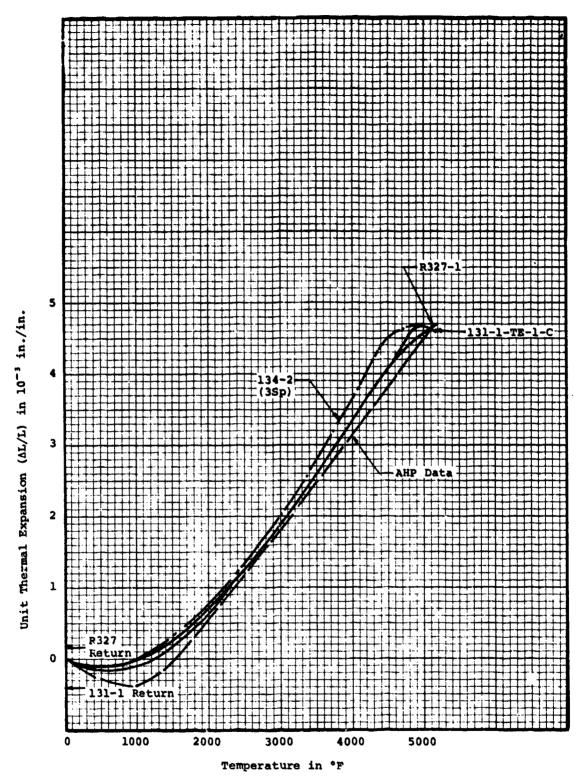


Figure 101. Circumferential Thermal Expansion Data of Cylindrical AVCO 3DCC

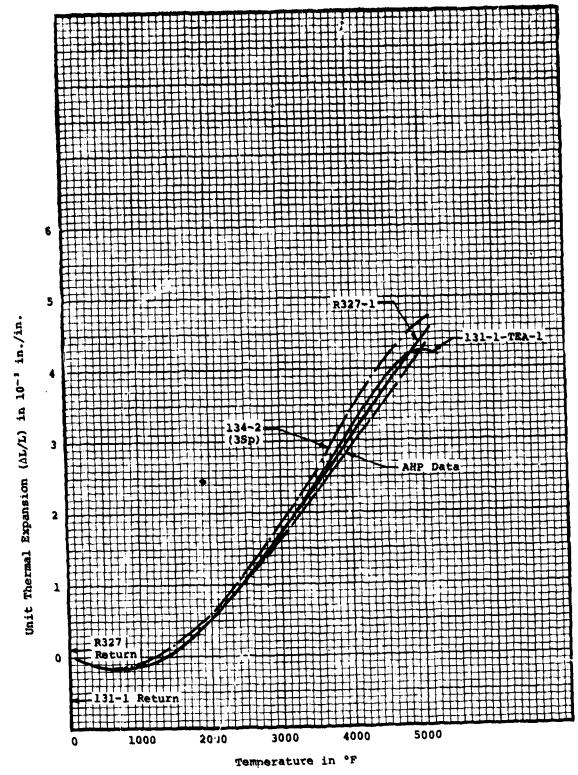


Figure 102. Axial Thermal Expansion Data of Cylindrical AVCO 3DCC

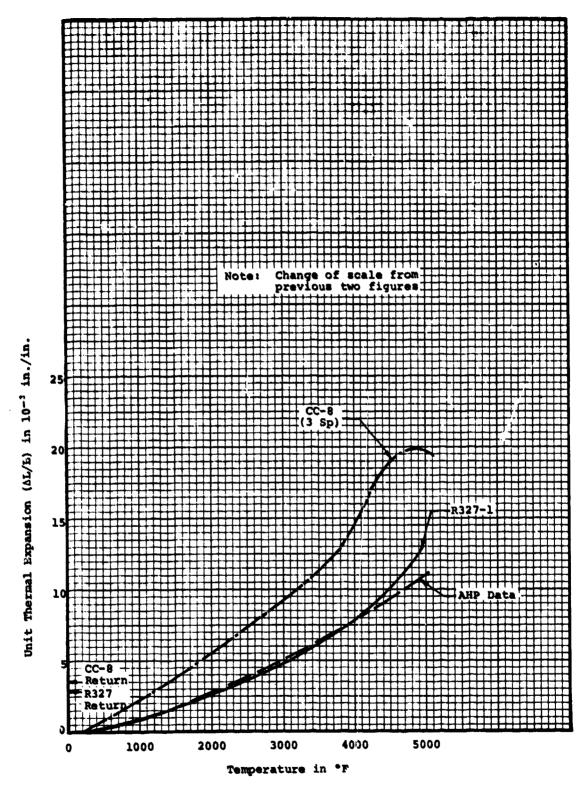
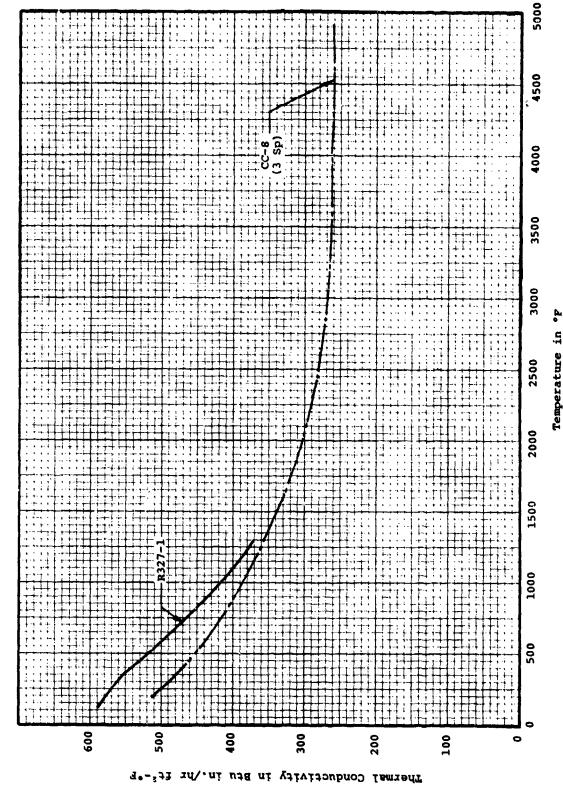
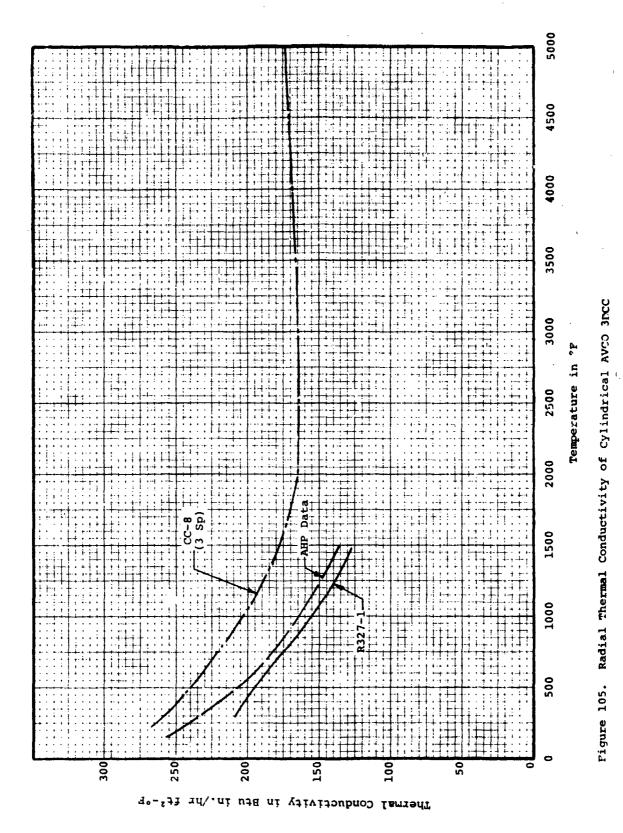
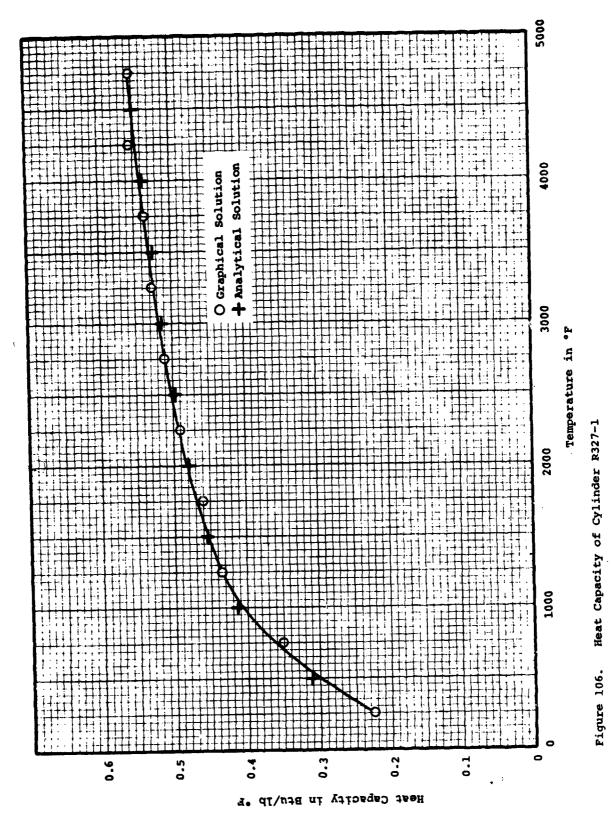


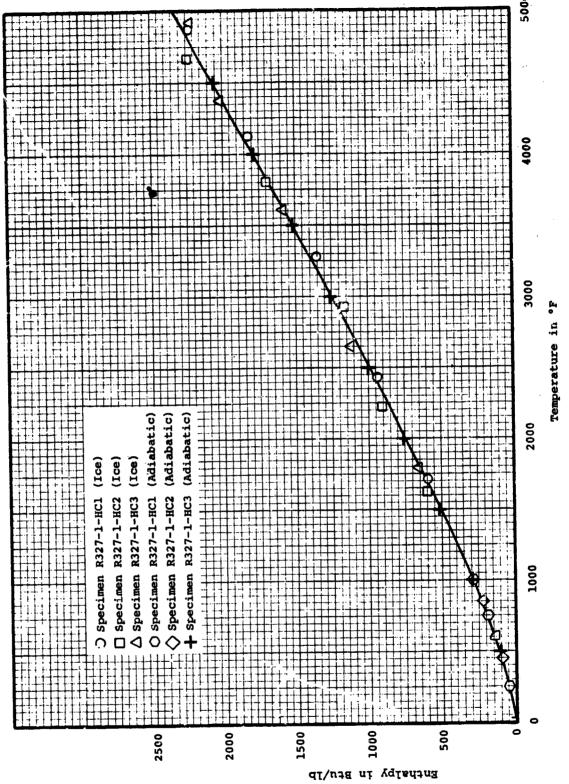
Figure 103. Radial Thermal Expansion Data of Cylindrical AVCO 3DCC



Pigure 104. Axial Thermal Conductivity of Cylindrical AVCO 3DCC







re 107. Enthalpy versus Temperature for Cylinder 327-1

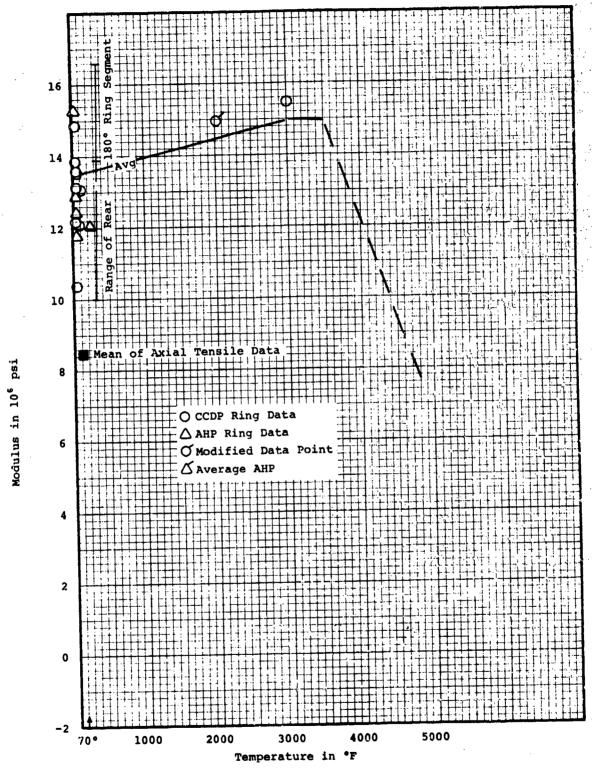


Figure 108. Circumferential Tensile Moduli versus Temperature

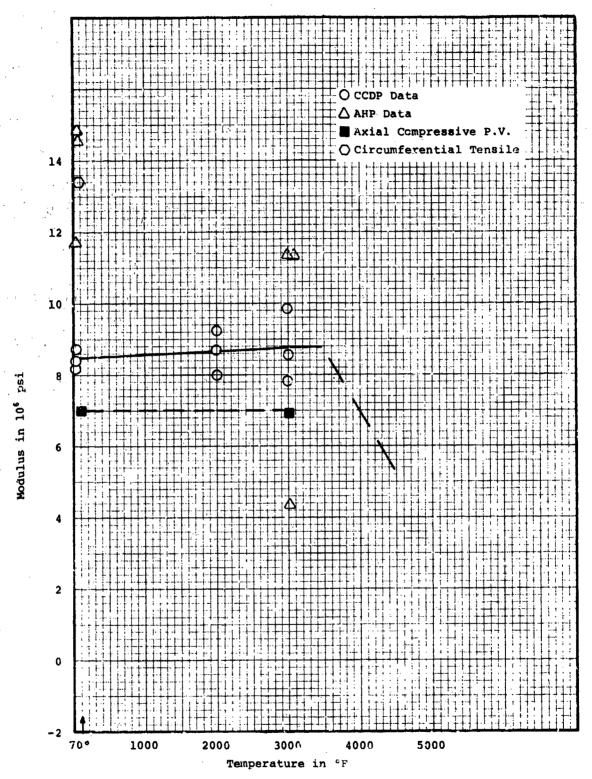


Figure 109. Axial Tensile Moduli versus Temperature

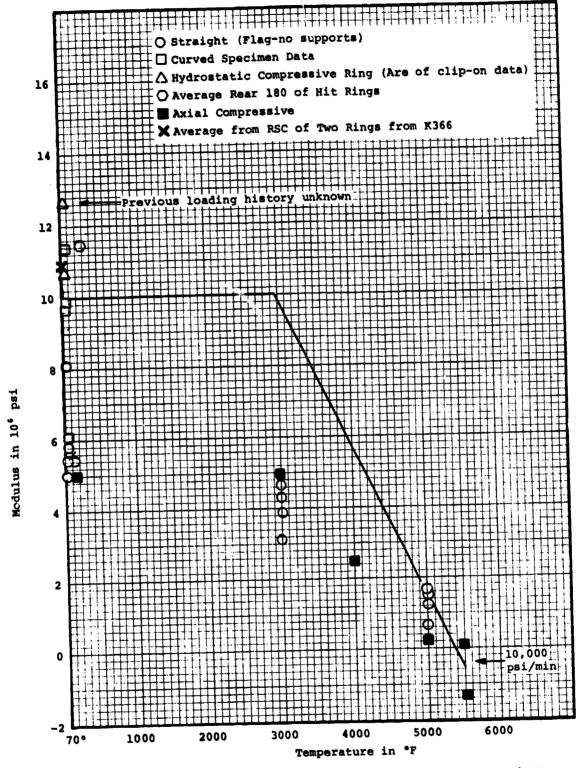


Figure 110. Circumferential Compressive Moduli versus Temperature

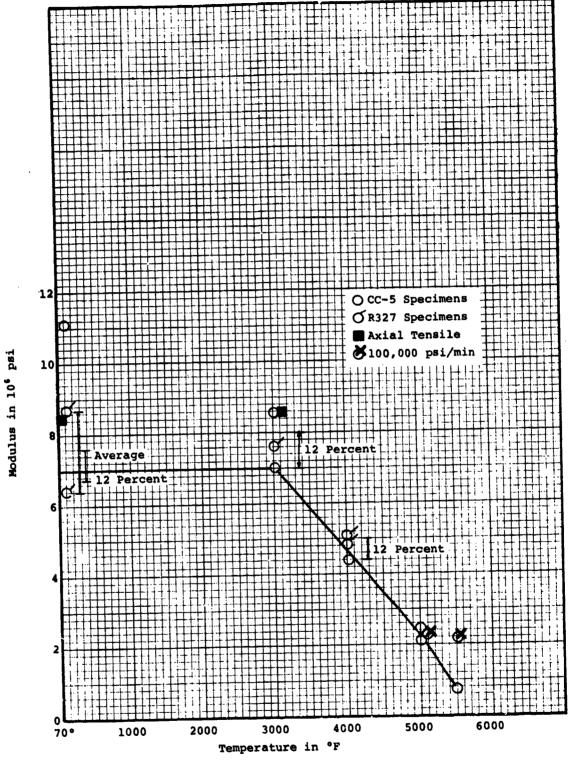


Figure 111. Axial Compressive Moduli versus Temperature

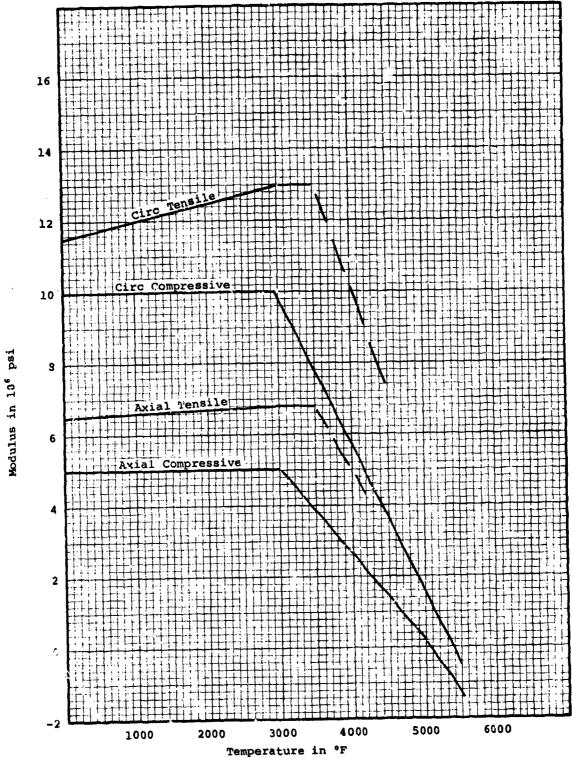


Figure 112. Recommended Moduli for Cylindrical 3DCC

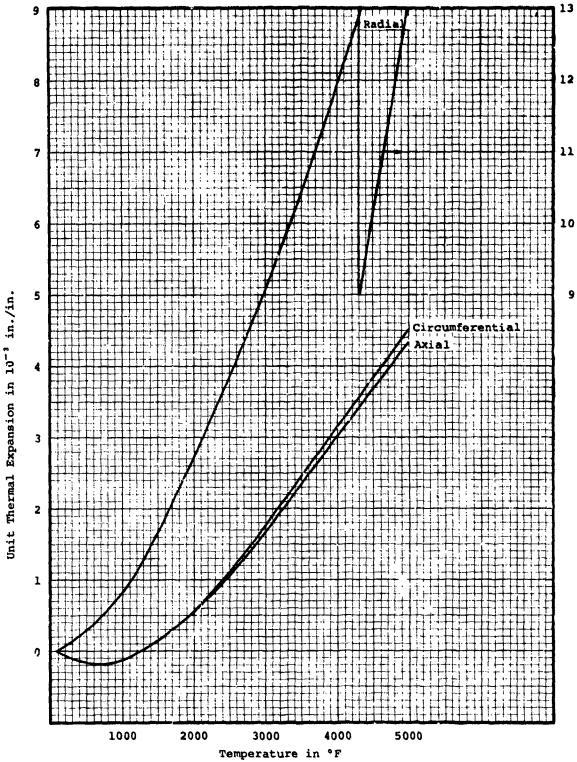
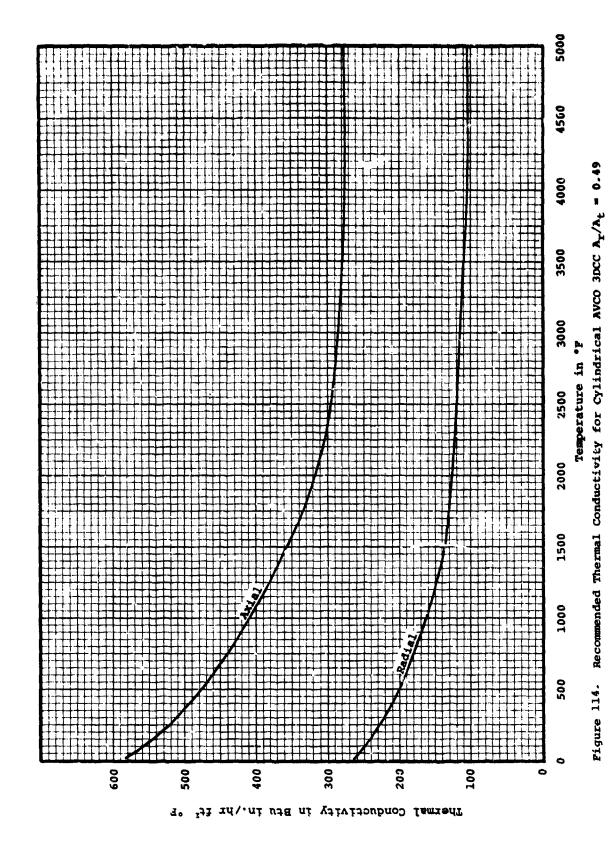


Figure 113. Recommended Thermal Expansion for Cylindrical AVCO 3DCC A_{r}/A_{t} = 0.49



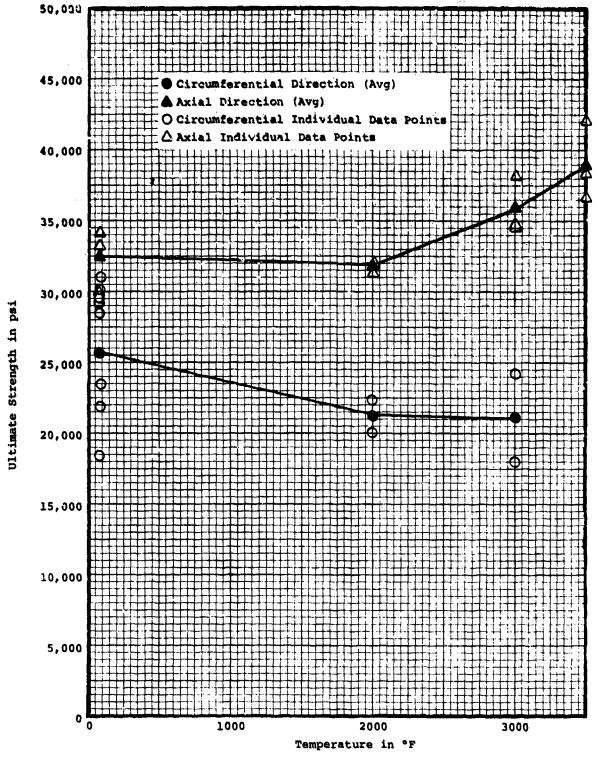


Figure 115. Tensile Strength Data for 3DCC Cylinders

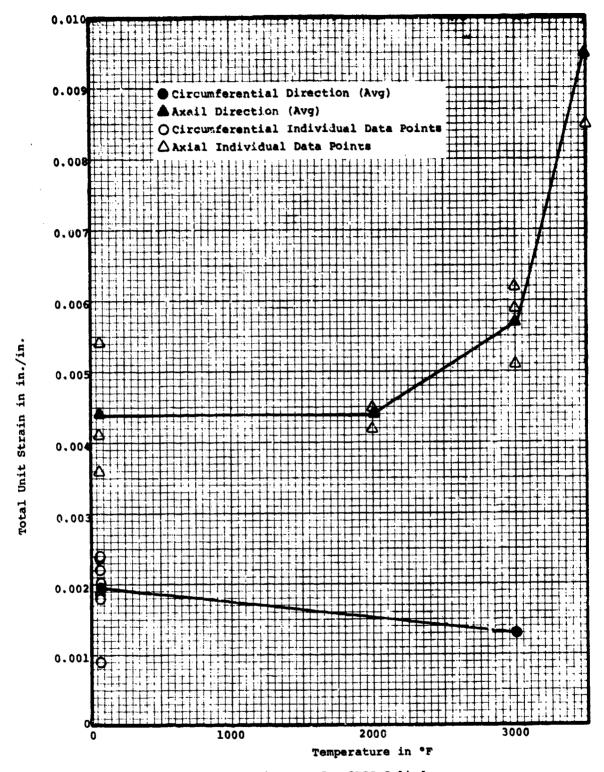


Figure 116. Tensile Strain Data for 3DCC Cylinders

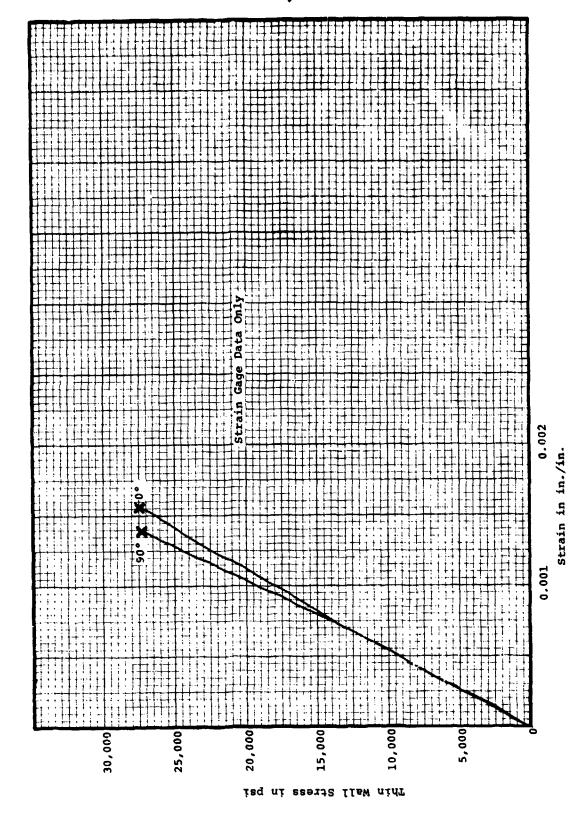
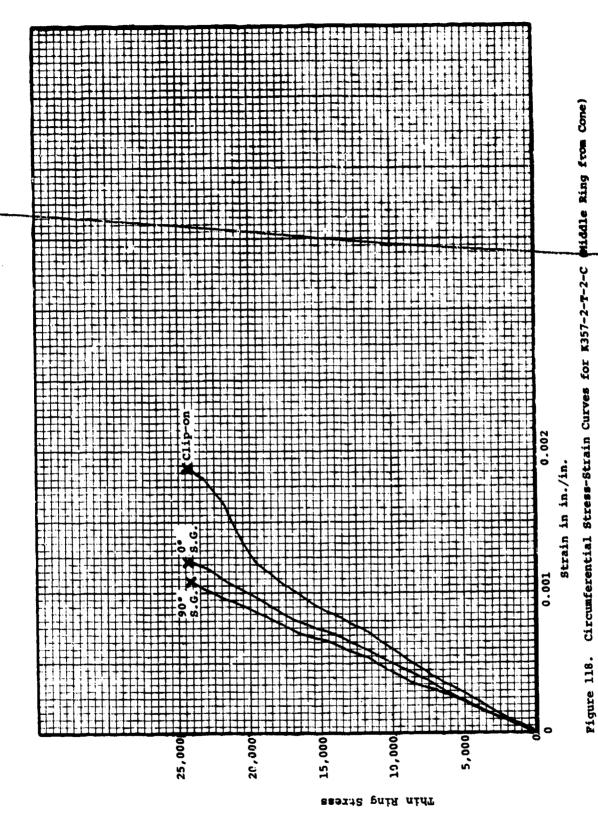


Figure 117. Circumferential Stress-Strain Curves for K357-2-T-1-C (Bottom Ring from Cone)



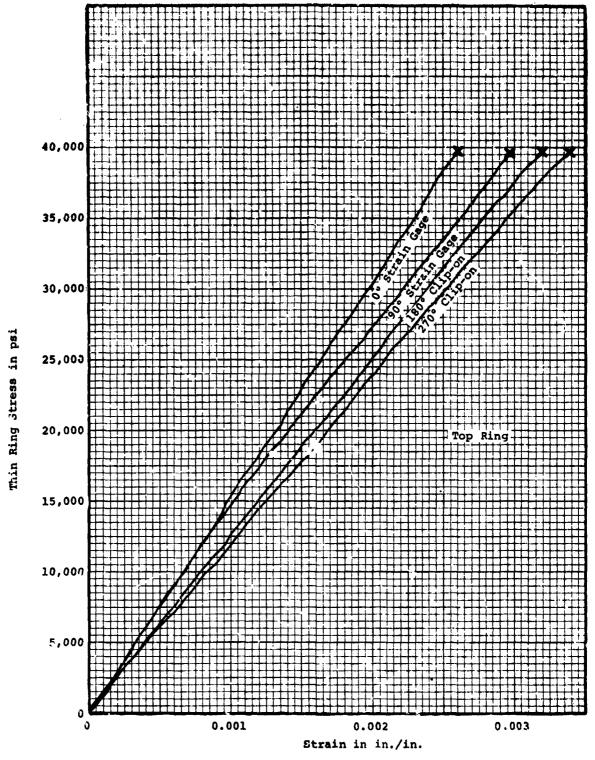


Figure 119. Circumferential Stress-Strain Curves for K357-2-T-3-C (Top Ring from Cone)

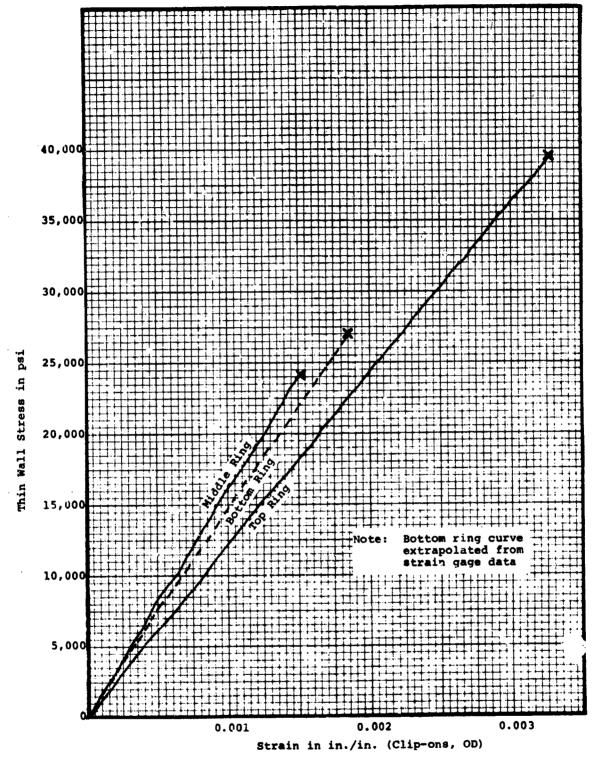


Figure 120. Probable Value Curves for Conical Ring Tensile Tests

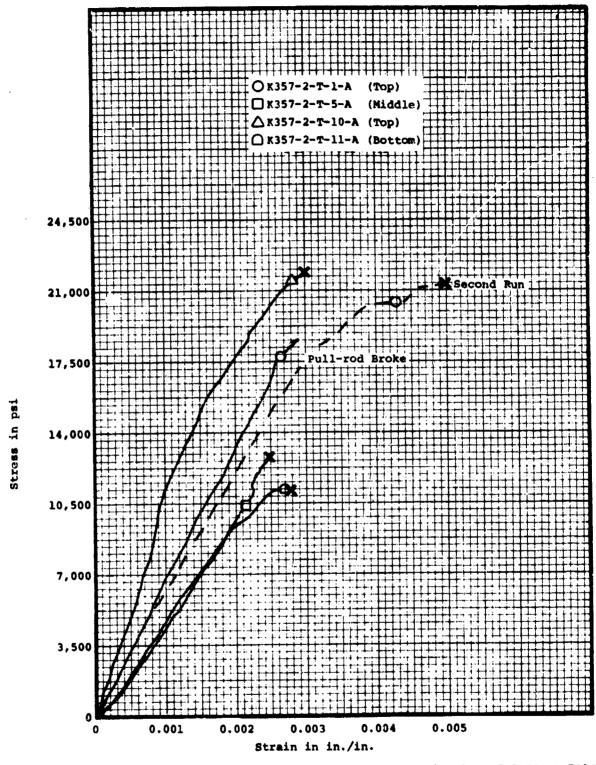


Figure 121. Composite Axial Tensile Stress-Strain Plot of 3DCC at 70°F

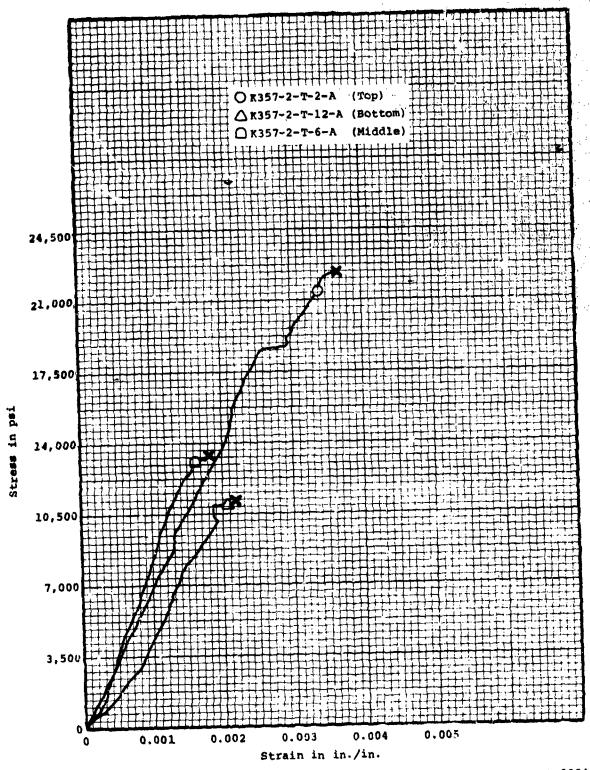


Figure 122. Composite Axial Tensile Stress-Strain Plot of 3DCC at 2000°F

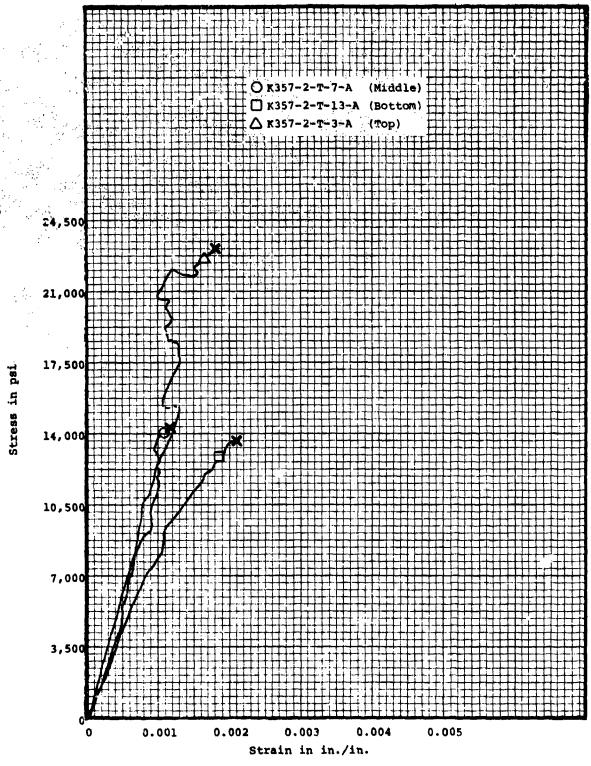


Figure 123. Composite Axial Tensile Stress-Strain Plot of 3DCC at 3000°F

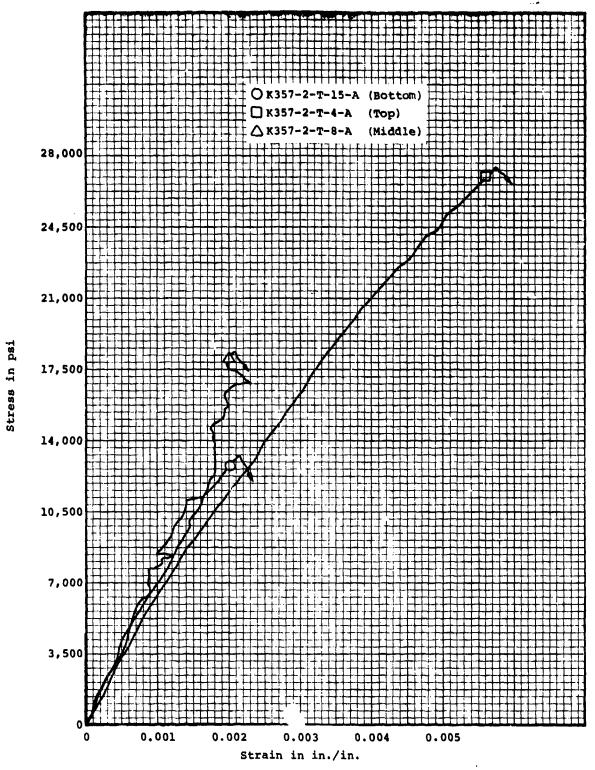


Figure 124. Composite Axial Tensile Stress-Etrain Plot of 3DCC at 3500°F

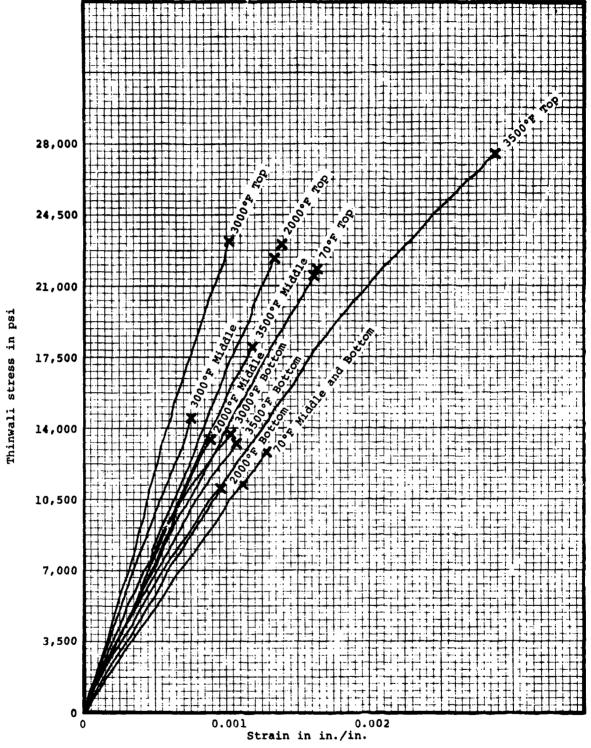


Figure 125. Composite Plot of Axial Tensile Specimens from Cone K357-2

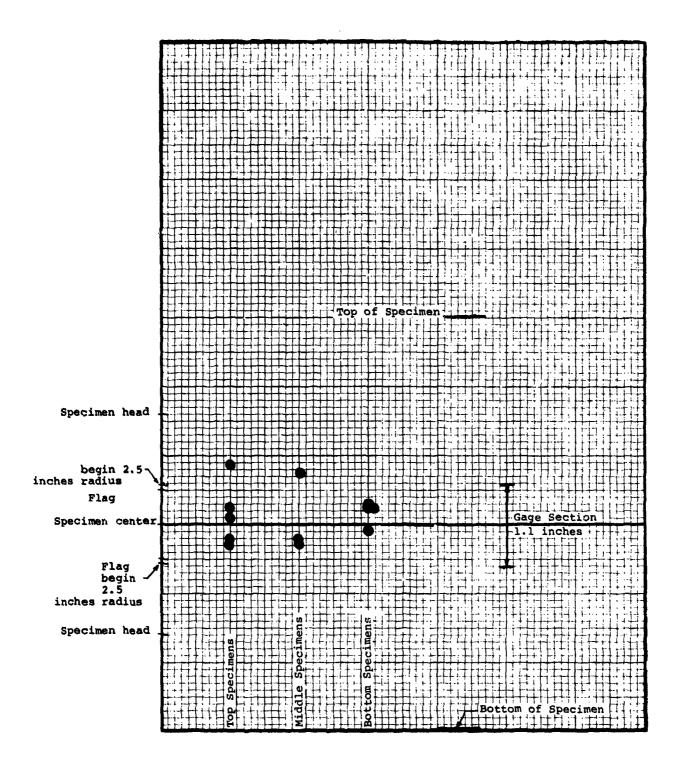


Figure 126. Fracture Locations for Axial Tensile Specimens

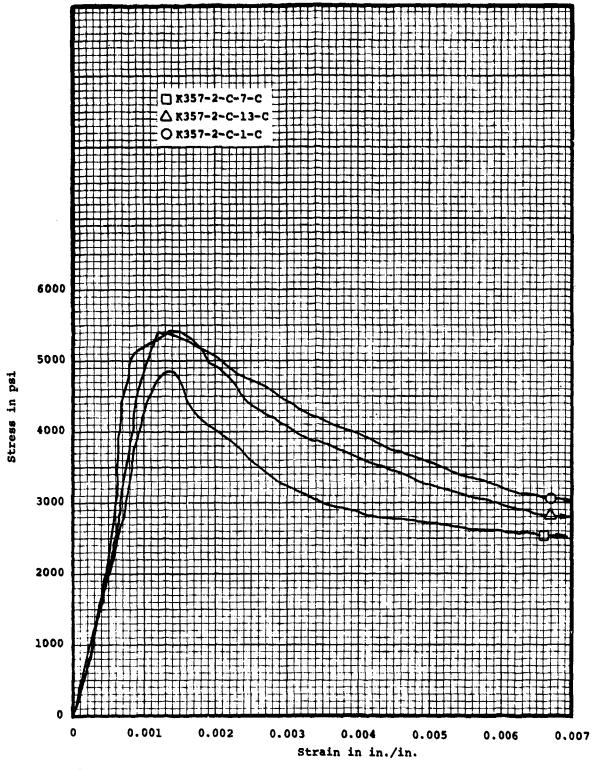


Figure 127. Composite Circumferential Compressive Plot for 3DCC at 70°F

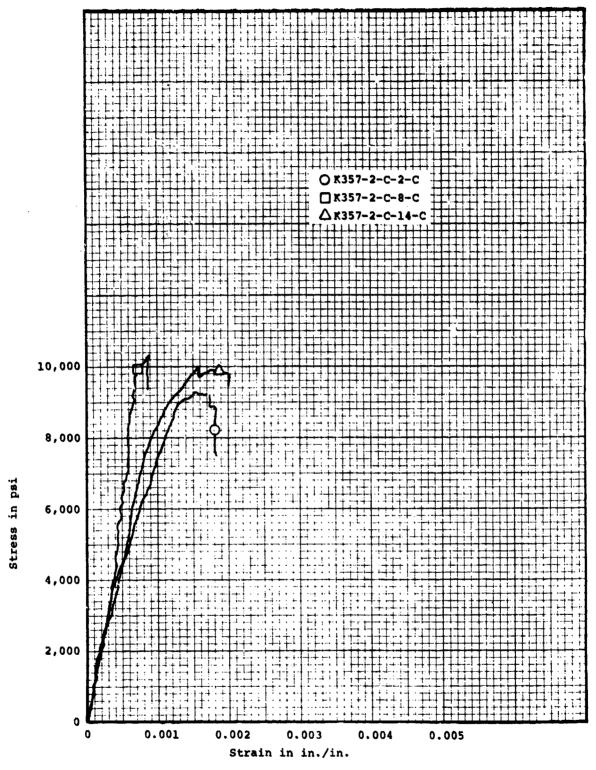


Figure 128. Composite Circumferential Compressive Plot for 3DCC at 3000°F

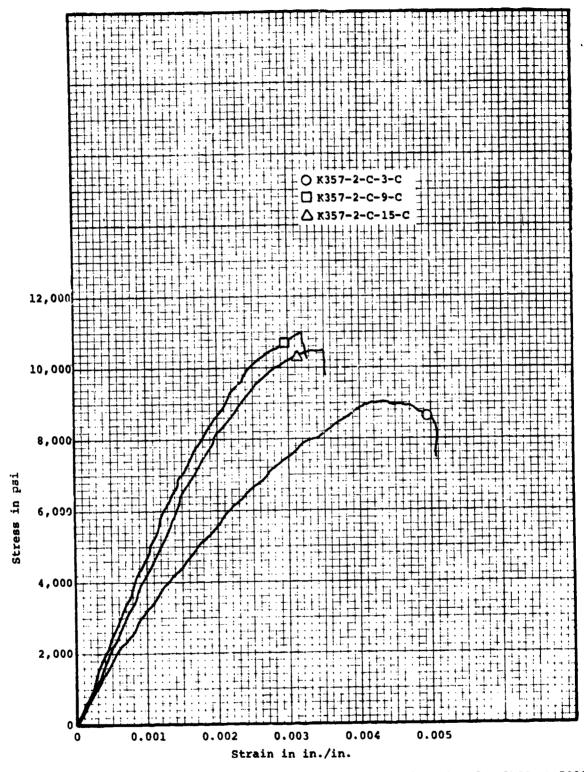


Figure 129. Composite Circumferential Compressive Plot for 3DCC at 5000°F

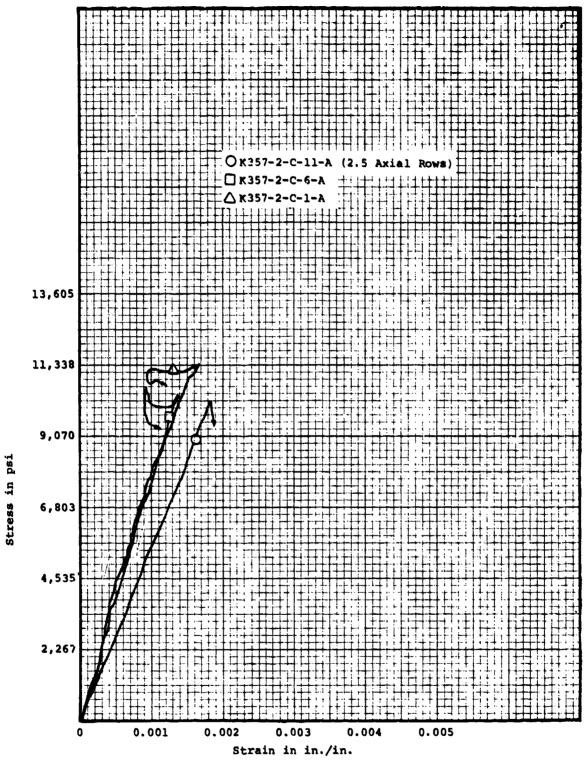


Figure 130. Composite Axial Compressive Stress-Strain Plot for 3DCC at 70°F

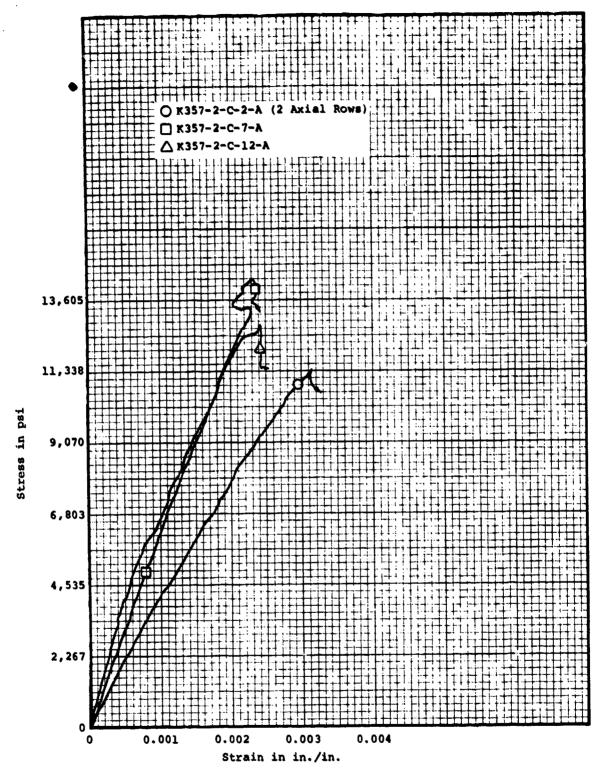


Figure 131. Composite Axial Compressive Stress-Strain Plot for 3DCC at 3000°F

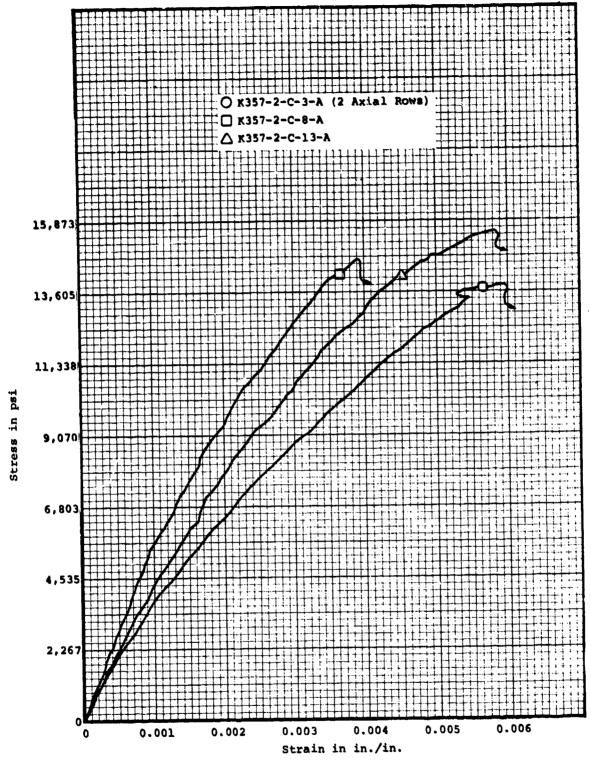


Figure 132. Composite Axial Compressive Stress-Strain Plot for 3DCC at 4000°F

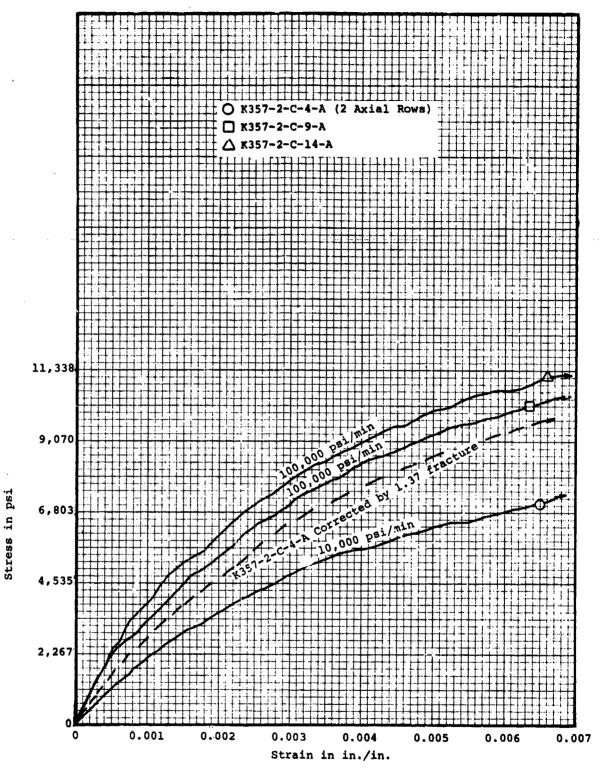


Figure 133. Composite Axial Compressive Stress-Strain Plot for 3DCC at 5000°F

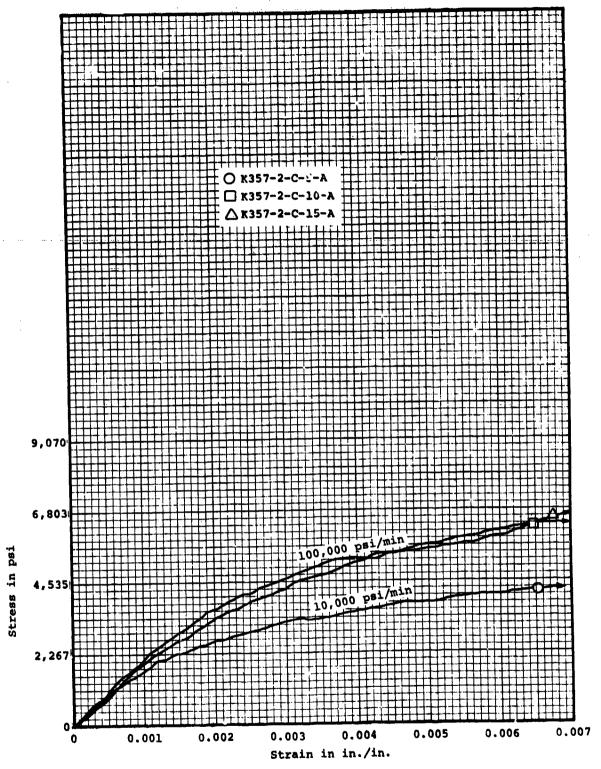


Figure 134. Composite Axial Compressive Stress-Strain Plot for 3DCC at 5500°F

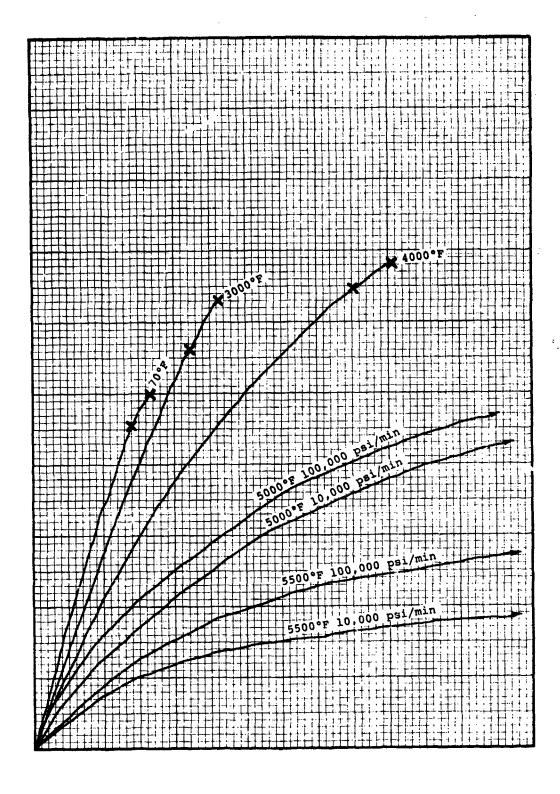


Figure 135. Axial Compressive Probable Value Curves for Conical 3DCC

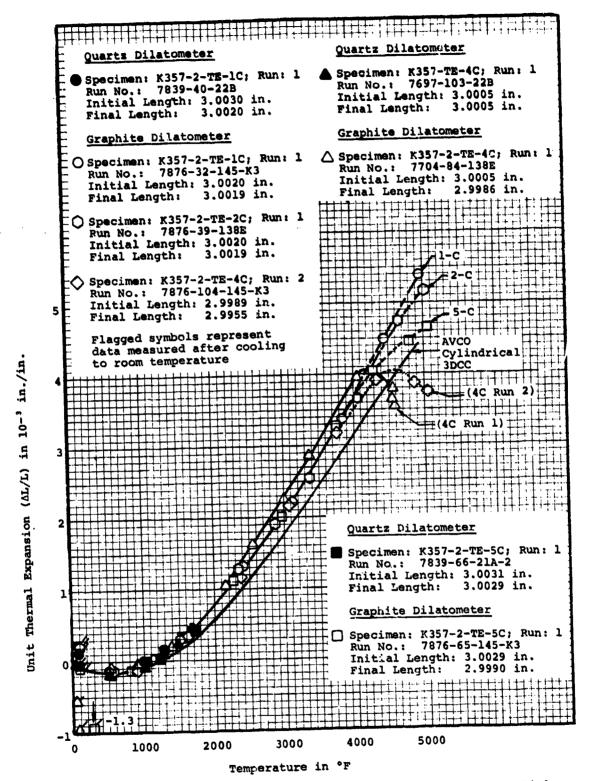


Figure 136. Thermal Expansion of Cone 357-2 in the Circumferential Direction

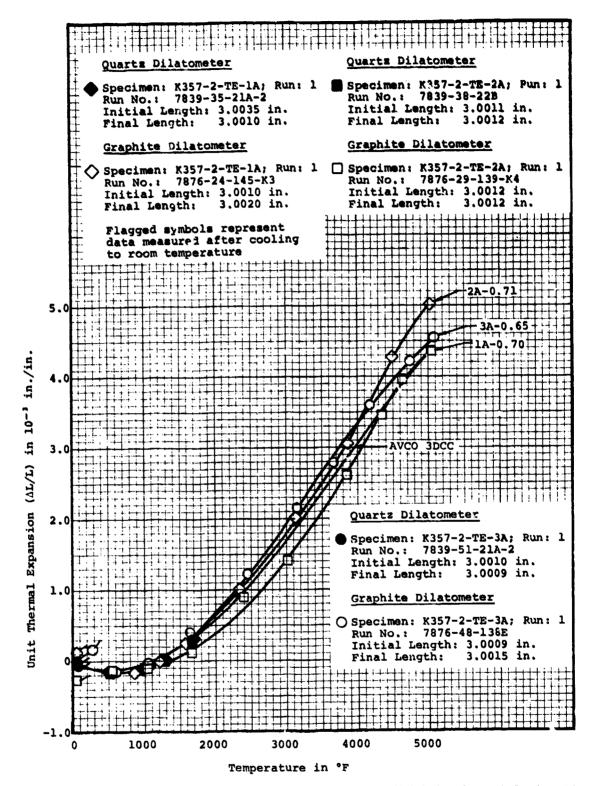


Figure 137. Thermal Expansion of 3DCC Cone K357-2 in the Axial Direction

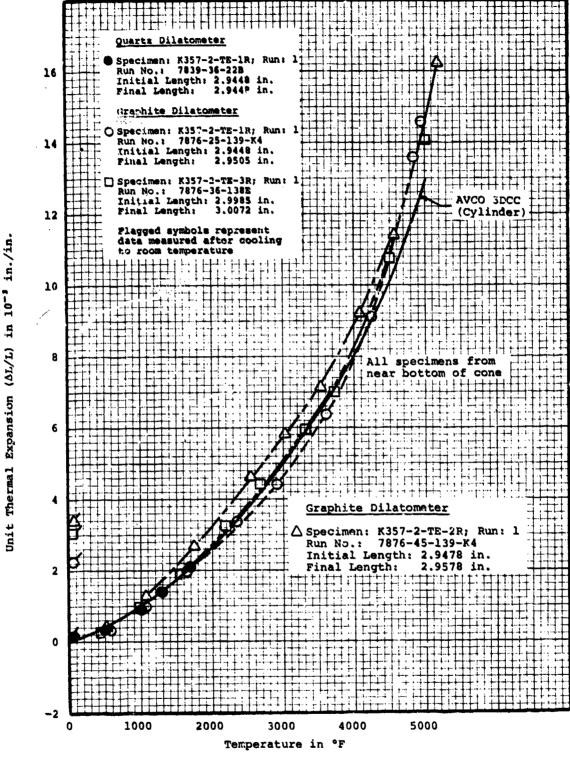
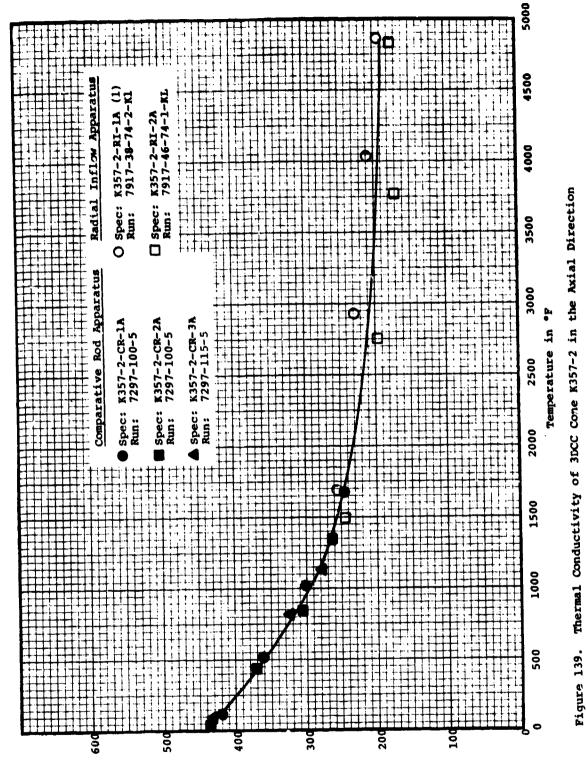
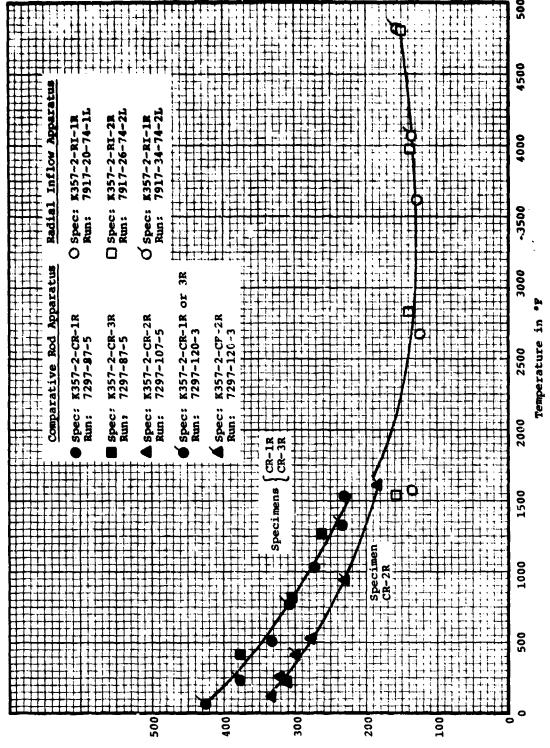


Figure 138. Thermal Expansion of 3DCC Cone K357-2 in the Radial Direction



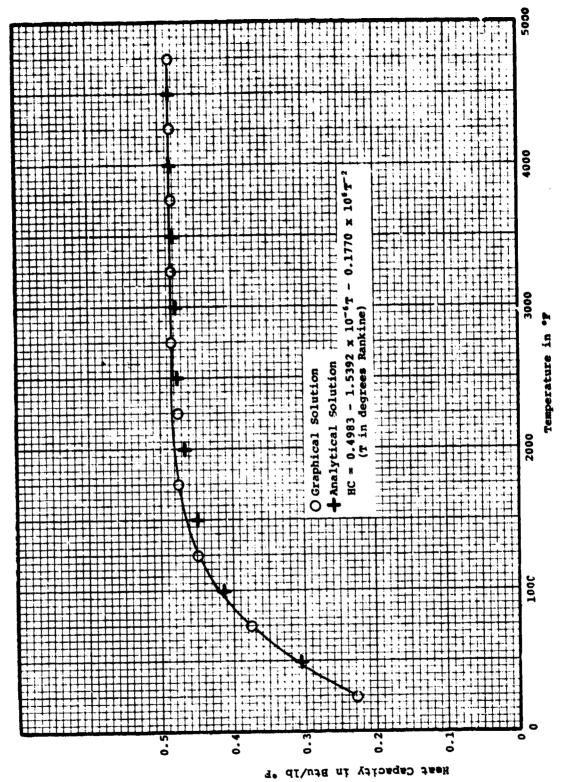
Thexmal Conductivity in Btu in./hr ft 9 °F



Thermal Conductivity of 3DCC Cone K357-2 in the Radial Direction

Pigure 140.

Thermal Conductivity in Btu in./hr ft² °F



Pigure 141. Heat Capacity of Come K357-2

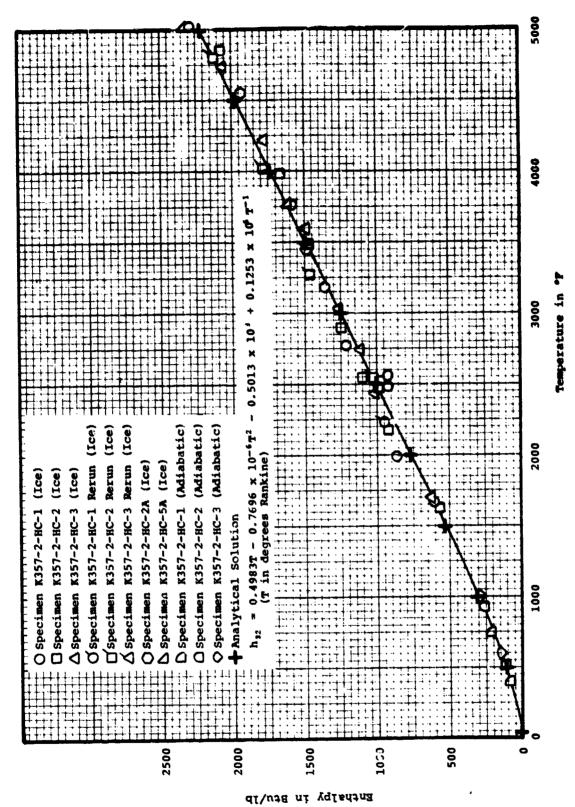


Figure 142. Enthalpy of Cone K357-2

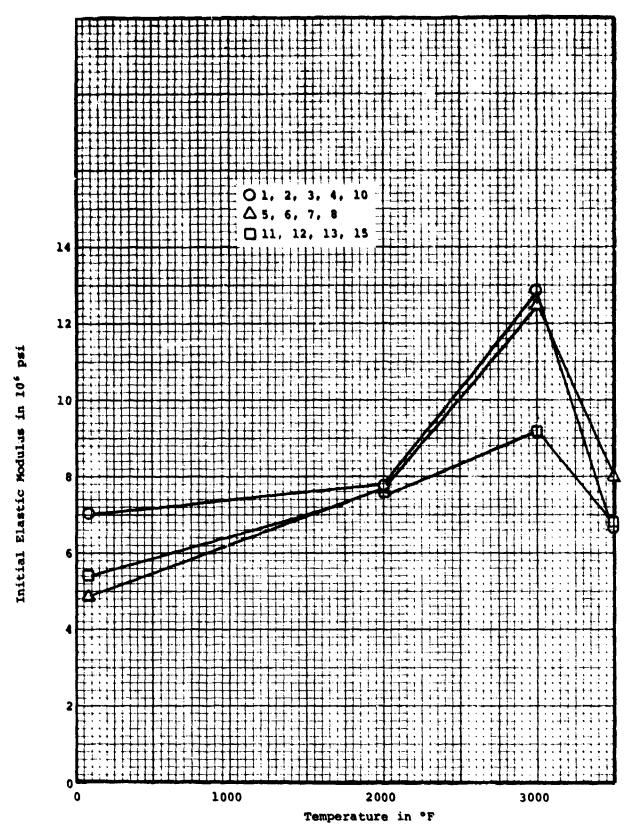


Figure 143. Tensile Data for 3DCC Cone K357-2

第一編題 門

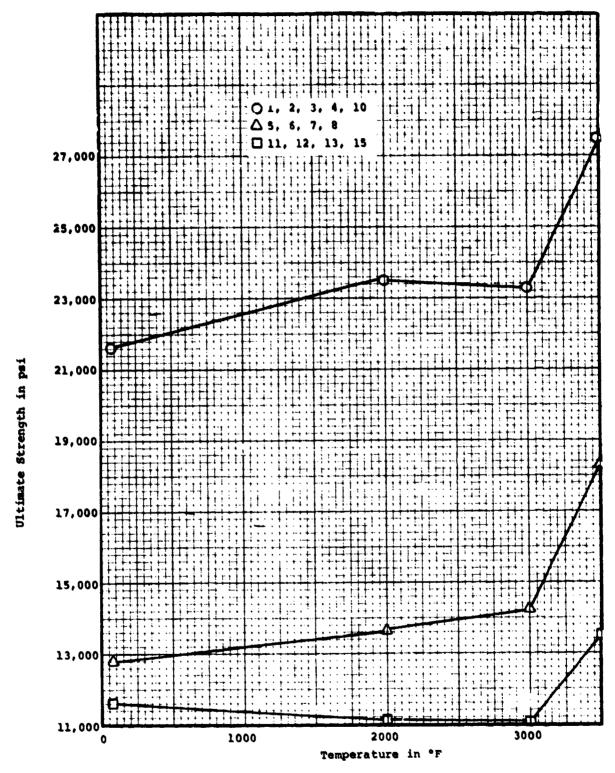


Figure 144. Tensile Data for 3DCC Cone K357-2

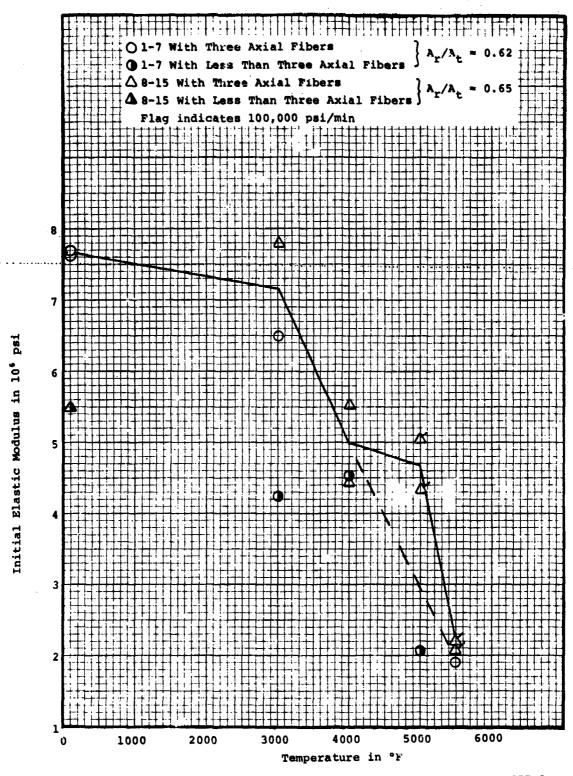


Figure 145. Individual Compressive Data Points for 3DCC Cone K357-2

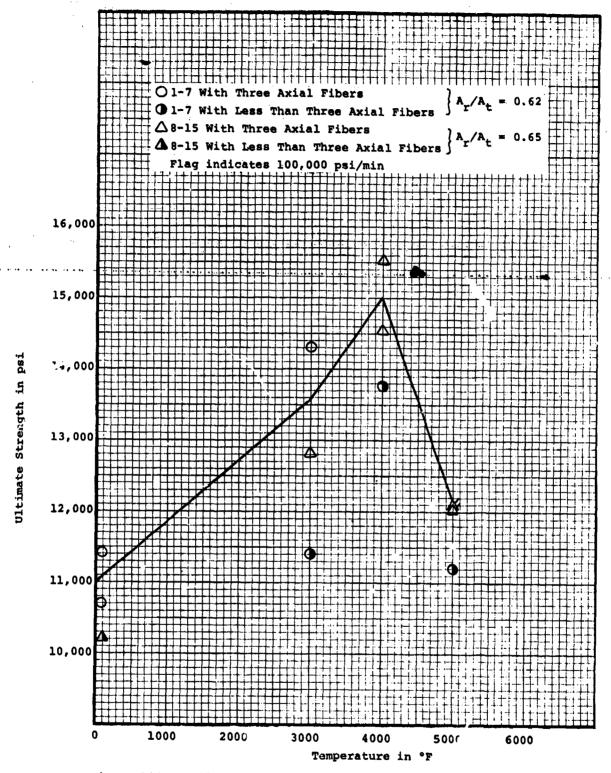
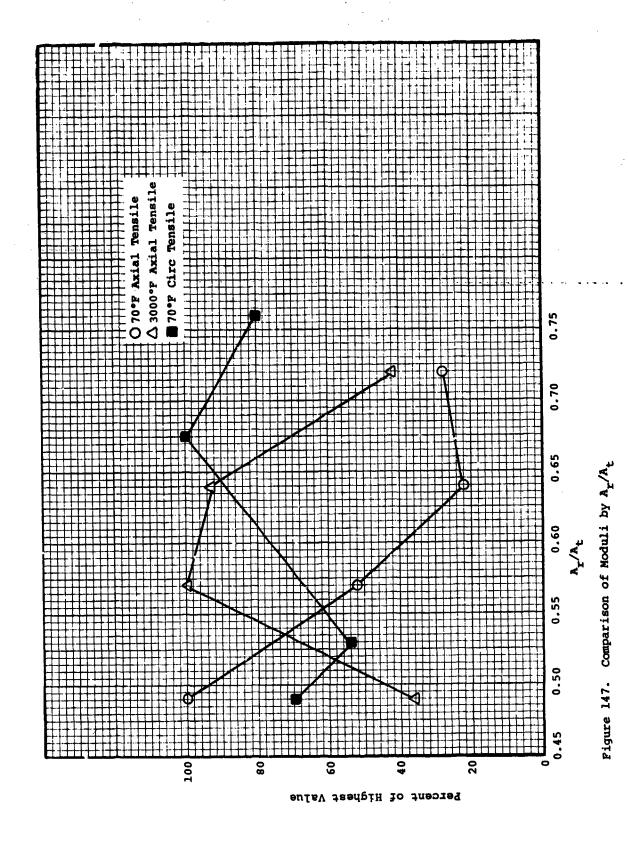
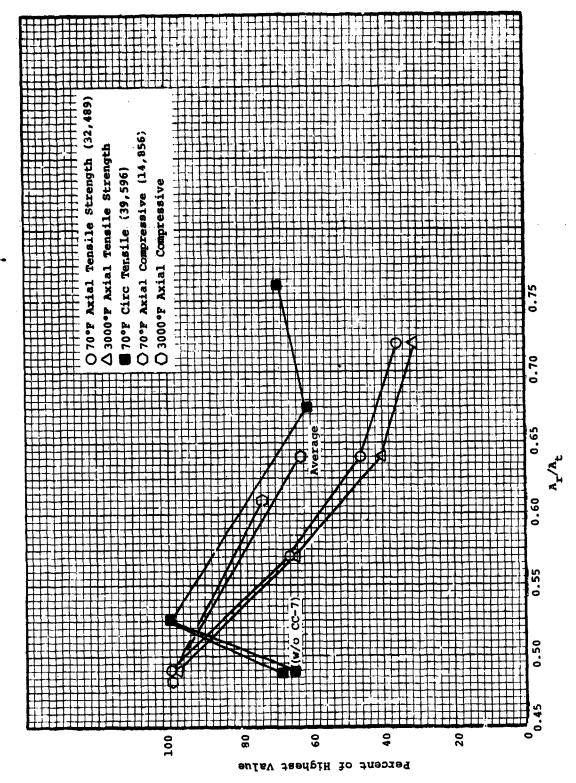


Figure 146. Individual Compressive Data Points for 3DCC Cone K357-2





ure 148. Comparison of Strengths by $A_{\rm L}/A_{\rm t}$

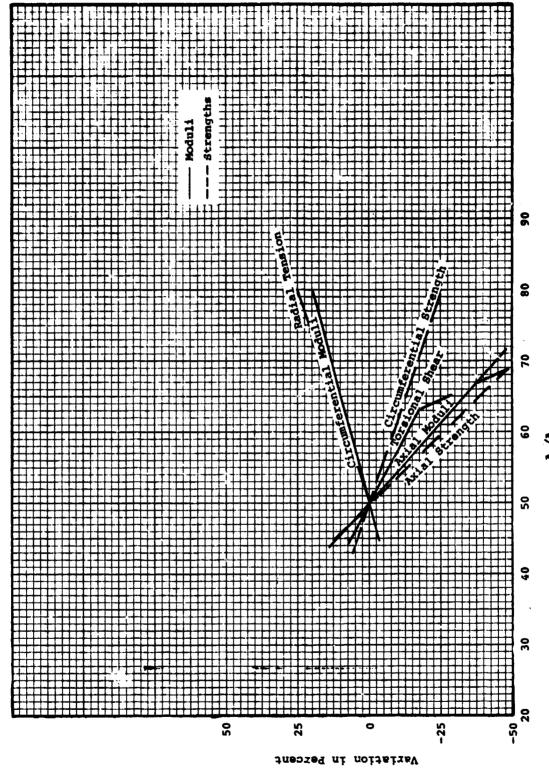


Table 1

,这是一个人,我们就是一个人,我们就是一个人,我们就是一个人,我们就是一个人,我们就是一个人,我们也会会会会会会会会会会会会会会会会会会会会会会会会会会会会会会 第一个人,我们就是一个人,我们就是一个人,我们就是一个人,我们就是一个人,我们就是一个人,我们就是一个人,我们就是一个人,我们就是一个人,我们就是一个人,我们就

ENGINEERING TEST MATRIX FOR 3DCC COMPOSITE CYLINDER (25 INCHES OF MATERIAL AVAILABLE)

	Benarks	Hydrostatic Ring Ring	Ring Coupon Specimen	Button Specimen	Coupon Specimen	Coupon Specimen	:				
-	Number of Specimen/ Orientation	44	***	- 4	m or or or or	m of of m	~ ~	₩ ₩₩	4	3	
•	Temp	70 2000	4000 70 2000	70	70 3000 4000 50001 55001	70 3000 4000 5000 5500	3000	70-5000 70-5000 70-5000	70-5000	70-5000	
	Orientation	Circ	Axia1	Radial	Circ	Axia1		Circ Axial Radial	Radial Axial		
	Property	Tension (T)			Compression (C)		Shear (G)	Thermal (a) Expansion	Thermal (K) Conductivity	Specific Heat	

Stress rate data on two of five specimens Note: NDC and monitors of cylinder and blanks

TABLE :

AVCO 3DCC ENGINEERING TEST MATRIX FOR 3DCC CYLINDERS

Remarks	Bydrostatic and	Quality control	rings		+4 Curved coupon						CRA apparatus RIA. apparatus	CRA apparatus RIA apparatus	
Specimens	6/RT, 2/2000,	9	3/Temp	.	6/RT, 4/3000,	4/5000 3/Teup	3/Temp	8	H	9 r 4	3/Range	3/Range	m
Temp °F	RT, 2000, 3000	RŢ	RT, 2000, 3000,	RT	RT, 3000, 5000	RT, 3000, 4000, 5000, 5500	RT, 3000	RT	RT	RT-5000 RT-5000 RT-5000	RT-1500 RT-5000	RT-1500 RT-5000	RT-5000
Orientation	Circ	Circ	Axial	Radia1	Circ	Axíal		Circ	Circ	Circ Axial Radial	Axial	Radial	
Property	Tension				Compression		Torsional Shear	Hydrostatic Compression Ring	Flexural Ring	Thermal Expansion	Thermal Conductivity		Specific Heat
Mechanical/ Thermal	Mechanical									Thermal			

TABLE 3

CONTRACTOR CONTRACTOR

AVCO 3DCC ENGINEERING TEST MATRIX FOR 3DCC CONE

Remarks	Hydrostatic Ring				CRA apparatus RIA apparatus CRA apparatus RIA apparatus	
Number of Specimens	3 5/RT, 3/Temp 3	3/Temp 3/Temp	3/Tenp	\$ \$		3
Test Temp °F	RT 2000, 3000, 4000 RT	RT, 3000, 5000 RT, 3000, 4000 5000, 5500	RT, 3000	RT-5000 RT-5000 RT-5000	RT-5000 RT-5000 RT-5000 RT-5000	RT-5000
Orientation	Circ Axial Radial	Circ Axial		Circ Axial Radial	Axial Radial	
Property	Tension	Compression	Torsional Shear	Thermal Expansion	Thermal Conductivity	Specific Heat

TABLE 4

A THE TOTAL THE TENT OF THE

NOC OF SOCC CYLINDERS

Parent Cylinder Identi- fication	Cylinder ID Number	Length (in.)	Thick- ness (in.)	Density (gm/cm ²)	Radial Velocity (in./wsec)	X-ray	Redigmetric Gaging	Visual	Reperks
cc-3	129-1	9.49	0.68	1.763	X=0.213 R=0.223-0.241 Good signal	strictions less severe then AMP	E= 1.77 Rel.69-1.85 4% overell scatter. Suttom 3-4" lower density	1. Machined and smooth 2. No anomalies	1. Good velocity signal 2. 40 overall scatter in X-ray gaging with mach cyl and 10 on ropest Measurement 3. Settom 1.0 ver density by X-ray gaging
œ-3	129-2	6,39	0.77	1.62	N=0.240 N=0.229-0.254 Signal highly attenuated	1. Circ low abs striations less severe then AUP 2. 132 view of wall revealed single low abs striation running full length cyl loc 0.5 from in- ner surface- low contr 3. Single 0.2" wide x 1.0" long (circ) high abs area 6 225° 6 5-1/2 in double wall exp in 0° and 30° views	X=1.62 R=1.57-1.69 Random vari- ation	1. Unmachined and rough 2. Single 0.2" wide x 1.0" long (circ) x 0.02" deep nick in outer surface 2 225" and 5.2" no apparent damage to mat. way from nicl 3. Circ y.b. in outer surface loose from mattrix at 3 places—estimated lengths 1.2", 1.2" an: 0.1"	
CC-5	131-1	19,90	0.78	1.66	系=0.226 R=0.212=0.237 Signal highly attenuated	striations less	Top 6" lower density matl	1. Minimum ma- chiming-surf. rough due to missing y.b. and missing matrix between radials 2. Single 0,75° compaction area with bro- ken y.b. in outer surface loc 100°, 8.5° Area was -0.0° deep and was incurred before final process as area conta- matrix appear: matrix appear;	length cyl and circ all way around cyl 2. Top 6" lower density mat! by X-ray gag-"ing with 1" 4-1/2% overall scatter and the circ are t
CC~6	132-1	9,65	0.77	1.71	原=0.230 R=0.222-0.242 Signal highly attenuated	0.5" from	X=1.72 R=1.60-1.84 78 overall scatter; Top 2-3" lower density; sin- gle high den- sity area (1.84) loc 180° and 1"	rough because	ual cracking along circ delams 2. 78 owerall scatter in X-ray gaging 3. Lower density matl in upper 2-3" of cyl by X-ray gaging 4. Single high

TABLE 3

MILE:	OF.	1000	CAFTHRES

					HOC OF 10CC	C. 102110210			
Parent Cylindes Identi- fication	Cylinder ID Humber	Length (in.)	Thick- ness (in.)	(de/ce,)	Redial Velocity (in./weec)	X-rey	Rediometric Gaging	Visual	Romazka
CC-6	132-2	19.91	0.76	1.66	No.224 No.198-0.234 Signal highly attenuated	1. No anomalies 2. Circ low abs strictions less sowers than ARP	%=1.66 Rw1,57-1.73 \$1 overeil scattes: Top and bot- tem 4" lower density	1. Minimum ma- chining-outer surface smooth with missing ma- trix between radials and inner sur- face rough because of missing pa- trix and missing pos y.b. 2. Single 0.10° matrix-filled nich in outer eurface with 2 broken cire located 190° and 12.2° fre index	attenuated 2. Top and hot- tem 4" lower density by X-ray paging with overall acatter of ft
66-7	133-1	9.44	0.82	1.66	N-0.235 n-0.223-0.249 signal highly attenuated	low abs stri-		1. Minimum ma- chining-sur- faces rough because of missing ma- trix and missing pcs y.b. 2. Large irreg discolors- tion (bright appearing) on outer surfaces located 135° to 270° and 4.5° from in- dex to top edge- ummachined area on cyl 3. Extensive chipping alon inner edge on bottom s.d (1 places). Chipp incurred site fabrication 4. Chipping alon inner edge on top edge on top edge 5. Volume cracki along circ de lams in top edge. Cracki extends aroun circ of edge singla length up to 1-1/2°	G-180° by K-ray gaging J. Velocity sig- nel highly attenuated I I I I I I I I I I I I I I I I I I
cc-8	134-2	19,02	0.82	1.57	R-0.226 R-0.216-0.237 Signal highly attenuated	Crows single circ low abs strictions frequently oxtenuing full length of cylloc about 0.7" from inner surface were apparent in cat view (cyllo better exposure)		1. Minimum xx- chining. Por- tions outer surface fair: amooth and portions roug because of missing matri and missing pos y.b. In- ner surface rough missing matrix and missing pos y lame in top edge (minimum mathining to	ials in outer y surface] J. Circ low abs h striation; by X-ray more concentrated in upper 13" to 16" of cyl 4. iddals 10" lower density math by X-ray b, gaing with - overall scat- ter at 5%

The second secon

TARLE 6

The second secon

NONDESTRUCTIVE CHARACTERIZATION OF 3DCC CYLINDERS

Remarks	Top helf high density Top 4 inches low radial velocity		No cylinder MDC on CC-4
Visual	Uneven radial separations	2 in. x 4 in. porous region at 225° on ID, 6 in. from bottom	Wo anomalies
Radio- metric Gaging gm/cm	1.636-	1.634-	•
Radial Velocity in./wsec	0.203	0.197	0.204
Density gm/cm	1.67	1.659	1.67
Thickness	0.71	0.744	0.25
Length	20.1	18.08	1.53
Cylinder ID Mumber	R327-1	R327-2	RI
Parent Cylinder Identi- fication			P-00

TABLE 7

RADIAL PUSHOUT FOR VARIOUS 3DCC MATERIALS

	ch TK AHP omp Shank)	0.447 Inc Stressed (h TK AHP (Comp Gage)	7/16 Inch of CCDP -		3/16 Inch TK CC-8 of CCDP - Virgin		
Pushout L	oad in lbs	Pushout Lo	ed in 1bs	Pushout Lo	ad in 1bs	Pushout Load in lbs		
Inside to Cutside	Outside to Inside	Inside to Outside	Outside to Inside	Inside to Outside	Outside to Inside	Inside to Outside	Outside to Inside	
25.5 28.0 26.5 27.5 25.0 26.5 Avg	24.5 30.0 32.0 22.0 26.5 27.0 Avg	23.0 23.25 25.0 21.0 25.5 23.55 Avg	20.25 20.0 18.5 24.0 20.69 Avg	32.0 40.0 44.0 40.0 35.0 28.0 42.0 44.0 32.0 38.0 37.5 Avg	40.0 36.0 34.0 33.0 30.0 34.0 30.0 36.0	31.0 22.0 33.0 41.0 42.0 34.0 31.0 43.0 37.0 34.0 37.0	20.0 29.0 34.0 30.0 33.0 30.0 40.0 44.0 27.0 23.0 31.0 23.0	
59.28*	60.4*	52.68*	46.29*	85.71*	78.01*	186.67*	161.6*	
1/2 Inch		1/2 Inch of CCDP -		End of C	TK of Tag VD Ring - Virgin	1/4 Inch TK of Middle of CVD Ring of CC-8 + Virgin Density: 1.66 qm/cm ³		
Pushout L	oad in lbs	Pushout Lo	ed in lbs	Pushout L	oad in 1bs	Pushout Load in 1bs		
Inside to Outside Outside to Inside		Inside to Outside	Outside to Inside	Inside to Outside	Outside to Inside	Inside to Outside	Outside to Inside	
>60	>60	25.0 28.0 27.0 28.0 21.0 36.0 27.5 Avg	27.0 42.0 37.0 32.0 36.0 32.0 34.3 Avg	30.0 55.0 58.0 35.0 32.0 18.0 34.0 32.0		21.0 20.0 37.0 49.0 21.0 12.0 10.0 11.0 23.0	24.0 24.0 39.0 30.0 24.0 22.0 27.0	
				36,75 Avg		1.0 20.5 Avg	27.1 Avg	

^{*}Pound/Thickness

THE PARTY

TABLE 8

NONDESTRUCTIVE CHARACTERIZATION SUMMARY TABLE

Cylinder Identi-		Density gm/cm³	≯ -	Axial Velocity in./usec	ं≯स	Radial Velocity in./wsec	> 4	Circ Velocity in./wsec
Number	Mean	Range	Mean	Range	Mean	Range	Mean	Range
129-1	1.63	1.622-1.684	•	١	0.233	0.223-0.241	0.358	0.351-0.365
129-2	1.62	1	ı	•	0.240	0.229-0.254	0.279	0.274-0.283
131-1	1.66	1.611-1.663	0.328	0.319-0.343	0.226	0.212-0.237	0.366	0.358-0.379
132-1	1.71	1.649-1.724	ı	ı	0.230	0.222-0.242	0.291	0.275-0.306
132-2	1.66	1.641-1.677	ı	1	0.224	0.198-0.234	0.320	0.301-0.340
133-1	1.66	1.655-1.675	ı	1	0.235	0.223-0.249	0.314	0.275-0.332
133-2	•	,	1	•	0.231	0.218-0.239	١	1
134-2	1.57	ı	ı	•	0.226	0.216-0.237	ı	,
R327-1	1.65	1.606-1.692	0.343	0.331-0.385	0.203	0.200-0.209	0.341	0.294-0.360

¹Care should be used in interpreting the ranges given as they represent data on from one to many specimens depending on the cylinder

TABLE 9

HONDESTRUCTIVE CHARACTERIZATION OF 3DCC CONES

Visual	Several porous regions. Joss of radials on large Ar/At edges	Three porous regions 15-60 bottom ID 100 4 in. from bottom ID 130° 5 in. from bottom	
Radiometric Gaging gm/cm	1.628 (Hear Top) 1.756 (1/3 up from bottom)	1.602 (Mear Top) 1.739 (Middle)	
Radial Velocity in./wec	0.181 Top 0.222 Bottom	0.227 Bottom	
Density gm/cm ³	1.695	1.683	
Average Thickness	0.50	0 ទ	
Length	19.99	20,38	_
Cone	K357-1	K357-2	

TABLE 10

所とは確認的には

RING CIRCUMPERENTIAL TENSILE DATA FOR 3DCC CYLINDERS

Cylinder		Bulk	Circ	Radial	ULE	Ultimate Strength psi	agth	Initial	fotal Unit Strain in Circ
	Number	gm/cm	velocity in./wsec	Velocity in./wsec	Thin	Outer	Inner	10° pei	(outside)
£-22	129-1-QC-6	1.684	١	0.231	21,907	20,706	23,460	12.20	0.00181
S-22	131-1-7c-1 ¹ 131-1-7c-2 ²	1.621	1 1	0.247	29,800	28,049	31,774	13.18	>0.0028
	131-1-0c-3 ³	1.663	1	0.230	•	•	1	,	•
	Average	1.634	-	0.232	>25,436	>23,889	>27,056	13.37	>0.0031
9-55	132-1-TC-54 132-1-TC-7	1.707	0.306	0.228	23,507	22,125	25,067	14.89	0.0022
	Average	1.712	0.306	0.230	23,507	22,125	25,067	12.65	0.0022
9-00	132-2-0C-2 ³	1.672	•	0.227	1	١	ı	1	1
CC7	133-1-0C-1	1.675	0.27910	0.233	15,344	14,532	16,465	17.84	0.00000
CC-7	133-2-0C-4	1.631	0.28210	0.226	31,165	29,515	33,542	13.58	0.00235
8-55	134-2-0c-5 ⁵	1.659	0.27910	0.219	28,428	26,428	29,944	13.18	0.00202
R327-1	R327-1-TC-10	1.654	0.28010	0.201	29,963	28,200	31,945	13.93	0.0019
	к366-16	1.688	0.310	•	29,219	28,384	30,102	12.07	0.0024
6-50	129-2-TC-3 ¹¹	1.669	0.27610	0.224	22,398	21,084	23,886	-	1
9-22	132-1-7C-6 ¹¹	1.721	0.28110	0.228	20,053	18,825	21,327	1	-
cc-3	129-2-TC-87,111	1.720	0.28210	0.227	>28,750	>27,033	>30,626	•	•
9-00	132-1-TC-4 ⁸	1.724	0.303	0.225	17,991	16,983	19,075	15.58	0.0013
R327-1	R327-1-TC-99, 11	1.653	0.294	0.203	24,312	22,968	25,804		١

Machine shut off once, bladder failed three times and ring failed on fifth run. Ultimate was reached on fifth run. Reported modulus is from first run. Bladder burst

Distance: July 2-1-QC-3 and 132-2-QC-2 had bed data
RFF55131-1-QC-3 and 132-2-QC-2 had bed data
RING 13:-1-TC-5 was to be tested at 3000°F. At 2780°F power went off, and ring broke. We results at E.T.
Reported modulus was measured at RT

Bladder failed twice, ring failed on third run. Ultimate was reached on third run King Nobel at the only speci-ng obtained from Cylinder King King 129-1-TC-8 was to be tested to failure at 3000°F, but membrane ruptured, ring did not fail. On the second trial, ring broke while heating. Modulus at RT = 12.55 x 10° psi. Reported modulus at 3000°F is questionable Ring 132-1-TC-4 had modulus = 15.06 x 10° psi at RT Ring R327-1-TC-9 was also compressed hydrostatically, had modulus = 12.55×10^6 psi at RT Circ velocity value from Sperry not consistent with baseline data obtained using Arenberg Strain data are not valid

TABLE 11

AXIAL TENSILE DATA FOR 3DCC CYLINDERS

Total Unit Axial Strain in./in.	0.0036 0.0054 0.0041	0.0042 0.0044 0.0045 0.0044	0.0062 0.0051 0.0059 0.0057	0.0085
Initial Elastic Modulus 10° psi	8.74 8.46 8.19 8.46	8.00 8.74 9.24 8.66	8.62 7.84 9.89 8.78	5.97
Ultimate Strength psi	34,220 30,018 33,230 32,489	31,759 31,699 31,819 31,759	38, 299 34, 653 34, 839 35, 930	38, 483 42, 324 36, 778 39, 195
Radial Velocity in./wsec	0.228 0.226 0.230 0.238	0.228 0.222 0.216 0.222	0.213 0.210 0.217 0.213	0.221 0.223 0.229 0.224
Sonic Velocity in./wsec	0.321 0.319 0.324 0.321	0.321 0.322 0.323 0.323	0.319 0.319 0.322 0.320	0.325 0.322 0.323 0.323
Bulk Density gm/cm³	1.637	1.630 1.632 1.633 1.633	1.634 1.632 1.635	1.634 1.632 1.636 1.636
Specimen Number	131-1-TA-1 131-1-TA-2 131-1-TA-3 Average	131-1-TA-4 131-1-TA-5 131-1-TA-6 Average	131-1-TA-7 ³ 131-1-TA-8 131-1-TA-9 Average	131-1-TA-16 131-1-TA-11 131-1-TA-124 Average
Temp F	701	20001	30001	3500 ²
Stress Rate psi/min	10,000			
Cylinder ID Number	131-1			

Strain was measured using clip-ons

Strain was measured using strain analyzer. Strain data are questionable due to suspected internal bending

Specimen number 131-1-TA-7 was tested twice. Pullrod broke during first run.

Maximum load was reached on first run

*Specimen number 131-1-TA-12 had machining defect. Strain data are not valid

TABLE 12

The state of the s

RADIAL TENSILE DATA FOR 3DCC CYLINDERS

Ultimate Strength psi	406	429	263	366	
Ultimate Load lbs	101.5	107.2	65.6	91.4	
Radial Velocity in./µsec	0.206	0.203	0.200	0.203	
Bulk Density gm/cm³	1.633	1.610	1.643	1.629	
Specimen Number	R327-1-TR-1	R327-1-TR-2	R327-1-TR-3	Average	
Temp	70				
Stress Rate psi/min	10,000				
Cylinder ID Number	R327-1				

Note: Specimen failed at bond line

TABLE 13

CIRCUPTERENTIAL COMPRESSIVE DATA FOR 3DCC CYLINDERS

Specimen Configuration	di i	Stress Rate psi/min	Cylinder ID Humber	Specimen	Bulk Density gm/cm	Axial Velocity in./weec	Radial Velocity in./wsec	Ultimate Strength psi	Initial Elastic Modulus 10 psi	Total Axial Strain in Circ Direction in./in.	
Straight With Lateral Supports)	0,	10,000	131-1	131-1-CC-1 ¹ 131-1-CC-2 131-1-CC-4 131-1-CC-7	1.6.8 1.618 1.619 1.623 1.623	0.360 0.358 0.366 0.366	0.216 0.218 0.211 0.219 0.216	4,914 6,615 6,735 6,414 6,170	7.43	0.0004	
			R327	R327-1-CC-11 R327-1-CC-16 Average	1.634	0.358 0.351 0.355	0.194 0.195 0.195	7,580	7.08	0.00197 0.00172 6.00184	
	3000	10,000	131-1	131-1-CC-3 131-1-CC-8 Average	1.619 1.624 1.622	0.361 0.366 0.364	0.211	9,822 9,560 9,691	5.14 6.68 5.91	0.0022	
			R327-1	R327-1-CC-13 R327-1-CC-14 Average	1.630 1.622 1.626	0.327 0.366 0.347	0.191 0.187 0.189	12,501 8,962 10,731	5.91 6.33 6.12	0.0018	
	2000	100,000	131-1	131-1-cc-5 131-1-cc-9 Average	1.623	0.368 0.363 0.366	0.209	9,285	3.30	0.0058	
		100,000	R327-1	R327-1-CC-12 R327-1-CC-15 Average	1.640	0.345 0.359 0.352	0.196 0.190 0.193	12,754	3.70	0.0083	
Curved	70		131-1	131-1-CC-17 131-1-CC-18 Average	1.632 1.654 1.643	0.381 0.386 0.384	0.191 0.204 0.198	16,200 15,298 15,749	8.11 11.88 10.00	0.0020 0.0023 0.0021	
			130-1	130-1-00-14 130-1-00-24 Average	1.686 1.676 1.681	0.350 0.352 0.351	0.210	18,900	11.70	0 : 029 0 : 022 0 : 0025	

Specimen 131-1-CC-1 was tested without using lateral supports

Strrin data for Specimen Number 131-1-CC-2 is not walid

 3 Strain data for Specimen Number 131-1-CC-7 is questionable

Appenies 130-1-CC-1 and 130-1-CC-2 are the only two that were obtained from Cylinder Number 130-1

ation to the state of the state

المواق الديمية المعطوط المقدية بالمستح فالماعات المراجات المناهاة

and the second of the second o

TABLE 14

HYDROSTATIC COMPRESSIVE RING DATA FOR 3DCC CYLINDERS

								Initia	Initial Elastic Modulus x 10° psi	Modulus	
						Maximum			•0	•06	•
Temp *P	Cylinder ID Number	Ring Number	Bulk Density gm/cm	Circ Velocity in./wsec	Radial Velocity in./wsec	Applied on Ring	Run Wunder	Using Strain Gage	Using Clip-ons	Using Strain Gage	Using Clip-ons
70	132-1	132-1-SORI-R2	-		•	3000	1	21.56	20.49	16.45	8.24
							7	18.90	17.98	17.70	12.84
							Avg	20.23	19.10	17.08	10.54
	R327-1	R327-1-TC-9	1.653	0.294	0.203	3000		11.85	14.57	12.83	10.94

TARLE 15

RING FLEXURAL (2-POINT LOAD) DATA FOR 3DCC CYLINDERS

Initial Elastic Modulus 10° psi	0°-180° 90°-270°	5.01
Initial Mod 10	00-180	5.14
1 1 1	Direction	0°-180° 90°-270°
Radial	velocity in./µsec	•
Circ	Velocity in./µsec	ı
Bulk	Density gm/cm³	
	Ring Number	132-1-SORI-R2
Cylinder	ID Number	132-1
	Temp	70

TABLE 16

Management of the control of the con

は、「一般のでは、「一般のでは、「一般のでは、「一般のでは、「一般のでは、「一般のでは、「一般のでは、「一般のでは、「一般のでは、「一般のでは、「一般のでは、「一般のでは、「一般のでは、「一般のでは、 「一般のでは、「一般のでは、「一般のでは、」というでは、「一般のでは、「一般のでは、「一般のでは、」というでは、「一般のでは、「一般のでは、」というでは、「一般のでは、「一般のでは、」というでは、「一般のでは、「一般のでは、」というでは、「一般のでは、「一般のでは、」というでは、「一般のでは、「一般のでは、」というでは、「一般のでは、「一般のでは、」というでは、「一般のでは、」というでは、「一般のでは、」というでは、「一般のでは、」というでは、「一般のでは、」というでは、「一般のでは、」というでは、「一般のでは、」というでは、「一般のでは、」というでは、「一般のでは、」というでは、「一般のでは、」というでは、「一般のでは、」というでは、「一般のでは、」というでは、「一般のでは、」というでは、「一般のでは、」というでは、「一般のでは、」というでは、「一般のでは、」というでは、「一般のでは、」」」というでは、「一般のでは、」」というでは、「一般のでは、」」というでは、「一般のでは、「一般のでは、」」というでは、「一般のでは、「一般のでは、」」というでは、「一般のでは、「一般のでは、「一般のでは、」」というでは、「一般のでは、「一般のでは、「一般のでは、」」というでは、「一般のでは

AXIAL COMPRESSIVE DATA FOR 3DCC CYLINDERS

Temp Stress Cylinder Specimen Bulk Axial **P Psi/min Number Number gm/cm³ in./wsec 70 10.000 3321 13321 13321	Specimen Density Number gm/cm ³	Bulk Density gm/cm ³		Axial Veloci in./wa	_ \$ %	Radial Velocity in./wsec	Ultimate Strength psi	Initial Modulus 10 ⁶ psi 11.15	Total Unit Axial Strain in./in.
R327-1 R327-1-CA-7 1.670	R327-1-CA-7 1.670 R327-1-CA-7 1.656	1.670	-	900	0.333	0.200	15,072	6.49	0.0023
Average 1.663	1.663	1.663			0.332	0.200	14,856	7.60	0.0020
3000 10,000 131-1 131-1-CA-2 1.629	131-1-CA-2		1.629		0.338	0.214	20,725	7.03	0.0034
R327-1-CA-8 1.666	R327-1-CA-8 R327-1-CA-13	3	1.666		0.334	0.204	20,712	8.60 7.58	0.0029
Average 1.666			1.666		0.333	0.202	20,268	8.09	0.0032
4000 10,000 131-1 131-1-CA-3 1.640	131-1-CA-3		1.640		0.336	0.224	20,936	4.37	0.0089
R327-1 R327-1-CA-9 1.665	R327-1-CA-9 R327-1-CA-14		1.665		0.331	0.202	21,744 21,960	4.86 5.10	0.0079
Average 1.667			1.667		0.331	0.202	21,852	4.98	0.0074
5000 100,000 131-1 131-1-CA-4 1.635 1.643	131-1-CA-4 131-1-CA-5		1.635		0.339	0.221	17,200	2.45	>0.0096 0.0280
Average 1.639			1.639		0.341	0.224	16,620	2.28	0.0280
10,000 R327-1 R327-1-CA-10 1.666	R327-1-CA-10		1.666		0.332	0.202	13,920	2.27	0.0215
5500 10,000 R327-1 R327-1-CA-6 1.675	R327-1-CA-6		1.675		0.332	0.205	8,760	0.73	0.0280
A-11 ² A-15	R327-1-CA-11 ² R327-1-CA-15		1.667		0.332	0.204	9,672	2.17	0.0216
Average 1.666			1.666		0.335	0.207	9,996	2.17	0.0216

Notes: 1. 2. 3.

1. Two specimen configurations were used, one for all specimens of each cylinder 2. Strain data are not valid for Specimen Number R327-1-CA-11 3. Bending evident near end of run

Africa of the Same and the second
TABLE 17

THE REPORT OF THE PARTY OF THE

TORSIONAL SHEAR DATA FOR 3DCC CYLINDERS

Shear Modulus 10 psi	0.180 0.157 0.169	0.291	0.310	0.303
Ultimate Strength psi	>2,025 4,275 4,275	>4,050	>3,950 >3,975 >3,950	>4,000
Radial Velocity in./µsec	0.224	0.201	0.218 0.232 0.325	0.202
Axial Velocity in./µsec	0.321 0.322 0.322	0.329	0.329	0.329
Bulk Density gm/cm ³	1.645 1.636 1.641	1.661	1.635	1.654
Specimen Number	131-1-TS-1 131-1-TS-3 ² Average	R327-1-TS-5	131-1-TS-2 131-1-TS-4 Average	R327-1-TS-6
Cylinder ID Number	131-1	R327-1	131-1	R327-1
Stress Rate psi/min	10,000		10,000	
Temp	70		3000	
Load Direction	Circ/ Radial Plane			

 $^{
m l}_{
m Every}$ specimen had four axial fibers

2 Specimen number 131-1-TS-1 was tested to failure

TABLE 18

DESIGN MODULUS FOR 3DCC

	70°F	2000°F	3000°F	70°F 2000°F 3000°F 4000°F 5000°F 5500°F	5000°F	5500°F
Circ Tension	13.5	13.5 14.5	15.0	1	•	ı
Axial Tension	8.5	8.7	8.8	ı	•	I
Circ Compression	12.0	1	12.0	7.7	3.5	1.51
Axial Compression	7.0	ı	7.0	4.6	2.25	0.75

110,000 psi/min - higher for higher stress rates

TABLE 19

See high consecutivity and the control with the control of the con

The second secon

RING CIRCUMPERENTIAL TENSILE DATA FOR 3DCC COME

Stress	ï	Bulk	Circ	Radial	Ultim	Ultimate Strength psi	igth	Initial Elastic Mcdulus 10 ⁶ psi	Initial Elastic Modulus	Total Unit Strain in Circ Direction in./in./(S.G. Fata)
Rate psi/min	Number	gm/cm³	in./wsec	in./wsec	Thin	Outer	Inner	S.G. Data)	Clip-on4	(outside)
								-		
10,000	K357-2-T-1-C ¹	1,680	0.375	0.225	27,321	25,867	28,537	17.07	,	0.0015
	K357-2-T-2-C ²	1.681	0.352	0.231	24,200	22,761	25,826	18.9	15.9	0.0012
	K357-2-T-3-C3	1.558	0.315	0.213	39,596	37,357	42,108	14.67	12.3	0.0027

Motes:

44 H

TABLE 20 AXIAL TENSILE DATA FOR 3DCC CONE K357-27

Cone ID Number	Stress Rate psi/min	Temp • F	Specimen Number	Bulk Density gm/cm ³	Axial Velocity in./weec	Radial Velocity in./wsec	Ultimates Strength psi	Initial Elastic Modulus 10° psi	Total Unit Axial Strain in./in.
K357-2	10,000	70	K357-2-T-1-A2 K357-2-T-5-A2 K357-2-T-9-A1 K357-2-T-10-A1 K357-2-T-11-A3	1.611 1.699 1.692 1.625 1.702	0.314 0.303 0.309 0.310 0.311	0.219 0.225 0.227 0.213 0.232	21,411 12,811 21,858 11,610	6.45 5.20 7.64 ⁹ 5.41	0.0050 ⁴ 0.0024 0.0030 0.0026
			Average	1.666	0.309	0.223	16,923	6.18	0.0033 (0.0029) 4
		2000	K357-2-T-2-A ¹ K357-2-T-6-A ² K357-2-T-12-A ³ Average	1.599 1.719 1.701	0.307 0.317 0.303 0.309	0.216 0.221 0.236 0.224	23,559 13,679 11,123 16,120	7.01 7.73 7.61 7.72	0.0037 0.0017 0.0018 0.0024
		3000	K357-2-T-3-A ¹ K357-2-T-7-A ² K357-2-T-7-A ³ Average	1.611 1.707 1.721 1.680	0.306 0.309 0.306 0.307	0.219 0.225 0.234 0.226	23,295 14,225 13,962 17,160	12.91 12.50 9.20 11.45	0.0018 0.0012 0.0021 0.0017
		3500	K357-2-T-4-A2 K357-2-T-8-A3,6 K357-2-T-14-A3 K357-2-T-15-A3	1.618 1.683 1.717 1.723	0.308 0.305 0.303 0.301	0.214 0.218 0.232 0.237	27,590 18,314 13,509	6.64 8.01 6.82	0.0056 0.0021 0.0021
ı			Average	1.685	0.304	0.225	19,804	6.05	0.0052

- Specimen is obtained from the top section of the cone. Specimen has five axial fibers in
- gage section Specimen is obtained from the middle section of the cone. Specimen has three axial fibers in gage section
- Specimen is obtained from the bottom section of the cone. Specimen has three exial fibers in gage section
- Specimen No. K357-2-T-1-A was tested twice. Pullrod broke during first run. Ultimate was reached on second run. Reported modulus is from first run. Extrapolated atrain from first run is 0.0035

- run is 0.0035

 5. Specimen No. K357-2-T-9-A broke while handling
 6. Specimen No. K357-2-T-9-A broke while handling
 7. All strain measurements were made using clip-ons
 8. In order to obtain true data for this test, it was important to maintain the number of axial fibers along the gage length. The edges of each specimen at the gage section were machined parallel to the outer axial fibers, so that the number of cells will be maintain I the same. Because these specimens are obtained from a cone, then the cruss sectional area of the gage section will vary along the length of the cone. The area at failure location for each specimen was measured, and used for calculating the ultimate strength. See individual data curves for dimensions at failure area
 9. Specimen showed evidence of bending difficult to calculate

TABLE 21

The second secon

RADIAL TENSILE DATA FOR 3DCC CONE

	_				
Ultimate Strength psi	1	•	515	515	
Ultimate Load lbs		1	129	129	•
Radial Velocity in./µsec	0.230	0.241	0.233	0.238	
Axial Velocity in./µsec	95t U	0,363	0.360	0.360	
Bulk Density gm/cm ³	1 744	1.724	1.714	1.727	
Specimen Number	x357-2-4-1-p1	K357-2-T-2-R ²	K357-2-T-3-R	Average	
Rate psi/min	000 01				
Temp	7.0	2			

lglue pulled loose between pullrod and specimen

²Specimen was broken while handling

TABLE 22

CIRCUMPERENTIAL COMPRESSIVE DATA FOR 3DCC COME*

Specimen Configuration	Temp	Stress Rate psi/min	Specimen	Bulk Density gm/cm ³	Axial Velocity in./wsec	Radial Velocity in./µsec	Ultimate Strength psi	Initial Elastic Modulus 10 ⁶ psi
Straight	70	10,000	K357-2-C-1-C K357-2-C-7-C K357-2-C-13-C	1.699 1.692 1.671 1.687	0.387 0.387 0.392 0.398	0.230 0.224 0.224 0.226	5,413 4,872 5,445 5,243	5.60 4.09 4.23 4.64
	3000	10,000	K357-2-C-2-C K357-2-C-8-C K357-2-C-14-C Average	1.695 1.676 1.678 1.683	0.387 0.393 0.388 0.389	0.227 0.228 0.227 0.227	9,319 10,316 10,029 9,888	11.45 10.22 10.34 10.67
	2000	10,000	K357-2-C-3-C K357-2-C-9-C K357-2-C-15-C Average	1.681 1.675 1.674 1.677	0.394 0.387 0.386 0.389	0.232 0.228 0.236 0.235	9,061 11,045 10,516 10,207	3.61 4.77 4.11 4.16

Note: *All specimens from near the bottom of cone, 1-3 slightly higher

The second secon

AXIAL COMPRESSIVE DATA FOR 3DCC COME

Totai Unit Arial Strain in./in.	0.00172	0.00310 0.00243 0.00240	0.00598 0.00396 0.00585 0.00526	>0.0140 >0.0090 >0.0090	>0.0160 >0.0160 >0.0140 >0.0126
Initial Elastic Modulus 10° psi	5.49	4.26 6.51 7.82 6.20	4.56 5.55 4.47 4.86	5.04 4.35 4.70	2.20 2.11 2.16
Ultimate Strength pei	11,405 10,703 10,204 10,771	11,406 14,308 12,834	13,786 14,558 15,556 14,633	11,224 12,018 12,132 12,075	>5,488 >8,050 >7,937 >7,994
Radial Velocity in./wsec	0.227 0.225 0.229 0.229	0.226 0.230 0.235 0.235	0.229 0.229 0.230 0.230	0.225 0.227 0.231 0.229	0.228 0.229 0.231 0.230
Axial Velocity in./wsec	0.358 0.342 0.348 0.349	0.359 0.342 0.359	0.362 0.357 0.358 0.359	0.353 0.361 0.355 0.358	0.358 0.362 0.358 0.360
Bulk Density gm/cm ¹	1.692 1.658 1.725 1.692	1.715 1.700 1.719 1.711	1.702 1.707 1.768 1.768	1.700	1.694 1.717 1.715 1.716
Specimen Number	K357-2-C-1-A ³ K357-2-C-6-A ³ K357-2-C-11-A ^{1,4} Average	K357-2-C-2-A ² , 3 K357-2-C-7-A ³ K357-2-C-12-A ⁴ Average	K357-2-C-3-A4 K357-2-C-8-A4 K357-2-C-13-AAAverage	K357-2-C-4-A ² , 3 K357-2-C-9-A ⁴ K357-2-C-14-A	K357-2-C-5-A ³ K357-2-C-10-A ⁴ K357-2-C-15-A Average
Stress Rate psi/min	10,000	10,000	10,000	10,000	10,000
Temp • P	70	3000	4000	2000	5500
Specimen Configuration	Straight				

Poorly machined, cut into one of three axials Poorly machined, centered on radial, two full axials $A_{\rm r}/A_{\rm t} \approx 0.62$ $A_{\rm r}/A_{\rm t} \approx 0.65$

TABLE 24

THE PARTY OF THE P

AXIAL TORSIONAL SHEAR DATA FOR 3DCC CONE

Shear 7 Modulus 10 ⁶ psi	0.191 0.180 0.0504	0.141	0.372 0.410 0.405	0.396
Ultimate Strength psi	>2,565 >2,565 1,025	>2,565	>4,615 >5,150 >4,835	>4,615
Circ Velocity in./µsec	0.363 0.361 0.380	0.368	0.376 0.376 0.368	0.373
Axial Velocity in./µsec	0.359 0.351 0.367	0.359	0.351 0.347 0.352	0.350
Bulk Density gm/cm³	1.584 1.592 1.690	1.622	1.599 1.590 1.590	1.593
Specimen Number	K357-2-TS-1 ^{1,5} K357-2-TS-2 ^{1,4} K357-2-TS-6 ^{2,6}	Average	K357-2-TS-31,4 K357-2-TS-43,4 K357-2-TS-51,4	Average
Stress Rate psi/min	10,000		10,000	
Temp	70		3000	

Nctes:

Specimen had three axial fibers Specimen had one axial fiber, this is the only specimen that was tested to failure Specimen had four axial fibers $A_{\rm L}/A_{\rm L} \approx 0.555$ 1:

≈ 0.615 ${\rm A_{r}/A_{t}}$ 5.

≈ 0.735 Ar/At

Mixed mode

LIST OF APPENDICES

		Page
Al.	Ultimate Strength, Elastic Modulus, and Poisson's Ratio to 5500°F in Tension	233
A2.	Ultimate Strength, Elastic Modulus, and Poisson's Ratio to 5500°F in Compression	247
A3.	Shear Modulus and Modulus of Rupture in Torsion to 5500°F	259
A4.	Thermal Expansion to 1800°F	265
A5.	Thermal Expansion to 5500°F	269
A6.	A Comparative Rod Apparatus for Measuring Thermal Conductivity to 2000°F	275
A7.	Thermal Conductivity to 5500°F by Radial Inflow Method	289
A8.	Heat Capacity to 1000°F	303
A9.	Heat Capacity to 5500°F	309
A10.	Ultrasonics	317
A11.	Sonic Evaluations Used for 3DCC	321
A12.	"ltrasonic Velocity at Room Temperature	325
A13.	Electrical Resistivity	329
Bl.	Circumferential Tensile Results	331
B2.	Axial Tensile Results	369
вз.	Radial Tensile Results	383
В4.	Circumferential Compression Results	387
в5.	Axial Compression Results	413
B6.	Torsional Shear Results	429
B7.	Hydrostatic Compression Ring Results	437
B8.	Flexural Ring Results	451

LIST OF APPENDICES CONCLUDED

		Page
Cl.	Circumferential Tensile Results	455
C2.	Axial Tensile Results	469
С3.	Radial Tensile Results	485
C4.	Circumferential Compressive Results	487
C5.	Axial Compressive Results	497
C6.	Torsional Shear Results	513

Preceding Page BLANN - FILMEN

APPENDIX Al

Ultimate Strength, Elastic Modulus, and Poisson's Ratio to 5500°F in Tension

ULTIMATE STRENGTH, ELASTIC MODULUS AND POISSON'S RATIO TO 5500°F IN TENSION

A typical tensile facility is shown in the photograph in Figure 1 and in the schematic in Figure 2. The primary components are the gasbearings, the load frame, the mechanical drive system, the 5500°F furnace, the optical strain analyzers and associated instrumentation for measurement of load and strain. The load capacity is 15,000 pounds.

The load frame and mechanical drive system are similar to those of many good facilities. The upper crosshead is positioned by a small electric motor connected to a precision screw jack. This crosshead is stationary during loading and is moved only when assembling the load train. The lower crosshead is used to apply the load to the specimen through a precision screw jack chain driven by a variable speed motor and gear reducer.

Nonuniaxial loading, and therefore bending stresses, may be introduced in tensile specimens not only from (1) misalignment of the load train at the attachment to the crossheads, but also from (2) eccentricity and non straightness within the load train, (3) unbalance of the load train and (4) external forces applied to the load train by such items as electrical leads and clip-on extensometers. Although the bending moments from some of these sources may seem relatively slight, the resulting stress distortions are quite significant in the evaluation of the extremely sensitive brittle materials. Now consider each individually.

To confirm that the gas-bearings had eliminated nonuniaxial loading at the point of attachment of the load train to the crossheads, the frictional moment was determined at a load of 5000 pounds by measuring the torque required to produce initial motion within the system with the bearings in operation. This torque was found to be a maximum of 6.6×10^{-3} inch-pounds. The calculated value of the coefficient of kinetic friction was 4.5×10^{-7} . The stress that could be induced in the specimen due to this bending moment was 0.16 psi, or less than 0.002 percent of the tensile stress produced within a typical graphite specimen. These low values clearly indicate the elimination of problems of bending stress in the specimen imposed by misalignment at the crosshead attachments, either initially or during loading.

Emphases in the design of the load train were placed on (1) large length-to-diameter ratios at each connection, (2) close sliding fits (less than 0.0005") of all mating connections, (3) the elimination of threaded connections, (4) the use of pin connections wherever possible and (5) increasing the size of components to permit precise machining of all mating surfaces. All members were machined true and concentric to within 0.0005", and the entire load train is checked regularly to ensure overall alignment following assembly of the individual members.

This process ensures concentricity and straightness in the system. The specimen is mounted in the pull rods and the assembly checked for non-straightness ("bow") and eccentricity ("kink") before each test. When the bow is limited to 10 mil TIR and the offset to 1-1/2 mils, the average parasitic strain is about 75 microinches and the maximum among several tests is 200 microinches on a 0.250 inches diameter specimen. Parasitics are checked weekly on many programs using specimens with 12 strain gages. Closer parasitics can be held by using smaller allowable bows and offsets. Unfortunately, the random error in the strain gages themselves is as high as 3 percent of the signal and which is about 21 microinches at a 7000 microinches signal. This is about the same order as the real parasitic.

The problems of unbalance within the load train and of external forces applied to the load train have been explored and corrected. The entire load train is statically balanced to less than 0.01 inch-pound for normal operation.

Standard and miniature configurations of the tensile specimen are shown in Figure 3. The standard specimen provides a relatively large L/D ratio in the gripping area to ensure good alignment. All surfaces in the gripping area are cylindrical in order to make precision machining easier and repeatable from specimen to specimen. The standard specimen also has double breakdown radii from the gripping area to the gage section. This double breakdown allows a uniform transition of the stress pattern and reduces the frequency of radius (out of gage) fractures. This specimen provides a uniform gage section which gives a definable volume of material under stress and permits accurate measurements of strain. The flags for the measurement of axial strain are positioned one inch apart so that unit strain is recorded directly. The flag attachment for measurement of lateral strain is positioned between the flags for axial strain; see Figure 4.

A schematic of the precision tensile grip is shown in Figure 5. The design is much like the jaws of a lathe head or the chuck of a drill motor made with precision. Observe from the figure the long surface contact of the mating parts and the close fits to establish precise alignment with the specimen. As the load is applied, the wedges maintain alignment to fracture.

Figure 6 is a sketch of the 5500°F furnace used for tension showing the basic components. The furnace consists of a resistively heated graphite element insulated from a water-cooled shell by thermatomic carbon. The furnace and specimen are purged with helium to provide an inert atmosphere. Ports with visual openings are provided on opposite sides of the furnace as a means of allowing the strain analyzers to view the gage flags on the specimen. Specimen temperatures are determined by optical pyrometer readings taken through another small sight port containing a sapphire window. A calibration curve was established for the loss through the sapphire window, and since the furnace cavity acts essentially as a blackbody, true temperature readings are obtained. Power is supplied to the heating element by means of a 25 KVA variable transformer. Specimen temperature profiles essentially are eliminated by regular calibrations using a dummy load train assembly with internally mounted thermocouples and optical pyrometer ports. Pull rod balance heaters are adjusted to maintain a zero-gradient.

Strain measurement consists of measuring optically the elongation between two flags, or targets, which are mounted on the specimen and separated initially by a predetermined gage length. The travel of the targets is measured by sensing the displacement of the image of the edge of the targets and then electromechanically following the image displacement. The relative travel of the two targets provides the strain. Readout is continuous and automatic on a millivolt recorder. A schematic of the analyzer is shown in Figure 7.

A brief summary of the mechanical motions of the components involved in monitoring the strain is helpful in understanding the detailed performance. A tracking telescope follows the upper target and carries a second telescope mounted on its carriage. The second telescope is capable of independent motion to follow the lower target. The relative displacement between the upper and lower telescope, as strain occurs, defines the strain. The system usually is operated so that the tracking telescope follows the upper target and the strain is monitored by the relative displacement of the aperture rather than the telescope following the lower target. With this procedure the maximum range is the maximum displacement available for the lower aperture, of about 1/8 inch, and the sensitivity is limited by the optics and the noise level of the detector. Using both telescopes, the range is about 3/4 inch.

To provide optical references on the specimens, targets are affixed to the test specimen as mentioned. When the specimen is heated to temperature, the targets are self-luminous and are observed optically. The optics view past the luminous targets into a cooled cavity in the opposite furnace wall. The self-luminous targets are then visible against a dark background. To obtain data below 2000°F, a light beam is directed from behind the flags providing a shadow image for the detection system.

西は横西端である。

| 100mm | 100mm | 100mm | 100mm | 100mm | 100mm | 100mm | 100mm | 100mm | 100mm | 100mm | 100mm | 100mm | 100mm | 100mm | 100mm | 100mm | 100mm | 100mm | 100mm | 100mm | 100mm | 100mm | 100mm | 100mm | 100mm | 100mm | 100mm | 100mm | 100mm | 100mm | 100mm | 100mm | 100mm | 100mm | 100mm | 100mm | 100mm | 100mm | 100mm | 100mm | 100mm | 100mm | 100mm | 100mm | 100mm | 100mm | 100mm | 100mm | 100mm | 100mm | 100mm | 100mm | 100mm | 100mm | 100mm | 100mm | 100mm | 100mm | 100mm | 100mm | 100mm | 100mm | 100mm | 100mm | 100mm | 100mm | 100mm | 100mm | 100mm | 100mm | 100mm | 100mm | 100mm | 100mm | 100mm | 100mm | 100mm | 100mm | 100mm | 100mm | 100mm | 100mm | 100mm | 100mm | 100mm | 100mm | 100mm | 100mm | 100mm | 100mm | 100mm | 100mm | 100mm | 100mm | 100mm | 100mm | 100mm | 100mm | 100mm | 100mm | 100mm | 100mm | 100mm | 100mm | 100mm | 100mm | 100mm | 100mm | 100mm | 100mm | 100mm | 100mm | 100mm | 100mm | 100mm | 100mm | 100mm | 100mm | 100mm | 100mm | 100mm | 100mm | 100mm | 100mm | 100mm | 100mm | 100mm | 100mm | 100mm | 100mm | 100mm | 100mm | 100mm | 100mm | 100mm | 100mm | 100mm | 100mm | 100mm | 100mm | 100mm | 100mm | 100mm | 100mm | 100mm | 100mm | 100mm | 100mm | 100mm | 100mm | 100mm | 100mm | 100mm | 100mm | 100mm | 100mm | 100mm | 100mm | 100mm | 100mm | 100mm | 100mm | 100mm | 100mm | 100mm | 100mm | 100mm | 100mm | 100mm | 100mm | 100mm | 100mm | 100mm | 100mm | 100mm | 100mm | 100mm | 100mm | 100mm | 100mm | 100mm | 100mm | 100mm | 100mm | 100mm | 100mm | 100mm | 100mm | 100mm | 100mm | 100mm | 100mm | 100mm | 100mm | 100mm | 100mm | 100mm | 100mm | 100mm | 100mm | 100mm | 100mm | 100mm | 100mm | 100mm | 100mm | 100mm | 100mm | 100mm | 100mm | 100mm | 100mm | 100mm | 100mm | 100mm | 100mm | 100mm | 100mm | 100mm | 100mm | 100mm | 100mm | 100mm | 100mm | 100mm | 100mm | 100mm | 100mm | 100mm | 100mm | 100mm | 100mm | 100mm | 100mm | 100mm | 100mm | 100mm | 100mm | 100mm | 100mm | 100mm | 100mm | 100mm | 100mm | 100mm | 100mm | 100mm | 100mm | 100mm | 100mm | 100mm | 100mm | 100mm | 100mm | 10

The image of the target is focused through a rotating shutter (chopper) and onto a rectangular aperture. Small slits in the aperture pass a portion of the upper and lower edges of the light beam. A photocell receives the light thus transmitted, and an electronic circuit detects whether the energy passed by the two slits is equal. A servo drives the apertures to let a balanced quantity of light pass through the two slits and thus maintains an optical null.

To obtain lateral strain, a p:rain analyzer is supported horizontally on the tensile frame to view the diametrical or lateral strain of the specimen. A flag attachment, with the general configuration as shown in Figure 8, was developed to follow and transmit lateral motions of up to a few mils. The three-piece assembly consists of a ring and two rams bearing on the specimen.

Calibrations of the analyzers are performed in various ways including absolute correlations to precision micrometers, absolute reading to a driven dilatometer assembly. Strain gage extensometers, and direct plots of stress-strain for reference materials such as steel, plexiglas, magnesium and aluminum. Precision is within ±0.000020 inch.

Instrumentation includes primarily a stress-strain measurement system composed of a strain sent plot load cell with 0.0003 inches total deflection/1000 pounds, constant d.c. voltage power supply, two optical strain analyzers, and two X-Y recorders. Specimen temperature is monitored with an optical pyrometer. Stress (load) is measured by a commercial load cell. The cell receives a constant d.c. voltage input from the power supply and transmits a millivolt signal (directly proportional to load) to an X-Y recorder. Simultaneously, the optical strain analyzers measure both the axial and lateral strain and transmit a millivolt signal (proportional to strain) to the X-Y recorders. Thus, continuous plots of stress-axial strain and strain-lateral strain are recorded simultaneously.

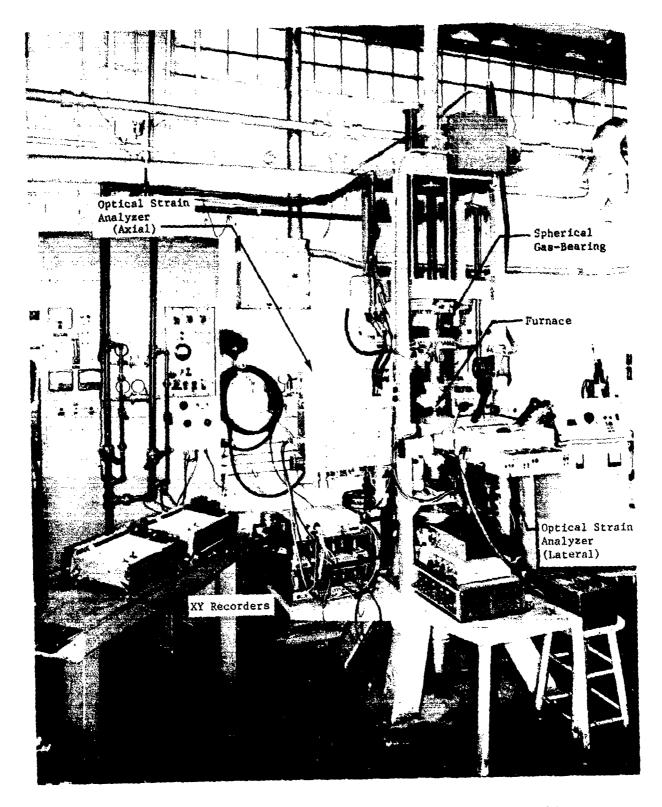


Figure 1. Picture of a Tensile Stress-Strain Facility

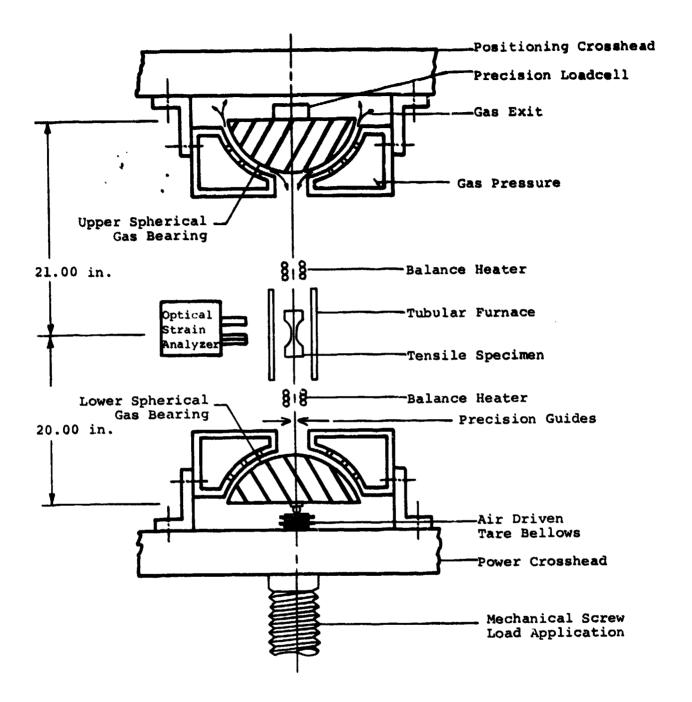
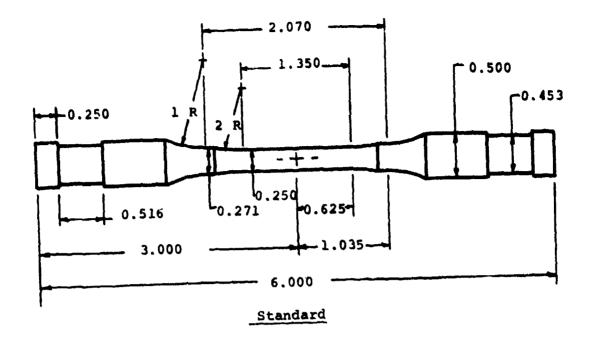
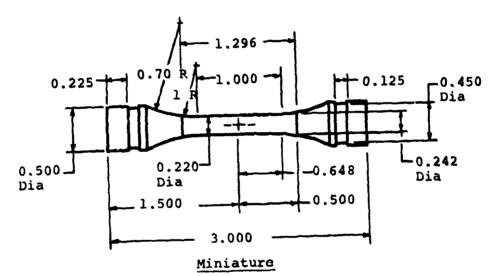


Figure 2. Schematic Arrangement of Gas-Bearing Universals, Specimen and Load Train

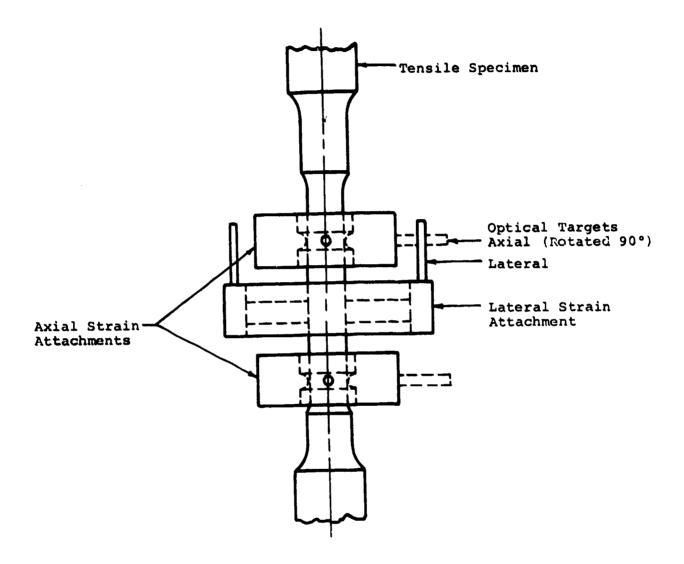




Notes:

- 1. All diameters true and concentric to 0.0005 in.
- 2. Do not undercut radius at tangent points
- 3. Both ends to be flat and perpendicular to 0.0005 in.
- 4. Tolerances unless otherwise noted: Decimals ±0.001 on diameters and 0.005 on length fractions ±1/64
- 5. All dimensions are in inches

Figure 3. Tensile Specimen Configurations



The state of the s

Figure 4. Location of the Flag Attachments on the Tensile Specimens

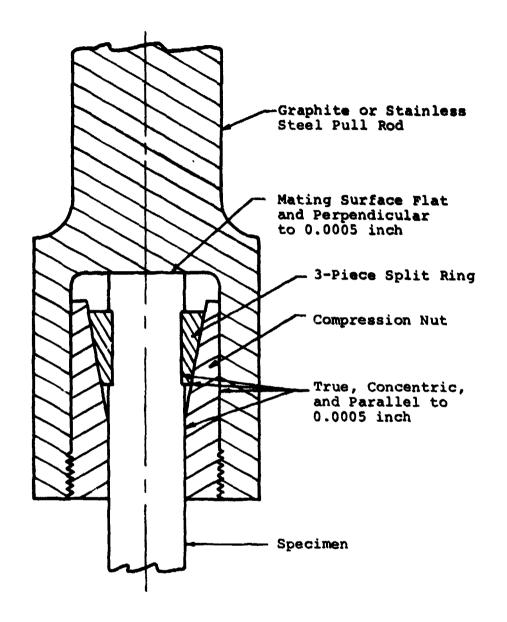


Figure 5. Precision Collet Grip for Tensile Specimen 2:1 Scale

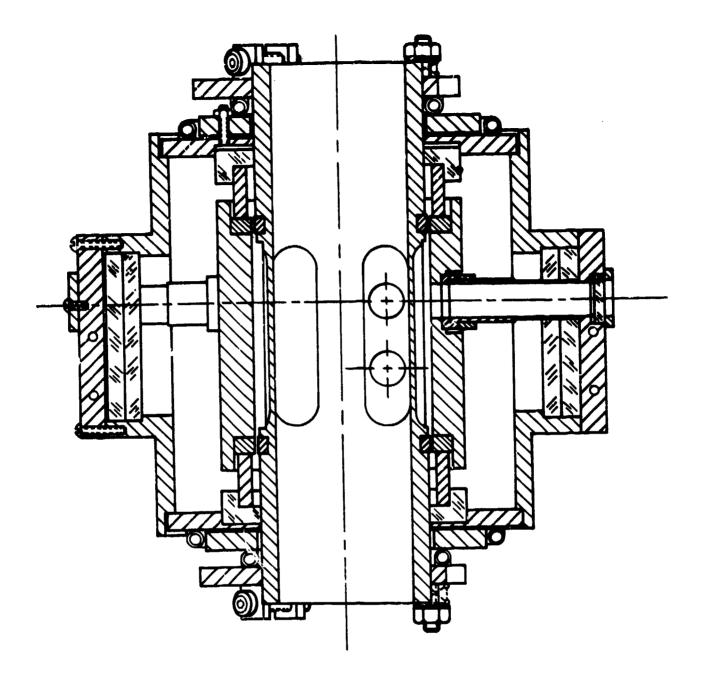
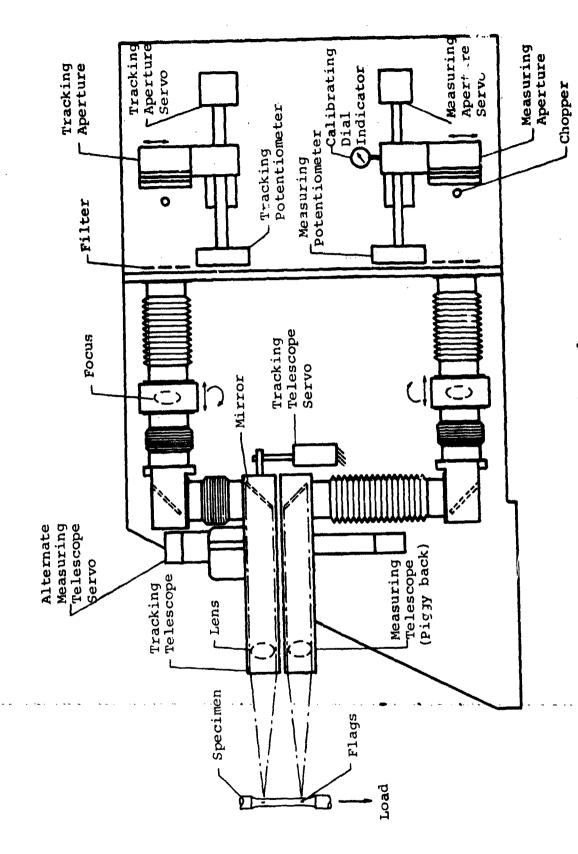


Figure 6. Small 5500°F Graphite Resistance Furnace



※ はないないないない

のでは、「ないのでは、「ない」というないでは、「ない」というでは、「ない」というできます。 「ない」というないできます。 「ない」というない。 これできます。 「ない」というない。 これできます。 「ない」というない。 これできます。 「ない」というない。 これできます。 「ない」というない。 これできます。 「ない」というない。 「ない」というない。」 「ない」というない。」 「ない」というない。」 「ない」というない。」 「ない」というない」というない。 「ない」というない。」 「ない」というない」というない。 「ない」というない。」 「ない」というない」というない。 「ない」というない。」 「ない」というない」というない。 「ない」というない。」 「ない」というない」というない。 「ない」というない。」 「ない」というない」というない。」 「ない」」 「ない」

Figure 7. Arrangement of Optical Strain Analyzer

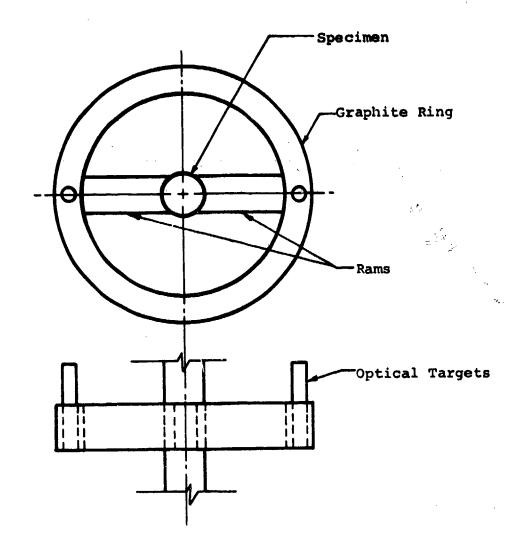


Figure 8. General Configuration of the Flag Attachment to Monitor Lateral Strain in Tension

Preceding Page BLANK - FILMES

APPENDIX A2

Ultimate Strength, Elastic Modulus, and Poisson's Ratio to 5500°F in Compression

ULTIMATE STRENGTH, ELASTIC MODULUS, AND POISSON'S RATIO TO 5500°F IN COMPRESSION

The compressive apparatus is shown in the photograph in Figure 1 and in the schematic in Figure 2 and consists primarily of a load frame, gas bearings, load train, 50-ton screw jack, variable speed mechanical drive system, strain analyzers, 5500°F furnace, and associated instrumentation for the measurement of load and strain.

The load frame is similar to most standard frames. It was designed to carry a maximum load of 100,000 pounds and to support the furnace optical strain analyzers, and other related equipment.

Gas bearings are installed at each end of the load train to permit precise alignment of the loading train to the specimen. The upper bearing is spherical on a radius of 6.5 inches. This radius is the distance from the top of the specimen to the spherical bearing surface. The load train, not the specimen, shifts to maintain radial alignment. The lower bearing is flat and is about 6 inches in diameter. The lower bearing permits transverse alignment of the load train. The gas bearings are floated for only a small initial amount of load so that precise alignment of the load train can be attained.

The load train near the furnace consists of the specimen loaded on each side by graphite and water-cooled steel push rods. The graphite push rods are counter-bored to permit insertion of a pyrolytic graphite disc which serves as a heat dam and to align the specimen to the center-line of the load train. Extreme care is exercised in the preparation of all parts of the load train to ensure concentricity of the mating parts to less than 0.0005 inch.

The 50-ton jack is a power screw type. The mechanical drive system consists of a gear reducer driven by a Louis Allis Synchro-Spede Unit (300-3000 rpm). The gear reducer is connected to the Synchro-Spede Unit through a chain coupling and to the 50-ton jack by a single roller chain and sprocket system. Different load rates are obtained by adjustment of the variable speed setting on the Synchro-Spede and by changeout of sprockets on the gear reducer and screw jack.

Figure 3 shows details of the "dumbbell" specimen which maintains a 0.500 inch diameter over the 1.2 inch long gage section. The specimen provides sufficient room for the flag attachments that follow the axial and lateral strains and also minimizes the influence of end restraint.

The flag attachments for the measurement of axial strain are positioned one inch apart so that unit strain is recorded directly. The flag attachment for the measurement of lateral strain is positioned between the flags for axial strain; see Figure 4. The lateral flag attachment used in compression is shown in Figure 5. The 4-piece assembly consists of a ring, two rams bearing on the specimen, and a screw to adjust the contact pressure. The ring was designed to track lateral motions as great as 0.030 inch without breaking.

Figure 6 is a sketch of the 5500°F furnace used for compression showing the basic components. The furnace consists of a resistivity heated graphite element insulated from a water-cooled shell by thermatomic carbon. The furnace and specimen are purged with helium to provide an inert atmosphere. Ports with visual openings are provided on opposite sides of the furnace as a means of allowing the strain analyzers to view the gage flags on the specimen. Specimen temperatures are determined by optical pyrometer readings taken through another small sight port containing a sapphire window. A calibration curve was established for the loss through the sapphire window, and since the furnace cavity acts essentially as a blackbody, true temperature readings are obtained. Power is supplied to the heating element by means of a 25 KVA variable transformer.

Strain measurement consists of measuring optically the elongation between two flags, or targets, which are mounted on the specimen and separated initially by a predetermined gage length. The travel of the targets is measured by sensing the displacement of the image of the edge of the targets and then electromechanically following the image displacement. The relative travel of the two targets provides the strain. Readout is continuous and automatic on a millivolt recorder. A schematic of the analyzer is shown in Figure 7.

A brief summary of the mechanical motions of the components involved in monitoring the strain is helpful in understanding the detailed performance. A tracking telescope follows the upper target and carries a second telescope mounted on its carriage. The second telescope is capable of independent motion to follow the lower target. The relative displacement between the upper and lower telescope, as strain occurs, defines the strain. The system usually is operated so that the tracking telescope follows the

upper target and the strain is monitored by the relative displacement of the aperture rather than the telescope following the lower target. With this procedure the maximum range is the maximum displacement available for the lower aperture, or about 1/8 inch, and the sensitivity is limited by the optics and the noise level of the detector. Using both telescopes, the range is about 3/4 inch.

To provide optical references on the specimens, targets are affixed to the test specimen as mentioned. When the specimen is heated to temperature, the targets are self-luminous and are observed optically. The optics view past the luminous targets into a cooled cavity in the opposite furnace wall. The self-luminous targets are then visible against a dark background. To obtain data at below 2000°F, a light beam is directed from behind the flags providing a shadow image for the detection system.

The image of the glowing target is focused through a rotating shutter (chopper) and onto a rectangular aperture. Small slits in the aperture pass a portion of the upper and lower edges of the light beam. A photocell receives the light thus transmitted, and an electronic circuit detects whether the energy passed by the two slits is equal. A servo drives the apertures to let a balanced quantity of light pass through the two slits and thus maintains an optical null.

To obtain lateral strain, a strain analyzer is supported horizontally on the load frame to view the diametrical or lateral strain of the specimen.

Calibrations of the analyzers are performed in various ways including absolute correlations to precision micrometers, strain gage extensometers, and direct plots of stress-strain for reference materials such as steel, plexiglas, magnesium, and aluminum. Precision is ± 0.000020 inch.

Instrumentation includes primarily a stress-strain measurement system composed of a 20,000-pound SR-4 Baldwin load cell, constant d.c. voltage power supply, two optical strain analyzers, and two X-Y recorders. Specimen temperature is monitored with an optical pyrometer. Stress(load) is measured by a commercial load cell. The cell receives a constant d.c. voltage input from the power supply and transmits a millivolt signal (directly proportional to load) to an X-Y recorder. Simultaneously, the optical strain analyzers measure both the axial and lateral strain and transmit a millivolt signal (proportional to strain) to the X-Y recorders. Thus, continuous plots of stress-axial strain and axial strain-lateral strain are recorded simultaneously.

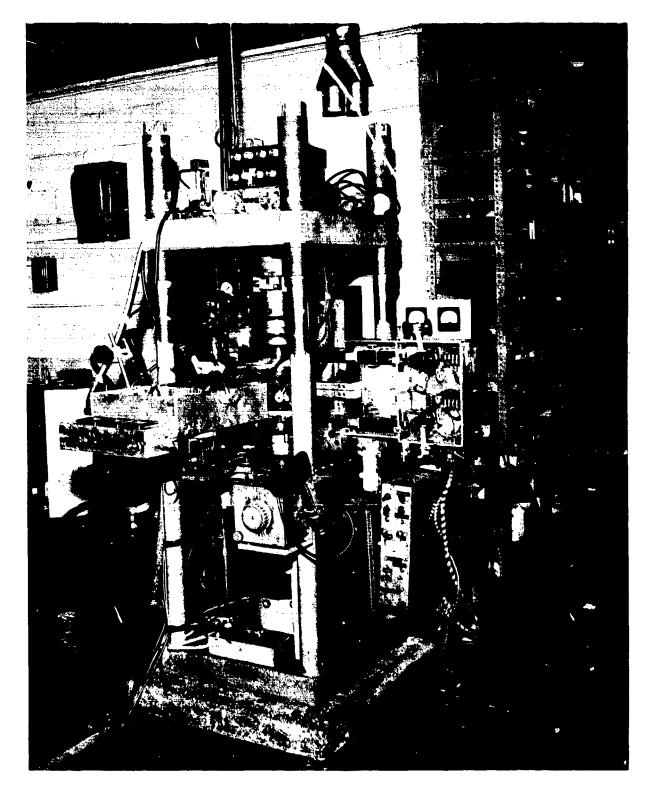


Figure 1. Picture of the Compressive Facility with Gas Bearings and Optical Strain Analyzer

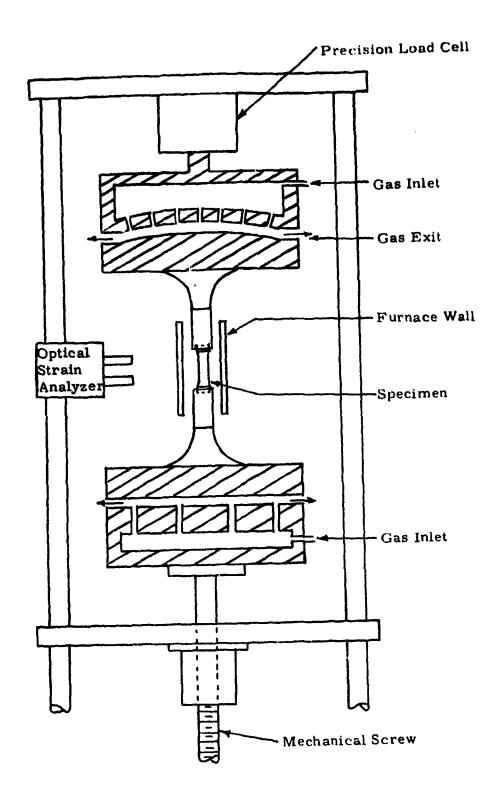


Figure 2. Schematic Arrangement of Gas-Bearing Universals, Specimen, and Load Train

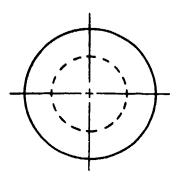


Figure 3. Compressive Specimen Configuration

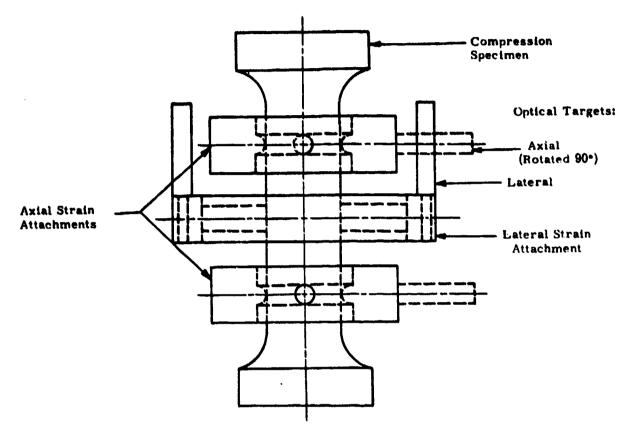
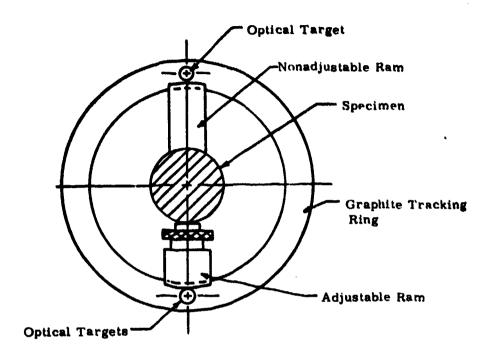


Figure 4. Location of the Flag Attachments on the Compressive Specimen



・ 1 である。 1 できない 1 できな

Figure 5. Lateral Strain Flag Attachment for Compressive Specimen

The state of the s

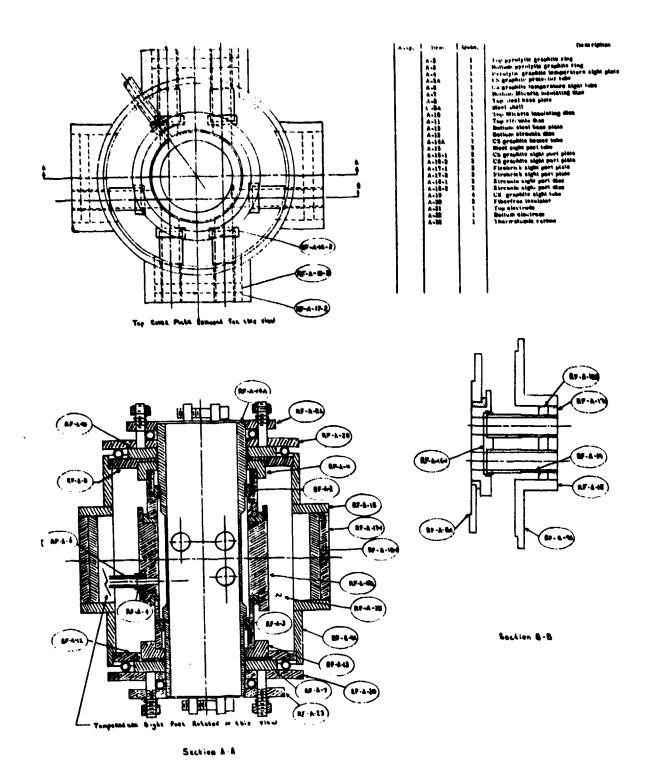
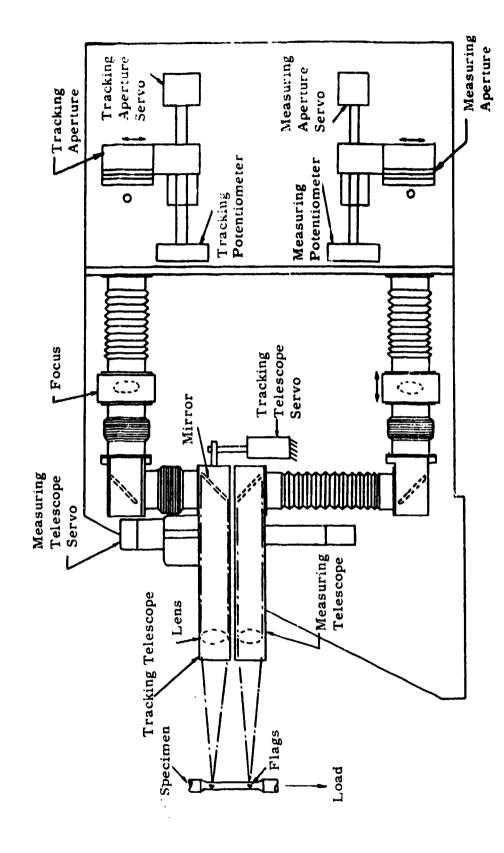


Figure 6. Small 5500°F Graphite Resistance Furnace



の一世紀の大学を表している。

Figure 7. Arrangement of Optical Strain Analyzer

Preceding Page Blank - Filmed

APPENDIX A3

Shear Modulus and Modulus of Rupture in Torsion to 5500°F

SHEAR MODULUS AND MODULUS OF RUPTURE IN TORSION TO 5500° F

A schematic of the gas beging torsion apparatus employed to determine the shear modulus and modulus of rupture in torsion is shown in Figure 1.

The torque is applied at the upper end of the load train by a shaft acting through a loose pin-slot connector at the geometric center of the special gasbearing, ensuring the application of pure torque only to the load train. The shaft is driven by a synchronous constant speed motor through a double reduction chain drive to provide the rotational speed equivalent to a shearing stress rate of 500 psi per second on the specimen. The lower end of the load train is restrained from rotating by an aluminum rod extending through the lower pull rod and contacting a fixed point. This rod is $\frac{1}{4}$ inch diameter with a section milled down to $\frac{1}{8}$ inch thickness where strain gages are installed to measure the applied torque. Low friction guides prevent lateral movement of the load train.

The system employed for measurement of anuglar rotation of the specimen is shown in Figure 2. Two graphite rings similar to those used for the measurement of lateral strain in tension and compression are mounted concentric to the specimen and separated by a f 1 inch gage length. Graphite yarn is attached to the rings and wound around the outer periphery in V-grooves. The free ends of the yarn are then attached to two strain measuring devices. which are calibrated to give equal millivolt response for linear movement. Thus, as the specimen and load train rotate, the rings act as spools and "rolled up" the yarn. Fifteen mils of linear movement of the yarn equal 0.02 radians of angular rotation of the specimen. The strain gages on each measuring device are connected into a full bridge circuit which gives a millivolt response on the X-Y recorder proportional to the difference of the two movements. In orther words, the recorder measures the actual angular rotation of the specimen across the 1 inch gage section versus applied torque. To ensure that each run is colibrated properly, the following procedure is followed: The pin is pulled out of the lower pull rod so that the load train is free to rotate at zero torque. Then the graphite yarn is attached to the upper measuring device only.

The X-Y recorder is set to record strain versus time, and adjustments are made until this relationship is achieved. The upper device is then disconnected and the lower one is connected and a strain versus time plot is made. Adjustments are made until a straight line is plotted, which indicates that both devices are reading the same strain, and the difference in the readings is zero.

After this is done on each run, the pin is replaced and the torque applied at the desired rate to failure. Thus, a plot of torque versus angular rotation is made for each specimen.

The equations used for determining the required mechanical properties are:

$$S_{s} = \frac{Tc}{J}$$

$$G = \frac{T1}{J\theta}$$

where

S_g Ultimate Shear Stress

T Applied torque

c Distance from the centerline to the outer surface

J Polar moment of inertia

G Shear modulus

1 Gage length

 θ Angular rotation of the gage section

The Derivation of these equations assumed a linear relation between shear stress and shear strain.

Pure shear is not attained in a rod subjected to torsion in the same sense that pure tension is attained in a tensile rod because the shear stress varies from zero at the center to a maximum at the outside edge. A somewhat analogous case is found in flexure where a kind of "average" tensile/compressive stress-strain curve is obtained from load-deflection measurements.

The torsion apparatus is equipped with a tubular electrical resistance furance which has a 5500°F Capability.

The configuration of the standard torsion specimen is shown in Figure 3.

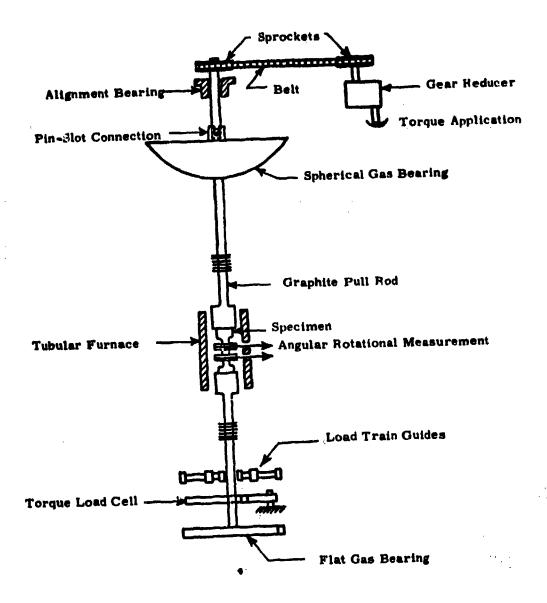
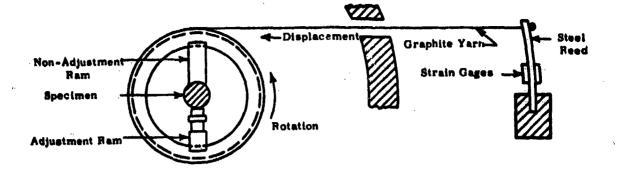


Figure 1. Diagram of Torsional Load Train



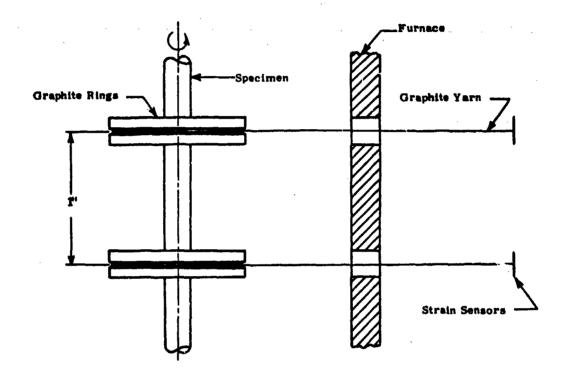
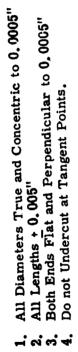


Figure 2. Schematic of System Employed for Measurement of Angular Rotation of Torsional Specimen



← 양 & 4:

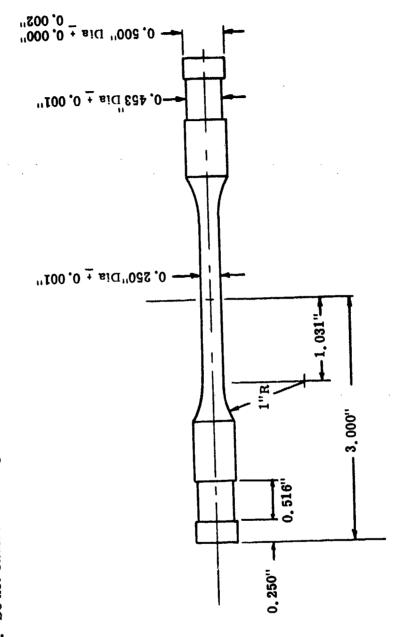


Figure 3. Torsion Specimen

APPENDIX A4 Thermal Expansion to 1800°F

THERMAL EXPANSION TO 1800°F

Thermal expansion measurements are made utilizing quartz tube dilatometers of the Bureau of Standards design. The dial gages (B. C. Ames Co., Model 212, Shockless) are graduated in 0.0001-inch divisions with a total range of 0.500 inch. The manufacturer's stated mechanical accuracy for any given reading is ± 0.0001 inch at any point in the range. This accuracy has been checked with a precision micrometer.

Figure 1 shows a schematic drawing of a quartz tube dilatometer. The dilatometer head was designed to minimize any extraneous motions that would induce error in the monitored data. Water cooling was used to prevent temperature fluctuations and gradients that would induce erroneous motion in the dial gage. The parts were precision machined to allow for proper alignment and minimize spurious motions from excessive clearance. The core of a linear variable differential transformer is attached to the quartz rod, which rests on top of the quartz tube. By feeding the output of the LVDT into an oscillator-demodulator and employing an X-Y recorder, a continuous plot of expansion versus temperature may be obtained. Dial gage readings may also be taken concurrently.

For temperatures above room temperature, each dilatometer is heated by an individual heater. The temperature of the heater is maintained by a manual setting of a variable voltage transformer.

Cold specimen temperatures are obtained by use of a Dewar flask filled with dry ice and trichloroethylene. The flask surrounds the dilatometer tubes and the cold liquid level rises to a height above the specimens.

日間のは、日本のでは、日本には、日本のでは、

Liquid nitrogen is used in the Dewar flask for temperatures down to -300°F. A cooling coil has also been designed to provide better control of temperatures in the cryogenic range.

Thermocouples are placed at each end and the center of the specimens to monitor the temperature throughout. The specimens are nominally 1/2 inch diameter by 3 inches in length with the ends rounded on a 3 inch radius. Other diameters and cross-sectional configurations are employed where necessary due to configuration of supplied material.

To calibrate the dilatometers we employ a primary standard of fused silica purchased from NBS and designated as SRM 739. A secondary standard of fused silica developed in house is also used. From our calibrations and experience we have found no systematic error in this system. Based on the initial calibrations of this equipment a precision level has been determined. At 1300°F the standard deviation is no greater than ±0.025 x 10⁻³ in./in.

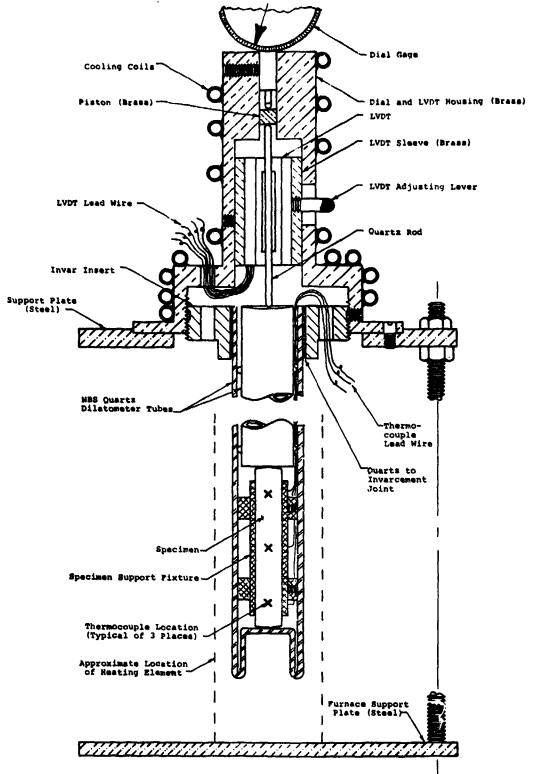


Figure 1. Assembly of Quartz Tube Dilatometer for Thermal Expansion Messurements

The state of the s

Preceding Page Blank - FILMED

APPENDIX A5

Thermal Expansion to 5500°F

THERMAL EXPANSION TO 5500°F

Thermal expansion is measured in a graphite tube dilatometer developed by Southern Research Institute for performance to 5500°F, see Figure 1. The specimen required is about 1/2" diameter and 3" long, although the exact size can vary somewhat if it appears desirable from the standpoint of specimen availability. Specimens 3/4" in diameter and only 1/4" thick can be evaluated, but with a reduced precision. Discs can be stacked to provide more length in many cases. Of course, specimens can always be pinned together from smaller pieces to provide both length and columnar strength.

In the dilatometer, the specimen rests on the bottom of the cylinder with a graphite extension rod resting on the specimen to extend to the top of the cylinder. When required, tungsten pads are inserted at the ends of the specimens to eliminate graphite diffusion from the dilatometer parts into the specimen. This entire assembly is inserted into one of the 5000°F furnaces described in another brochure.

The motion of the specimen is measured by a dial gage attached to the upper end of the cylinder with the stylus bearing on the extension rod. The system accurately indicates total motions of 0.0001" - or less than 0.00004" per inch of specimen.

Either a helium or an argon environment can be employed. Nitrogen has been used on occasion. The equipment will permit operation at hard vacuums, but this procedure is rarely used.

A CS graphite, which has a fairly low expansion relative to other grades of graphite, is used as the material for the dilatometer. Prior to calibrations, the dilatometers are heat soaked to a temperature several hundred degrees above the maximum temperature to which they would be exposed during normal service. Dimensional stability is confirmed by measuring the lengths of the dilatometer tube and rod after each run. Past experience has shown that following the initial heat soak the expansion is reproducible in subsequent repeated cycles to lower temperatures. Reproducibility is also confirmed by repeated runs on standards.

To calibrate the dilatometers we have developed in-house primary and secondary standards of ATJ graphite. ATJ graphite was selected as a standard because of our vast experience with it, its stability after repeated exposure to high temperatures, and its relatively low expansion.

The true expansion of the primary standard was determined by a direct optical technique using a traveling Gaertner telescope. total error in the telescope readings, based on calibration data, was estimated to be 0.2 x 10⁻³ in./in. For the direct optical measurements, the 3.5 inch long specimen was heated in a graphite furnace, and the expansion was determined by sighting on "knife" edges machined on the ends of the specimen. Typically a total of 11 runs have been made in two different furnaces both in vacuum The two environments are used to check and helium environments. effects of refraction as reported in the literature. standard was then machined to the configuration of a regular dilatometer specimen and several runs were made in our precision quartz dilatometers. The optical expansion data were fitted to a quadratic equation over the temperature range from 2500°F to 5000°F using the method of least squares and statistically analyzed to determine the uncertainty (primarily the scatter). Below 2500°F, the quartz dilatometer data were fitted by hand since the uncertainty of this apparatus has been well established, and the imprecision is small (<0.1 \times 10⁻³ in./in.). A typical plot of all data points with the curve fit is shown in Figure 2.

A check of the expansion of the standard was obtained by making runs on round robin specimens of various graphites and synthetic sapphire which had been previously evaluated by others, including the National Bureau of Standards. Our data on these specimens agreed within a 2.5 percent random difference with the data reported by the other laboratories.

After establishing the expansion of the ATJ standard, several graphite dilatometers were then calibrated by making runs on this standard. These dilatometers were used to establish the expansion of secondary standards (also ATJ graphite) which are used to calibrate new dilatometers and to make periodic checks on dilatometers currently in service. This use of secondary standards thus minimizes the wear and tear on the primary standard and prolongs its life.

Table 1 lists the uncertainties in the dilatometer measurements in 10^{-3} in./in. Observe that most of the uncertainty is in the expansion of the standard and includes both random and systematic uncertainties. Other sources of uncertainty, resulting from such factors as dial gage and temperature measurement, are small amounting to less than 0.2×10^{-3} in./in. at any temperature. The precision in the dilatometer measurements is quite good and amounts to about 0.1×10^{-3} in./in. From Table 1, it can be seen that the maximum total uncertainty, which occurs at a temperature of $4500\,^{\circ}\text{F}$, is $\pm 0.45 \times 10^{-3}$ in./in. For a low expansion graphite, such as ATJ, this amounts to an uncertainty of ± 4.5 percent at $4500\,^{\circ}\text{F}$ (see Figure 2). For graphites having higher expansions, the percentage uncertainty would be lower.

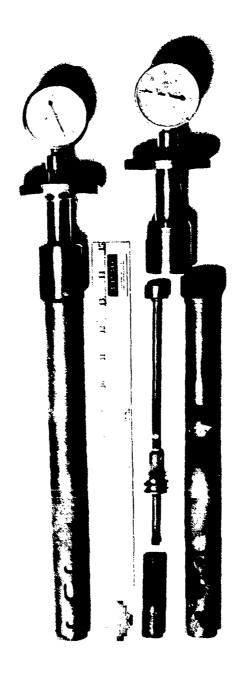


Figure 1. Picture of the Graphite Dilatometer Tubes for Measuring Thermal Expansion to 5500°F

一日の佐藤部園のことが、こ

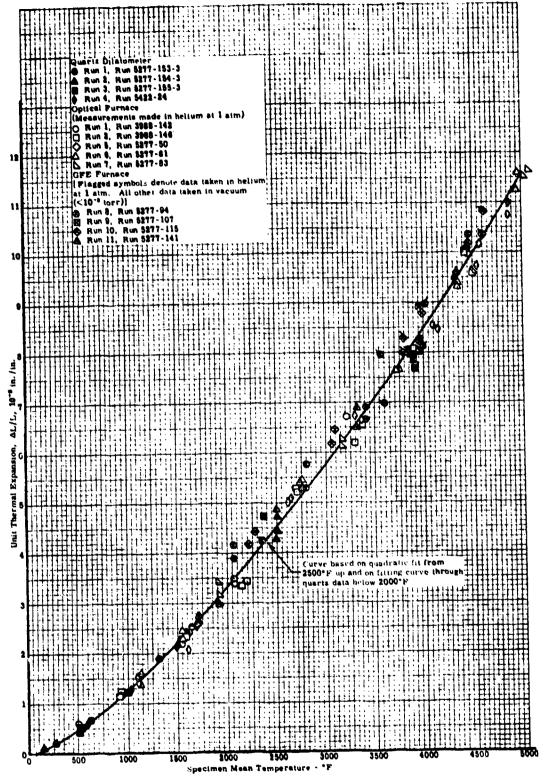


Figure 2. The Thermal Expansion of ATJ Graphite (wg) Standard No. 5 by In-House Optical Calibration

Table 1
Uncertainty in Thermal Expansion Measurements
Made in Graphite Dilatometers

Uncertainty in Expansion of Standard in 10 ⁻³ in./in.		Random Uncertainty	Total Uncertainty in Dilatometer Measurements	
Random Uncertainty (See Note 1)	Systematic Uncertainty (See Note 2)	in Dilatometer Measurements in 10-1 in./in.	from all in 10 ⁻³	
±0.04	0	±0.03	0.05	0.05
±0.04	o	±0.03	0.05	0.05
±0.05	0	±0.04	0.07	0.07
±0.17	+0.03	±0.05	0.21	0.18
±0.11	+0.20	±0.07	0.33	0.13
±0.12	+0.21	±0.08	0.35	0.14
±0.19	-0.02	±0.10	0.21	0.23
±0.14	-0.09	±0.12	0.18	0.27
±0.14	±0.25	±0.14	0.45	0.45
±0.19	-0.12	±0.16	0.25	0.37
	Standa in 10 ⁻¹ Random Uncertainty (See Note 1) ±0.04 ±0.04 ±0.05 ±0.17 ±0.11 ±0.12 ±0.19 ±0.14	Standard in 10 ⁻³ in./in. Random Systematic Uncertainty (See Note 1) (See Note 2) ±0.04 0 ±0.04 0 ±0.05 0 ±0.17 +0.03 ±0.11 +0.20 ±0.12 +0.21 ±0.19 -0.02 ±0.14 -0.09 ±0.14 ±0.25	Standard in 10 ⁻³ in./in. Random Uncertainty in Dilatometer Uncertainty (See Note 1) Systematic Uncertainty (See Note 2) In Dilatometer Measurements in 10 ⁻³ in./in. ±0.04 0 ±0.03 ±0.05 0 ±0.03 ±0.17 +0.03 ±0.05 ±0.11 +0.20 ±0.07 ±0.12 +0.21 ±0.08 ±0.19 -0.02 ±0.10 ±0.14 -0.09 ±0.12 ±0.14 ±0.25 ±0.14	Standard in 10 ⁻³ in./in. Random Uncertainty in Dilatometer from all in 10 ⁻³ in./in. In Dilatometer from all in 10 ⁻³ in./in. Uncertainty (See Note 1) Uncertainty (See Note 2) 10 ⁻³ in./in. + ±0.04 0 ±0.03 0.05 ±0.05 0 ±0.04 0.07 ±0.17 +0.03 ±0.05 0.21 ±0.11 +0.20 ±0.07 0.33 ±0.12 +0.21 ±0.08 0.35 ±0.19 -0.02 ±0.10 0.21 ±0.14 -0.09 ±0.12 0.18 ±0.14 ±0.25 ±0.14 0.45

Notes: 1. 95% confidence limits.

2. Represents deviation between average measured value and least squares curve through all data.

APPENDIX A6

A Comparative Rod Apparatus for Measuring Thermal Conductivity to 2000°F

では、一般を確認されば、

A COMPARATIVE ROD APPARATUS FOR MEASURING THERMAL CONDUCTIVITY TO 2000°F

Southern Research Institute's comparative rod apparatus is used to measure thermal conductivities of a wide variety of materials from -300°F to 2000°F. This apparatus shown schematically in Figure 1, consists basically of two cylindrical reference pieces of known thermal conductivity stacked in series with the cylindrical specimen. Heat is introduced to one end of the rod, composed of the references and specimen, by a small electrical heater. A cold sink or heater is employed at the opposite end of the rod as required to maintain the temperature drop through the specimen at the preferred level. Cylinders of zirconia may be inserted in the rod assembly to assist in controlling the temperature drop. Radial losses are minimized by means of radial guard heaters surrounding the rod and consisting of three separate coils of 16, 18 or 20-gage Kanthal wire wound on a 2 or 4- inch diameter alumina core. The annulus between the rod and the guard heaters is filled with diatomaceous earth, thermatomic carbon, bubbled alumina or zirconia powder. Surrounding the guard is an annulus of diatomaceous earth enclosed in an aluminum or transite shell.

The specimens and references (see Figure 2) are normally 1-inch diameter by 1-inch long. Thermocouples located 3/4 inch apart in radially drilled holes measure the axial temperature gradients. Thermocouples located at matching points in each guard heater are used to monitor guard temperatures, which are adjusted to match those at corresponding locations in the test section.

In operation, the apparatus is turned on and allowed to reach steady state. The guard and rod heaters are adjusted to minimize radial temperature gradients between the rod and guard sections consistent with maintaining equal heat flows in the references. Temperatures are measured on a Leeds and Northrup Type K-3 potentiometer, and the temperature gradients calculated. A typical temperature profile in the test section is shown in Figure 3.

The thermal conductivity of the specimen is calculated from the relation

$$K_{S} = \frac{K_{1}\Delta T + K_{2}\Delta T}{2\Delta T_{S}} \frac{\Delta X_{S}}{\Delta X_{T}}$$

where K_1 and K_2 are the thermal conductivities of the upper and lower references; ΔT_1 , ΔT_2 and ΔT_8 are the temperature differences in the upper and lower references and specimen, respectively; ΔX_8 and ΔX_T are the distances between thermocouples in the specimen and references.

Note that for purely axial heat flow, the products $K_1\Delta T_1$ and $K_2\Delta T_2$ should be equal. Due to imperfectly matched guarding and other factors, this condition is seldom attained in practice; therefore, the average of the two values is used in the calculations. Their difference is maintained as small as possible, usually within 5% of the smaller.

For identical specimens, the ratio $\Delta X_S/\Delta X_T$ should be unity but may vary due to the uncertainty in hole locations. To prevent introducing an additional error in calculations, ΔX is determined as follows: the depth of the hole is measured by inserting a snugly fitting drill rod in the hole, measuring the projecting length and subtracting it from the total length of the rod. The slope, or angle the hole makes with the perpendicular to the specimen axis, is determined by making measurements to the face of the hole and the outer end of the drill rod with respect to a datum plane, using a dial gage. From these measurements, the location of the bottom of the hole can be calculated.

うる

Generally, measurements with the comparative rod apparatus are performed in an inert helium environment. The apparatus can also be operated in vacuum and at gas pressures of up to 100 psig. We have had experience operating under all conditions.

The primary reference materials which we use are Code 9606 Pyroceram and Armco iron for measurements on materials with low and high thermal conductivities, respectively. Primary standard reference sets are kept and are used to calibrate other references made from the same materials. The standards of Code 9606 Pyroceram were made from a batch of material which NBS purchased shortly after their measurements on a sample of Code 9606 Pyroceram. The curve which Flynn presented for the thermal conductivity of the Pyroceram is given in Figure 4. Note that the curve is in good agreement

Robinson, H.E. and Flynn, D. R., Proceedings of Third Conference on Thermal Conductivity, pages 308-321, 1963 (with author's permission)

with the recommended values from NSRDS-NBS 82. The standards of Armco iron were made from the stock which was used in the Lound-robin investigations from which Powell' developed the most probable values for Armco iron. The curve used for the Armco iron standards is shown in Figure 5. Powell estimated the uncertainty to be within 22 percent over the temperature range from 0° to 1000°C. Note in Figure 5 that numerous evaluations of Armco iron from other batches of material have agreed within ±3 percent (coefficient of variation about curve) with Powell's original data.

In addition to Code 9606 Pyroceram and Armco iron several other materials have been used as references. These include copper for high conductivity specimens, 316 stainless steel for specimens of intermediate thermal conductivity and Teflon or Pyrex for low conductivity materials.

Copper references have been calibrated against Armco iron and excellent agreement with literature data has been obtained. Thermal conductivity values obtained from calibrations of 316 stainless steel against Pyroceram, Armco iron and a set of 316 stainless steel standards are presented in Figure 6. Note the consistency of the data obtained with the three different sets of references. The coefficient of variation of the data shown in Figure 6, about the curve value, was ±3.3%. These data indicate the internal consistency of the stainless steel and the reference materials. Note that the thermal conductivity values for 316 stainless steel presented in Figure 6 lie between values reported by several steel manufacturers and Lucks and Deem.

The calibrations indicate that for materials with moderate to high thermal conductivities the apparatus operates with a precision of about ±3 percent and a total uncertainty of about ±5 percent at temperatures above 0°F if temperatures between the guard and test section are closely matched. Below 0°F, the precision achieved to date has been about ±7 percent with a total uncertainty of about ±10 percent. We anticipate that the precision and uncertainty at cryogenic temperatures can be improved by additional calibrations.

Powell, R. W., C. Y. Ho and P. E. Liley, <u>Thermal Conductivity</u> of Selected Materials, NSRDS-NBS 8, Department of Commerce, November 25, 1966

Powell, R. W., Proceedings of Third Conference on Thermal Conductivity, pages 322-341, 1963

WADC TR58-476, "The Thermophysical Properties of Solid Materials," Armour Research Foundation, November, 1960.

Some additional data obtained on the comparative rod apparatus are shown in Figure 7 and 8. Figure 7 shows thermal conductivity data for ATJ graphite, with grain, using Armco iron as the reference material. These data show excellent agreement with earlier data obtained here and by other sources⁵ 7. The maximum scatter of the comparative rod points was about 5 percent.

Figure 8 shows data for thermocouple grade constantan obtained on the comparative rod apparatus using Armco iron references, and on Southern Research Institute's high temperature radial inflow apparatus. Note the excellent agreement. These data also show close agreement with data obtained by Silverman on an alloy of very similar composition.

ASD-TDR-62-765, "The Thermal Properties of Twenty-Six Solid Materials to 5000°F or Their Destruction Temperatures," Southern Research Institute, August, 1962

Pears, C. D., Proceedings of Third Conference on Thermal Conductivity, 453-479 (1963)

NSRDS-NBS 16, "Thermal Conductivity of Selected Materials", Part 2, by C. Y. Ho, R. W. Powell and P. E. Liley, National Bureau of Standards, 1968.

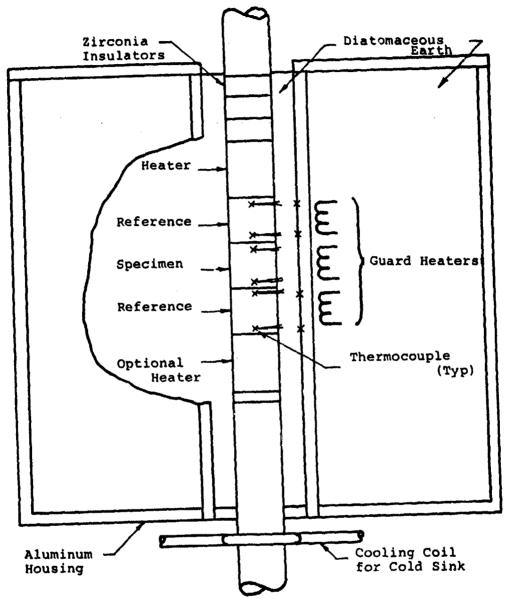
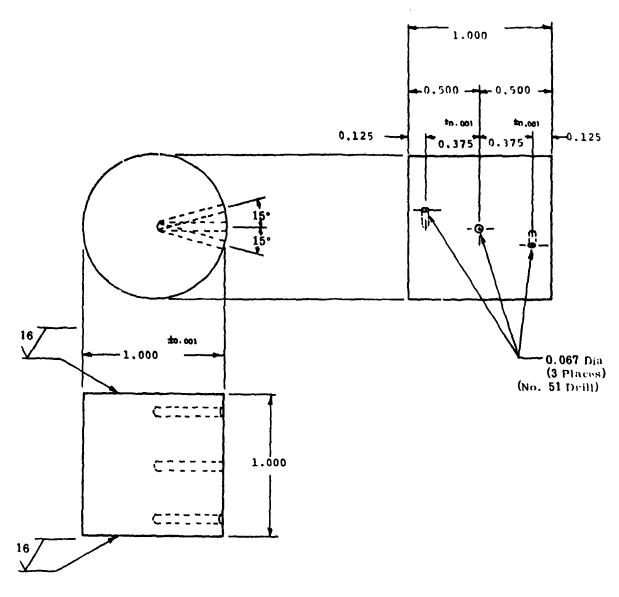
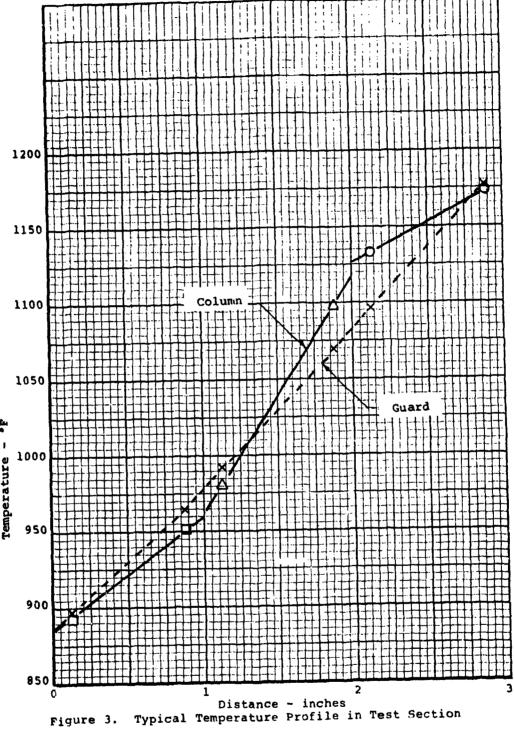


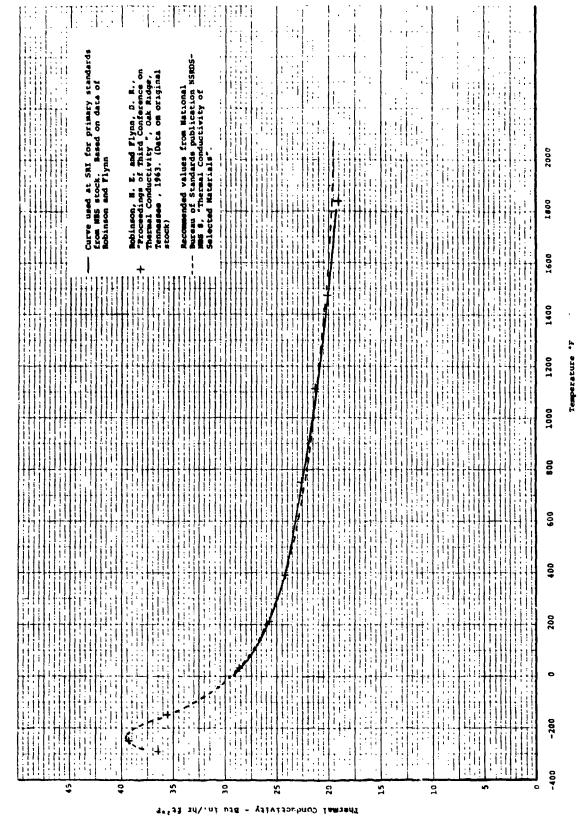
Figure 1. Schematic of Comparative Rod Thermal Conductivity Apparatus



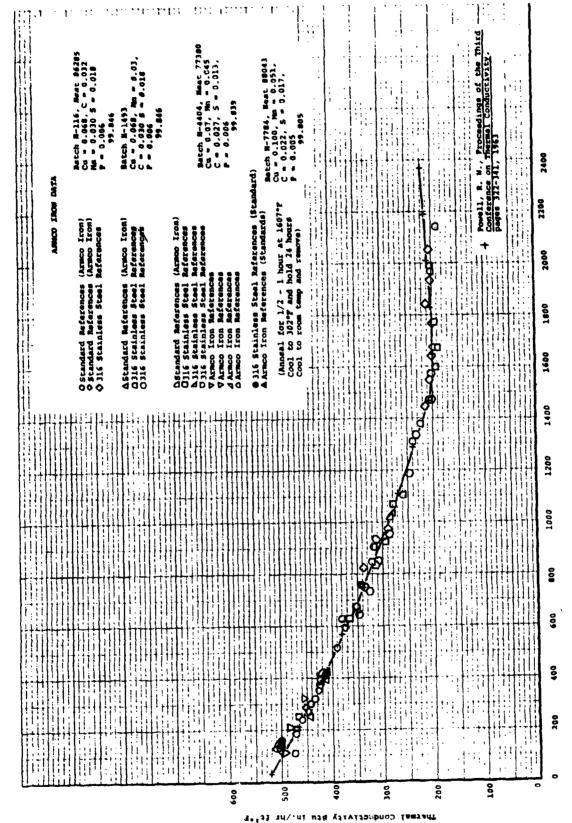
Note: All dimensions ± 0.005 except where noted

Figure 2. Drawing of Specimen for Thermal Conductivity Measurements in Comparative Rod Apparatus to 1800°F



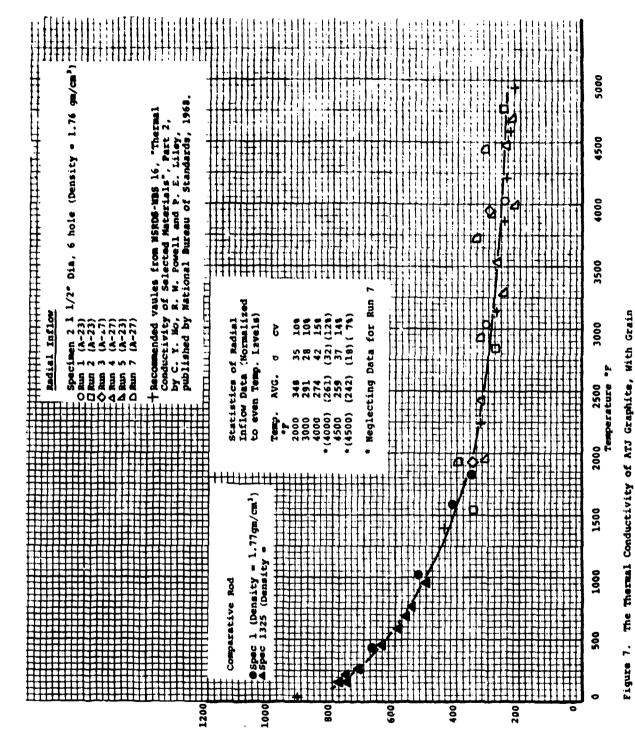


igure 4. The Thermal Conductivity of Primary SRI Standards from NBS Stock of Code 9606 Pyroceram



e 5. The Thermal Conductivity of

figura 6. The Thermal Conductivity of 316 Stainless Steel



する。最初はいい

Thermal Conductivity - Btu in,/hr ft²*P

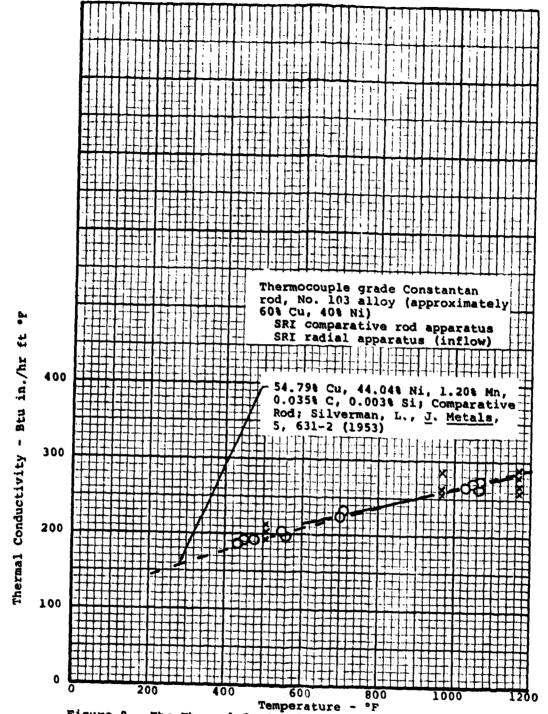


Figure 8. The Thermal Conductivity of Thermocouple Grade Constantan Rod

Preceding Page Blank - FILMED



APPENDIX A7

Thermal Conductivity to 5500°F by Radial Inflow Method

THERMAL CONDUCTIVITY TO 5500°F BY RADIAL INFLOW METHOD

The thermal conductivity is determined with a radial heat inflow apparatus that utilizes a central specimen 1" long. apparatus is normally employed for measurements over the temperature range from 1500°F to 5500°F. Comparative rod apparatus is used at temperatures below 1500°F where radiant heating is less effective. The radial inflow apparatus gives a direct measurement of the thermal conductivity rather than a measurement relative to some standard reference material. A picture of the apparatus ready to be installed in the furnace is shown in Figure 1. The furnace and associated equipment for the thermal conductivity work is shown in Figure 2. In addition to the specimen, the apparatus consists primarily of (1) a water calorimeter that passes axially through the center of the specimen, (2) guards made from the same specimen material at both ends of the specimens to reduce axial heat losses, (3) sight tubes that allow the temperature at selected points in the specimen to be determined either by thermocouples or optical pyrometer and (4) an external radiant heat source (see Figure 3). The water calorimeter provides a heat sink at the center of the specimen to create a substantial heat flow through the specimen and allows the absolute value of the heat flow to be determined. Thermocouples mounted 1/2" apart in the calorimeter water stream measure the temperature rise of the water as it passes through the gage portion of the specimen. By metering the water flow through the calorimeter, it is possible to calculate the total radial heat flow through the 1/2" gage section of the specimen from the standard relationship $Q = MC\Delta T$. M is the weight of water flowing per hour, C is the specific heat of water and AT is the temperature rise of the water as it passes through the gage section.

The standard specimen configuration is shown in Figure 4. The specimen is 1.062" O.D. x 0.250" I.D. x 1" long. Holes 0.073" in diameter are drilled on radii of 0.233 and 0.437" to permit measurement of the radial temperature gradient. In specimens which are anisotropic in the diametral plane (for example, certain graphites) a second pair of holes is drilled 90° to the first pair. The diameters joining each pair of holes is located to coincide with the principal planes of anisotropy in the material.

A 1/2" long upper guard and a 1/2" long lower guard of specimen material are placed above and below the 1" long specimen to maintain a constant radial temperature gradient throughout the entire specimen length and thereby prevent axial heat flow in the

specimen. The outer ends of the specimen guards are insulated with graphite tubes filled with thermatomic carbon. These tubes also hold the specimen in alignment. The combined effect of specimen guards and thermatomic carbon insulation permits a minimum axial temperature gradient within the specimen. This gradient is not detectable by optical pyrometer readings. Visual inspection of the specimens after runs have verified that no large axial temperature gradient exists in the specimen. The guards, made of specimen material display axial distortion of the isothermal lines for approximately 1/4" from the outer ends before reaching an apparent constant axial temperature.

When sufficient material is available the alternate specimen configuration shown in Figure 5 is employed. This specimen, being 1.5" in diameter, provides a larger gage length (0.357") between temperature wells and allows the installation of three holes on each radius without excessively distorting the radial temperature profiles. Thus this specimen configuration permits a more precise measurement of the average temperature at each radial location. As with the smaller specimen, the location of the temperature wells must be altered for transversely anisotropic specimens.

The annulus between the specimen inside diameter and the 7/32" outside diameter of the calorimeter tube is packed with either copper granules, graphite or zirconia powder. This packing provides a positive method for centering the calorimeter within the specimen and promotes good heat transfer between specimen and calorimeter.

Temperatures up to 2000°F are measured with Chromel/Alumel thermocouples inserted into the specimen through the sight tubes. At high temperatures, the temperatures are measured through the certical sight tubes using a right-angle mirror device and optical pyrometer.

In Figures 1 and 3 showing a typical conductivity calorimeter apparatus ready for insertion into a furnace for a run, a water-cooled copper section can be seen at the top of the unit. This section provides permanent sight tubes to within about 2-1/2" of the guard specimen, in addition to a permanent mount for the ritangle mirror device used with the optical pyrometer. Within the short zone between the water-cooled section and the top guard, thin-walled graphite sight tubes are fitted. The remainder of the annulus is filled with thermatomic carbon insulation.

During thermal conductivity runs, the following data are recorded: (1) power input, (2) specimen face temperature, (3) specimen temperatures in the gage section at the two radii, (4) temperature of the calorimeter water at two points 1/2" apart axially within the specimen center and (5) water flow rate through the calorimeter. At least 5 readings are made at each general temperature range to determine the normal data scatter and to minimize the error that might be encountered in a single reading.

All thermocouple readings are measured on a Leeds and Northrup K-3 null balance potentiometer used in conjunction with a galvanometer of 0.43 microvolts per mm deflection sensitivity. All optically measured temperatures are read with a Leeds and Northrup Type 8622 optical pyrometer. The flow rate of the calorimeter water is measured with a Fischer and Porter Stabl-Vis Flowrater.

The thermal conductivity values are computed from the relation

$$K = \frac{Q \ln \frac{r_2}{r_1}}{2\pi L (T_{r_2}^{-}T_{r_1})}$$

where

Q = the heat flow to and measured by the calorimeter

 r_2 = the radius to the outer temperature well r_1 = the radius to the inner temperature well

 $T_{r_2} = temperature at r_2$

 $T_{r_1} = temperature at r_1$

L = the gage length over which the calorimeter AT is measured, for our present calorimeter is 1/2 inch

Based on an extensive error analysis and calibrations on homogeneous isotropic materials of known thermal conductivities, such as Armco iron and tungsten, the precision (coefficient of variation) in the measurements has been established at ±7 percent over the temperature range. For multiple runs on samples having similar properties, the uncertainty in a smooth curve through the data can be established to within ±7 percent. A devailed error analysis has been presented in a paper by Mann and Pears.

Data obtained here on several high temperature materials are presented in Figures 6, 7 & 8. Figure 6 is a plot of data obtained here on tungsten. The specimen for these determinations were fabricated from stacks of 0.060 inch washers cut from hot rolled sheet stock. Also plotted are values reported by other investigators including "recommended values" given by Powell, Ho and Liley based on a compilation of 103 sets of data. Agree-

¹Mann, W. H. Jr., and C. D. Pears, "A Radial Heat Flow Method for the Measurement of Thermal Conductivity to 5200°F", presented at the Conference on Thermal Conductivity Methods, Battelle Memorial Institute, October 26-28, 1961.

²Powell, R. W., C. Y. Ho and P. E. Liley, "Thermal Conductivity of Selected Materials", NSRDS-NBS 8, National Standard Reference Data Series - National Bureau of Standards - 8, 1966, pp. 11, 54-59.

ment of the recommended values is excellent throughout the temperature range.

Figure 7 shows data obtained here on ATJ graphite, with grain. This material is premium grade, medium grain graphite having a density range of 1.73 to 1.78 gm/cm³. The crosses (+) shown in the figure are "recommended values" given by Ho, Powell and Liley. Again agreement is excellent.

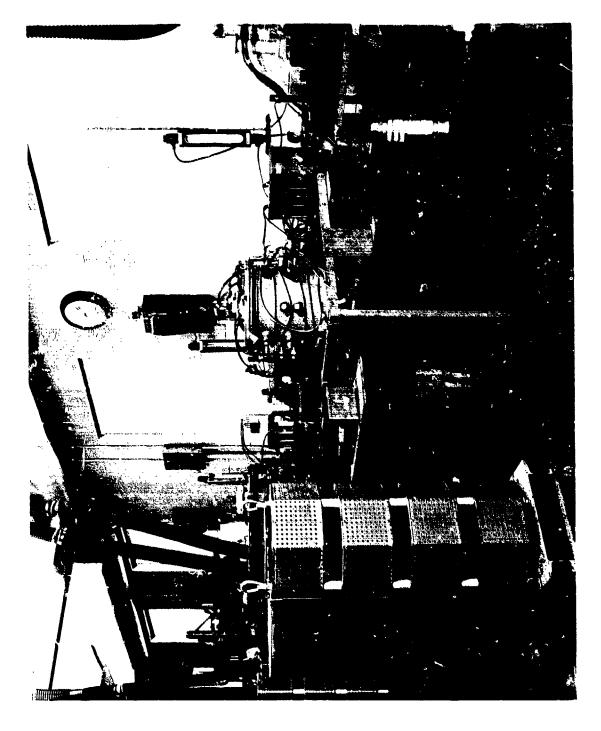
Figure 8 shows data obtained on AXM-5Ql. These data were obtained under a program sponsored by the Air Force Materials Laboratory to develop high temperature thermal conductivity standards. Measurements were made on this material by four laboratories in addition to Southern Research Institute. The bands shown in Figure 8 represent the range of data reported by the other participating organizations. A complete presentation and discussion of the data are given in AFML-TR-69-2.

³Ho, C. Y., R. W. Powell and P. E. Liley, "Thermal Conductivity of Selected Materials, Part 2, "NSRDS-NBS 16 National Standard Reference Data Series - National Bureau of Standards-16, pp. 89-128.

[&]quot;AFML-TR-69-2, "Development of High Temperature Thermal Conductivity Standards" submitted by Arthur D. Little, Inc., under Contract AF33 (615)-2874, 1969, pp. 115-127.



Figure 1. Picture of the Radial Thermal Conductivity Apparatus



295

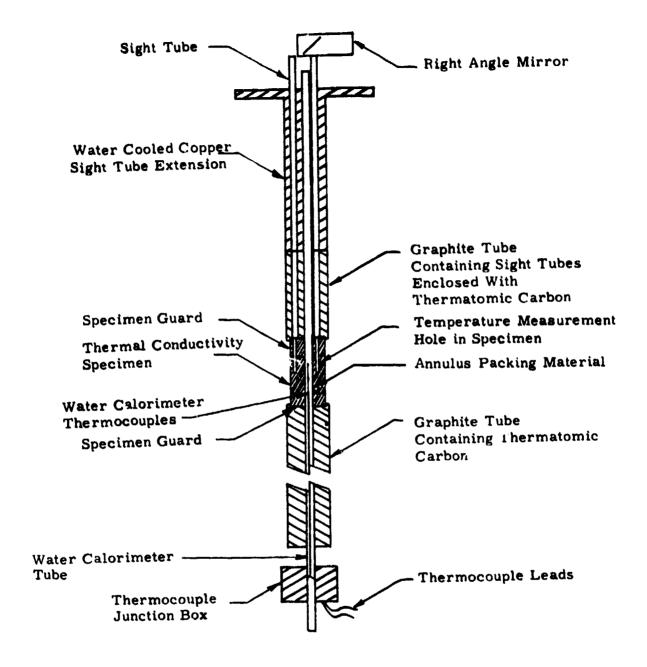


Figure 3. Cross-section Schematic of the Thermal Conductivity Apparatus

福川瀬 ら

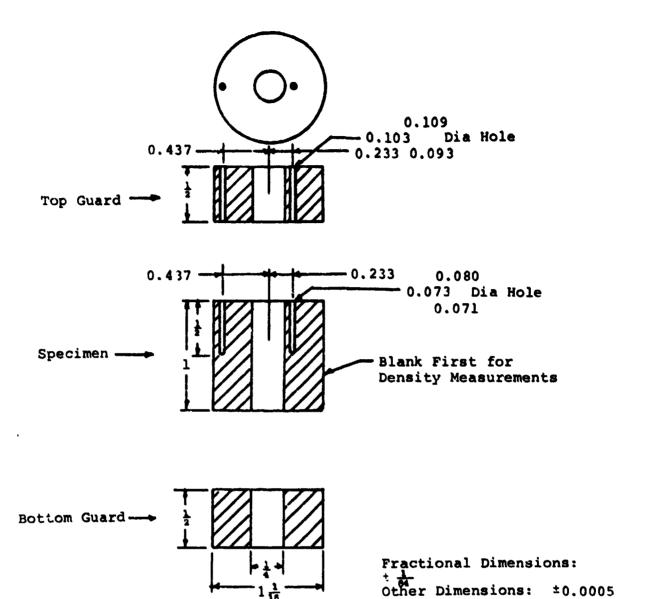
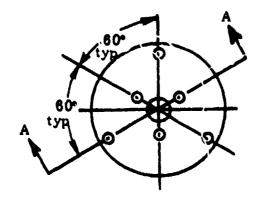


Figure 4. 1.06 Diameter Thermal Conductivity Specimen for Radial Inflow Apparatus



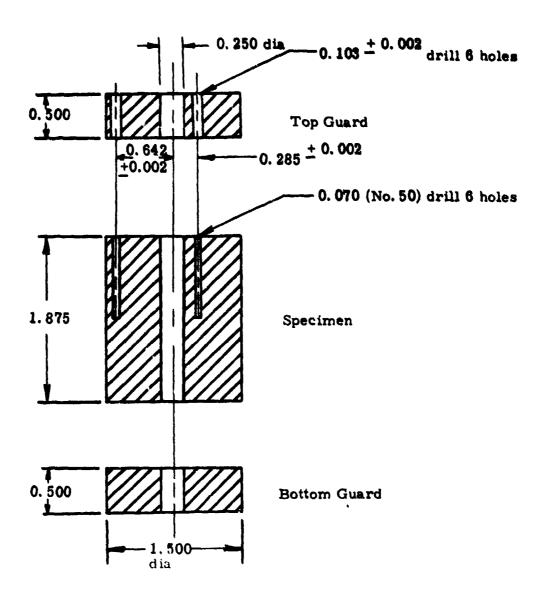
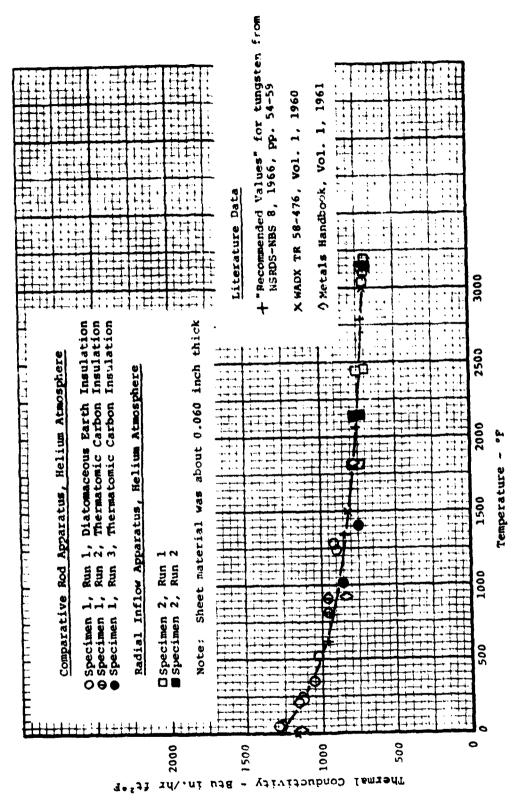
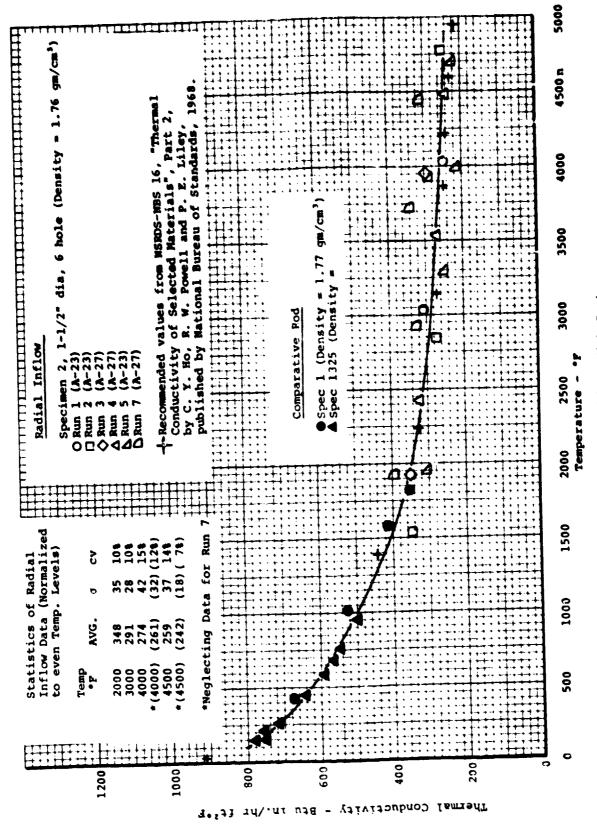


Figure 5. Dimensions of 1.50 Inch Diameter Specimen and Guards Used for Radial Inflow Thermal Conductivity Measurements

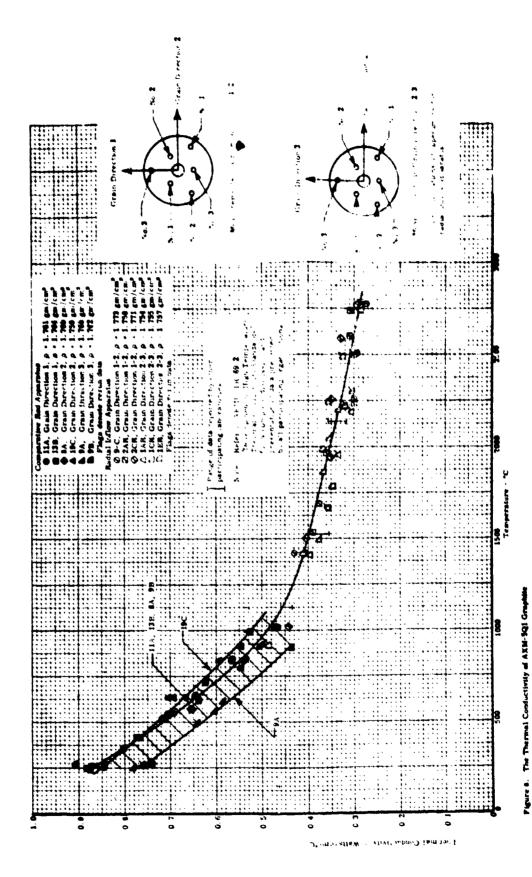


6. The Thermal Conductivity of Tungsten Sheet Parallel to the Plane

the Sheet



re 7. The Thermal Conductivity of ATJ Graphite, With Grain



Preceding Page Blank - Filmed

APPENDIX A8
Heat Capacity to 1000°F

HEAT CAPACITY TO 1000°F

The heat capacity to 1000°F is determined from data obtained in an adiabatic calorimeter. In this apparatus the heated specimen is dropped into a thermally guarded, calibrated cup, and the enthalpy is measured as a function of the increase in temperature of the cup. The heat capacity is the slope of the enthalpy versus temperature curve. A picture of the apparatus is shown in Figure 1.

A tubular furnace and a cold box are used to bring the specimens to temperature. By pivoting this equipment on a common post near the calorimeter, the samples are transferred to a position directly over the calorimeter cup. At this position the specimen is released from a suspension assembly that is triggered externally. Thermocouples located near the specimen are used to measure specimen temperature. The normal specimen size is about 1" x 1" x 1".

Elevated specimen temperatures are maintained by a manual setting of a variable voltage transformer, which controls the power input to the furnace. Cold sample temperatures are obtained by filling the cold box with dry ice and, when required, injecting liquid nitrogen vapors. The cold box consists of two concentric cylinders enclosed in a housing. The smaller cylinder (3" diameter by 16" high) is constructed of 1/4" mesh hardware cloth. The larger cylinder is made of galvanized sheet metal (15" diameter and 16" high). The annulus is partially filled with dry ice.

Specimens of the materials are heated or cooled to the desired temperature, and following a stabilization period, are dropped into the calorimeter cup. Adiabatic conditions are maintained during each run by manually adjusting cup guard bath temperature.

The covered cup of the drop-type adiabatic calorimeter is approximately 2-1/2" diameter by 2" deep. Three thermocouple wells are located in the bottom wall of the cup. The cup is mounted on cork supports, which rest in a silver-plated copper jacket. The jacket is immersed in a bath of ethylene glycol which is maintained at the temperature of the cup by means of a heater and copper cooling coils immersed in the liquid. Chilled trichloroethylene is circulated through the coils to cool the bath below ambient temperature when cold enthalpy measurements are made. A double-bladed stirrer maintains uniform bath temperature.

In the calorimeter six copper-constantan thermocouples, differentially connected between calorimeter cup and jacket, indicate temperature difference between cup and bath. The six thermocouples enable a difference of 0.03°F to be detected. This difference is maintained to within 0.15°F. During the runs, absolute temperature measurements of the cup are determined by means of the three thermocouple junctions, series connected, in the bottom of the calorimeter cup. All of the thermocouple readings are taken with instruments which permit readout to within 0.1°F; however, the system uncertainty is about 0.5°F.

The enthalpy of the specimen at any initial temperature is calculated from the following equation:

$$h = \frac{K}{W_S} (t_2 - t_1) \tag{1}$$

where

h = enthalpy above t₂
K = calorimeter constant, 0.2654 Btu/°F

 W_{S} = sample weight in lbs

t₁ = initial cup temperature in °F

t = final cup temperature in °F

The calorimeter constant of 0.2654 Btu/°F was determined by measuring the enthalpy of an electrolytic copper specimen of known specific heat.

The enthalpy is referred to a common base temperature of 85°F using the following linear interpolation:

$$h_{95} = h \frac{(t_3 - 85)}{(t_2 - t_2)} \tag{2}$$

where

 h_{85} = enthalpy above the reference temperature of 85°F in Btu/lb t_3 = initial sample temperature in °F

The base of 85°F is used because this is usually near the actual final cup temperature.

The enthalpy-temperature curve established is used to determine heat capacity (specific heat) by measuring its slope at different temperatures. This is done both graphically and by analytical methods which first fit the enthalpy data to an equation of the following type:

$$h_{a5} = aT + bT^2 + cT^{-1} + d$$
 (3)

The temperature (T) employed usually is in degrees Rankine. While this equation may not provide the best definition of the enthalpy data over the entire temperature range, it does anticipate the theoretical behavior and is consistent with methods recommended in WADC TR 57-308 and by K. K. Kelley. The derivative of this equation, the heat capacity, is used with the constant "c" adjusted so that the analytical solution agrees with the value determined graphically at 150°F. This technique is similar to that of Kelley in forcing the heat capacity equation through a known value. The equations are developed using a digital computer.

The accuracy of the apparatus has been confirmed by measuring the enthalpy of sapphire (SRM 734 from NBS) and other standard specimens. The results of the comparison on sapphire and other data indicate that the overall uncertainty of the apparatus is at ± 3 percent.

^{1.} Kelley, K. K., "Contributions to Data on Theoretical Metallurgy," Vol. XIII High Temperature Heat Content, Heat Capacity, and Enthalpy Data for Elements and Inorganic Compounds, Bulletin 584, U.S. Bureau of Mines, Nov. 1958.

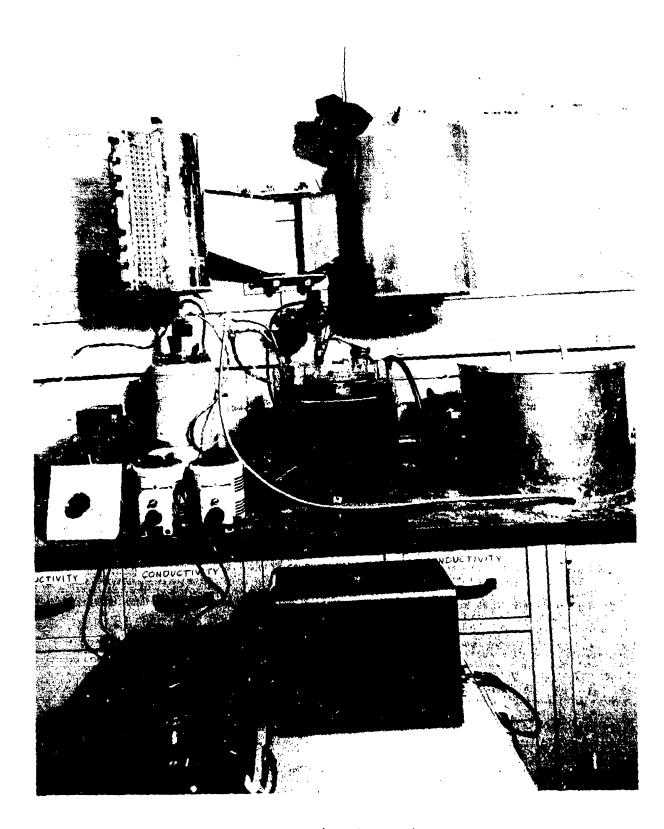


Figure 1. Heat Capacity Apparatus

Table 1

Comparison of the Specific Heat of Sapphire Obtained by the Adiabatic Calorimeter to Several Other Sources

	_		- *				1
International Critical Tables	Specific	Temp. Heat Temp. Btu/lb *F				0. 239	
						822	
Linde Company	Specific	Heat	Btu/lb .F		0.2125	0.2265	
Linde (Approx.	4.		200	1000	
Armour Research	and a	Specific	Rtu/lb °F		0.263	0.280	
	nno 4	Approx.	Temp.		200	1000	
SRI Ice	Calorimeter	Specific	Heat	Diu/10	0.210	0.241	
	Calo		Temp.	4	497	1008	
SRI Adiabatic	Calorimeter	Specific	Heat	Btu/ID F	0.233	0.240	
SRIA	Calo		Temp.	4	64	966	

APPENDIX A9
Heat Capacity to 5500°F

HEAT CAPACITY TO 5500°F

The apparatus used for heat capacity employs the drop technique in which the specimen is heated in a furnace and then dropped into an ice calorimeter. The calorimeter contains a cup surrounded by a frozen ice mantle. Water at an inlet temperature of 32°F is circulated through an annulus surrounding the mantle in order to absorb heat leak from the surroundings. The entire system is insulated with glass wool. The enthalpy of the specimen is sensed as a change in volume of the water-ice system of the calorimeter as the ice melts. The annulus containing the flooded ice mantle communicates with the atmosphere through a mercury column in order that the change in volume can be read directly in a burette. An assembly drawing of the calorimeter is shown in Figure 1 and a picture of the calorimeter is shown in Figure 3. The specimen nominally is 3/4 inch diameter x 3/4 inch long.

The specimen is placed in either a graphite or stainless steel basket and heated in the furnace in a controlled atmosphere such as helium. The specimen and basket are dropped into the calorimeter and the volume change due to the resultant melting of ice is measured. The flutter valve immediately above the cup and the diaphragm valve immediately below the furnace are major features of the apparatus since the first blocks off radiation losses from the specimen up to the drop tube, and the second blocks radiation gains from the furnace down the drop tube just prior to dropping. The volume changes due to the baskets are measured and correction curves are established. Separate basket calibration minimizes the radiation error accompanying drop techniques. These errors are reported to be only about 0.5 percent¹. Our theoretical calculations indicate even smaller errors from this source.

The heat necessary to melt enough ice to cause a volume change of 1 cc has been established by the U.S. National Bureau of Standards² at 3.487 Btu. This value is reported as the theoretical one for any ice calorimeter. Figure 4 shows a typical curve of mercury

Furukawa, G.T., Douglas, McCoskey, and Ginnings, "Thermal Properties of Aluminum Oxide from 0° to 1200°K".

Ginnings, D.C. and R. J. Corruccini, "An Improved Ice Calorimeter", NBS Research Journal, Volume 38, 1947, p583.

displacement versus time for one drop using a synthetic sapphire specimen. The correction for the stainless steel basket is subtracted from the measured mercury displacement and the result used to calculate specimen enthalpy above 32°F. The heat capacity, which is by definition the slope of the enthalpy versus temperature curve, is determined both graphically and analytically. The analytical approach is to fit the enthalpy data to an equation of the form

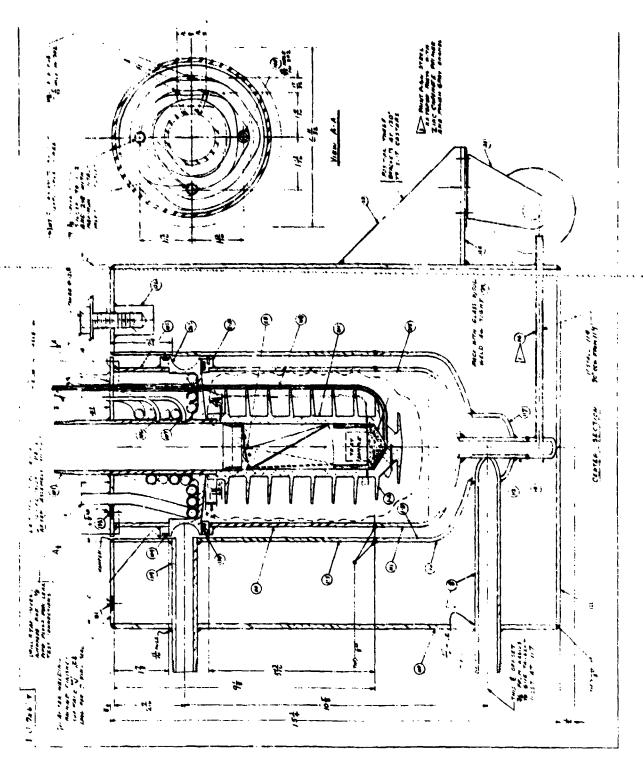
$$h_{32} = aT + bT^2 + cT^{-1} + d$$
 (1)

using a least squares technique. The derivative of this equation, the heat capacity, is computed with the constant "c" adjusted so that the analytical solution agrees with the graphical solution at 5000°F. This technique is similar to that of Kelley in forcing the heat capacity equation through a known value. The equations are developed using a digital computer.

A compilation of all errors has indicated that the apparatus is accurate to well within 5 percent uncertainty over the entire temperature range. Comparison of Southern Research Institute data on copper, Linde synthetic sapphire, and ATJ graphite all have confirmed this value.

William could be specially and the second of
Pears, C.D., and J. G. Allen, "The Thermal Properties of Twenty-six Solid Materials to 5000°F or Their Destruction Temperatures", ASD-TDR-62-765.

Kelley, K.K., "Contributions to Data on Theoretical Metallurgy", Volume XIII, High Temperature Heat Content, Heat Capacity and Enthalpy Data for the Elements and Inorganic Compounds, USBM 584, November, 1958.



THE PROPERTY OF THE PROPERTY O

Figure 1 Ice Calorimeter, Drop Type - Specimens to 5500°F

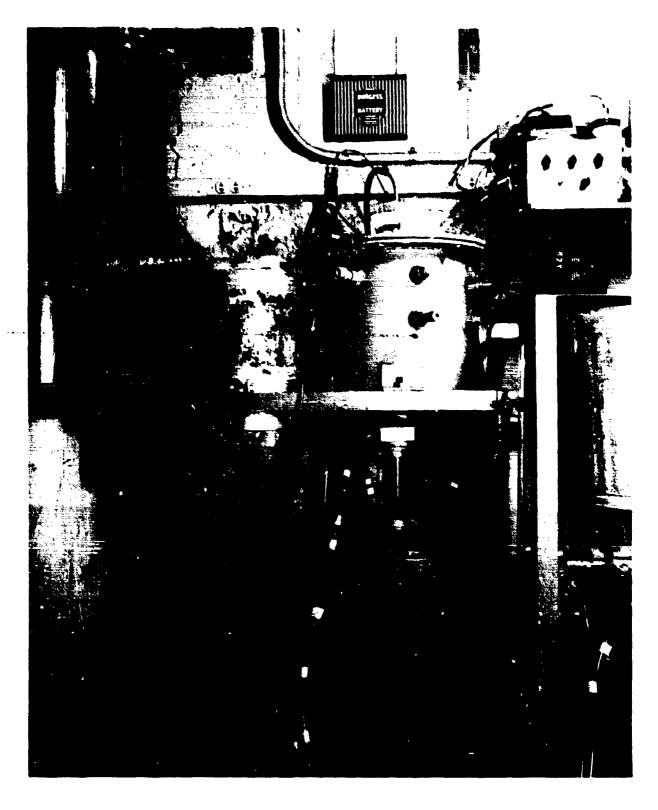
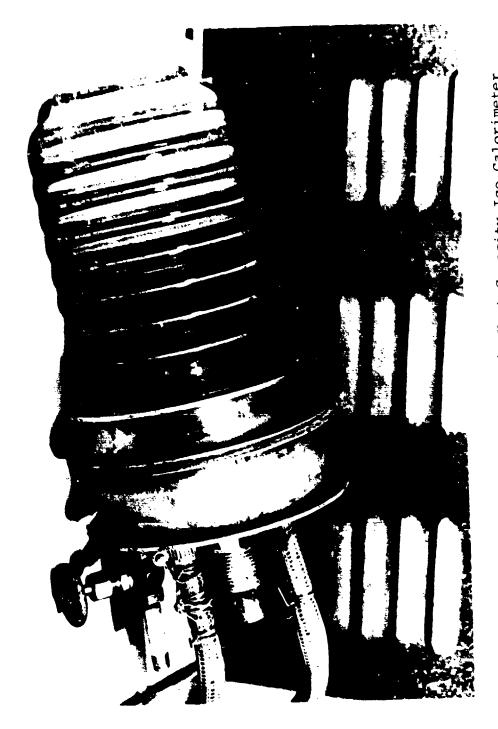


Figure 2. Picture of Heat Capacity Equipment with Drop Shield Tube in Place



Picture of Ice Mantle in Heat Capacity Ice Calorimeter Figure 3.

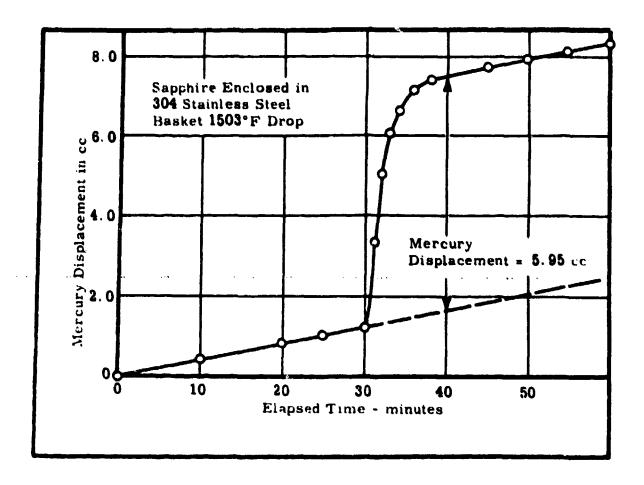


Figure 4. Mercury Displacement Due to Sapphire and 304 Stainless Steel Basket

Preceding Page BLANK - FILMED

APPENDIX A10
Ultrasonics

ULTRASONICS

The classical theory of the propagation of waves in elastic solid media describes the longitudinal motion of an element between two adjacent cross sections in a long prismatical bar by the equation

$$\frac{\partial^2 \mathbf{u}}{\partial \mathbf{t}^2} = \mathbf{V}_0^2 \quad \frac{\partial^2 \mathbf{u}}{\partial \mathbf{x}^2}$$

where

u = longitudinal displacement

 \dot{x} = distance along the longitudinal axis of the bar

t = time

 $V_{O} = (E/\rho)^{1/2}$

E # modulus of elasticity, and

ρ = mass per unit volume

The general solution to the equation of motion can be written in the form

$$u = f(x + V_0t) + g(x - V_0t)$$

and is seen to represent two waves traveling in opposite directions along the longitudinal axis of the bar with constant velocity $V_{\rm O}$. Thus $V_{\rm O}$ is the velocity of wave propagation and depends only on the modulus of elasticity and the density. It must be kept in mind, of course, that the assumption of a long prismatical bar infers that the transverse dimensions of the bar are small when compared to the length, and it is also assumed that the cross sections of the bar remain plane during deformation.

Sound transmission measurements for flaw detection and velocity are made utilizing a Sperry UM721 reflectoscope. The pulsed echo, reflection technique is used for detecting flaws. At 1 MHz, propagation is limited to a distance of approximately 12 inches -- or to state it another way -- a discontinuity at a depth below 6 inches of the surface is out of range. Sound velocity is determined! The through-transmission, elapsed-time method using the Sperry UM721 as a pulser unit and a Tektronix 564 oscilloscope complete with a 3B3 time base unit (time base precision of 1%) and a 3A3 vertical amplifier as measuring devices. Using this

method, a short pulse of longitudinal mode sound is transmitted through the specimen. An electrical pulse originates in a pulse generator and is applied o a ceramic piezoelectric crystal (SFZ). The pulse generated by this crystal is transmitted through a short delay line and inserted into the specimen. The time of insertion of the leading edge of this sound beam is the reference point on the time base of the oscilloscope which is used as a "high-speed stop watch". When the leading edge of this pulse of energy reaches the other end of the specimen, it is displayed on the oscilloscope. The difference between the entrance and exit times is used with the specimen length in calculating ultrasonic velocity. A short lucite delay line is used to allow time isolation of the sound wave from electrostatic coupling and to facilitate clear presentation of the leading edge of the entrant wave resulting in a more accurate "zero" in time. Reading time to inital rise portion of the sound wave gives some freedom from frequency distortion. This ultrasonic test system utilizes a longitudinal wave motion at frequencies near 1 MHz for graphites.

Preceding Page BLANK - FILMED

APPENDIX All

Sonic Evaluations Used for 3DCC

SONIC EVALUATIONS USED FOR 3DCC

The basic apparatuses used for measuring ultrasonic velocity, attenuation, and performing pulse-echo inspections were a Sperry UM 721 Reflectoscope and a Tektronix 564 Oscilloscope. Velocity was evaluated using the through transmission, elapsed-time technique. The Sperry UM 721 was used as the pulser, and the Tektronix 564 complete with a 3B3 time base (precision of 1 percent) and a 3A3 vertical amplifier was used as the signal measuring device. Attenuation measurements were made using the reflection technique (Tbt) with an in-line attenuator to measure attenuation at various locations of a piece of material. The Sperry UM 721 was used as the signal pulser, the Tektronix 564 as the signal measuring device, and a Kay Model 20-0, 41 dB, in-line attenuator as the attenu tion measuring device. Inspection for flaws using the pulseecho reflection technique was accomplished using the Sperry UM 721 as the signal generating and signal receiving device.

In using the through-transmission, elapsed-time technique for measuring velocity, a short pulse of longitudinal-mode sound is transmitted through the specimen. electrical pulse originates in a pulse generator and is applied to a ceramic piezoelectric crystal (SF2). The pulse generated by this crystal is transmitted through a short delay line and inserted into the specimen. The time of insertion of the leading edge of this sound beam is the reference point on the time base of the oscilloscope which is used as a high-speed stopwatch. When the leading edge of this pulse of energy reached the other end of the specimen, it was displayed on the oscilloscope. The difference between the entrance and exit times was used with the specimen length in calculating ultrasonic velocity. A short Lucite delay line was used to allow for time isolation of the sound wave from electrostatic coupling and to facilitate clear presentation of the leading edge of the entrant wave resulting in a more accurate "zero" for time.

Using 0.5/1.0 MHz transducers coupled with alcohol, the precision of this technique for measuring velocity has been established for graphites such as ATJ-S as ± 0.002 inch per microsecond for a four inch long x 1/2 inch diameter specimen, and as ± 0.010 inch per microsecond for a 1/4 inch long by 1/4 inch diameter specimen.

In using the Tbt technique for measuring attenuation, ultrasonic energy originated in a pulse generator was applied to a piezoelectric crystal which is in contact with the

The state of the s

specimen surface. Alcohol was usually used as the couplant. The signal was transmitted through the specimen, and the reflected signal from the backface was then retransmitted back to the piezoelectric crystal which performs intermittently as a transmitter and receiver. The received signal was then transmitted through the in-line calibrated step attenuator to the oscilloscope which displays the received waveform. The gain of the oscilloscope is held constant, and the calibrated step attenuator was used to maintain the displayed waveform at a constant amplitude. The attenuation value, then, was the amount of additional attenuation that must be provided with the step attenuator to maintain the constant amplitude of the developed waveform.

The attenuation results are reported as a relative attenuation index. This index is arrived at by relating the attenuation of one inch of test material to one inch of aluminum standard. Thus, the index represents variations (in dB) of the test material from the one inch aluminum standard. Graphite and aluminum dB versus length curv are linear (for some intermediate length) and parallel (graphite to graphite, aluminum to aluminum, but not graphite to aluminum) for various amplifier gains. The graphite/aluminum curves intercept near zero length. The aluminum reference curve is obtained from measurements of three inch diameter aluminum cylinders (bars) accurately machined to various lengths. graphite curve is derived by using the average of the attenuation readings from billet profiles. The following equation which defines the difference between the aluminum and the graphite curves in dB for one inch of the material is then used in calculating the relative attenuation index:

Relative Attenuation =
$$\frac{\left[dB_{\underline{i}} + (\ell-1) \left(\frac{dB_{\underline{i}} - dB_{\underline{d}}}{\ell} \right) \right] \left[dB_{\underline{g}} + (\ell-1) \left(\frac{dB_{\underline{i}} - dB_{\underline{g}}}{\ell} \right) \right] }{|A| \cdot |A| $

where

 dB_a = attenuation value (in added dB) for aluminum standard length of ℓ

l = length (in inches) of test specimen or aluminum
 standard

dB_g = attenuation value (in added dB) for graphite
 test specimen of length l

To obtain the relative attenuation index, the above equation was solved for each evaluation.

APPENDIX Al2 Ultrasonic Velocity at Room Temperature

ULTRASONIC VELOCITY AT ROOM TEMPERATURE

Ultrasonic velocity (V_L) was measured with a pulsed through-transmission technique. A block diagram of the ultrasonic measuring apparatus is shown in Figure 1. The pulsed ultrasonic generator provided both the voltage to the transmitting SFZ crystal and trigger input to the oscilloscope, from which delay time was measured. The received signal was fed to the vertical axis of the oscilloscope. Pulse travel time in the material was measured accurately by adjusting the delay time multiplier until the leading edge of the pulse was realigned to its calibration position on the cathode ray tube. Delay time was then recorded from the product of the delay time setting and delay time multiplier.

Transducers $\frac{1}{2}$ inch in diameter having a resonance frequency of 10 megahertz were used. Isopropyl alcohol was used as a couplant.

Ultrasonic velocity (V_L) was calculated by the following relation

$$V = \frac{T}{(t)(t^i)}$$

where

T = specimen thickness

t' = delay time

t = multiplier for delay time

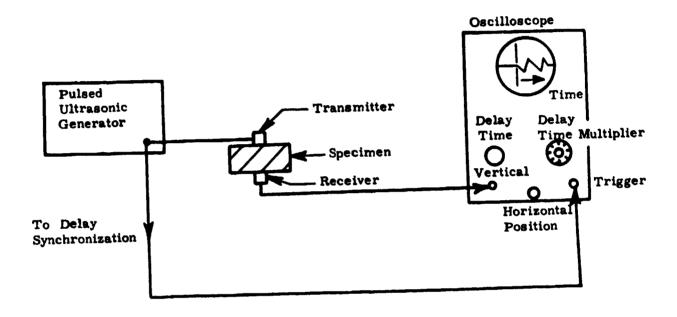


Figure 1. Block Diagram of Ultrasonic Velocity Measuring Apparatus

The second secon

Preceding Page BLANK - FILMED

APPENDIX A13
Electrical Resistivity

ELECTRICAL RESISTIVITY

Electrical resistivity is obtained by measuring the voltage across a specimen while passing a known current. The test specimen may be either a specimen blank or a finished specimen having a uniform gage length of 1 inch or more. The attachment taps are spring-loaded graphite discs which press against the specimen. Potential contacts normally having a 1-inch gage length are clipped onto the specimen. The current passing through the specimen is accurately determined by measuring the potential across a resistor of known resistance which is connected in electrical series with the specimen.

A full-wave rectified dc power supply operated by an ac regulated power source is used to enduce current flow through the specimen. A galvanometer having a sensitivity of 0.8 μV per millimeter with a 1000 ohm series resistor is used with a potentiometer having a dial graduation of 0.0005 μV to measure voltage. The normal uncertainty for determining electrical resistivity with this system is ±2%.

Using these measurements, the volume electrical resistivity is calculated from the following equation

 $\rho = \frac{A}{L} \frac{V}{I}$

where

 ρ = volume electrical resistivity,

A = cross-sectional area of specimen,

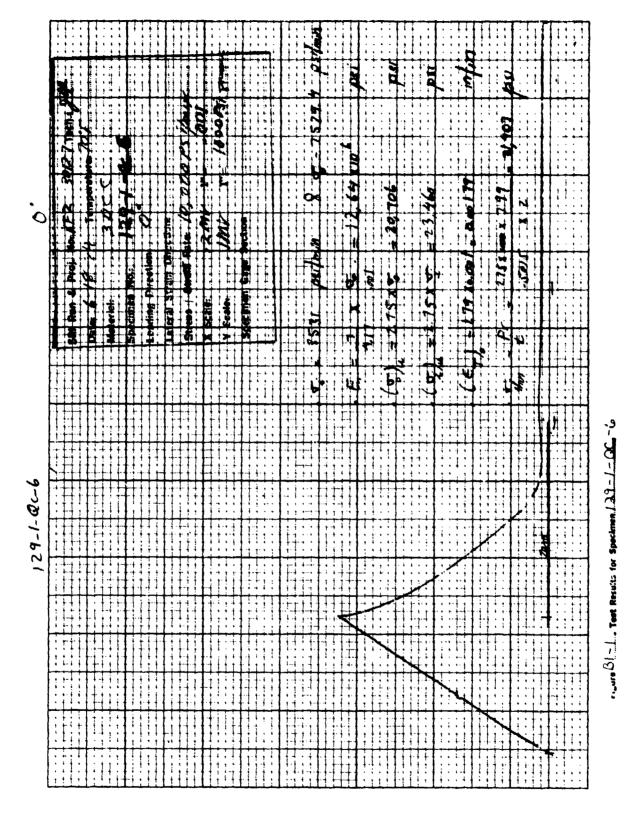
V = voltage drop across gage length of specimen (corrected for open-circuit voltage),

I = current flow through specimen and

L = gage length of specimen.

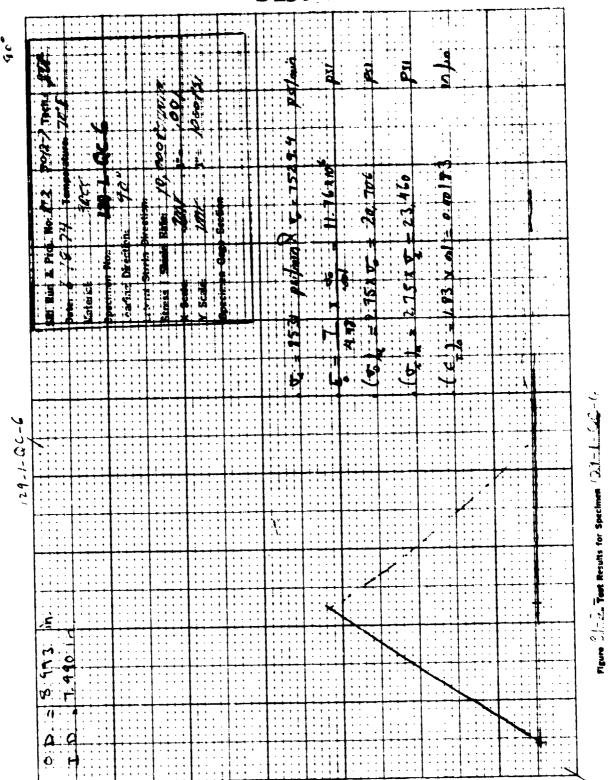
The second secon

APPENDIX Bl Circumferential Tensile Results



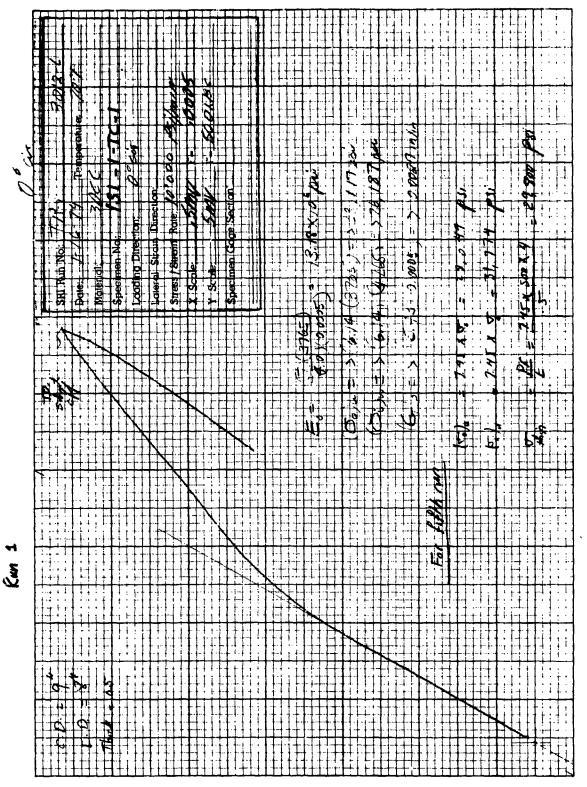
332

BEST AVAILABLE COPY

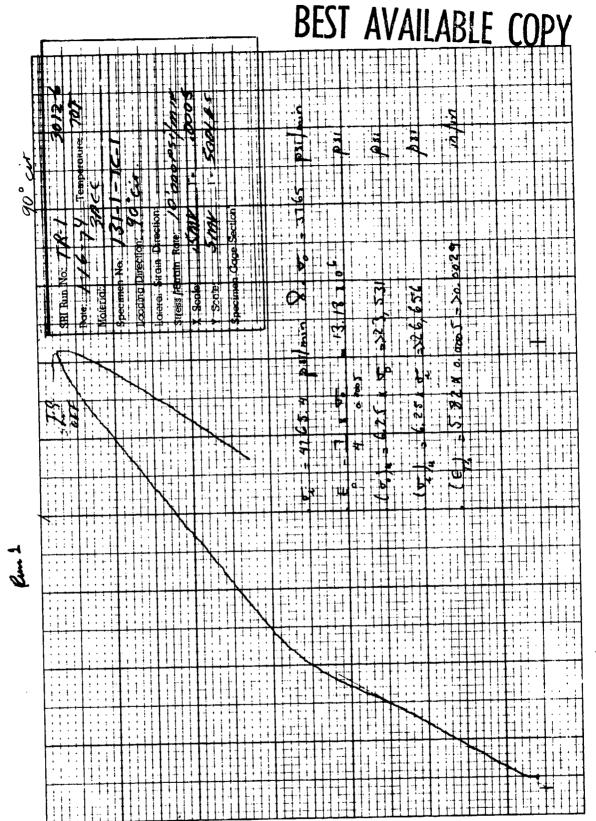


333

BEST AVAILABLE COPY

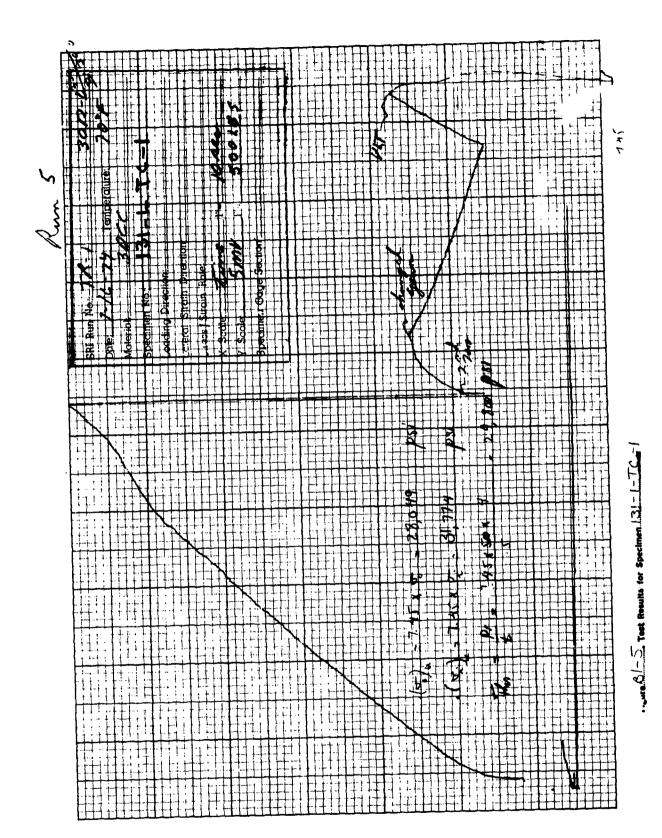


Cure C. - 2. Test Results for Specimen 131-1-TC-1

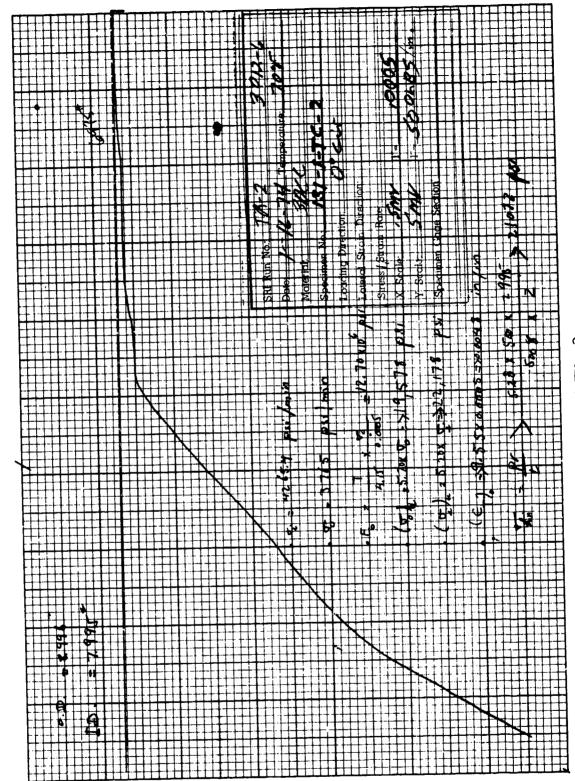


は、

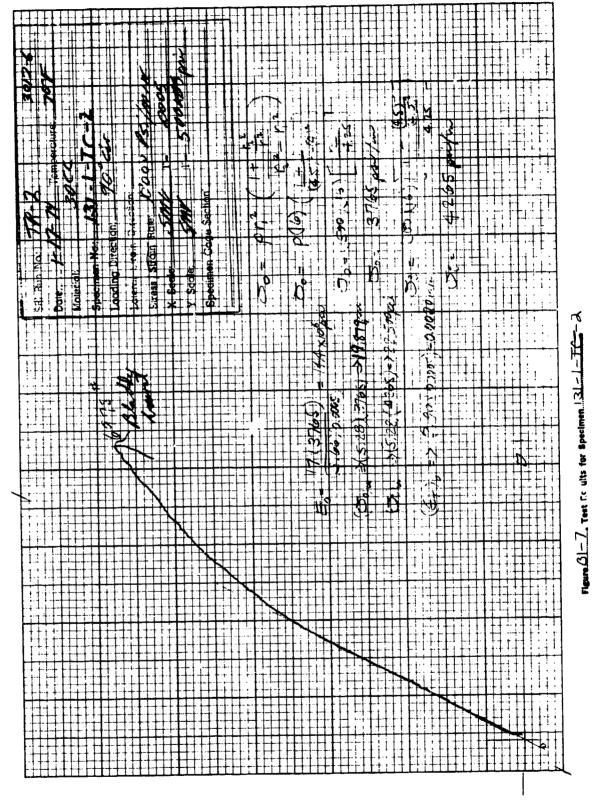
Figure 31-4. Test Results for Specimen 131-1-7C-



Sure, 61-6/3 Test Re-uits for Spinimen, 131-1-TC-1



re 61-66 Test fe ults for Specimen 131-1-T



The second secon

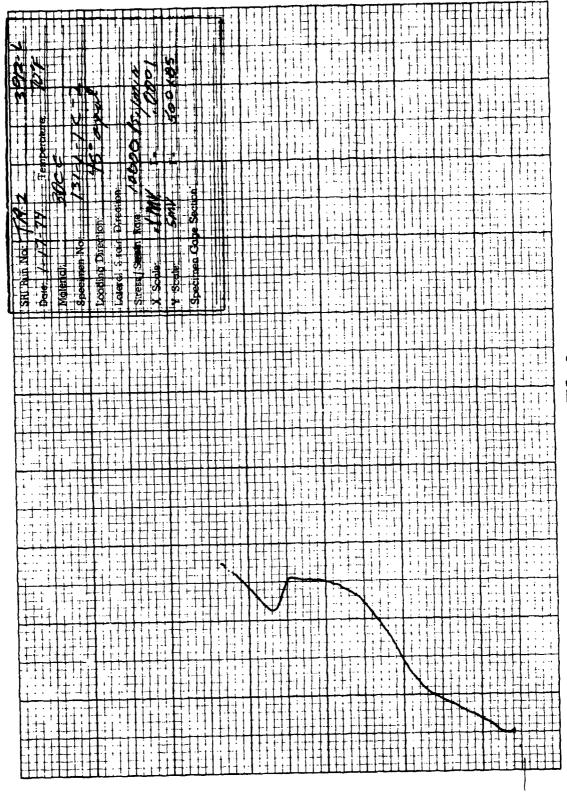


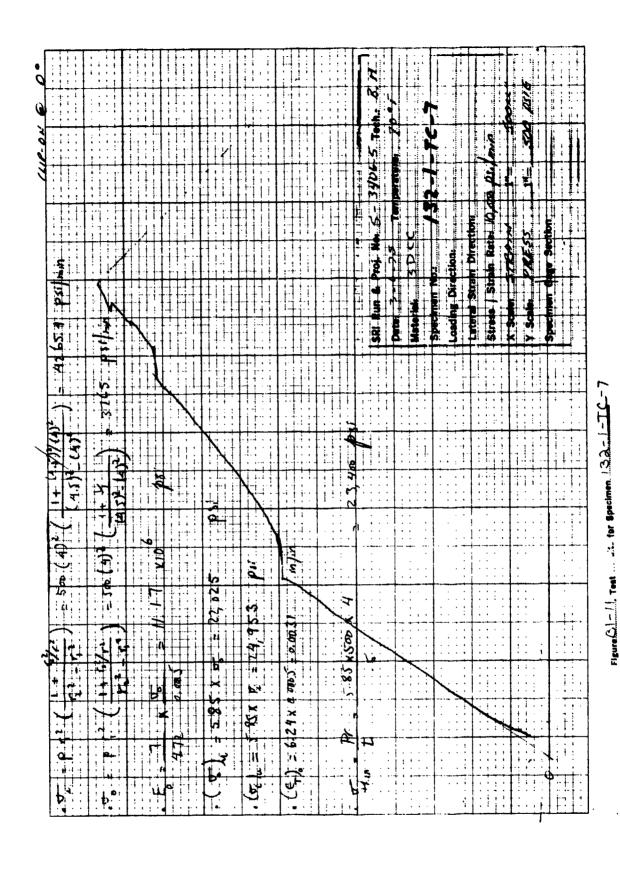
Figure 31-8. Test Rezults for Specimen 131-1-FE- 2

	, , , , , , , , , , , , , , , , , , , 	 		 	T-18:8	, , .	,		<u>g:</u>	····	, .		
				1	1			,	7	· i i			· !
						777			2 C			ì	
* · ·		11.				1	7		500 K		1:1		
		7.3				ra:	7	1		r			; ; ; ; ; ; ; ; ; ; ; ; ; ; ; ; ; ; ;
		#			(1)	Tempera	[-7¢	ë 🔪	À	n. .2.4.			!
		sult			No.	5) LIO	Strain Direction	14.	Section		.	
		No. 7			SRI Run & Proj. No. 14D	Material:	Specimen No.: Loading Direction:	P' _		cimph Gag			!!!!
		12			88	Date: Materia	Specific	Leteral Stress	X Scale	Specimen (2) 5 0 0 2	1-1-1		
		9		: <u> </u>					756				
	. 4	1 1 1 1						7	1 - 5.99			7	
	2	and	7		• • •			7.7+	4.495			N	
	4	34	72				7	26.34			13		1
1 .			2 a	†-† †-† † 			brat))			d g on		
-	7 7	2	Ziza GilZi				1/4				684	¢	D:
	 	-			+		0000	- 1	1,4		= 14		
#1 #		0.5	3	+++++			7	+	777		100025		
	- 1 - 13	AT 2780°E	tulus				Modulus a	0 72.6	760		7 Lo1		
11.	1		1100				godu.	0	0 V		11/		:
::	7	3		+ :- 	;		- 	.			4		
1 7	•		1 1 10	 									

AND THE PROPERTY OF THE PROPER

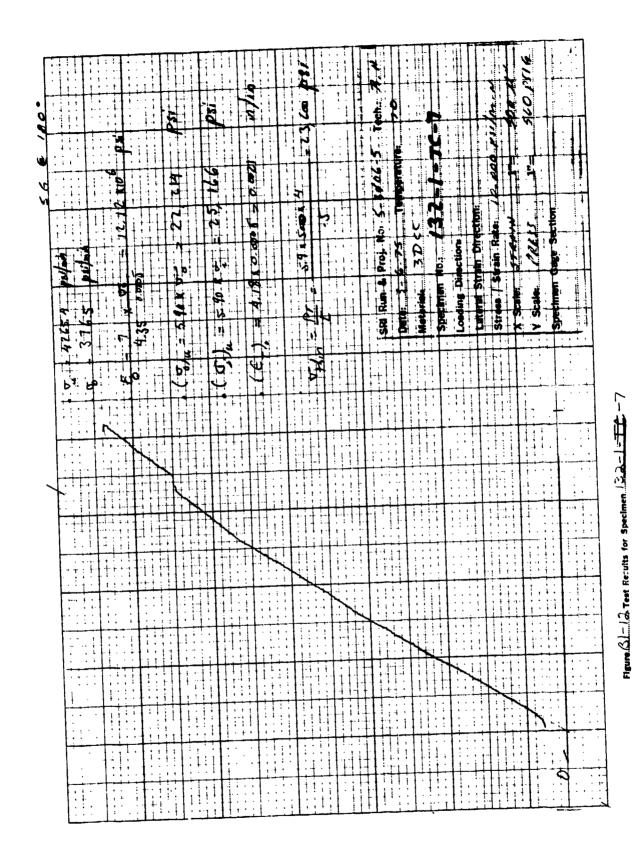
june 31-9. Teet fit uits for Specimen Listaline

urd poid



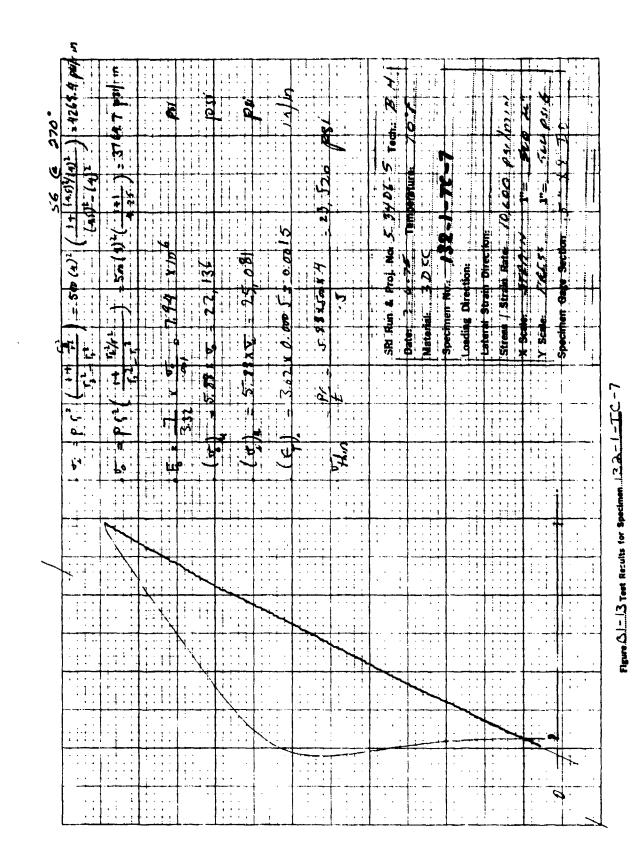
下一一种

343



に被談し

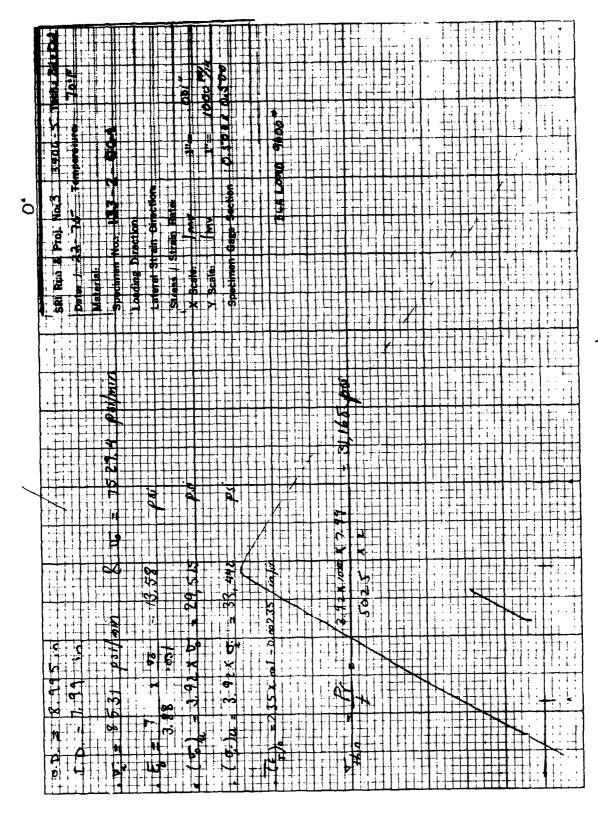
344

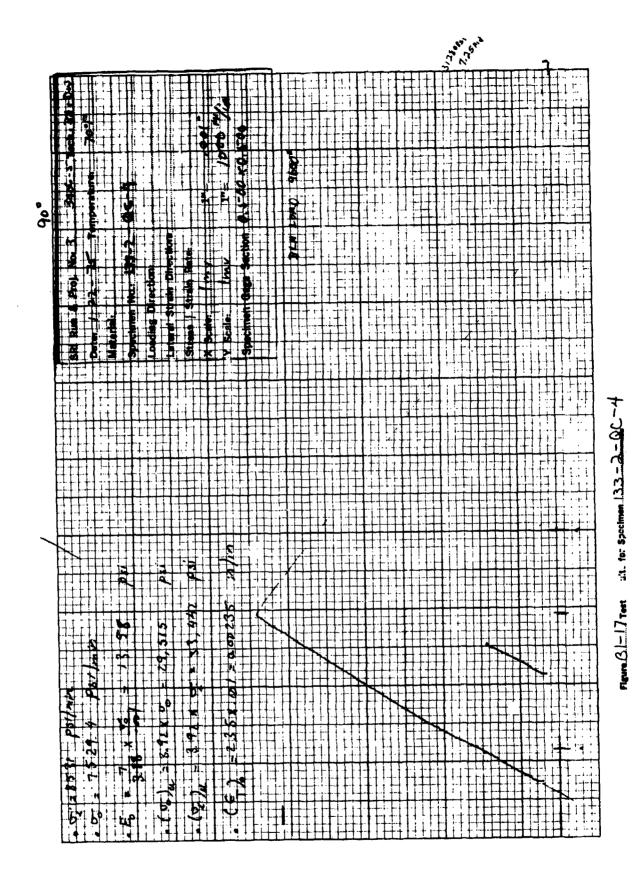


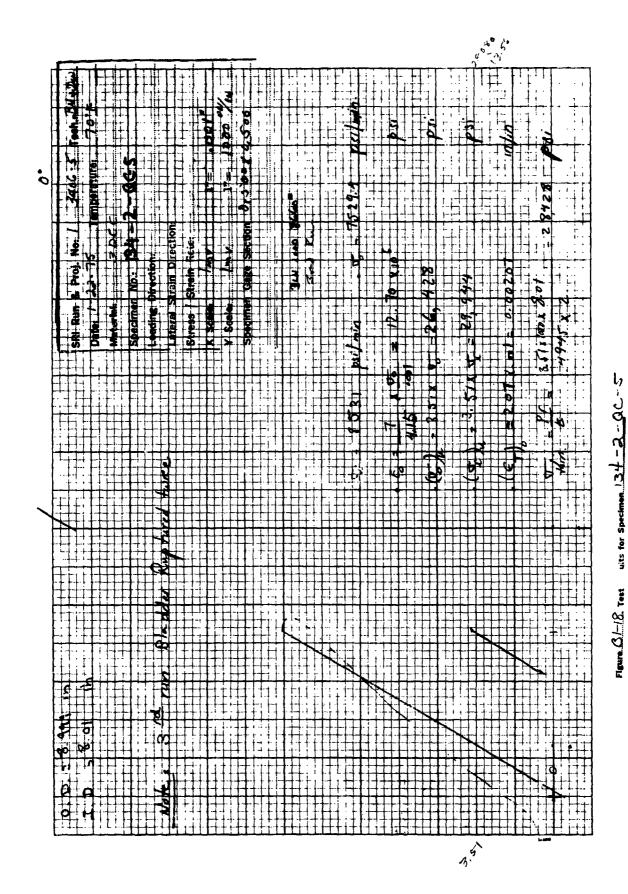
14 1 1		13	_	Ii.		I			_		1-					Г		T			<u> </u>	٠.	T	11	• •	T		-	,
સ	- •				ţ.		+	٠		L					· •	↓.		.	· •-				. 4-	• •	Ţ				
F. 24							2	00.5			 	: :		i					. :		_				:			. - -	
				+	-	9	10/	D X		1:		! !		1			1		!										
3404-8		÷ L	- -		;	-	-#	47.5		•	\	1 .		•	11	+			T:	: : İ	-	1	:	i	+				
	SDCC	4	+		+		:	0	160	1	100	} }	_	1		 	: :	:		:		: 1					••••••••••••••••••••••••••••••••••••••		
Proj.	9	1	ection-	- E	Greis Dir		Ē							 .						! ;								+	
-		; E;	뷴	1	_			++	כונגיפעו ופי		-	2								+	-	1 1		1		1		+	-
SRI Run	Date:	Spectmen	Loading	Latera	Stress	-	د. د ز	-	5					1	+							1		Ŧ				++-	
	1 .		ί.	Trad		4.10	. jj	. i.		1:		. :	1	1	<u>. :</u> . † ! !	+	1			- 1 1	+	1	+	!	1	-	-1 4-1		
				23		t psr			-	•	+		•				1 :	• •			+	. ! . !				-		+	-1
	1::		+ -			5214		!	<u> </u>		+	: : : !	- : - :	-	: : : 		: : :	1				61.7		1	1;		1 1		::
	- -		1.7	77	1.0	-		1	+	i		÷ !		-			: :	**		+ 1		14C-			1 1		+		
	1 1				<u> </u>) T	38		+;	- 1 1	-	+7	11	 	1:		5) (: !	1	1:		<u>:</u>
	1		i . '	7(4)6	: ; , : ; ,	けんせい	7		1	3		. 6	<u>,</u>	+	3		/"	,			<u>;</u>	-	-	1	1 1				
-	Ē		1	=1000	. :	1) 6	1 ,	:			1	1	2	+	2		9	· · · · · · · · · · · · · · · · · · ·		1 1		199	7	y !					-
*	r V		!!		-	† ‡I			1	0/X //	;	•	4,5		465		3000106		1	11		×	1 '						
14	_			1	11	<u> </u>	2.2	_		2			11		(€ = /6		0 = 1		++	1 1		1.93×100	1	170		· · · · · · · · · · · · · · · · · · ·	/	<u></u>	! : -
4	1 :		1	1 I	t.	1+	1))	. 1		100		٦		Ь		100 X		,	11			·				H :		
345			;	1,7,4		7	_	1	 	*	i		(2) - 193 X		4	•	1.06			11	<u> </u>	1,7	'n		· · · · · · · · · · · · · · · · · · ·	-			
11	-		: ,	0	-			• •	t	1 20	1. S. T.		- 4					Ŀ					- //		1	7		<u> </u>	
A	A	· · ·	- -	Ų	R		aP.			μo	· ·	1	Pa			A ,	£ 6	•		4.1		7	1111		1	: i		• • •	

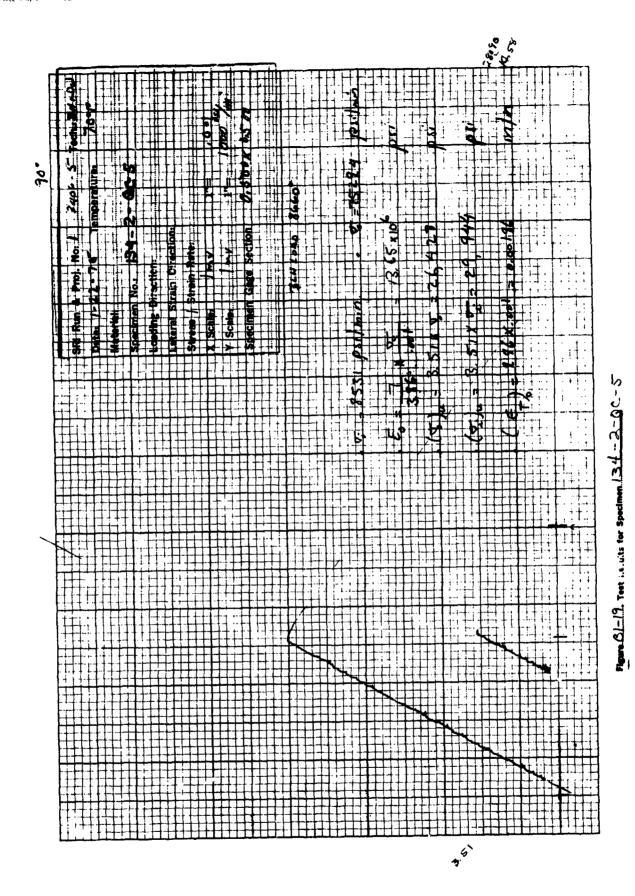
, b' (j'

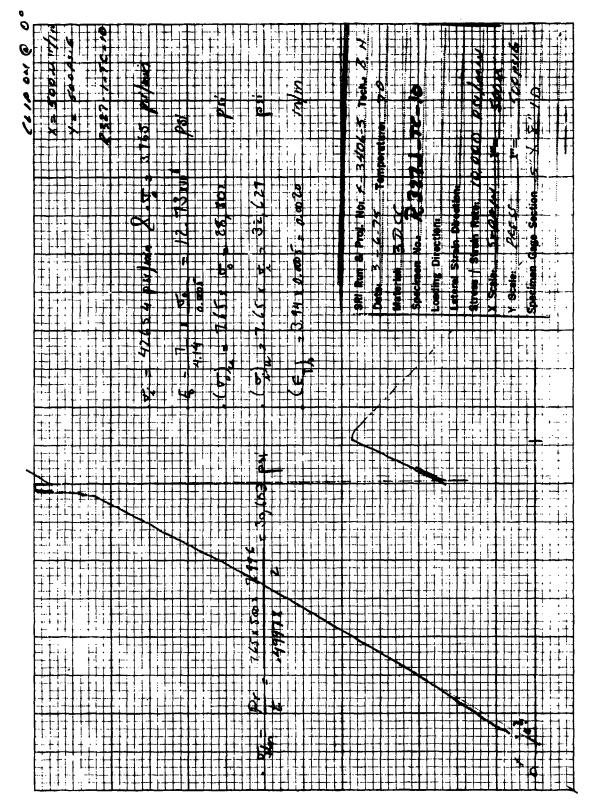
1-15Tex - 1: for Beachman | 33-1-06-1



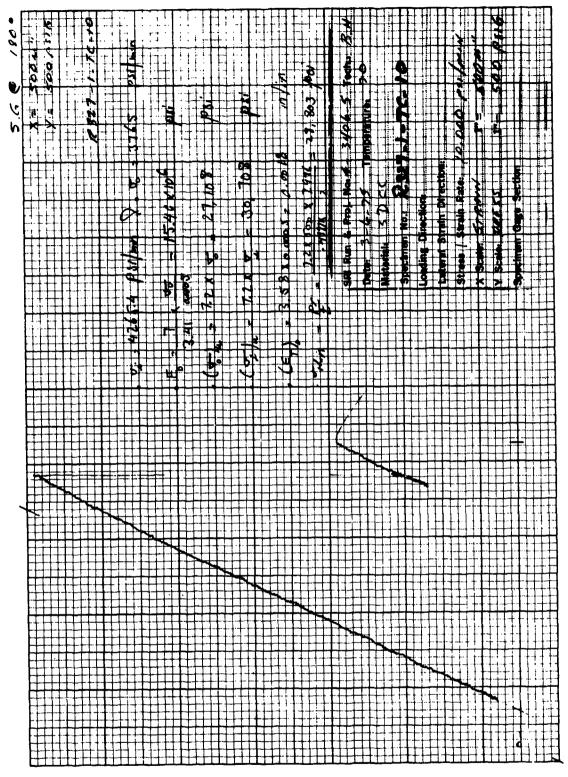




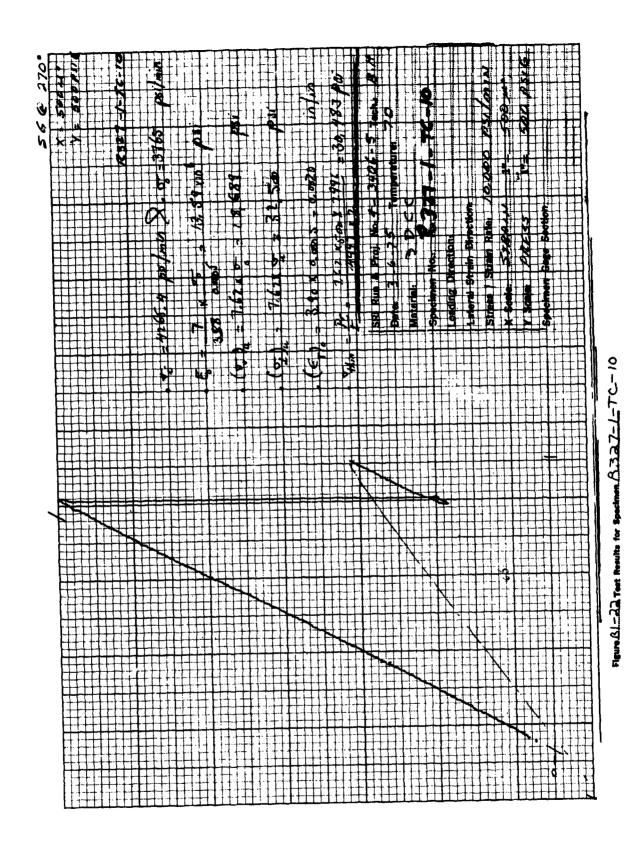


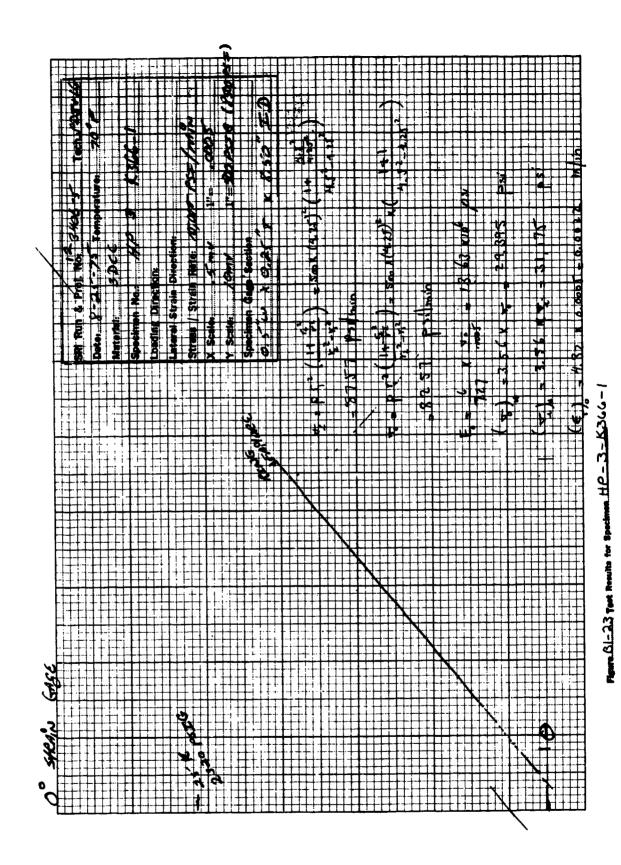


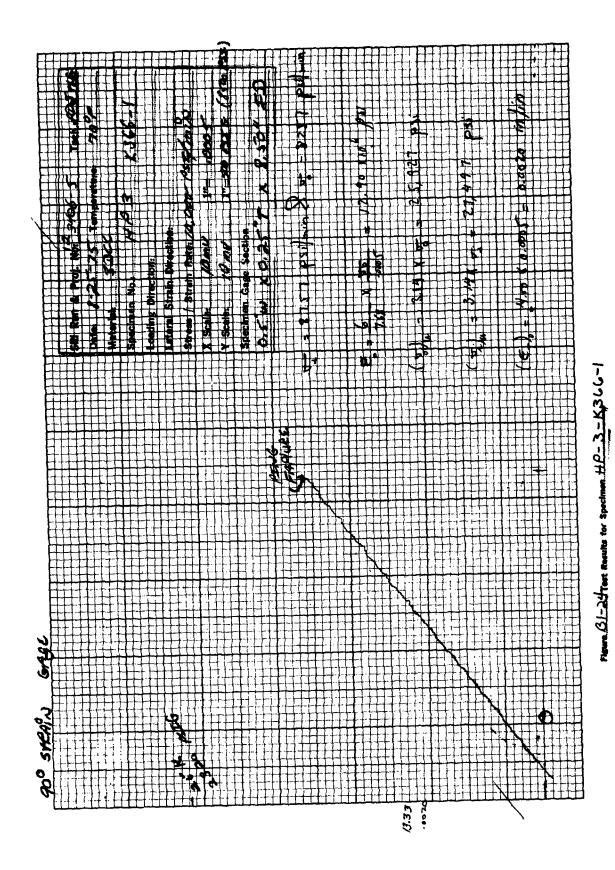
e. BL-20 Test Results for Specimen. B327-1-TC-10



M-2 Test Results for Specimen A32

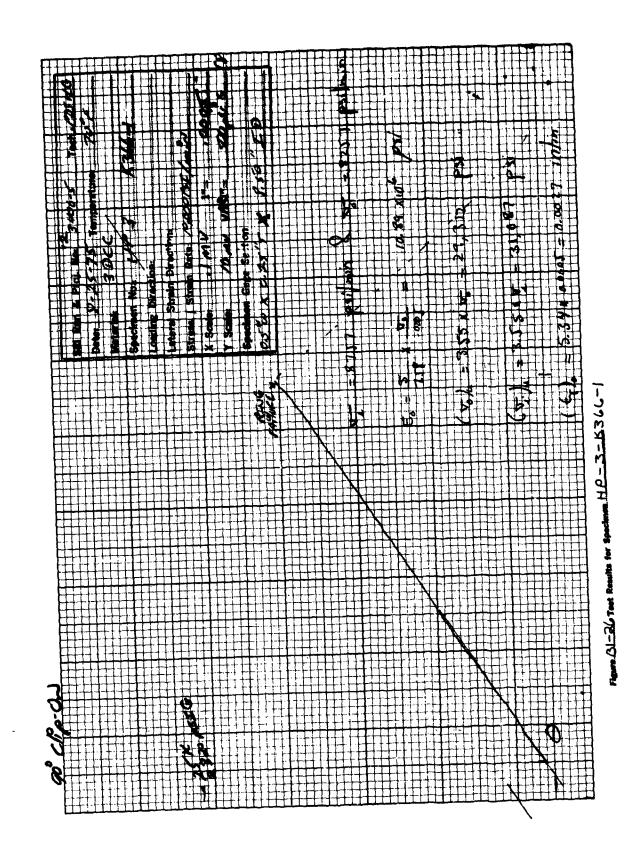




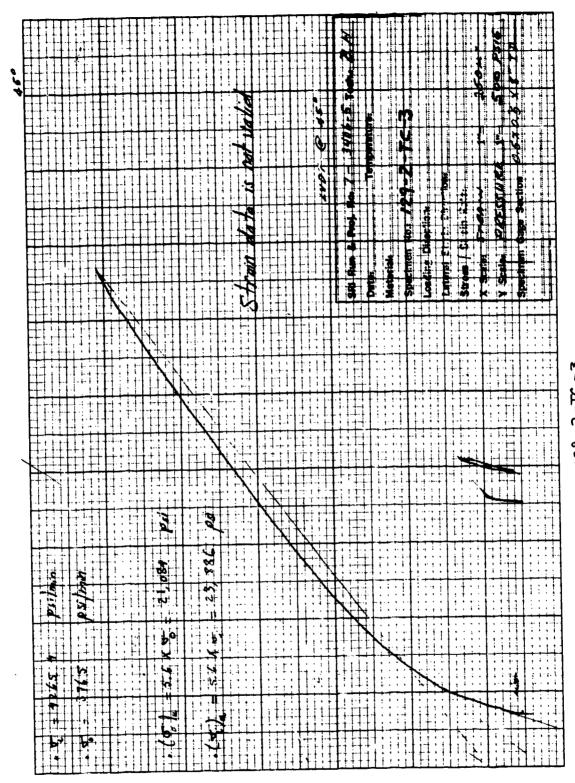


是一种,我们就是一种,我们就是一种,我们就是一种,我们就是一种的一种,我们就是一种的一种,我们就是一种的一种,我们就是一种,我们就是一种,我们就是一种,我们就是

Flavor 61-25 Toot Results for Specimen HP-3-53-6366-1

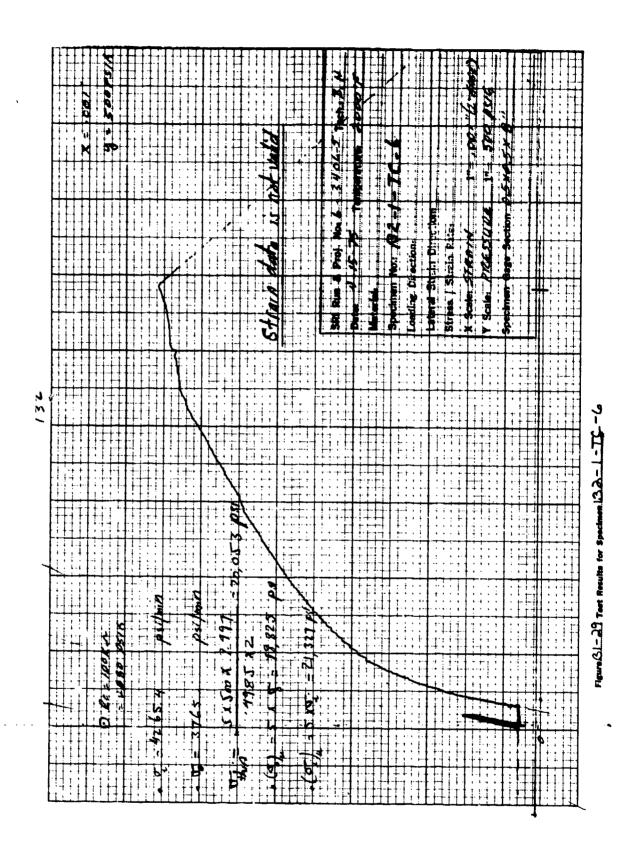


ABI-27 Test Results for Specimen 129-2-TC-3



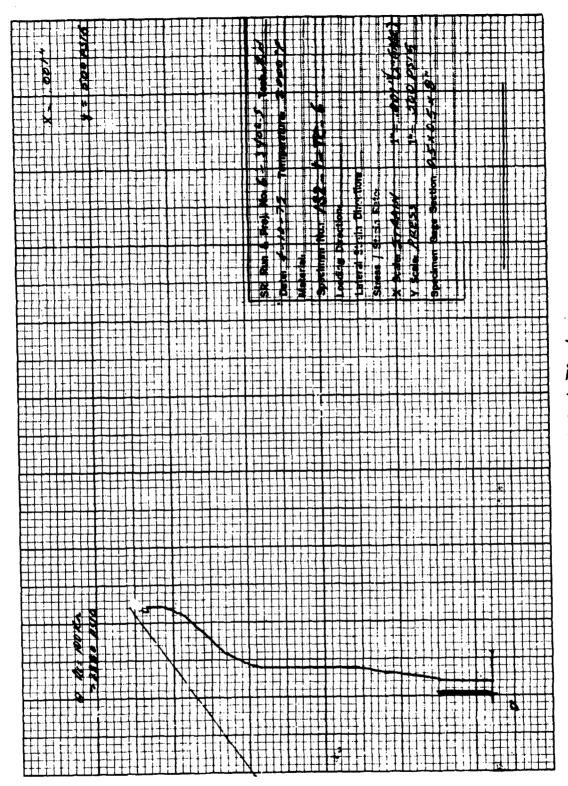
The state of the s

Figure 61-28 Test Results for Specimen 129-2-TC-3

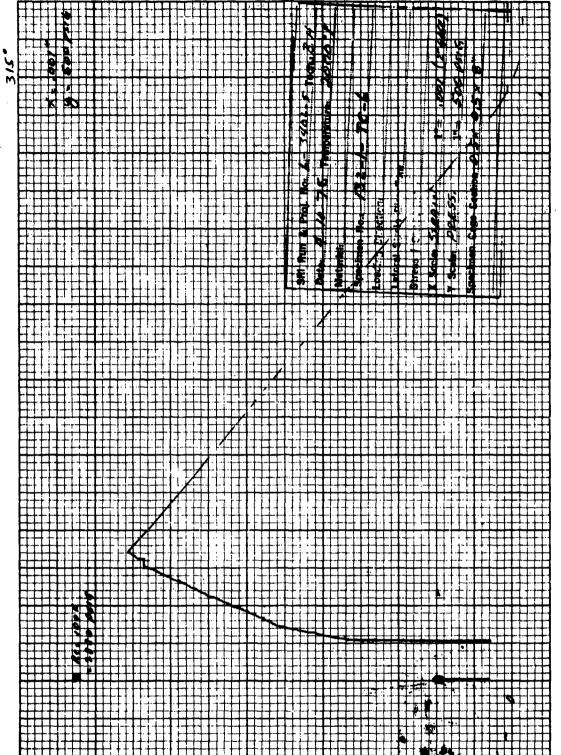


The state of

361



une 01-30 Tool Results for Specimen 1.32-1-TC -- 6



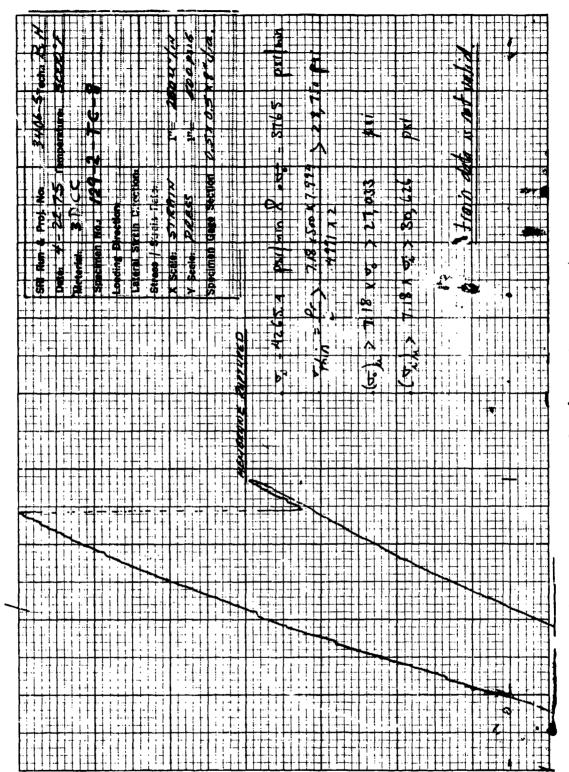


Figure 51-32 Test Results for Specimen 1 29-2 LTC -8

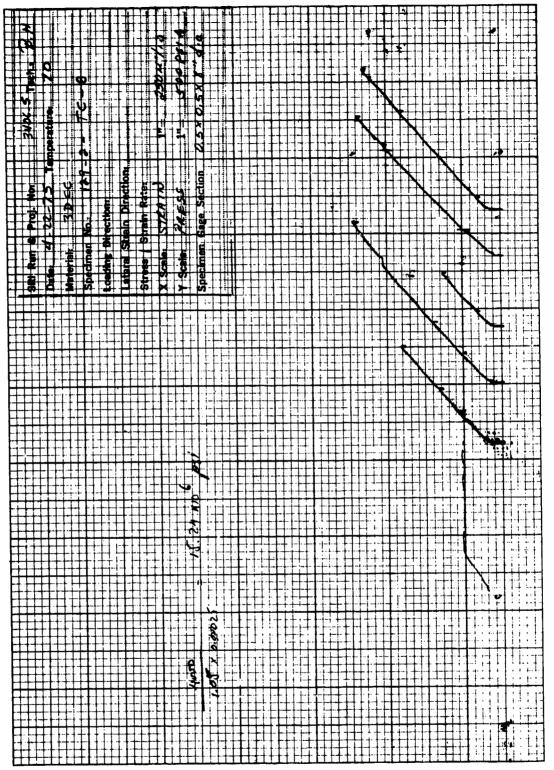
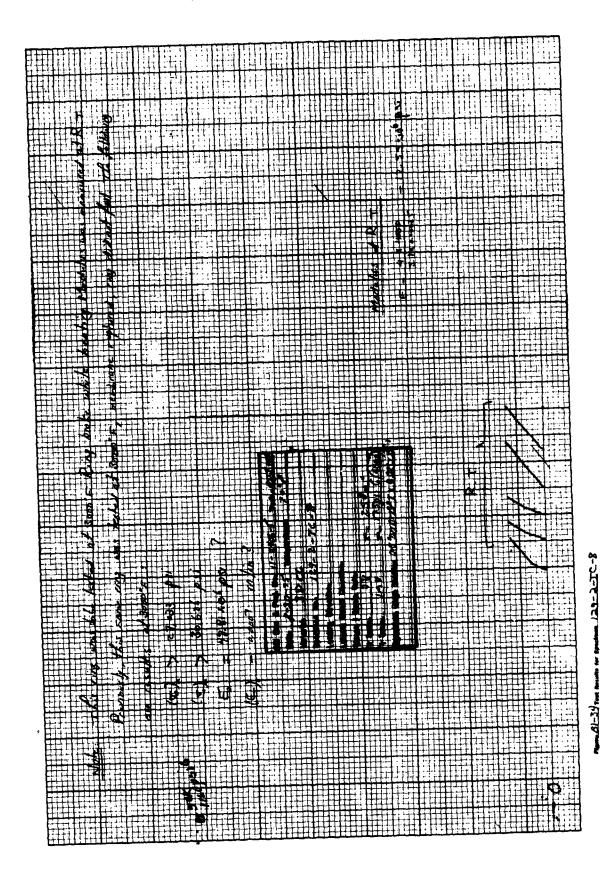
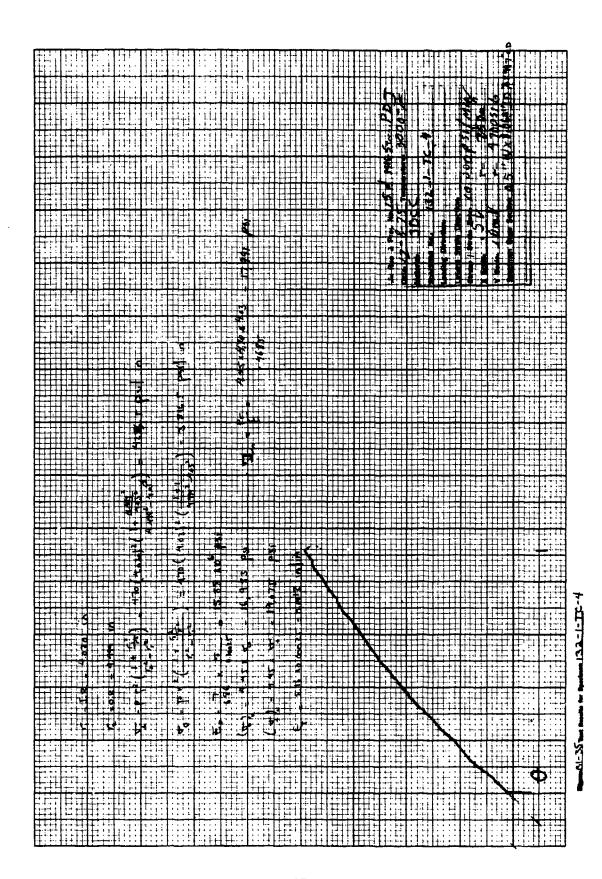
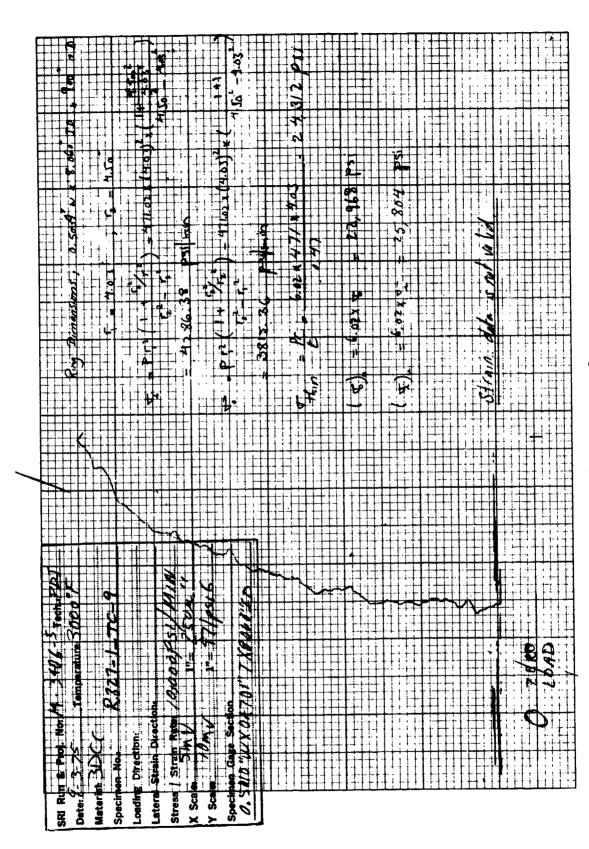


Figure 61-33 Teet Results for Specimen 129-2-TC-8

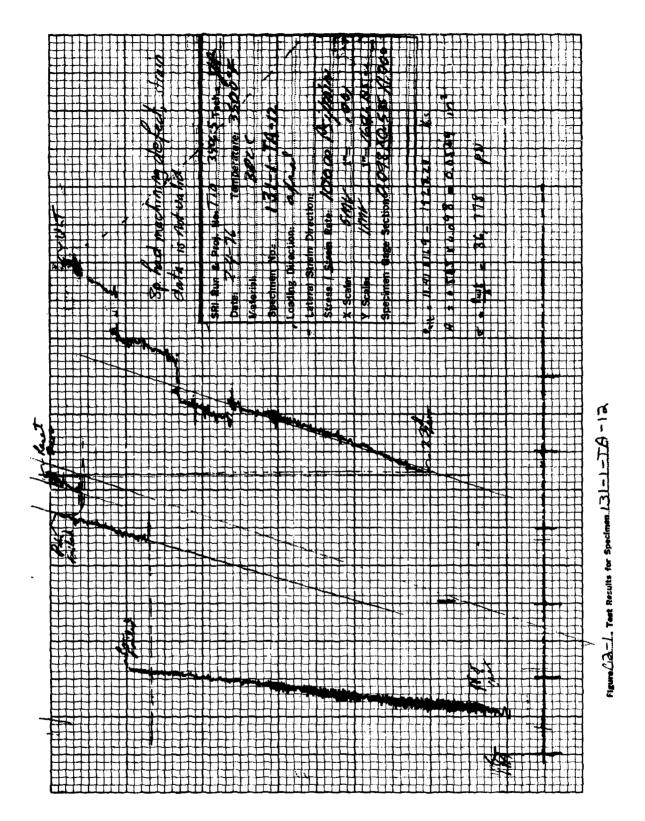


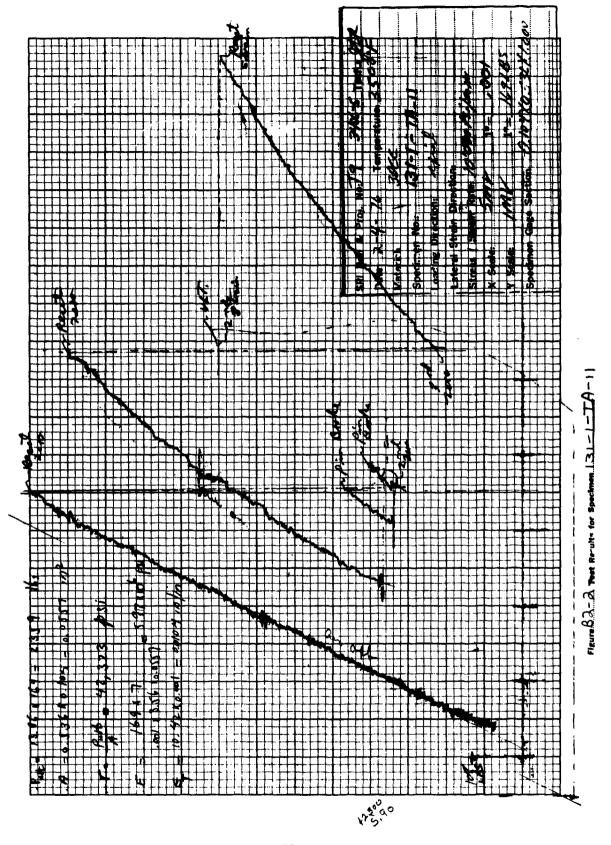


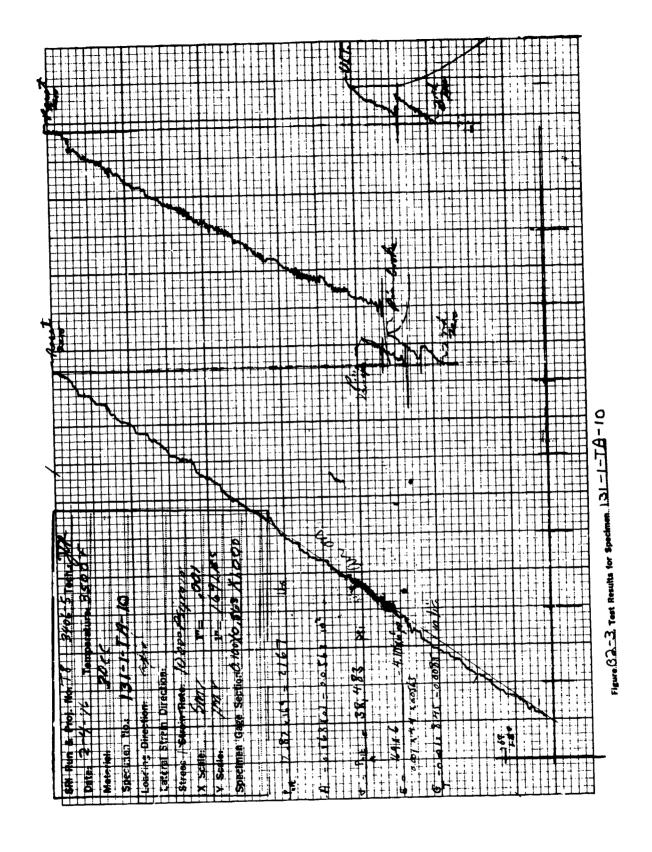


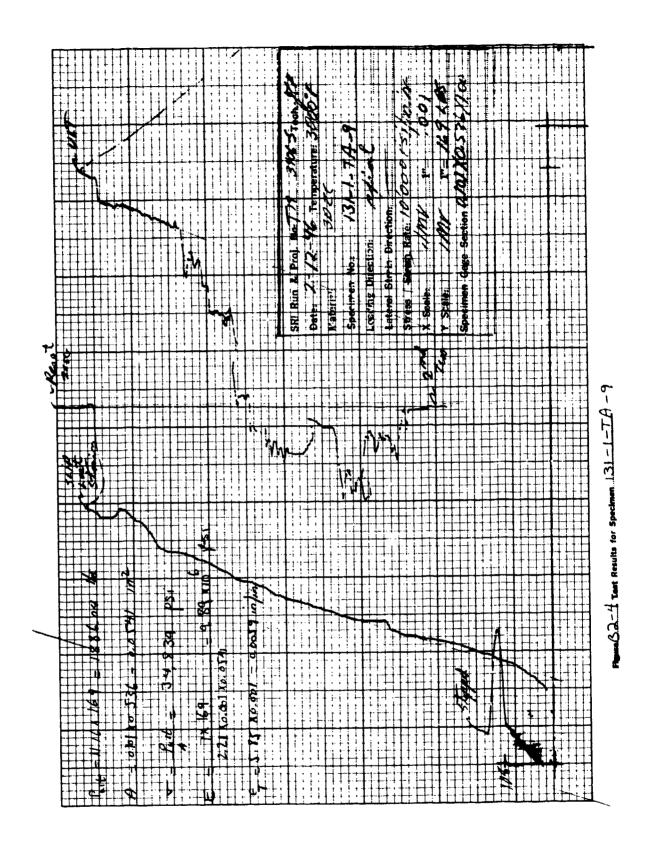
Ngare 81-36 Test Results for Specimen 63227-1-TC-9

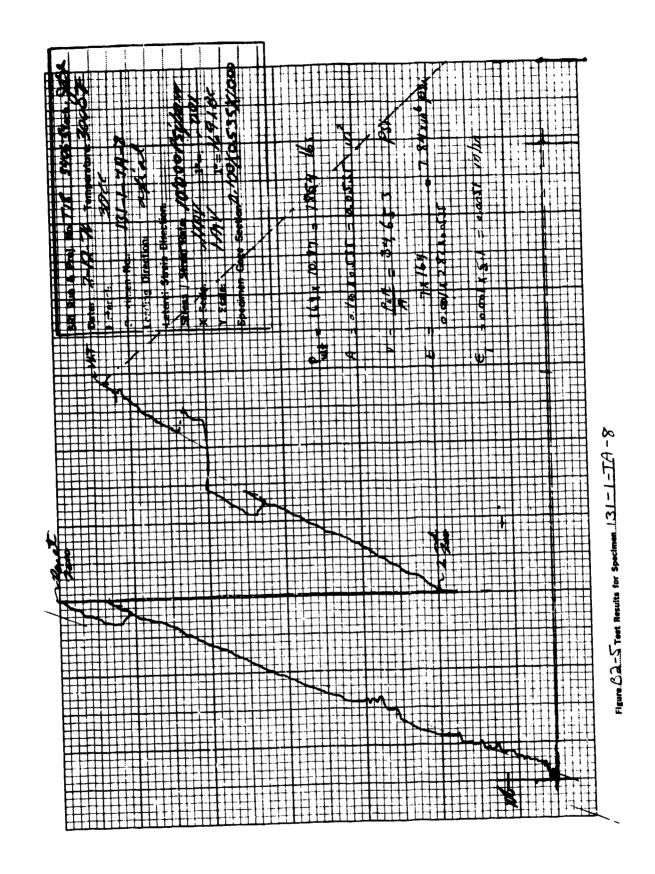
APPENDIX B2 Axial Tensile Results

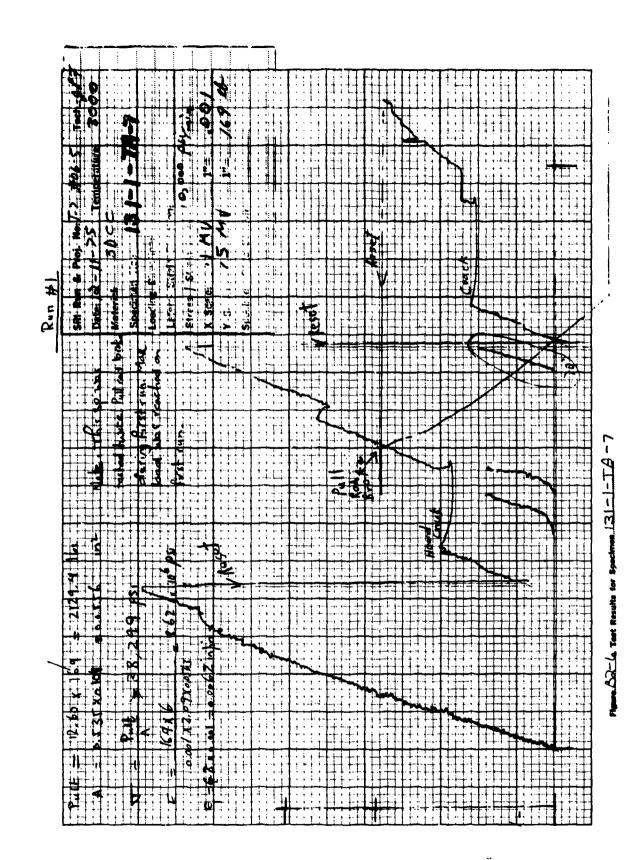


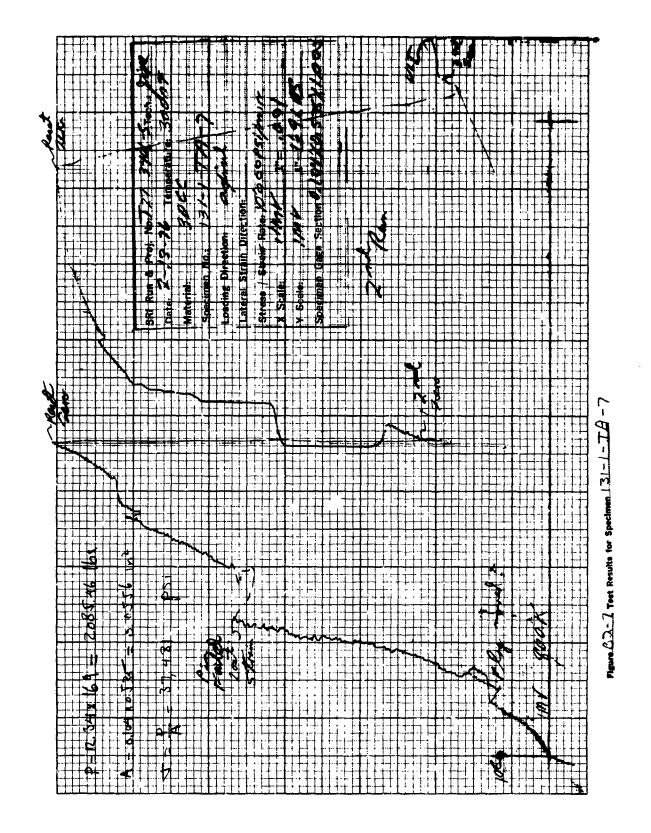


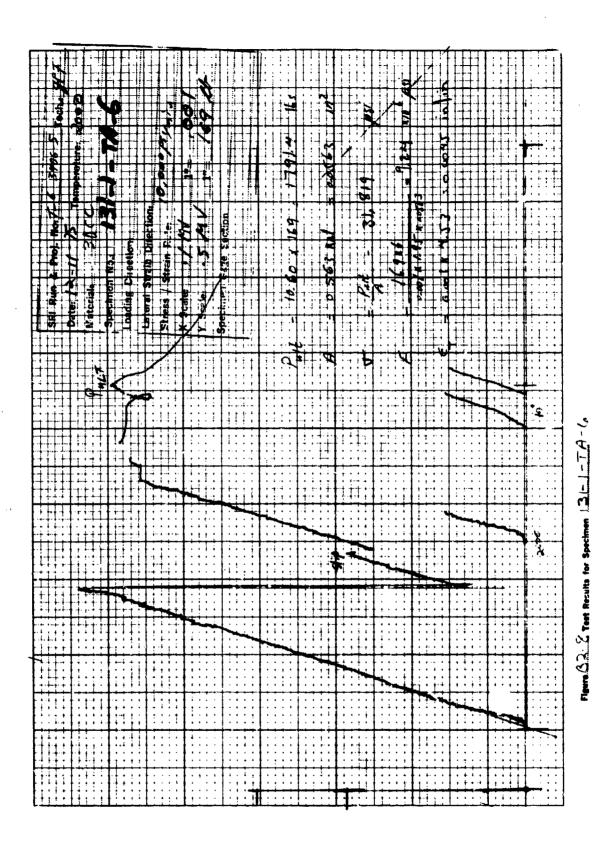


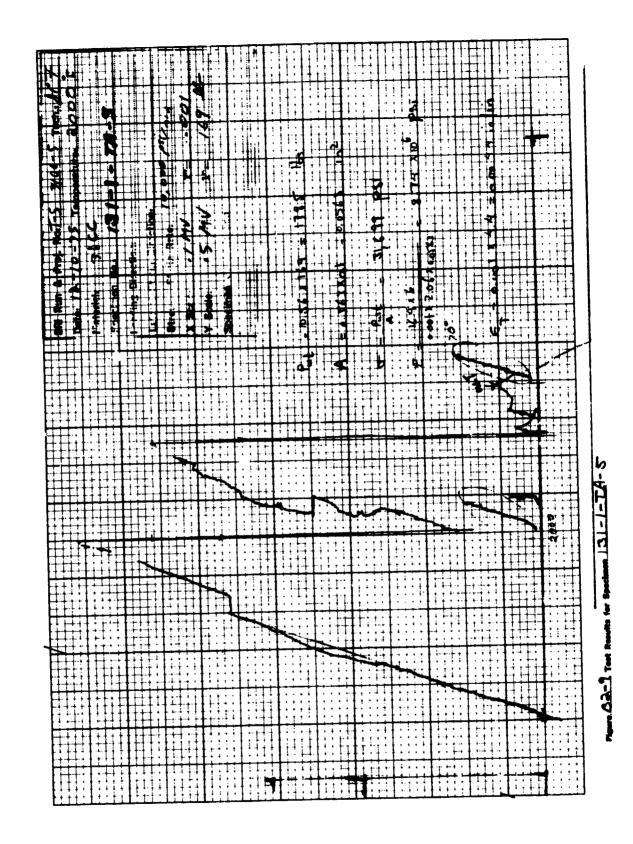


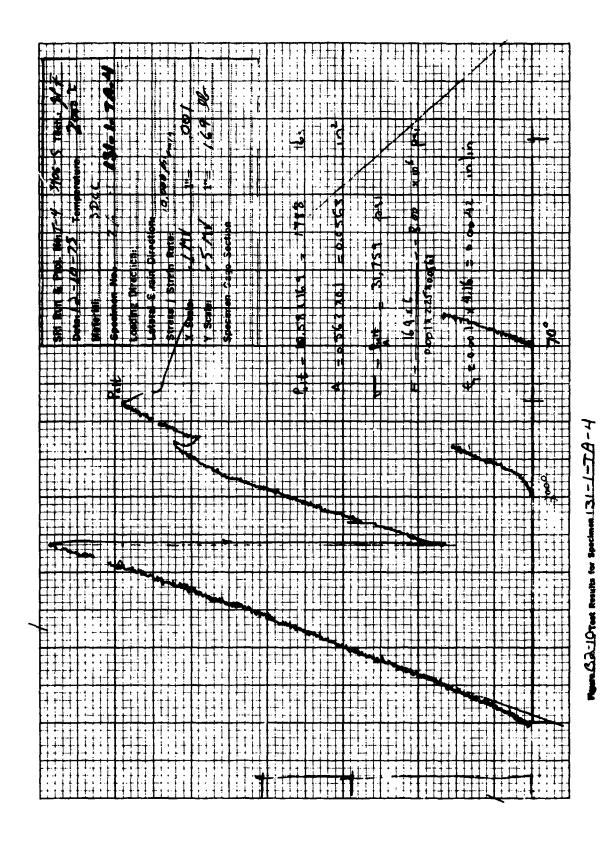


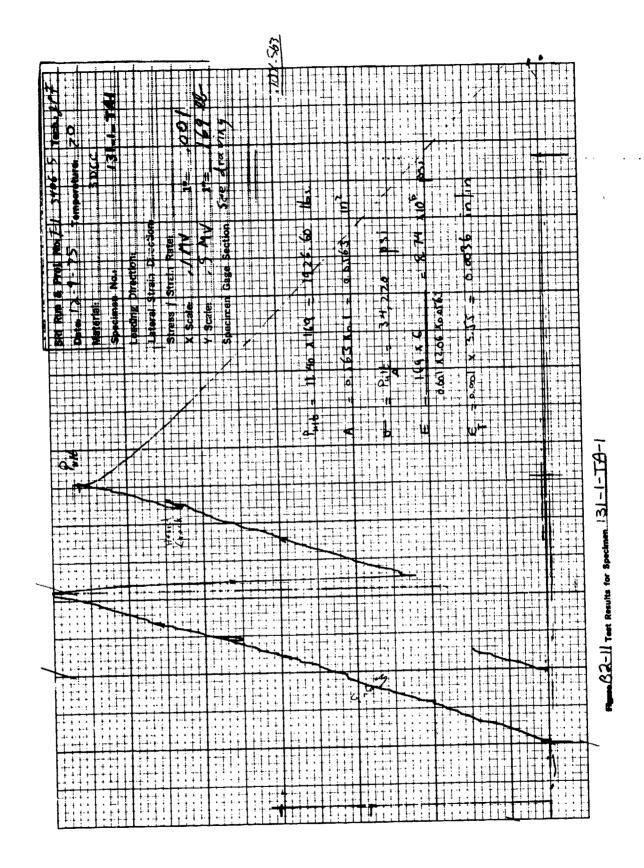


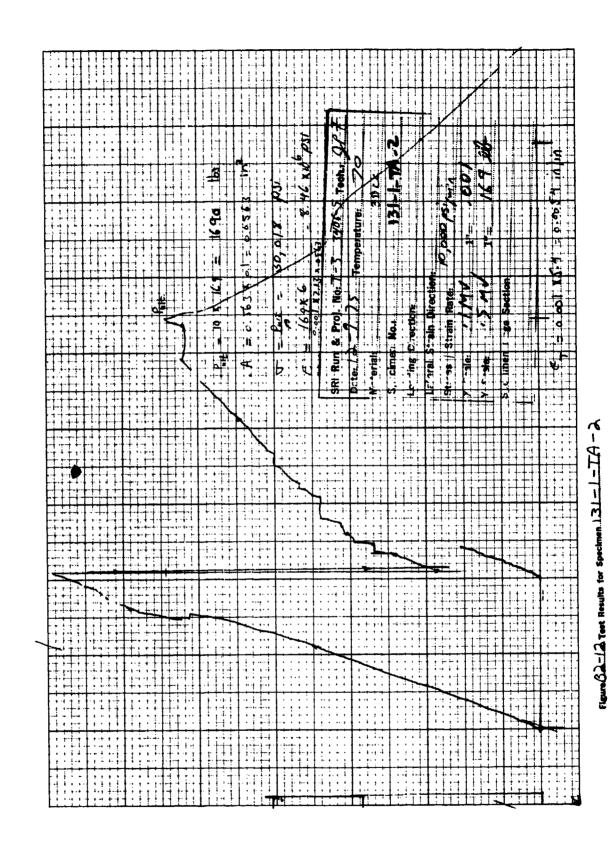


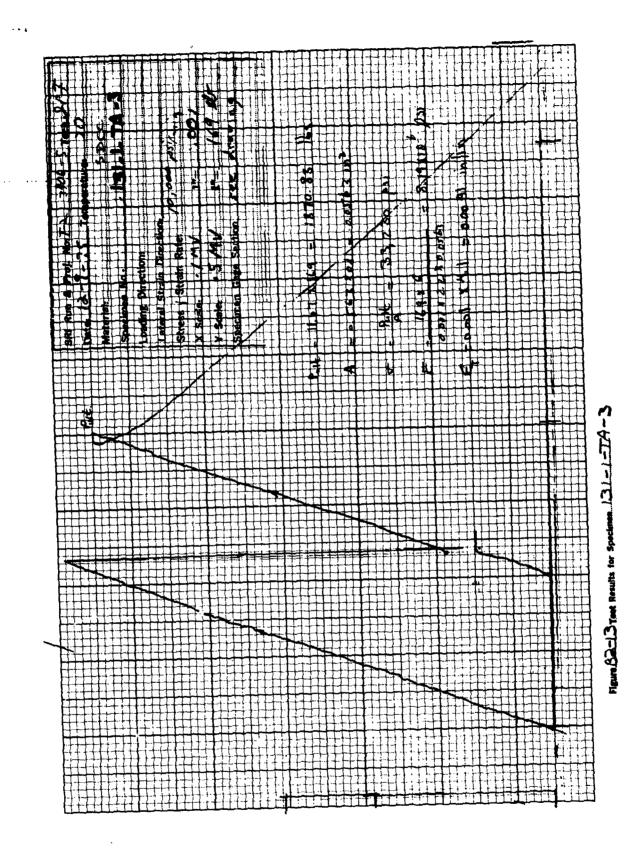




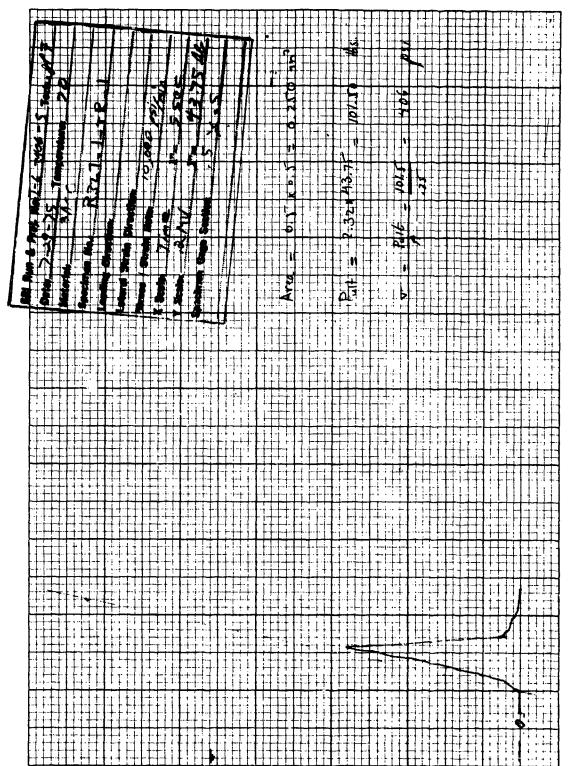






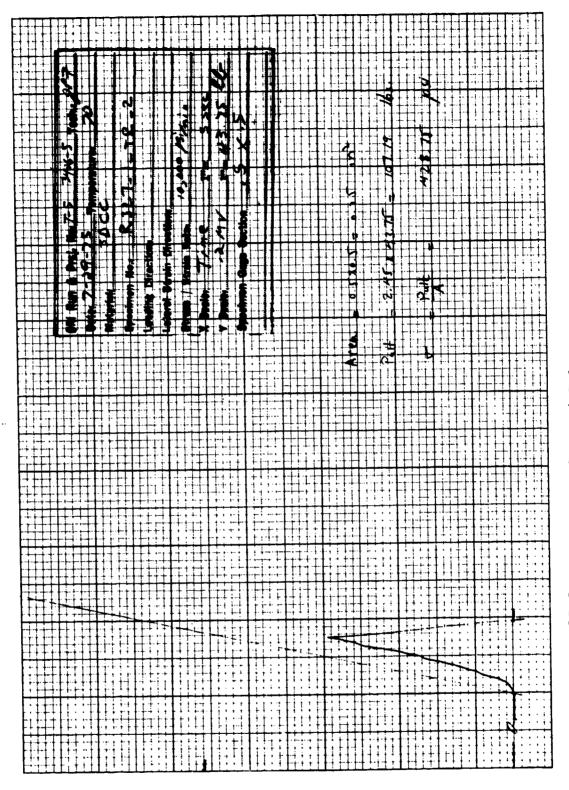


APPENDIX B3 Radial Tensile Results

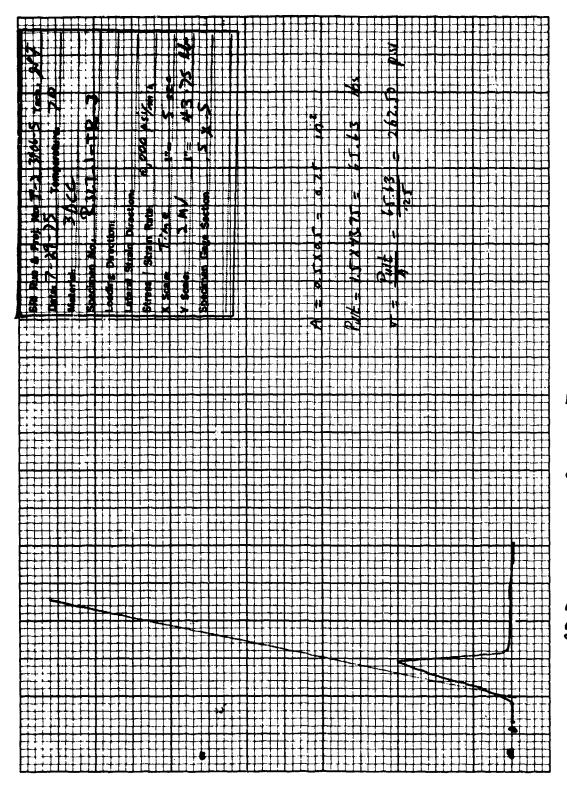


年 二個の いい

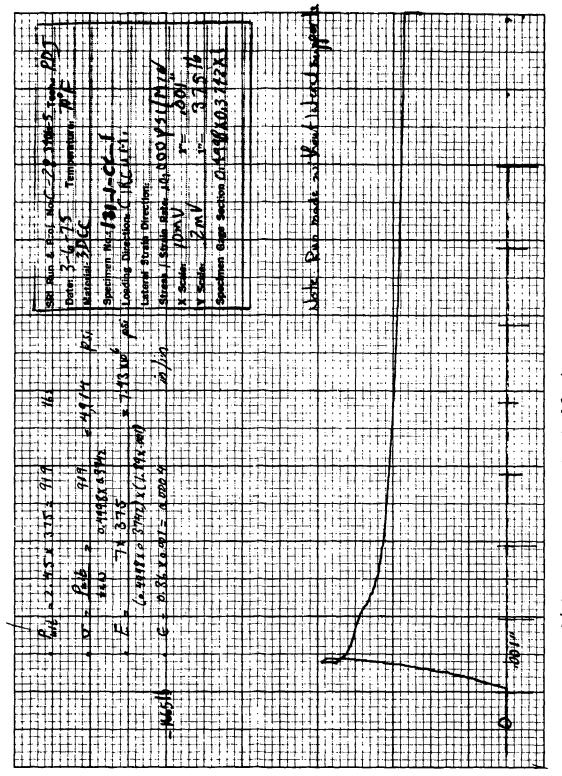
we 33-1. Test Results for Specimen R322-1-TR-1



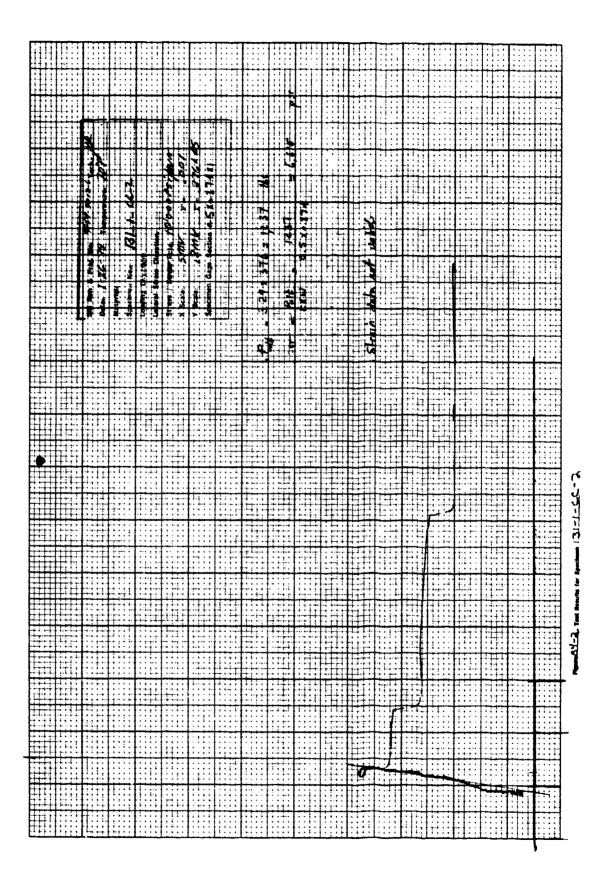
163-3 Test Results for Specimen B. 327-1-TR-3

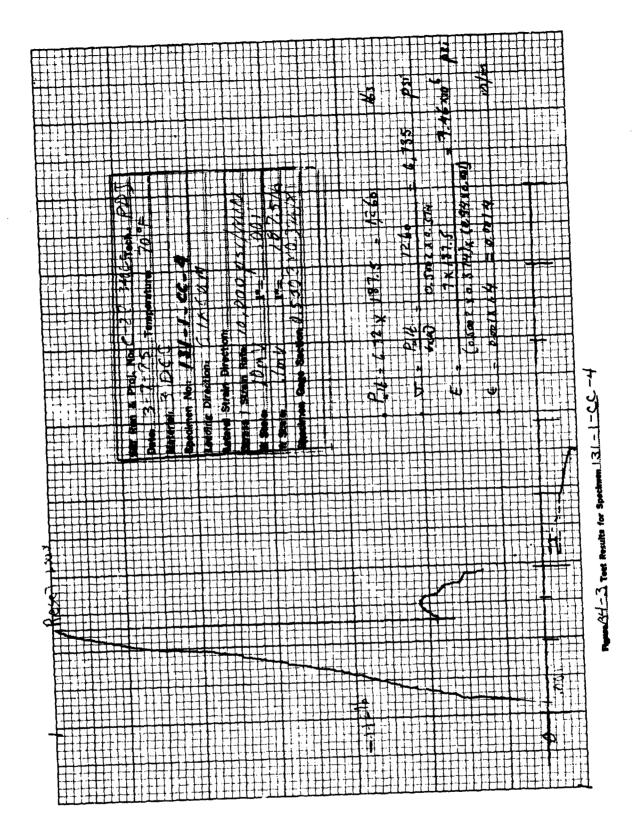


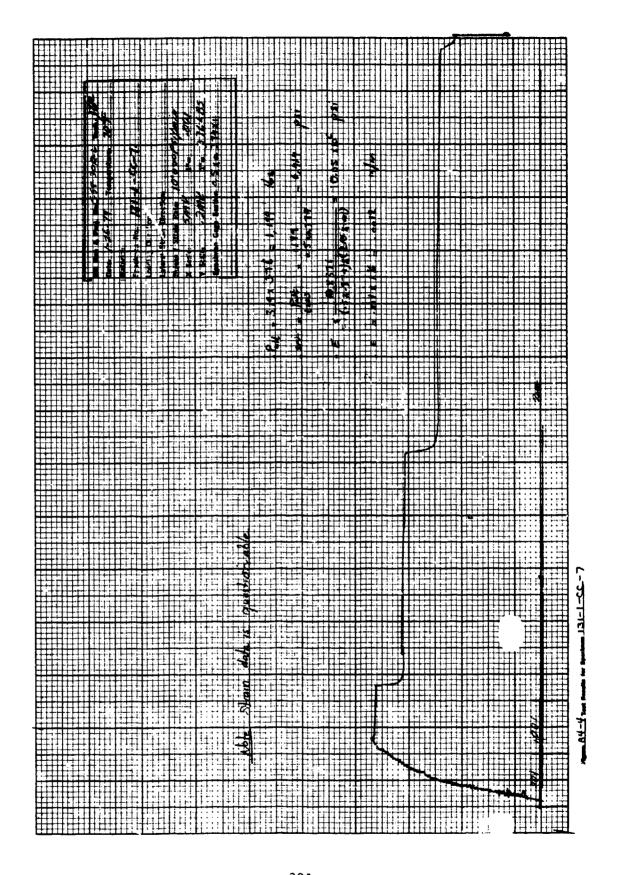
APPENDIX B4 Circumferential Compression Results

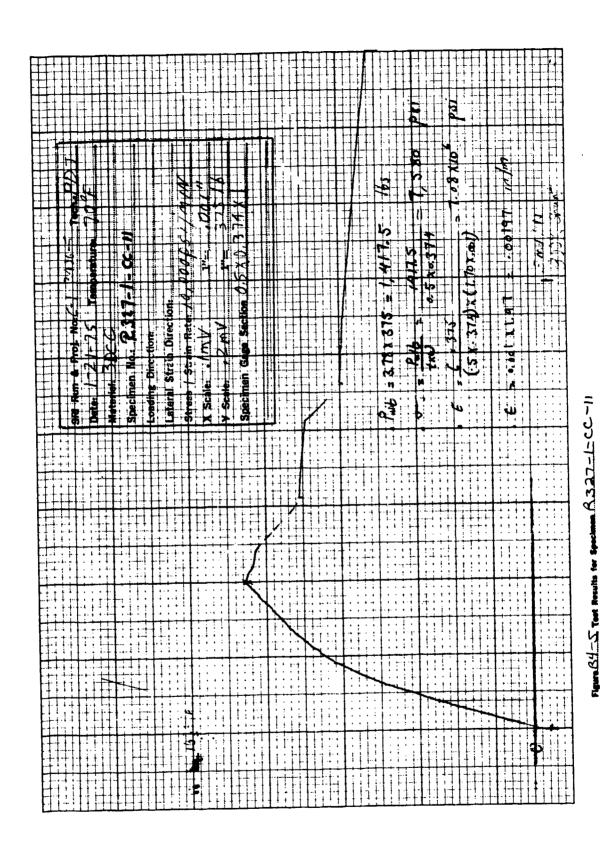


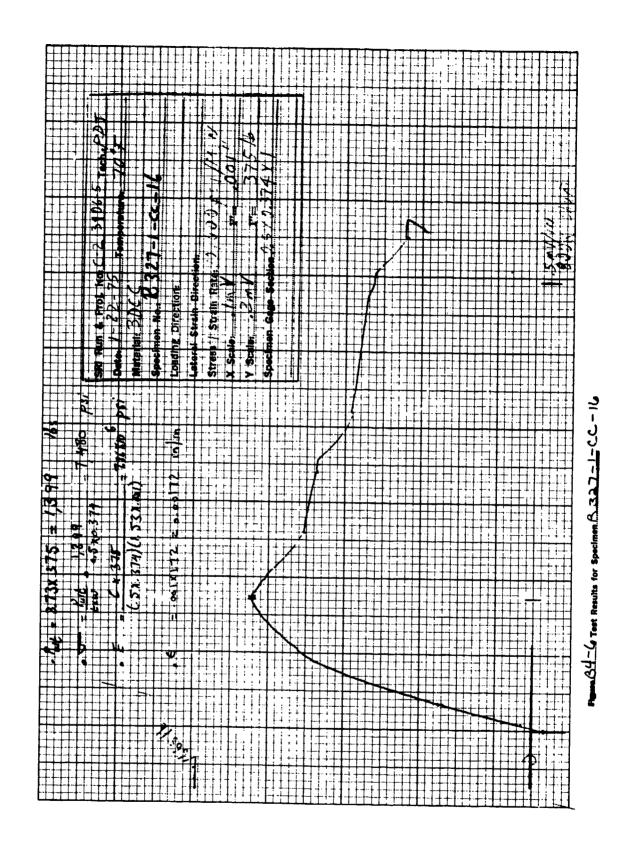
84-1. Test Results for Specimen 131-1-CC-1

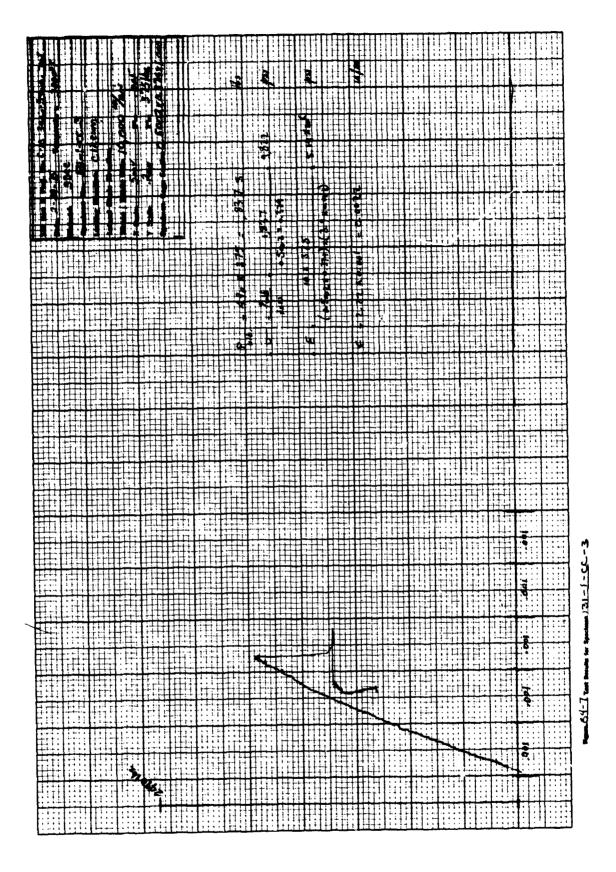


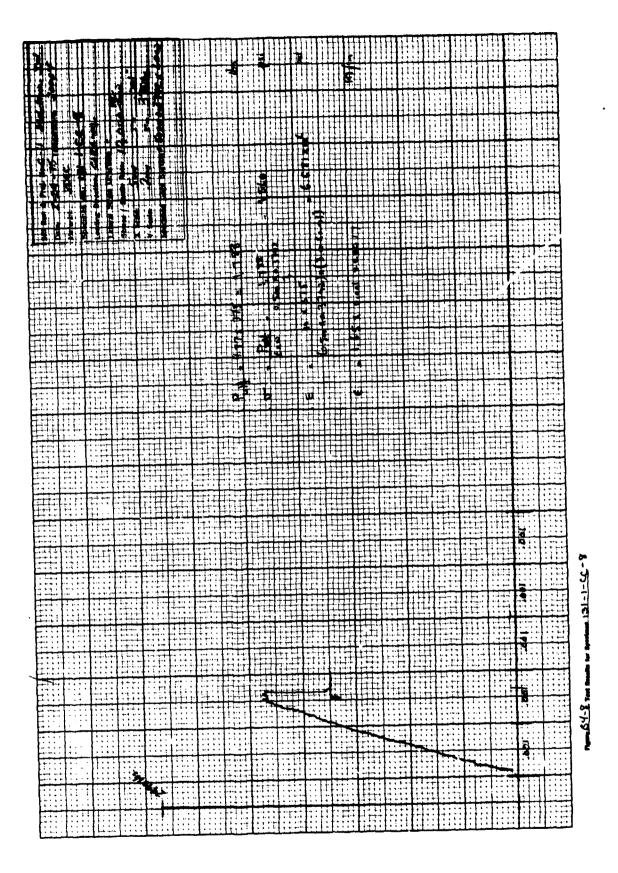












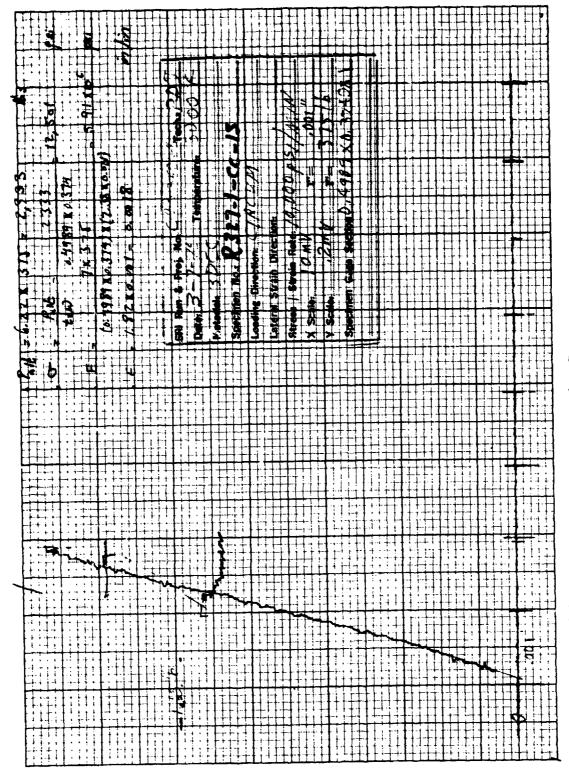
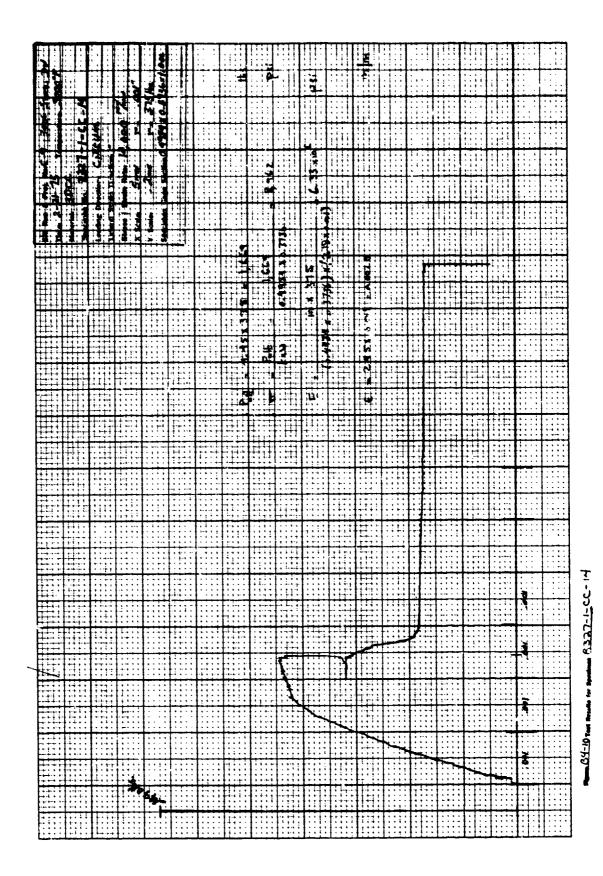
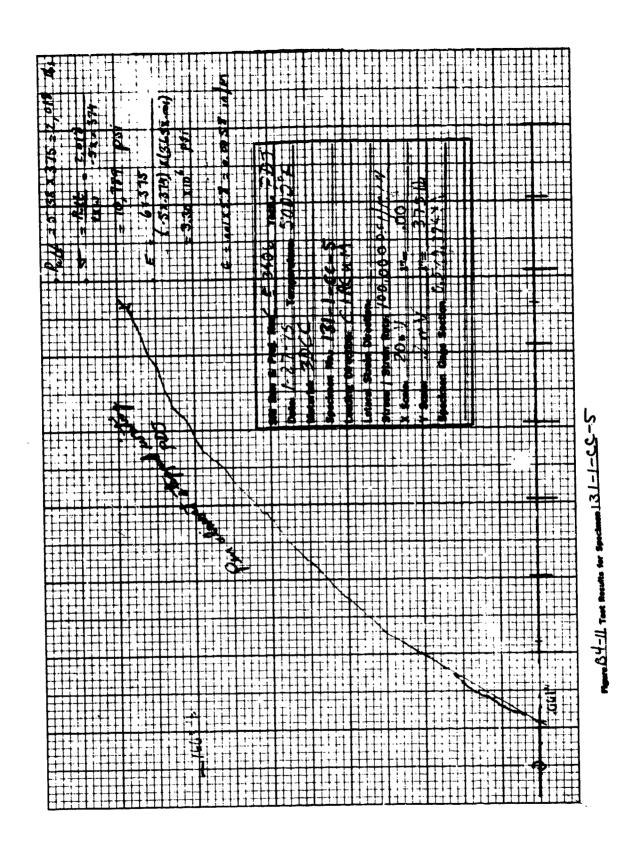


Figure 34-9 Test Recuts for Specimen B327-1- CC-13

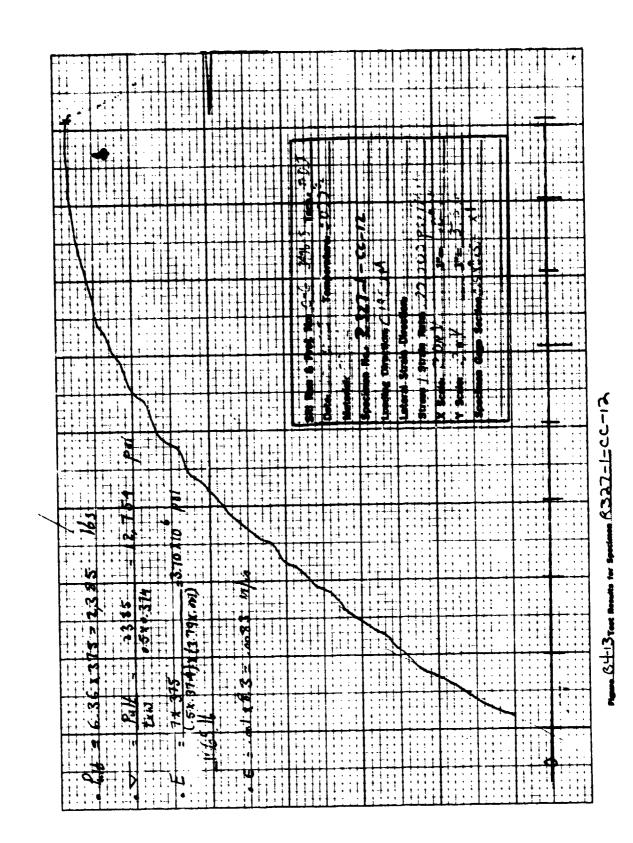


A THE

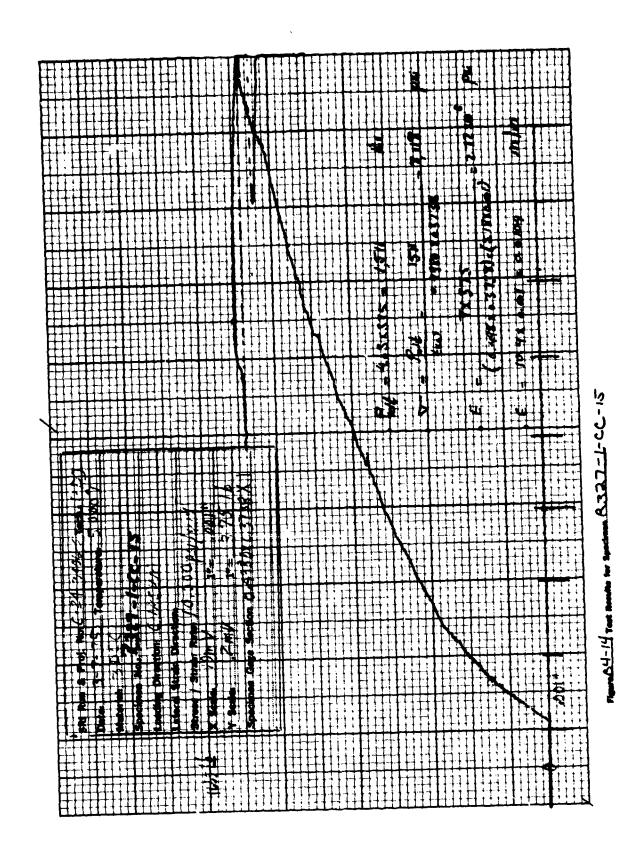
397

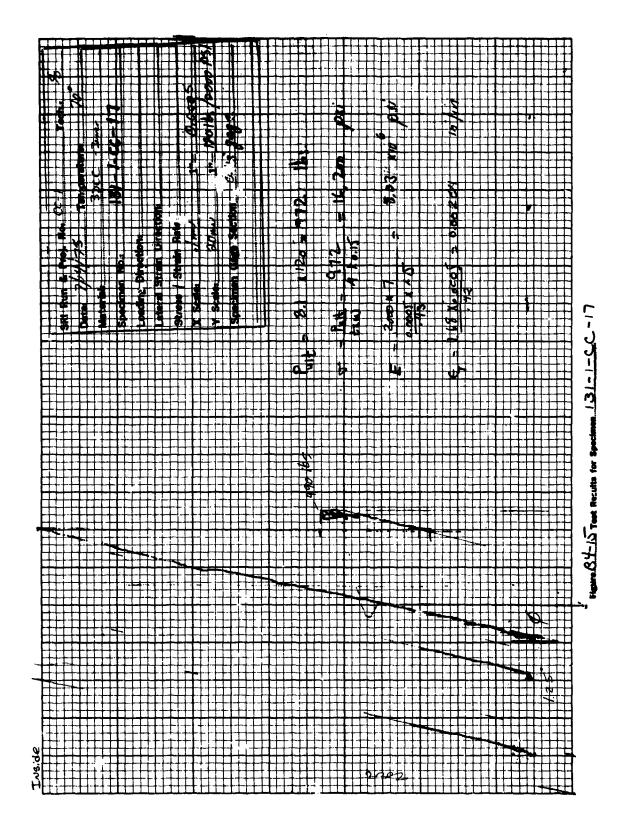


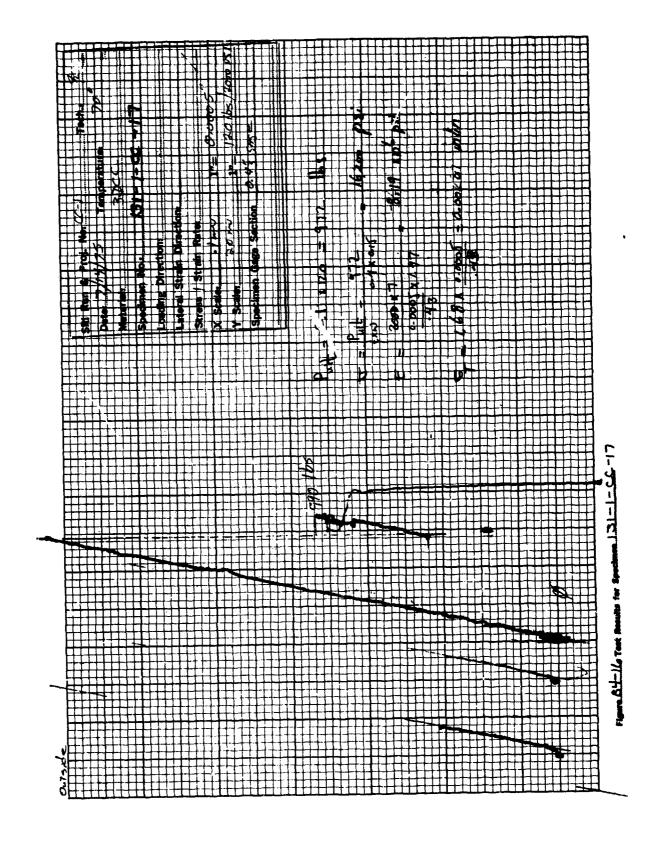
64-12 Toe names to Specimen 131-1-62 -9

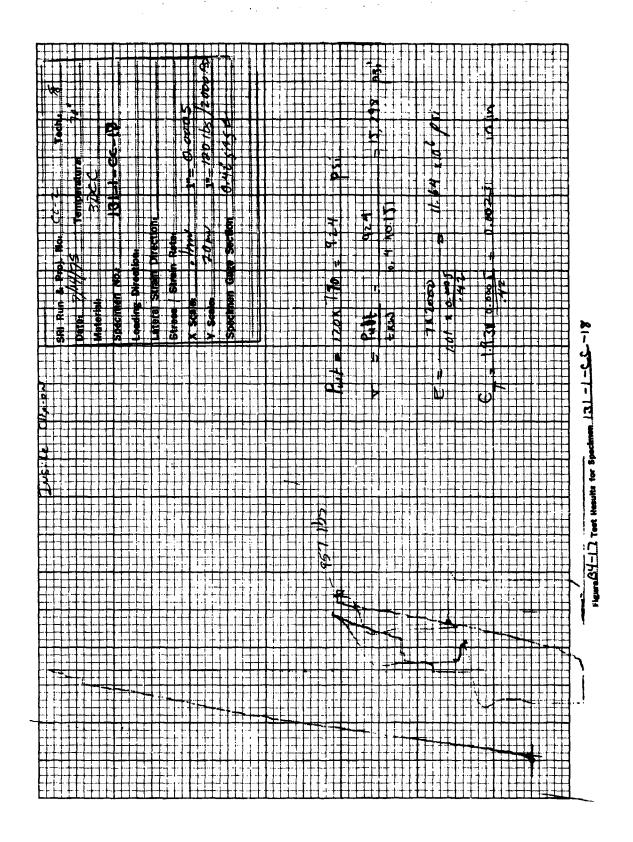


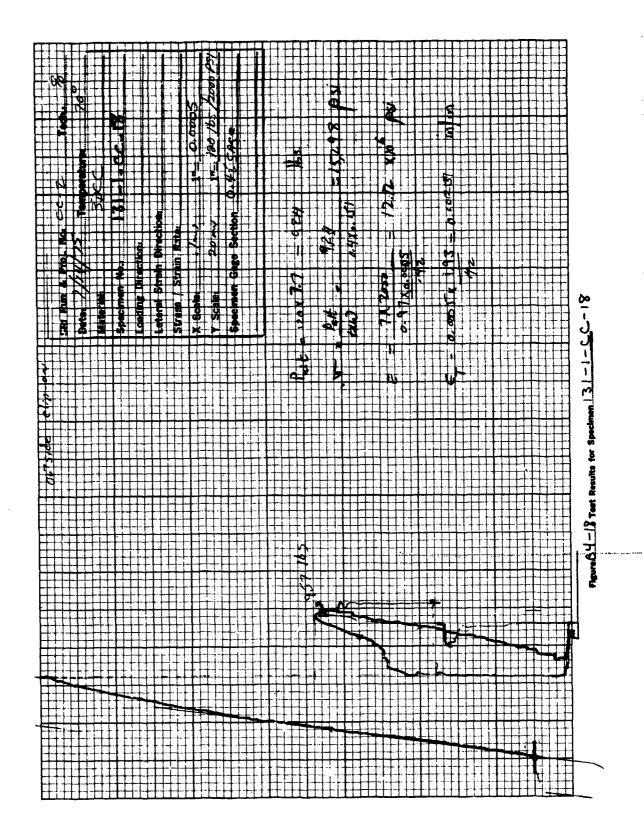
T. T.

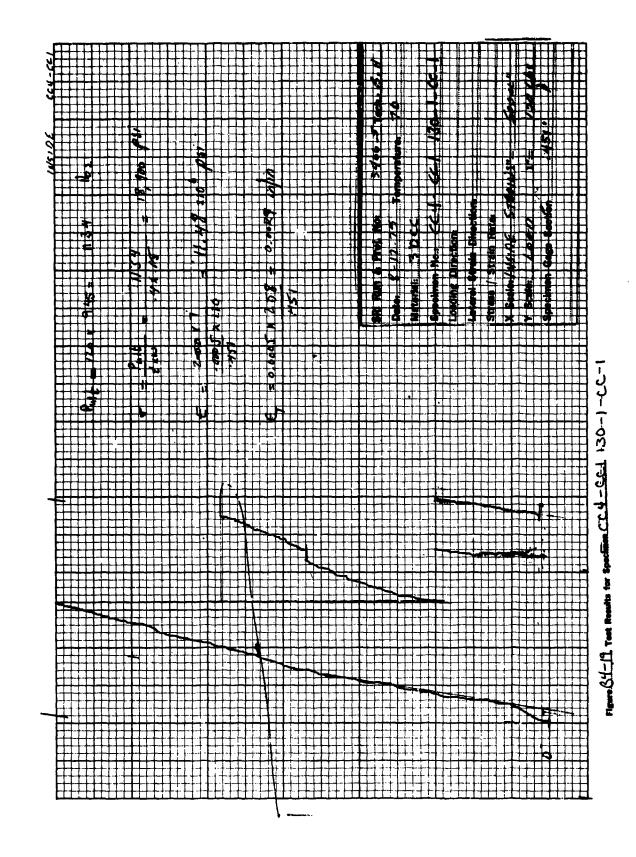


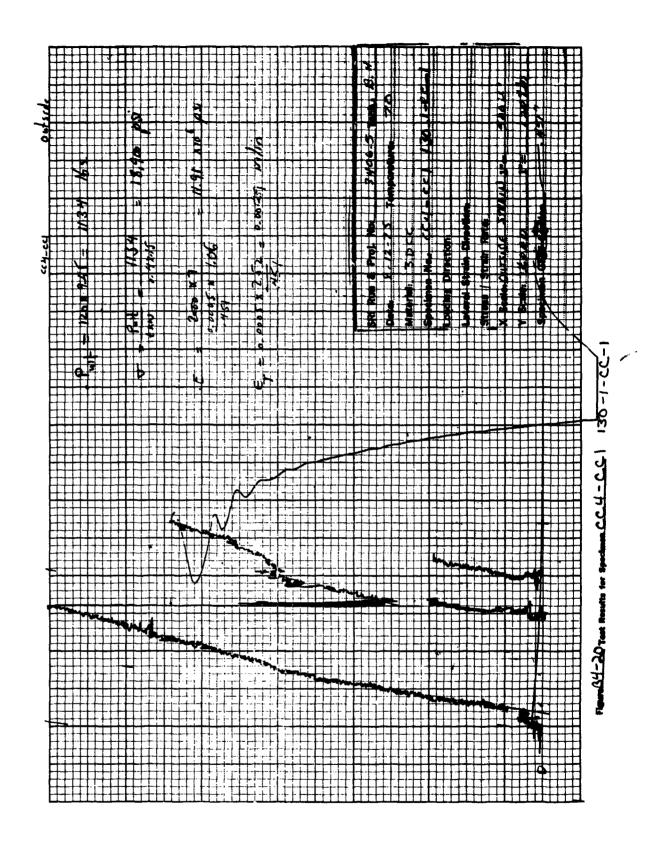




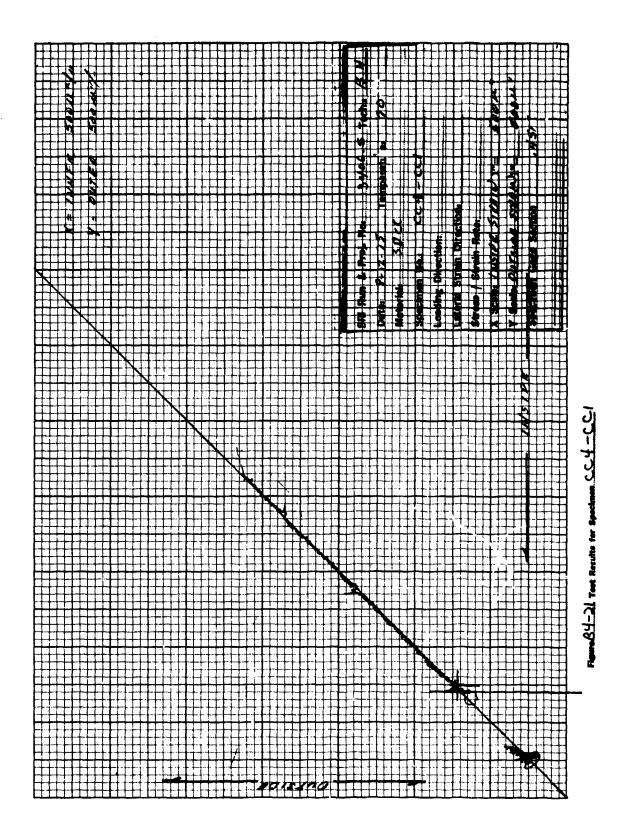


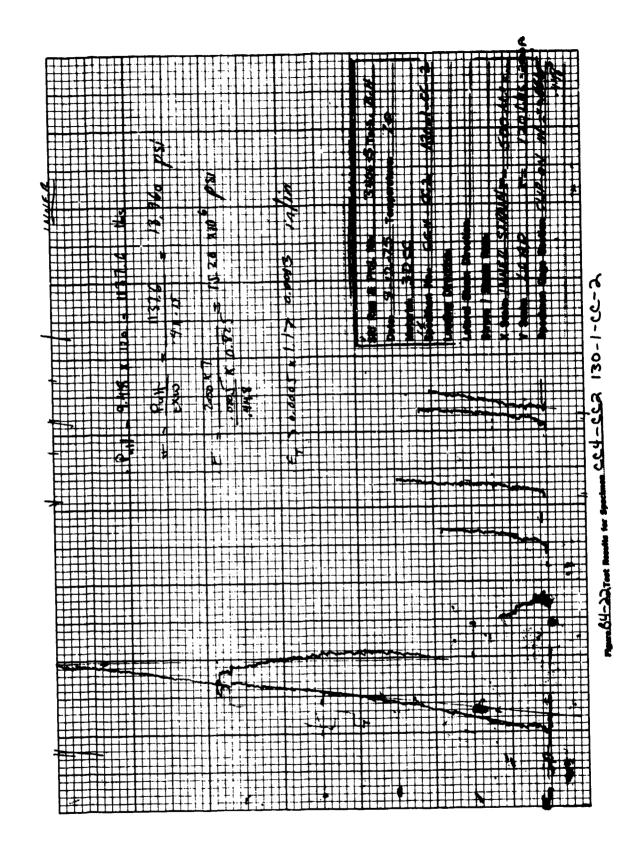


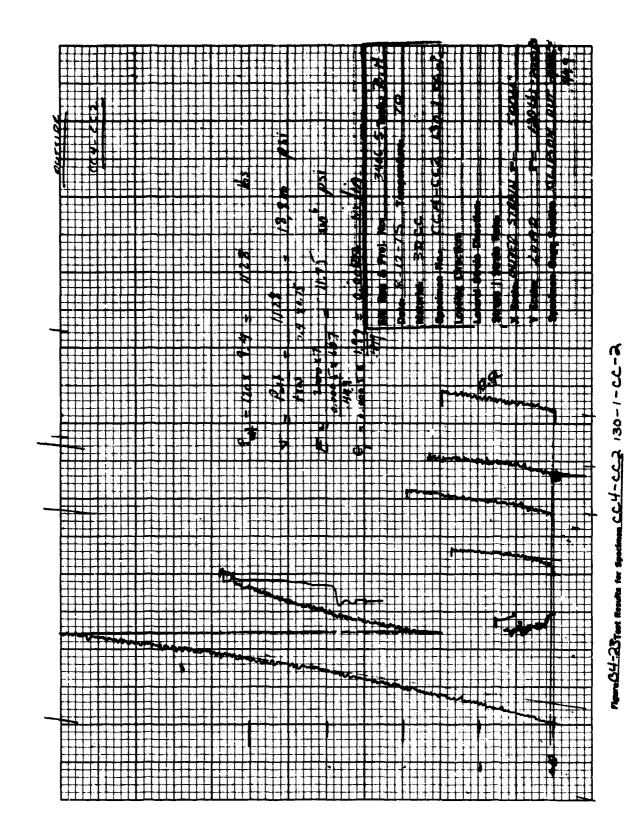




神子の動物の

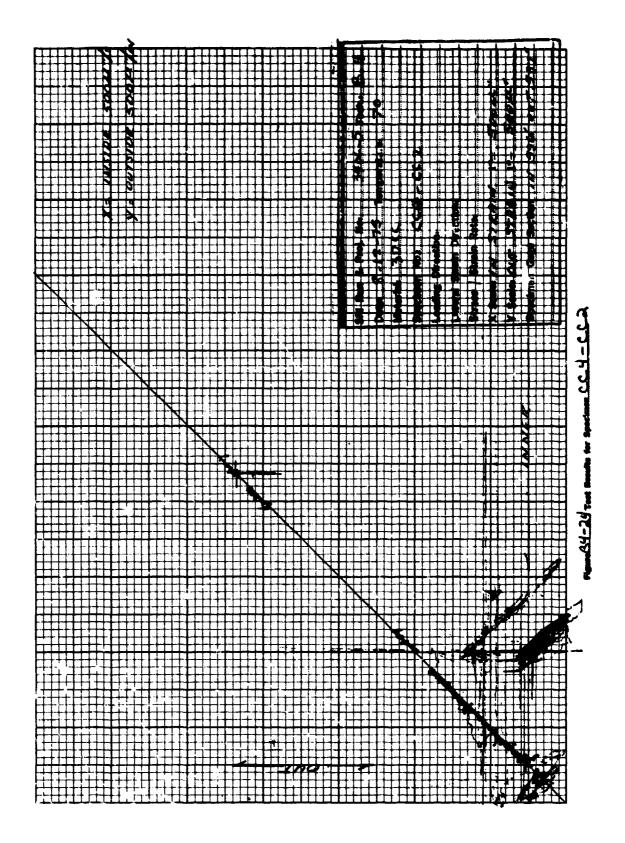






410

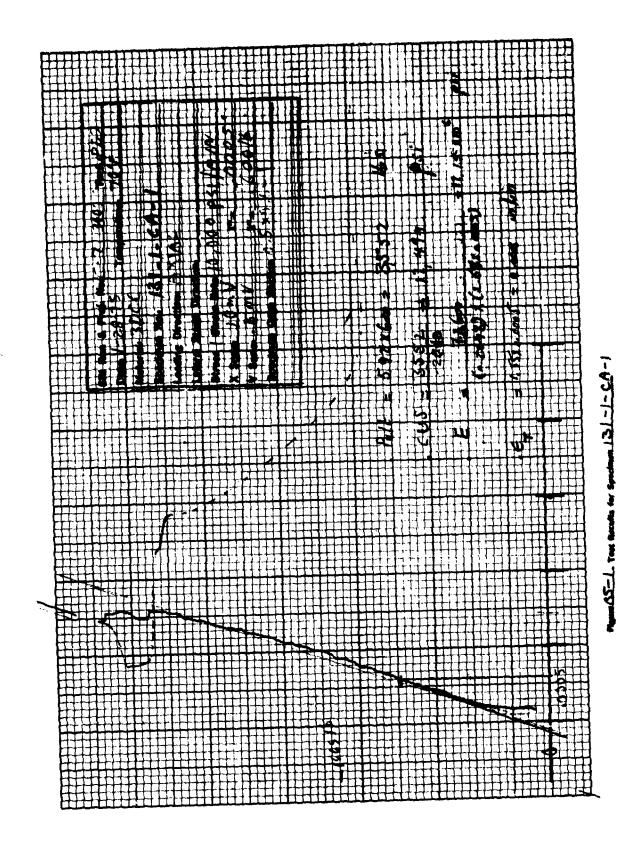
· 國門縣 於

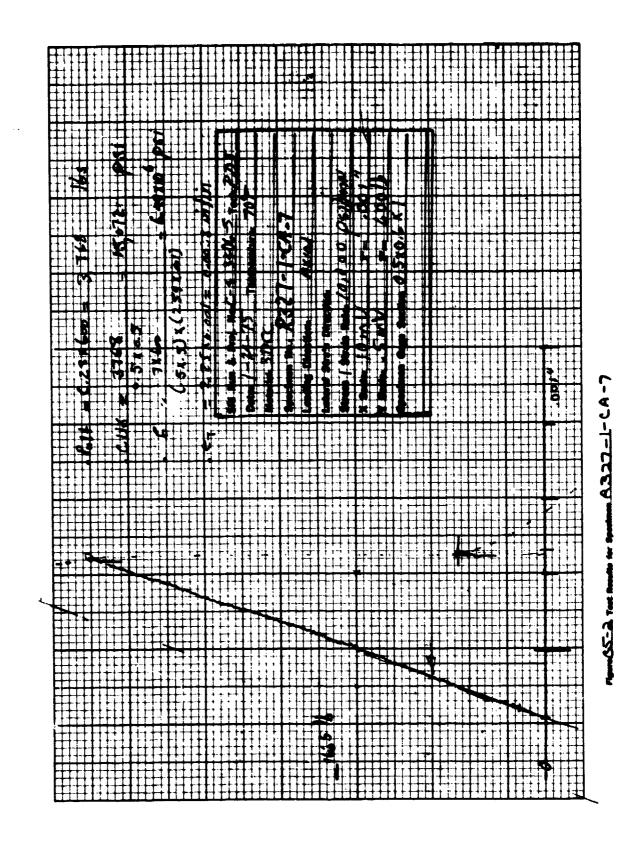


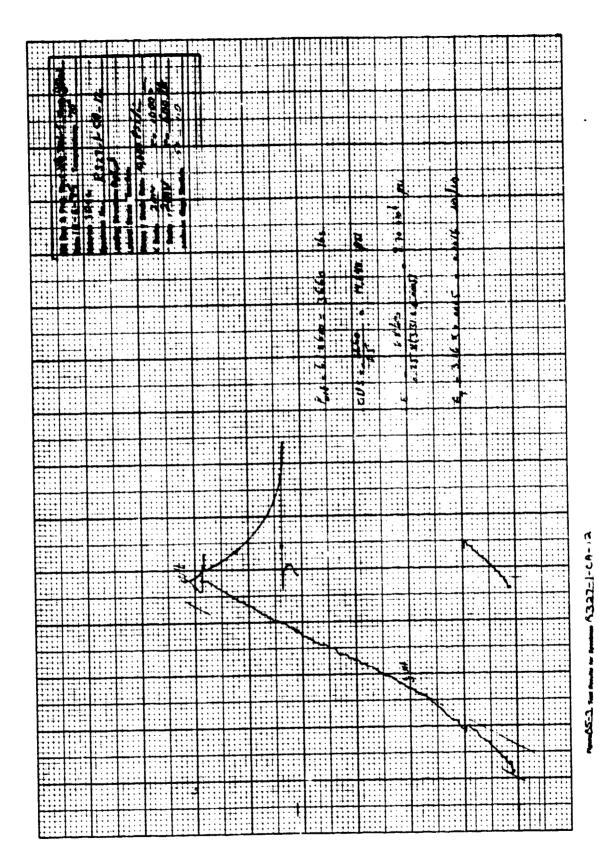
Preceding Page BLank - FILMED

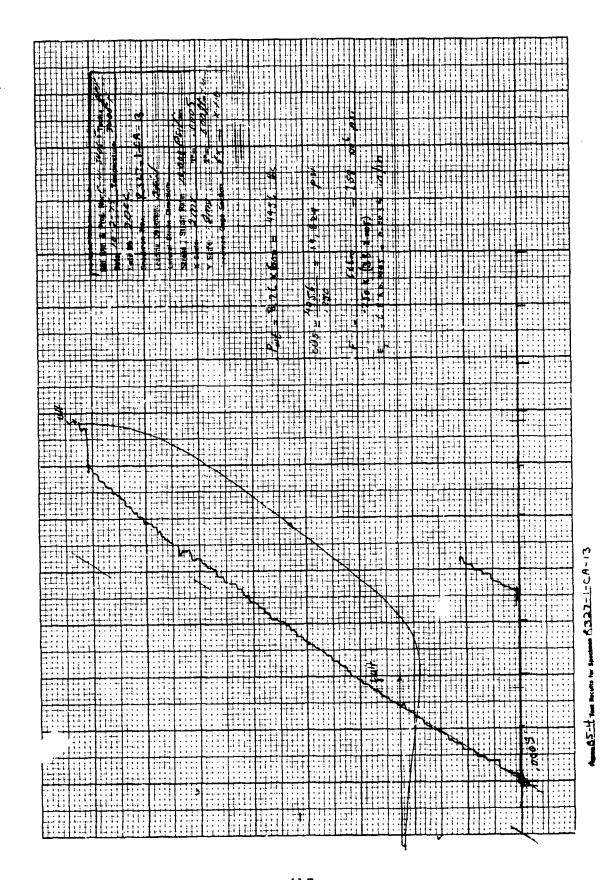
APPENDIX B5

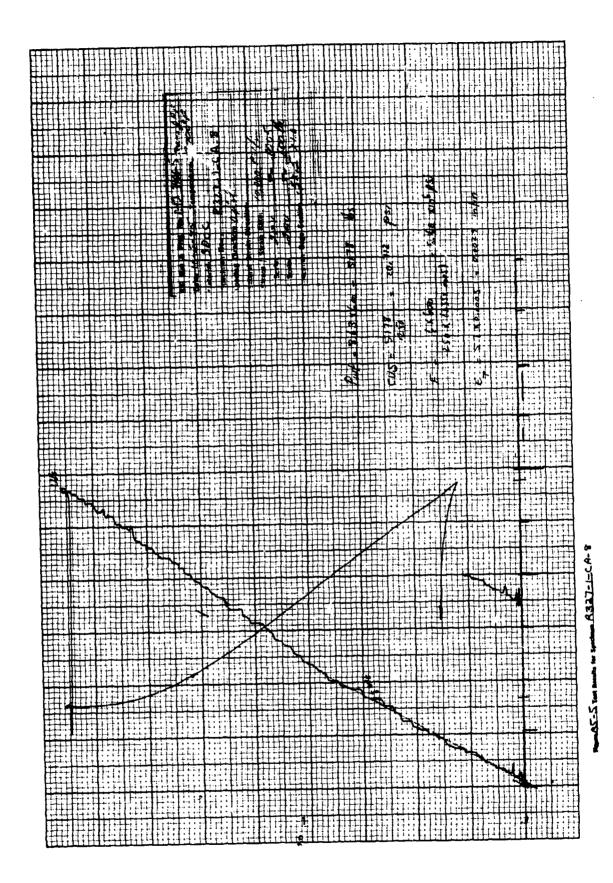
Axial Compression Results

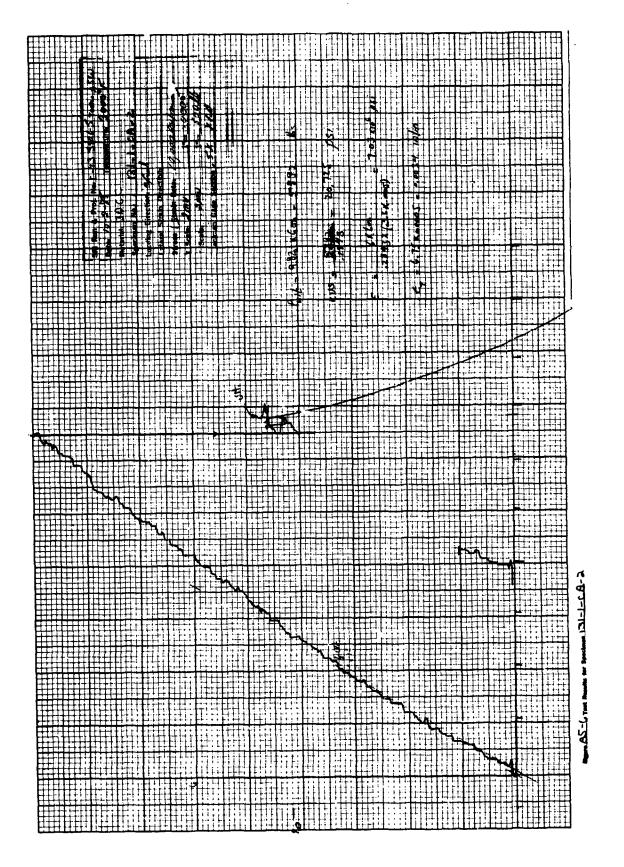


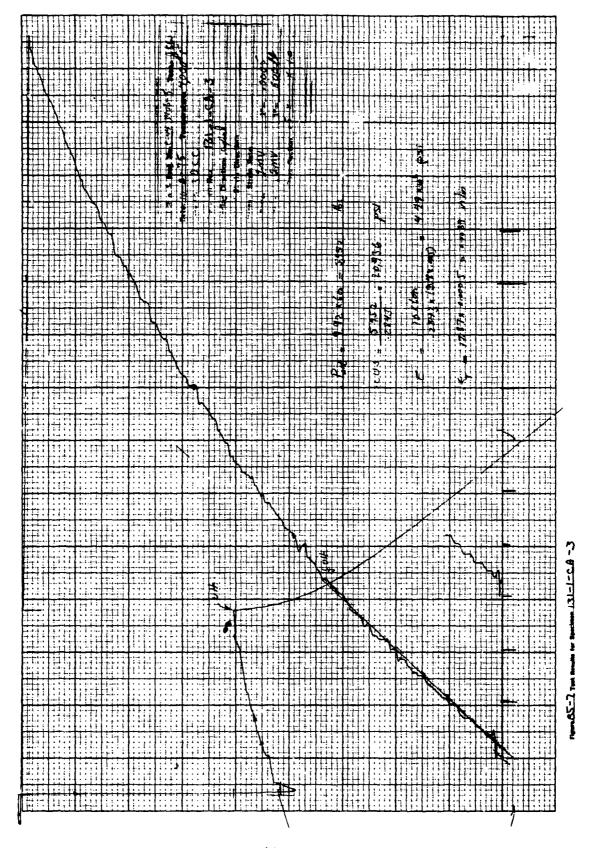


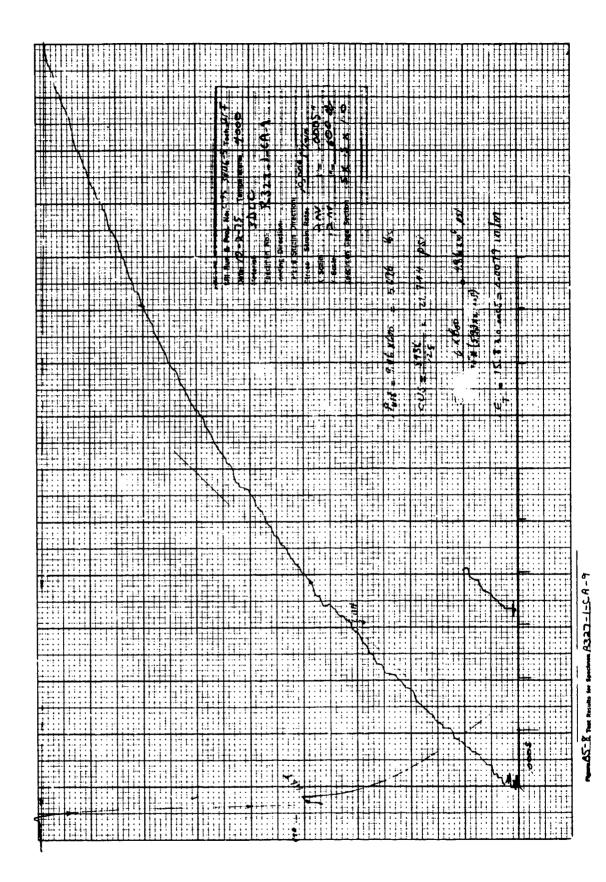


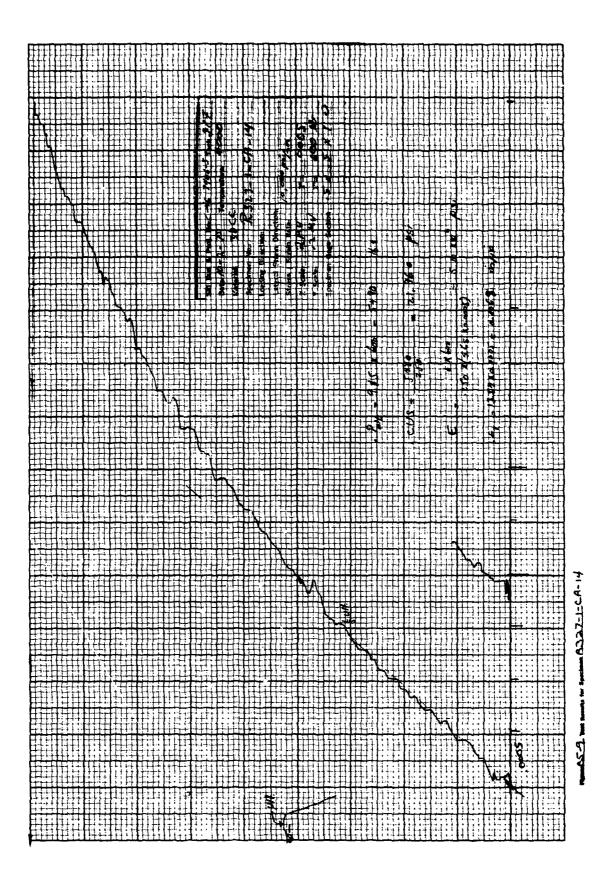


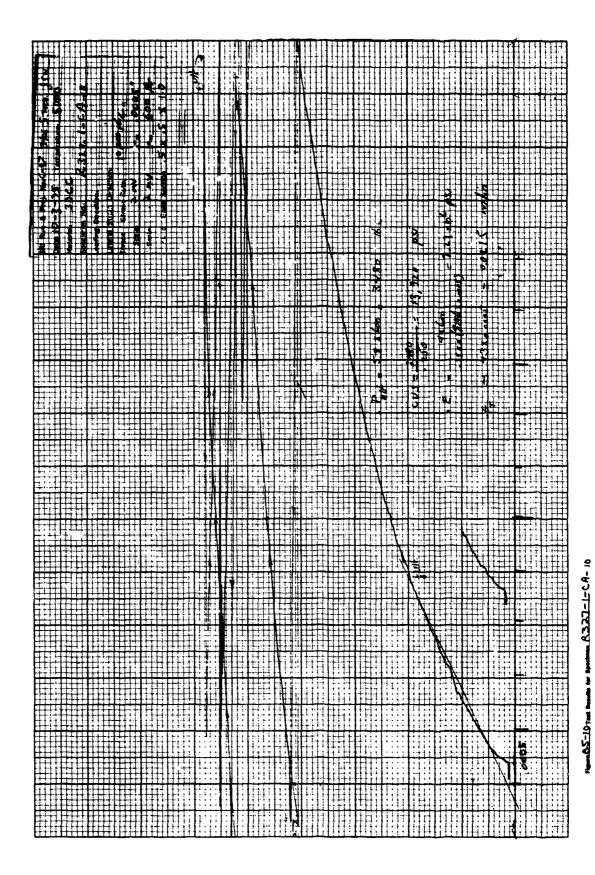








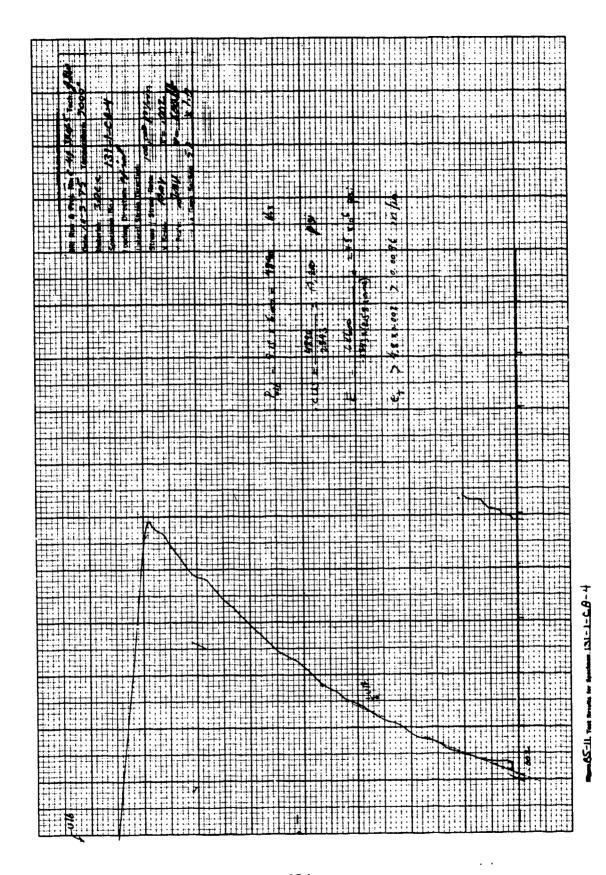


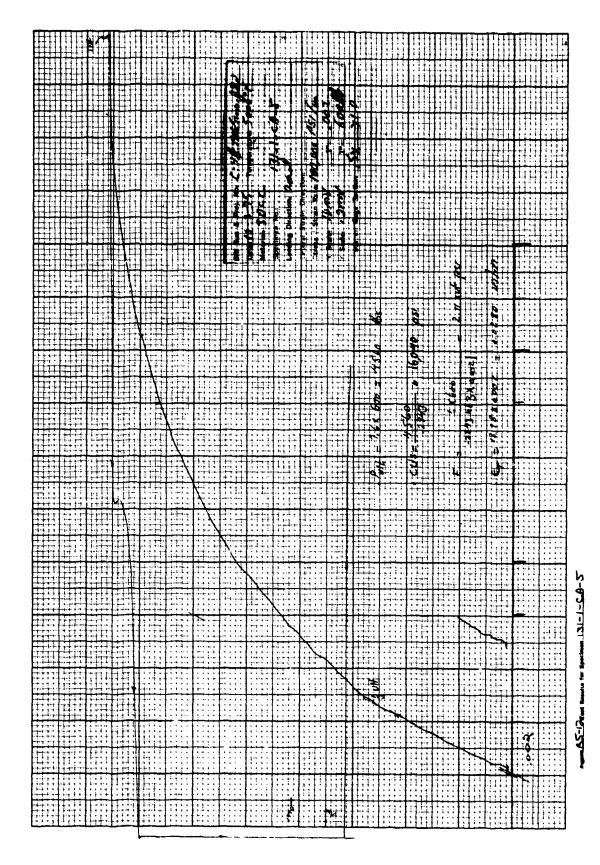


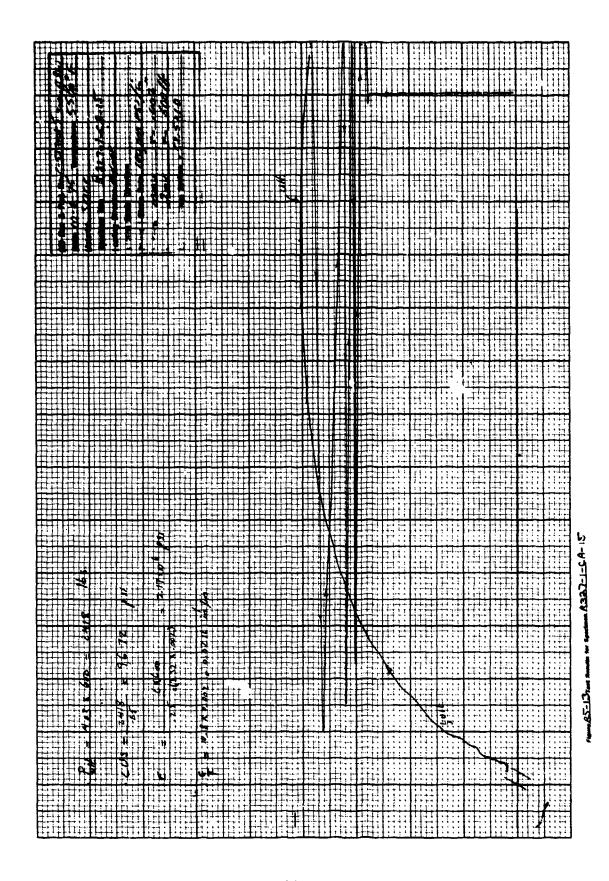
2.000 D. 1.000 D. 1.

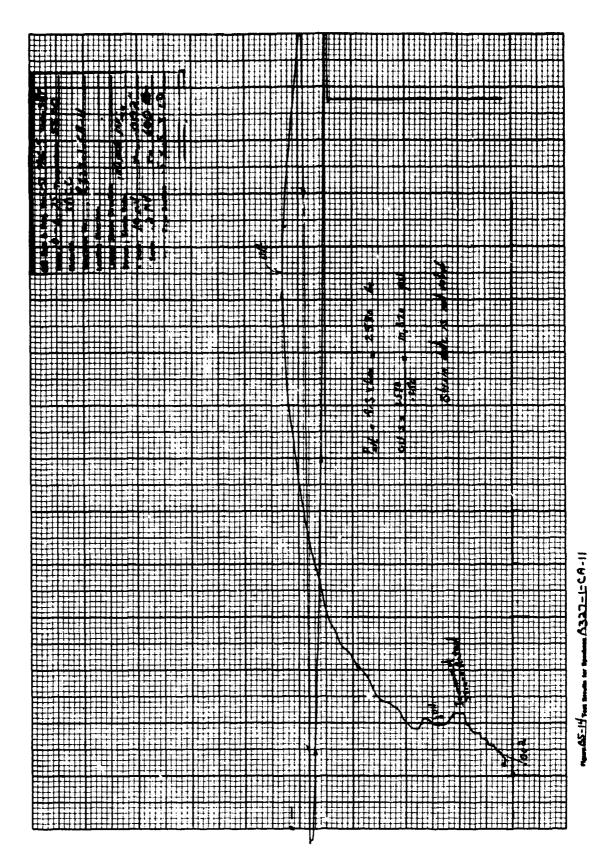
する は無だ器 のこ

423



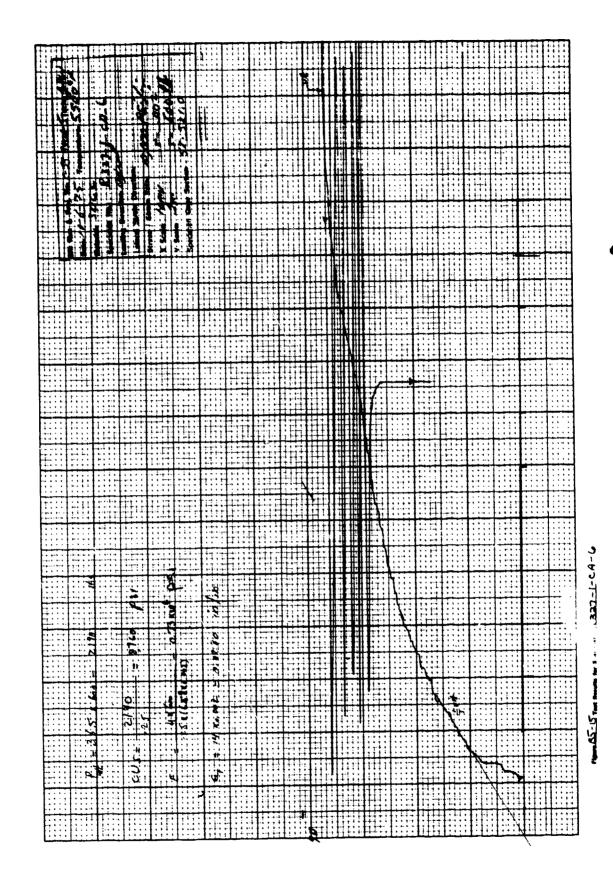




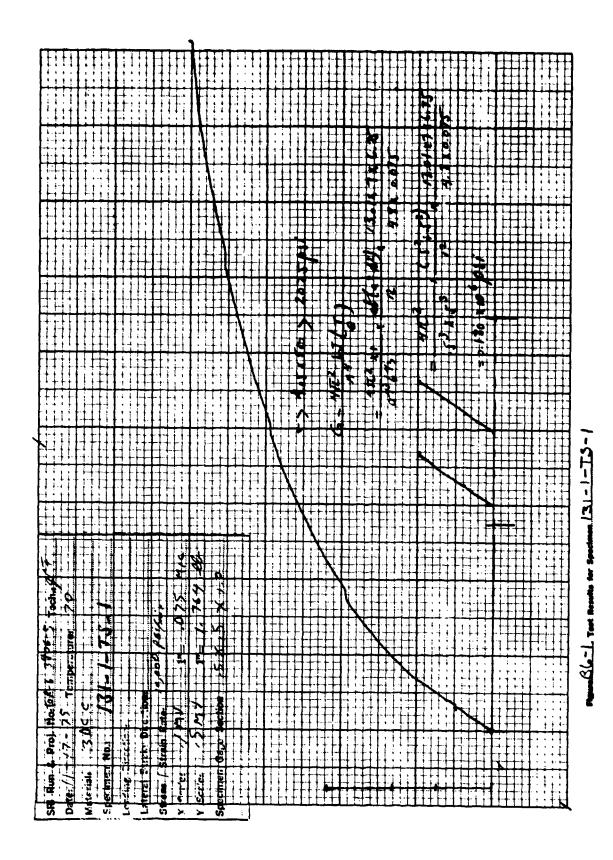


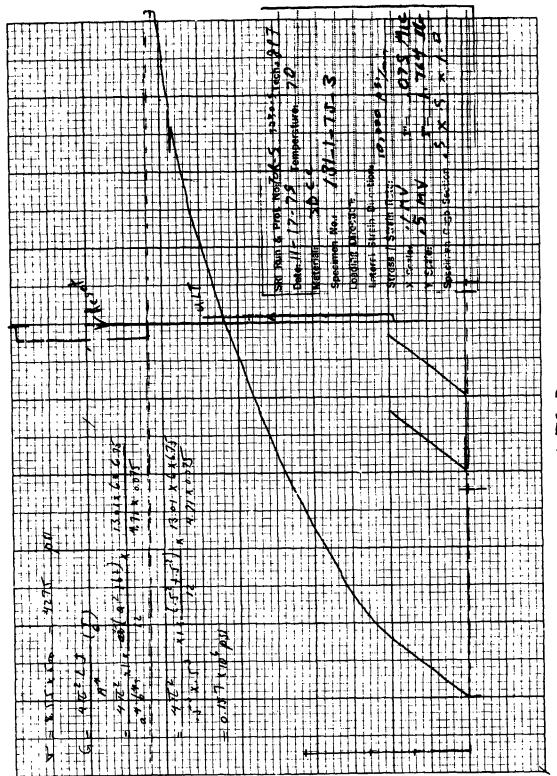
事で、編の書 むいい

427

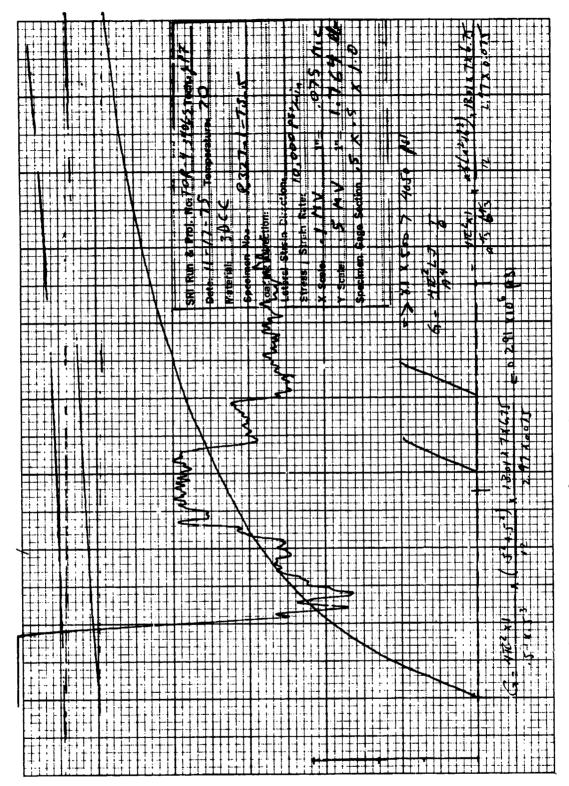


APPENDIX B6 Torsional Shear Results

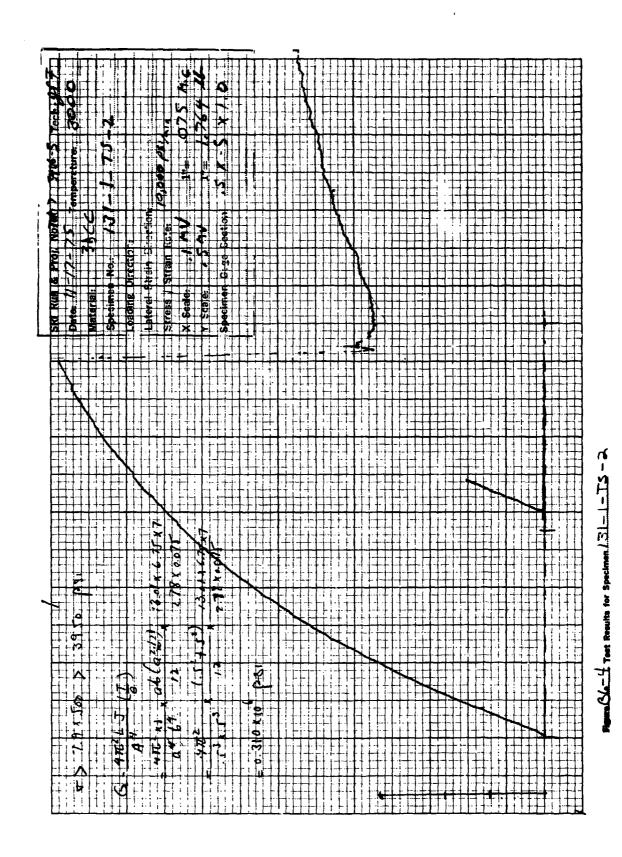




BL-2 Teat Results for Specimen 131-1-15-3

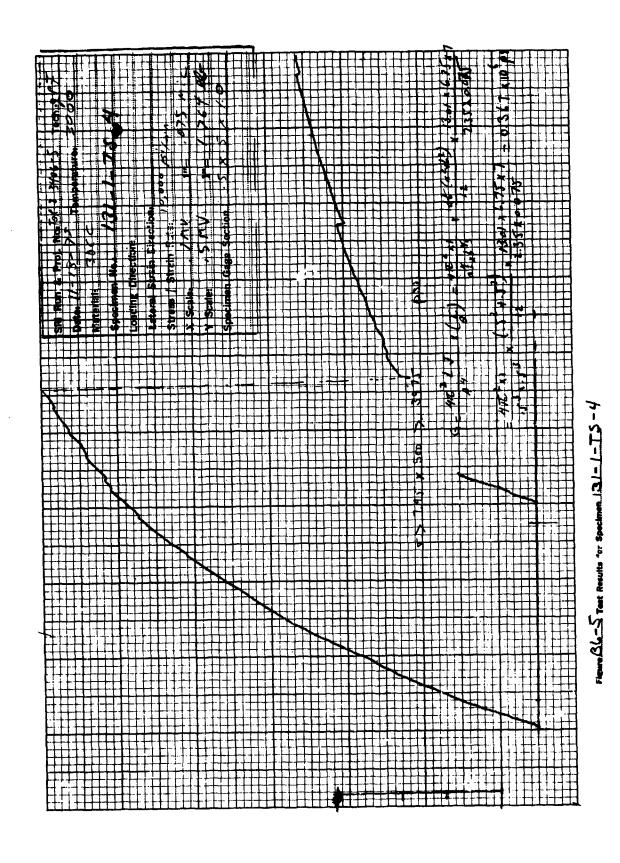


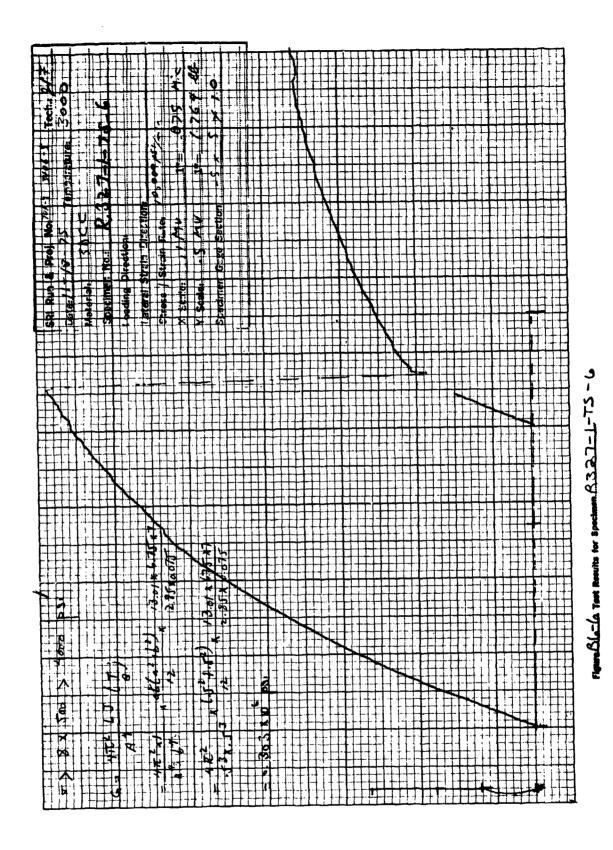
186-3 Test Results for Specimen R327-1-TS-5



孝子 温泉製 ないり

433

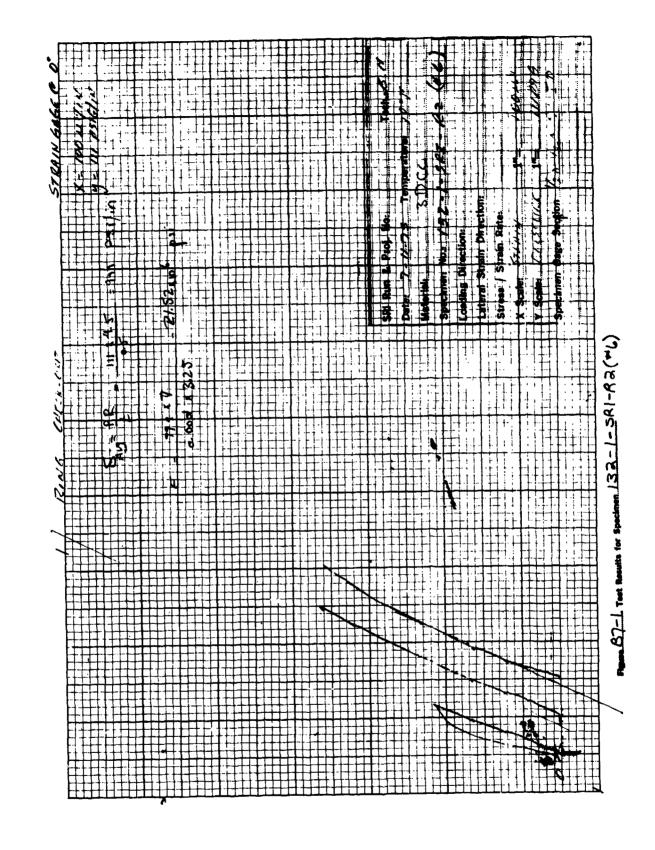


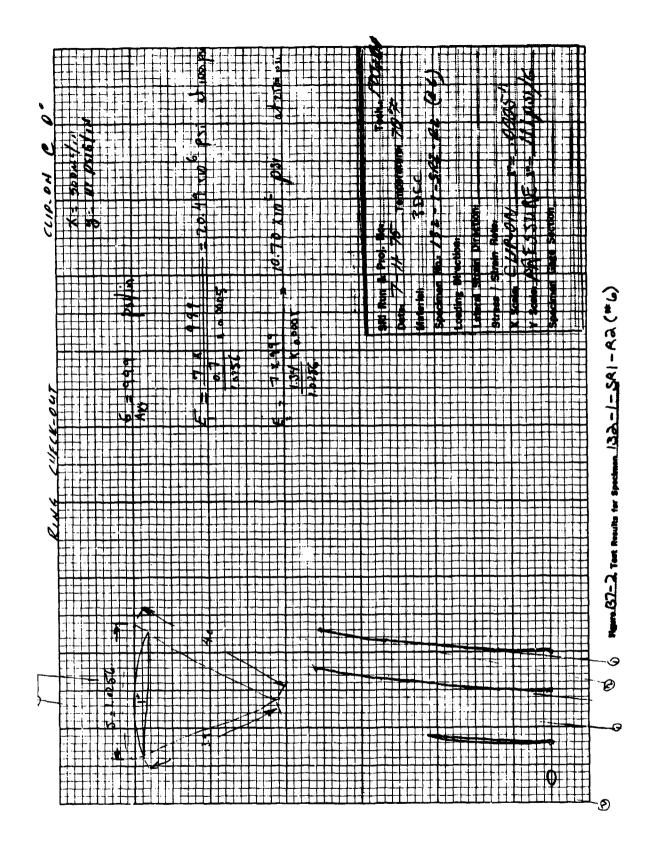


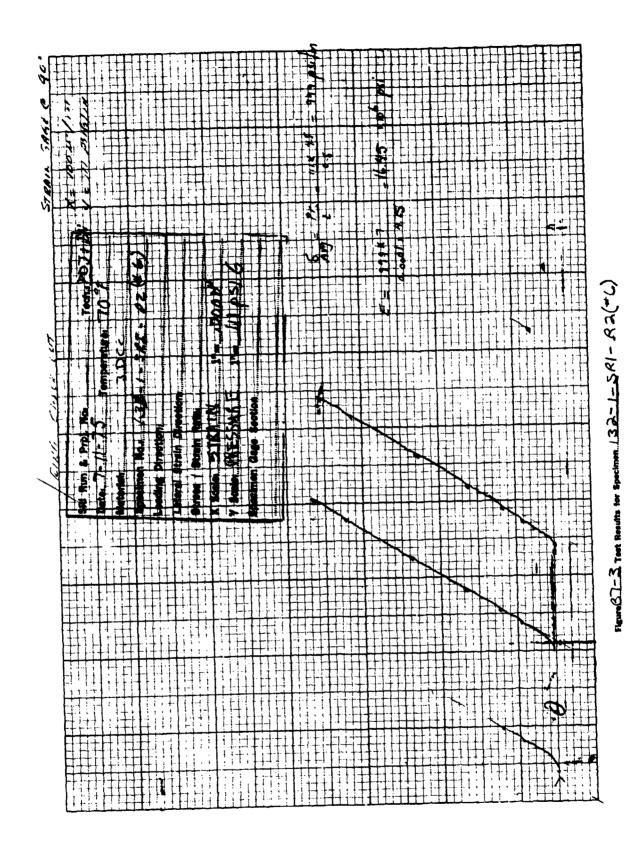
Preceding Page Blank - FILMEN

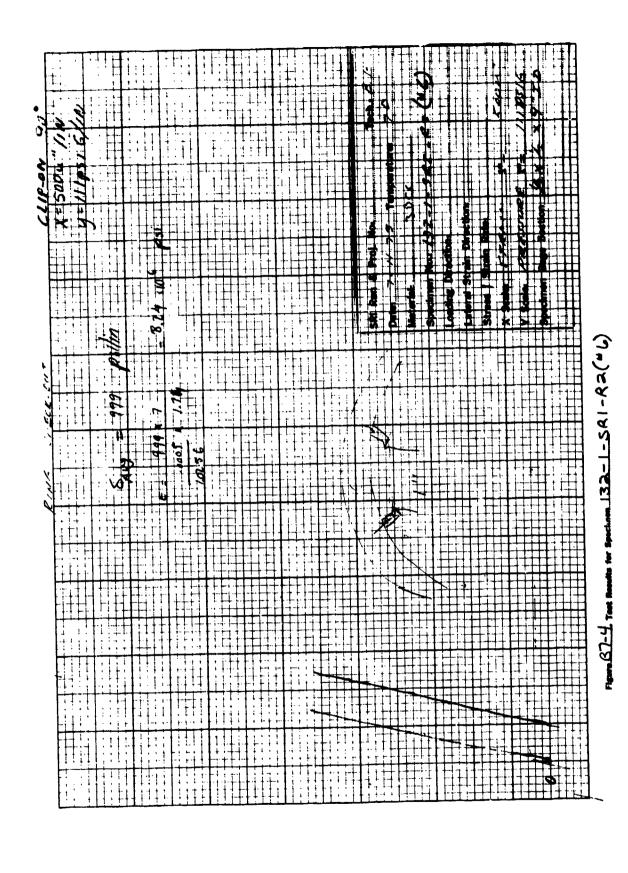
APPENDIX B7

Hydrostatic Compression Ring Results



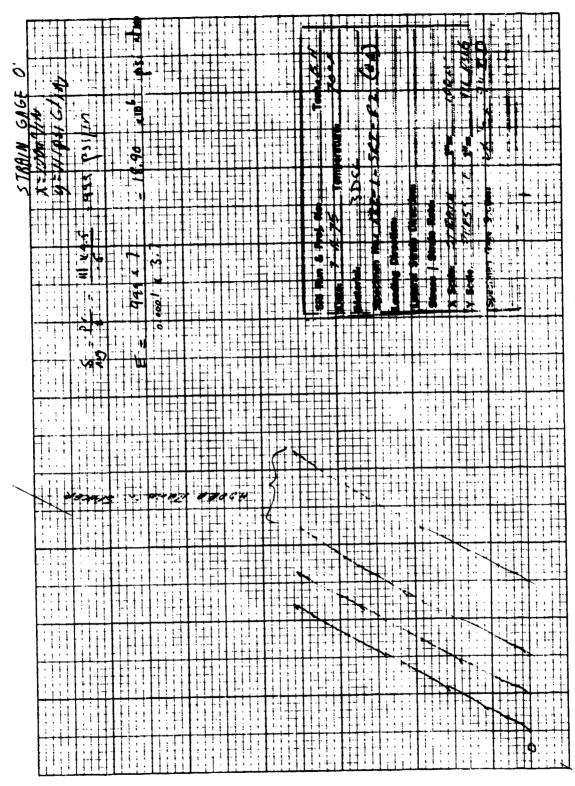






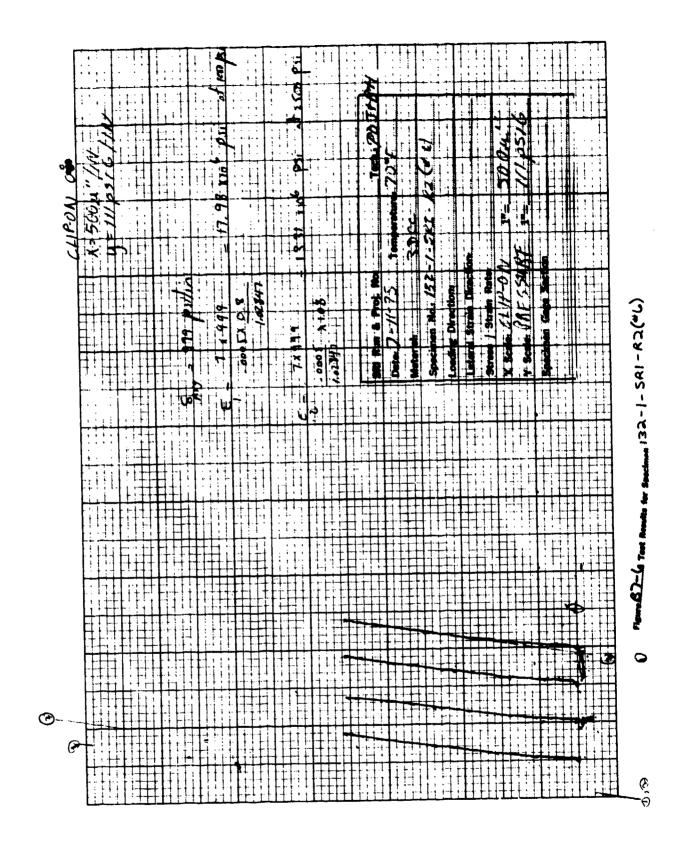
₹.

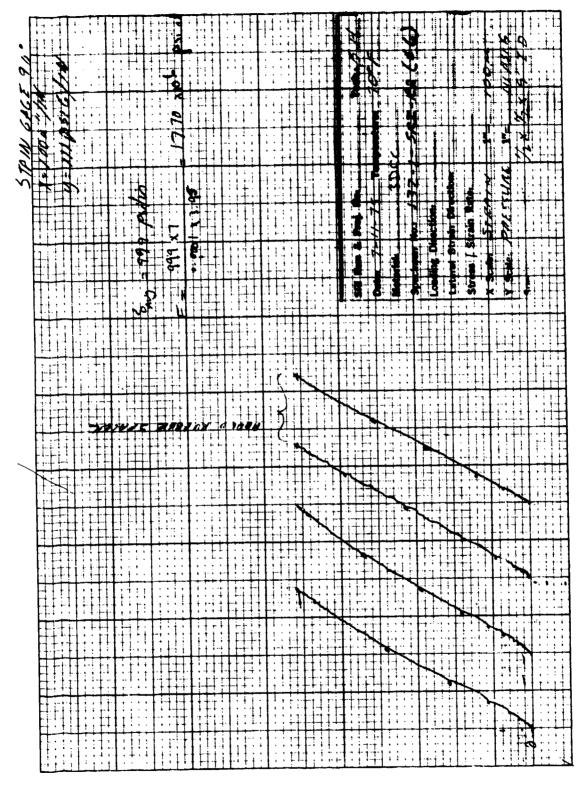
441



の記し

Figure 87-5 Teor Results for Specimen 133-1-5A1-A2 (# L)

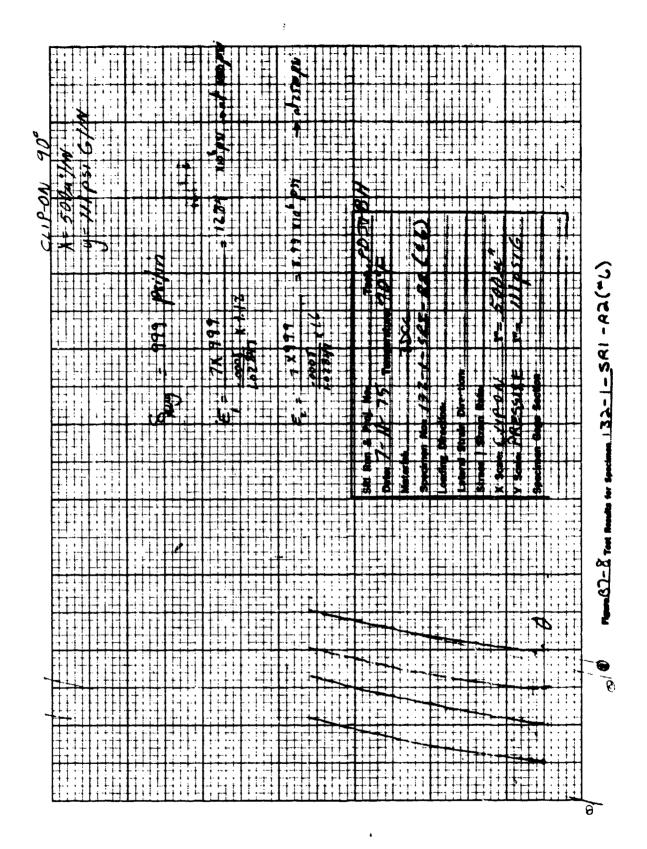


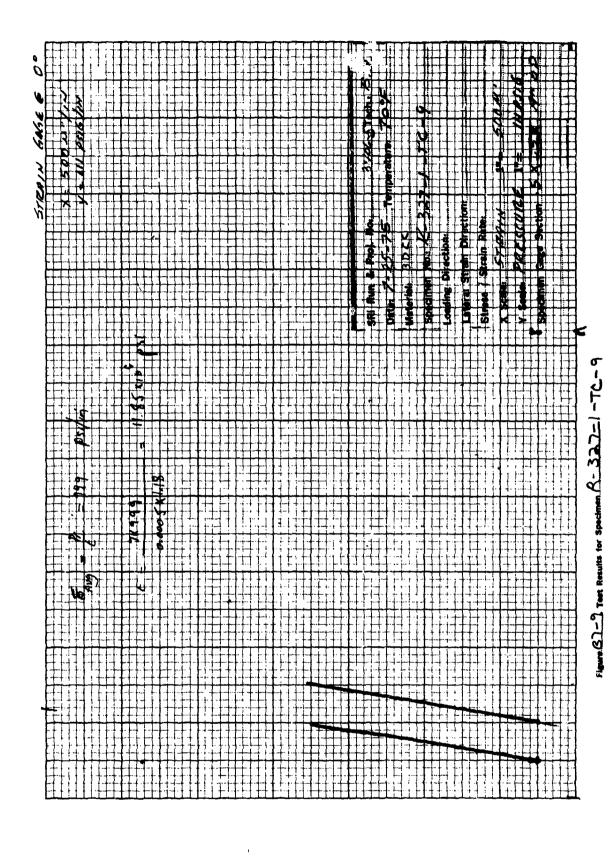


120

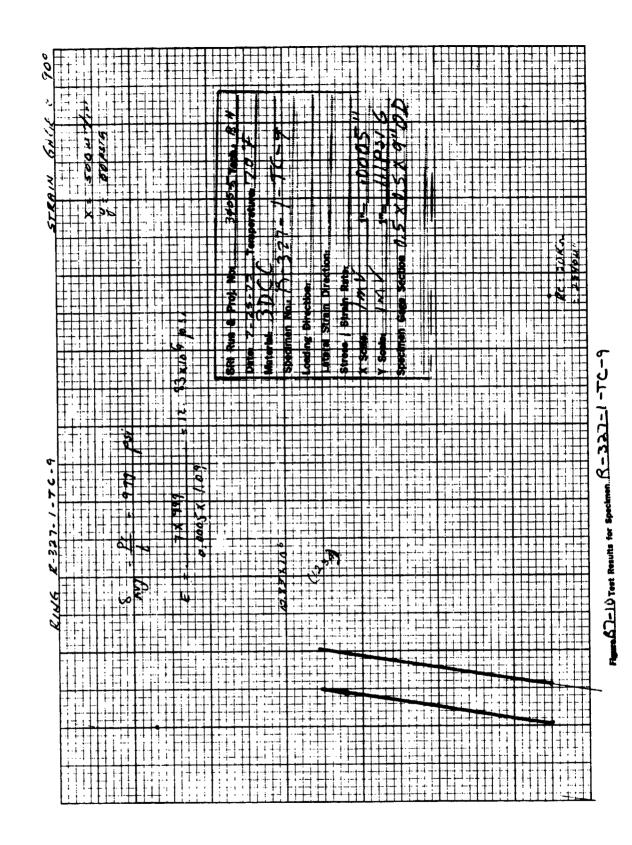
....

Towns 87-2 Took Results for Spectmen [32-1-581- A 3 (* 6)

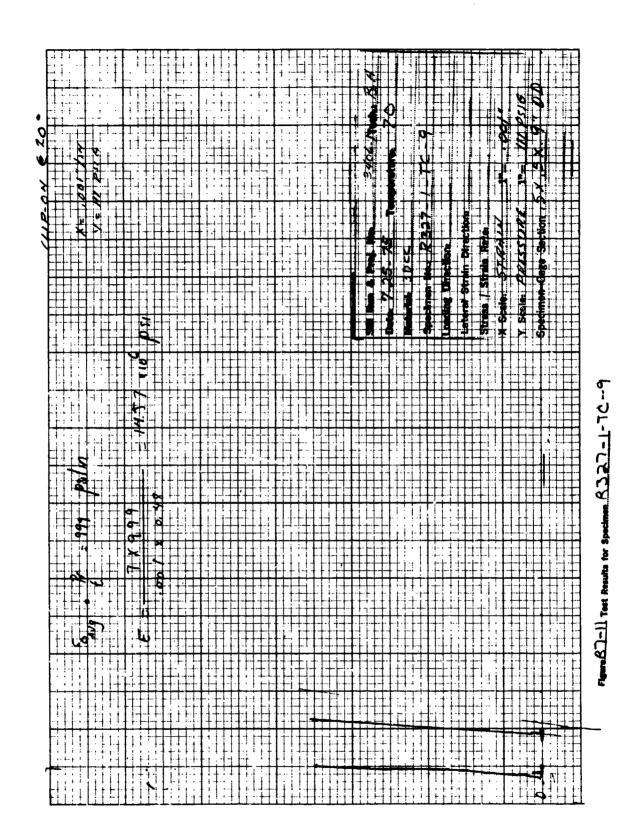


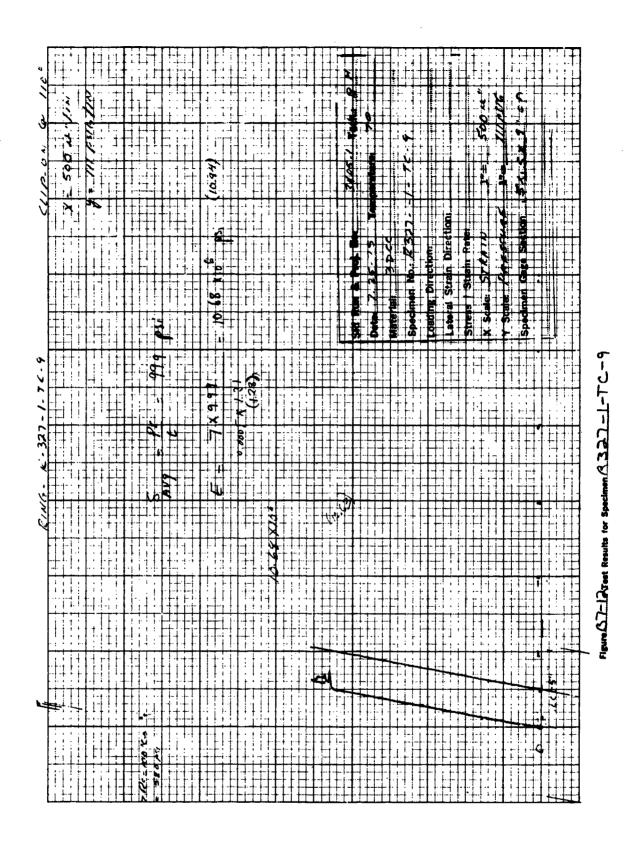


· 1985年 | 1985年 | 1985年 | 1985年 | 1985年 | 1985年 | 1985年 | 1985年 | 1985年 | 1985年 | 1985年 | 1985年 | 1985年 | 1985年 | 1985年 | 1985年 | 1985年 | 1985年 | 1985年 | 1985年 | 1985年 | 1985年 | 1985年 | 1985年 | 1985年 | 1985年 | 1985年 | 1985年 | 1985年 | 1985年 | 1985年 | 1985年 | 1985年 | 1985年 | 1985年 | 1985年 | 1985年 | 1985年 | 1985年 | 1985年 | 1985年 | 1985年 | 1985年 | 1985年 | 1985年 | 1985年 | 1985年 | 1985年 | 1985年 | 1985年 | 1985年 | 1985年 | 1985年 | 1985年 | 1985年 | 1985年 | 1985年 | 1985年 | 1985年 | 1985年 | 1985年 | 1985年 | 1985年 | 1985年 | 1985年 | 1985年 | 1985年 | 1985年 | 1985年 | 1985年 | 1985年 | 1985年 | 1985年 | 1985年 | 1985年 | 1985年 | 1985年 | 1985年 | 1985年 | 1985年 | 1985年 | 1985年 | 1985年 | 1985年 | 1985年 | 1985年 | 1985年 | 1985年 | 1985年 | 1985年 | 1985年 | 1985年 | 1985年 | 1985年 | 1985年 | 1985年 | 1985年 | 1985年 | 1985年 | 1985年 | 1985年 | 1985年 | 1985年 | 1985年 | 1985年 | 1985年 | 1985年 | 1985年 | 1985年 | 1985年 | 1985年 | 1985年 | 1985年 | 1985年 | 1985年 | 1985年 | 1985年 | 1985年 | 1985年 | 1985年 | 1985年 | 1985年 | 1985年 | 1985年 | 1985年 | 1985年 | 1985年 | 1985年 | 1985年 | 1985年 | 1985年 | 1985年 | 1985年 | 1985年 | 1985年 | 1985年 | 1985年 | 1985年 | 1985年 | 1985年 | 1985年 | 1985年 | 1985年 | 1985年 | 1985年 | 1985年 | 1985年 | 1985年 | 1985年 | 1985年 | 1985年 | 1985年 | 1985年 | 1985年 | 1985年 | 1985年 | 1985年 | 1985年 | 1985年 | 1985年 | 1985年 | 1985年 | 1985年 | 1985年 | 1985年 | 1985年 | 1985年 | 1985年 | 1985年 | 1985年 | 1985年 | 1985年 | 1985年 | 1985年 | 1985年 | 1985年 | 1985年 | 1985年 | 1985年 | 1985年 | 1985年 | 1985年 | 1985年 | 1985年 | 1985年 | 1985年 | 1985年 | 1985年 | 1985年 | 1985年 | 1985年 | 1985年 | 1985年 | 1985年 | 1985年 | 1985年 | 1985年 | 1985年 | 1985年 | 1985年 | 1985年 | 1985年 | 1985年 | 1985年 | 1985年 | 1985年 | 1985年 | 1985年 | 1985年 | 1985年 | 1985年 | 1985年 | 1985年 | 1985年 | 1985年 | 1985年 | 1985年 | 1985年 | 1985年 | 1985年 | 1985年 | 1985年 | 1985年 | 1985年 | 1985年 | 1985年 | 1985年 | 1985年 | 1985年 | 1985年 | 1985年 | 1985年 | 1985年 | 1985年 | 1985年 | 1985年 | 1985年 | 1985年 | 1985年 | 1985年 | 1985年 | 1985年 | 1985年 | 1985年 | 1985年 | 1985年 | 1985年 | 1985年 | 1985年 | 1985年 | 1985年 | 1985年 | 1985年 | 1985年 | 1985年 | 198



する温泉で





2. 1995年 1995年 1995年 1995年 - 1995年 1995年 1995年 1995年 1995年 1995年 1995年 1995年 1995年 1995年 1995年 1995年 1995年 199

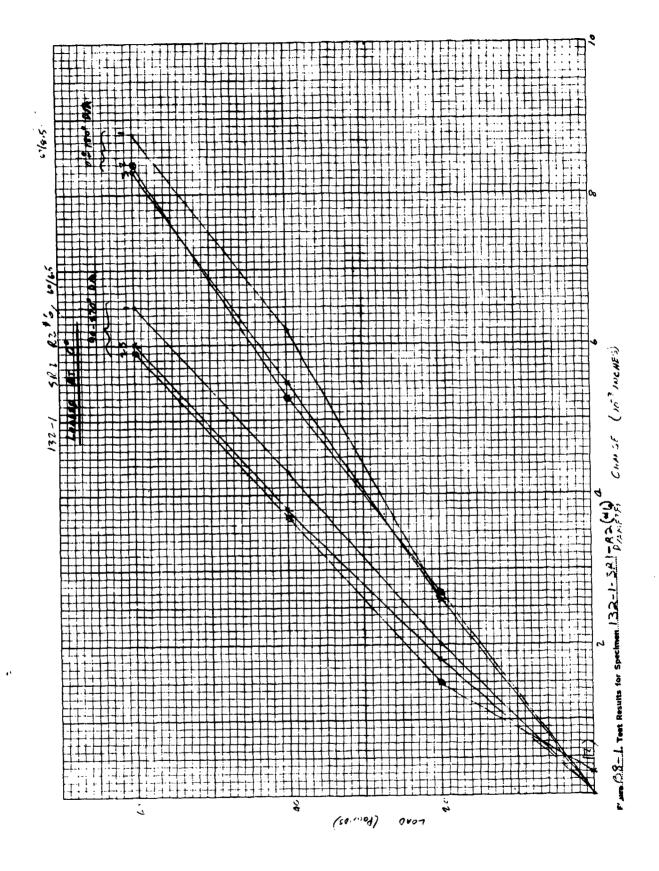
大学 一大学 一大学

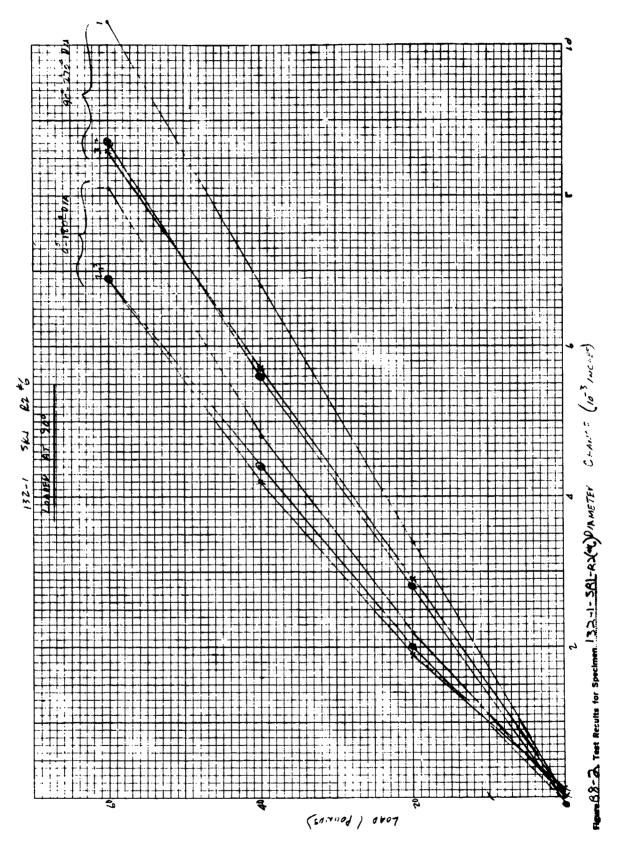
一

449

Preceding Page Blank - NOT - FILMED

APPENDIX B8
Flexural Ring Results

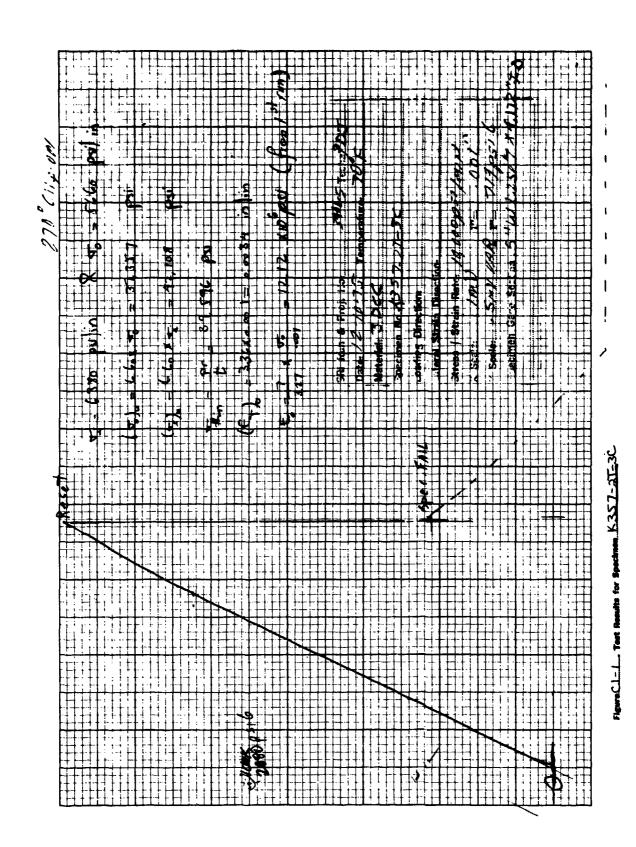




Preceding Page BLANK - FILMED

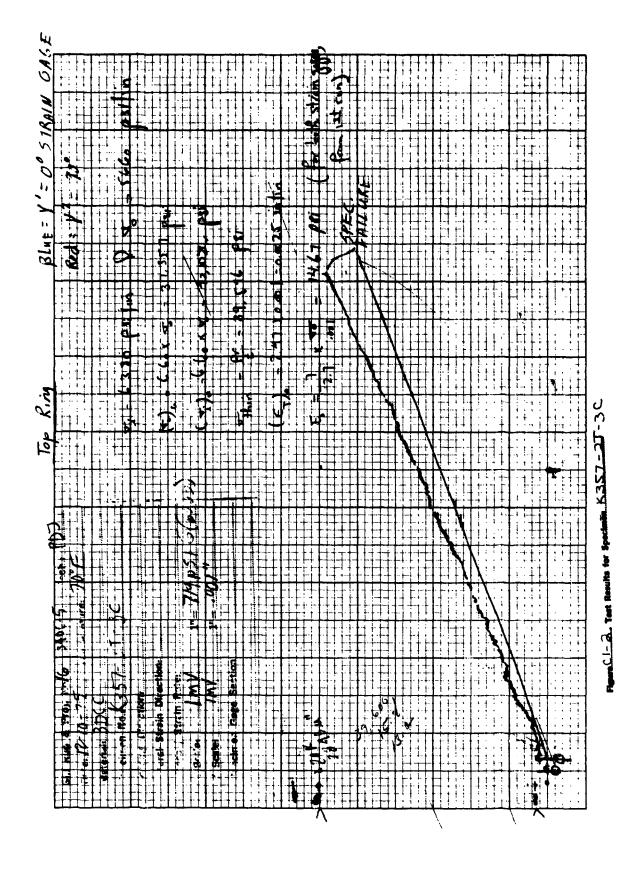
APPENDIX Cl
Circumferential Tensile Results

THE REPORT OF THE PARTY OF THE

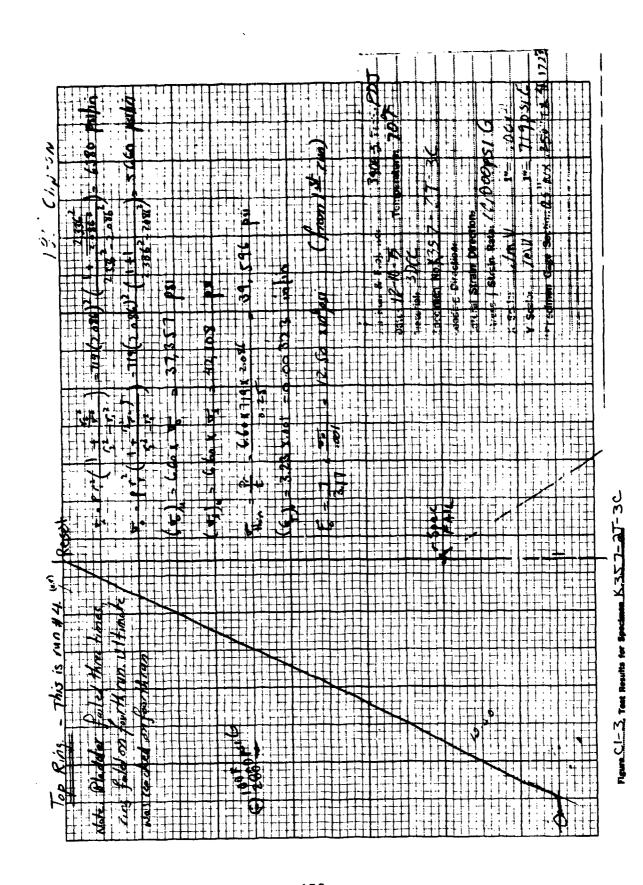


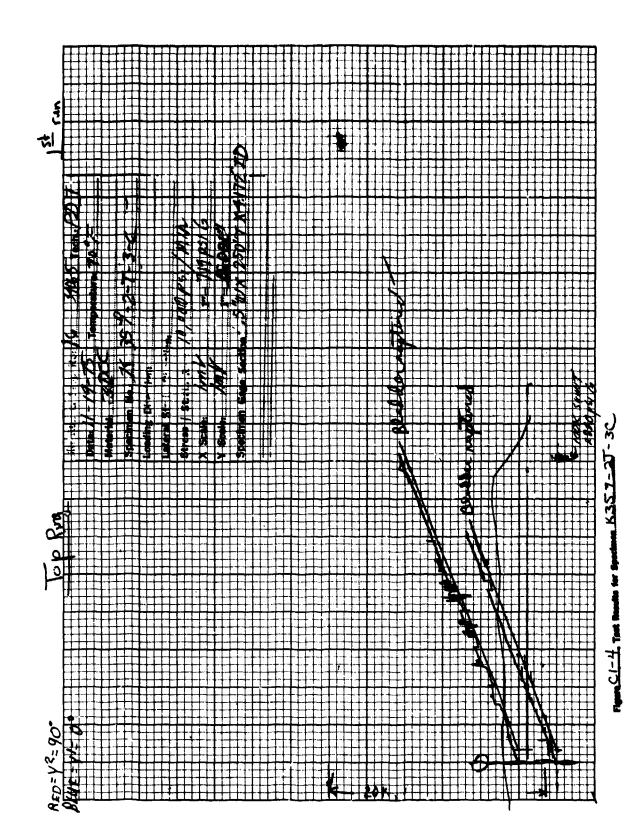
· ·

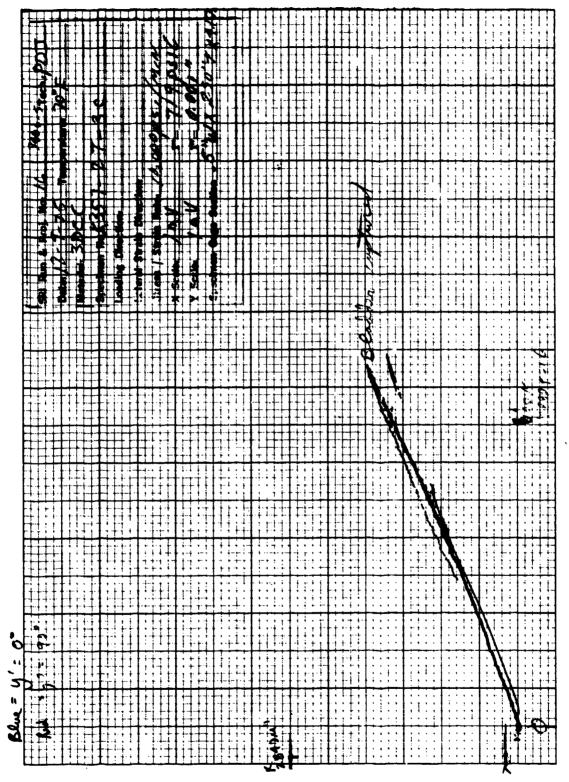
456



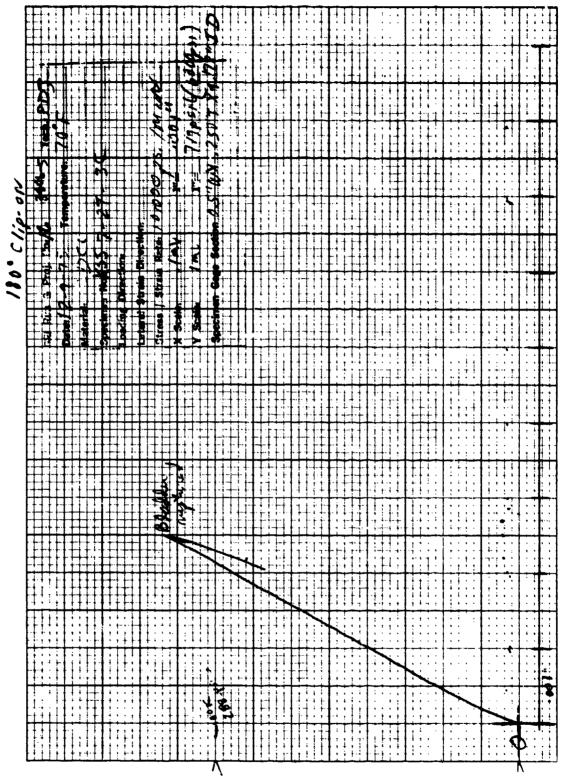
The second secon





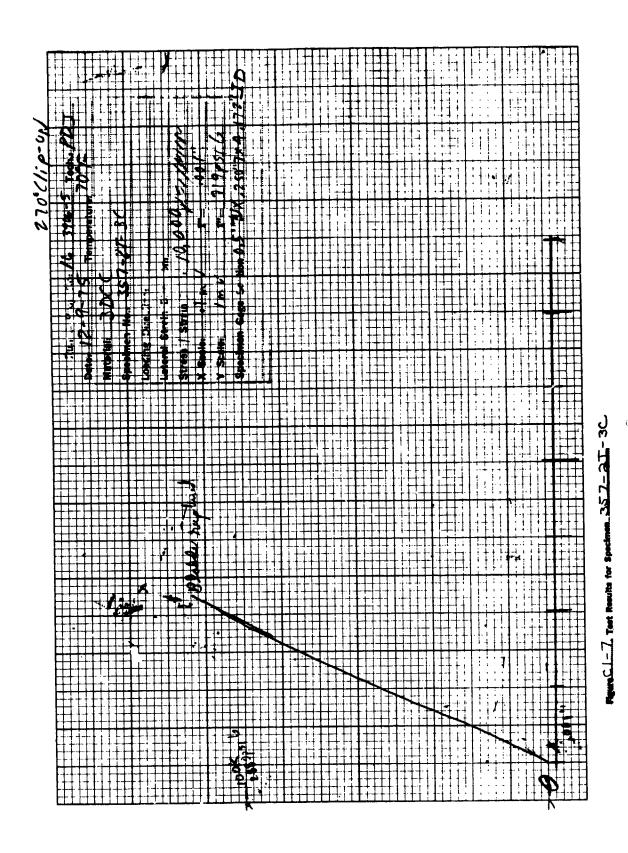


Names C.1-S. Trace Assacts for Spectrum, K.3S.7-3T-3C

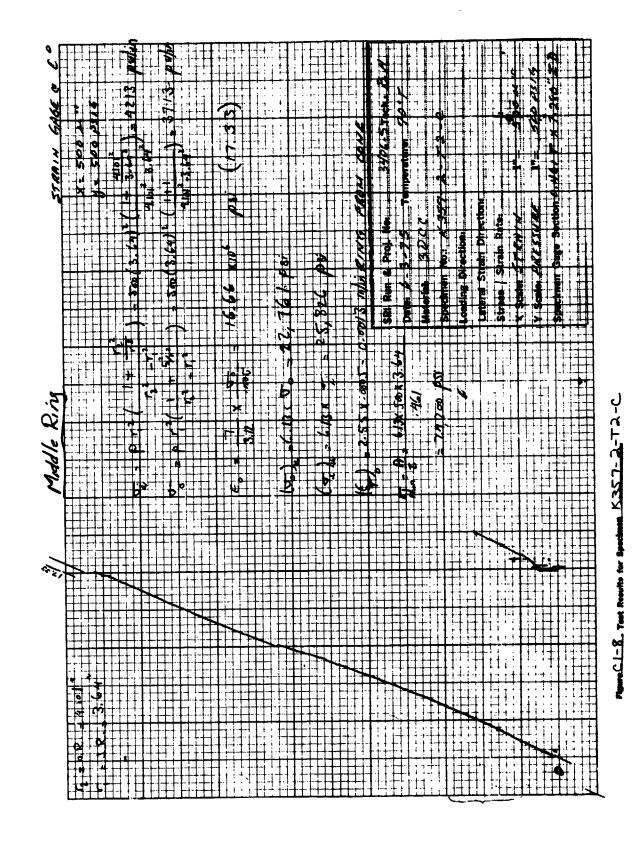


-

we C. 1 - La Test Results for Spectmen K3S 7 - 2I -

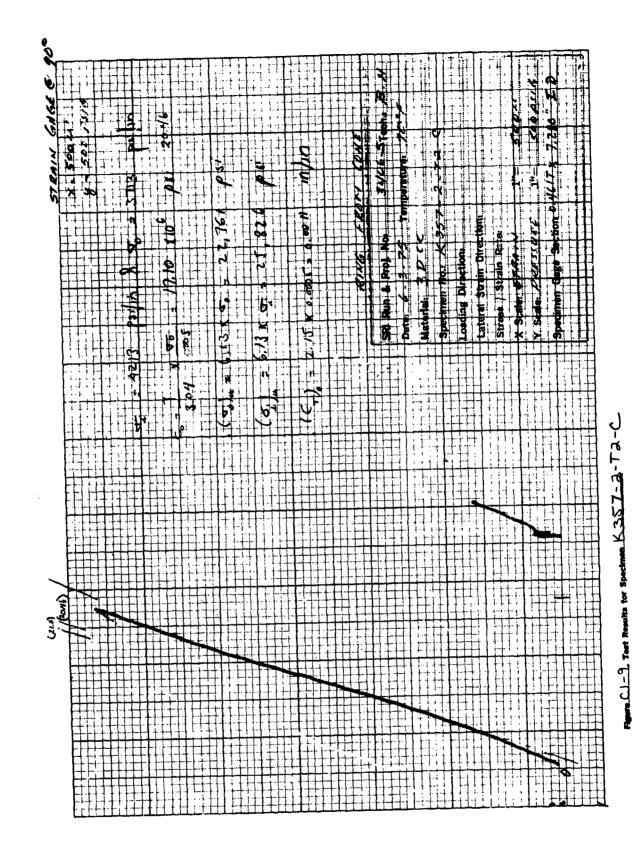


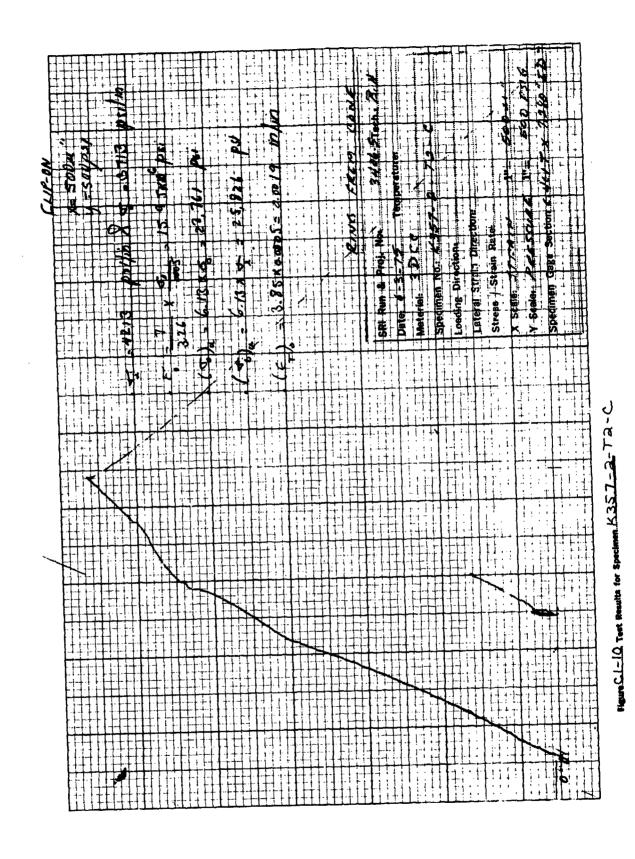
の金融ではから

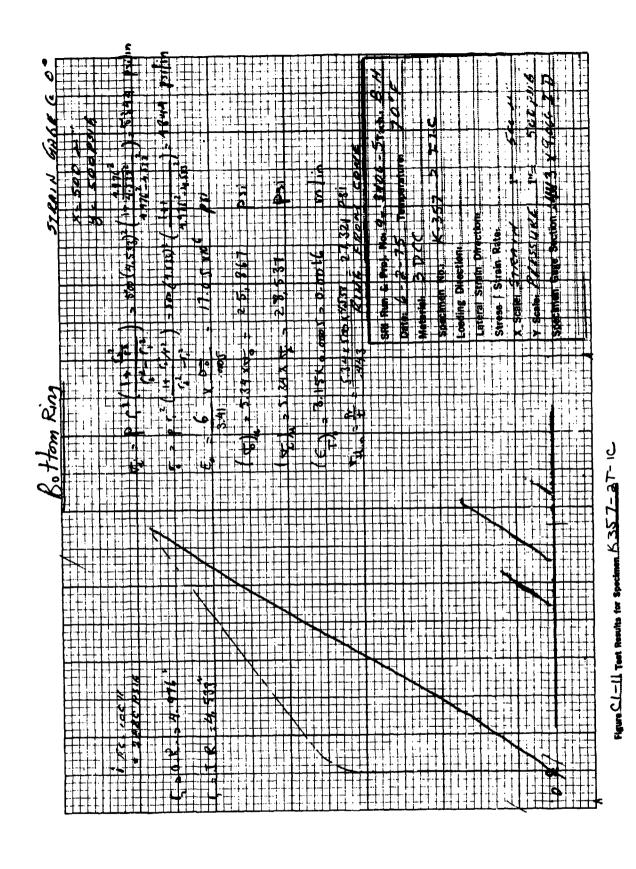


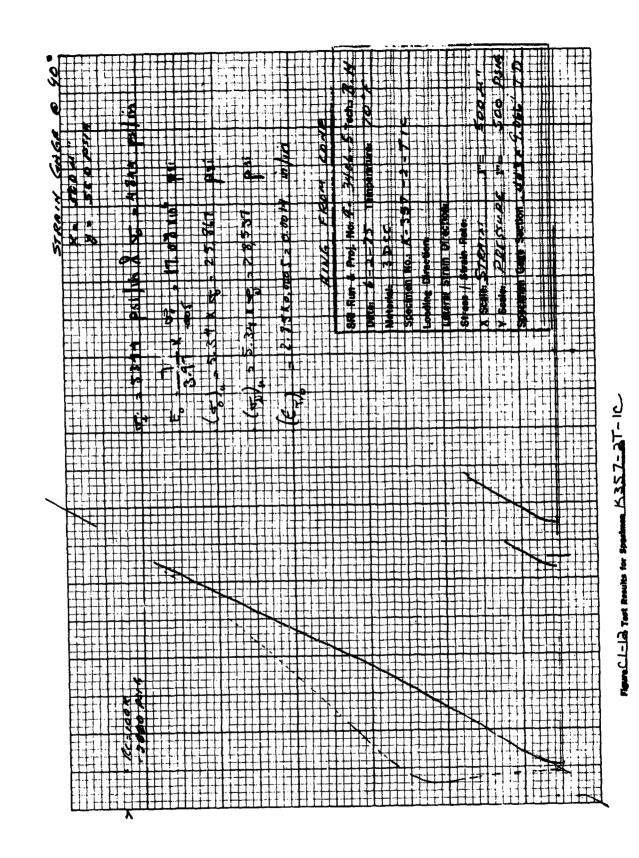
1,11

463





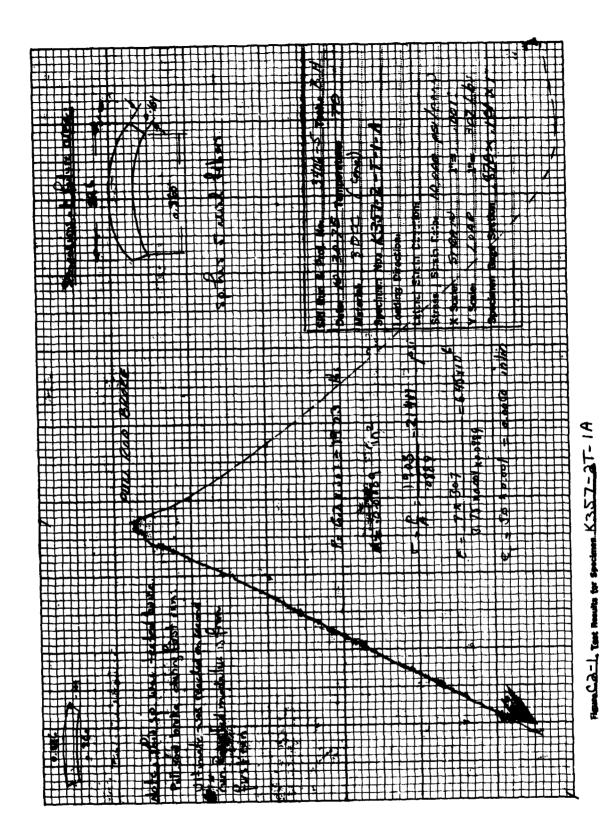


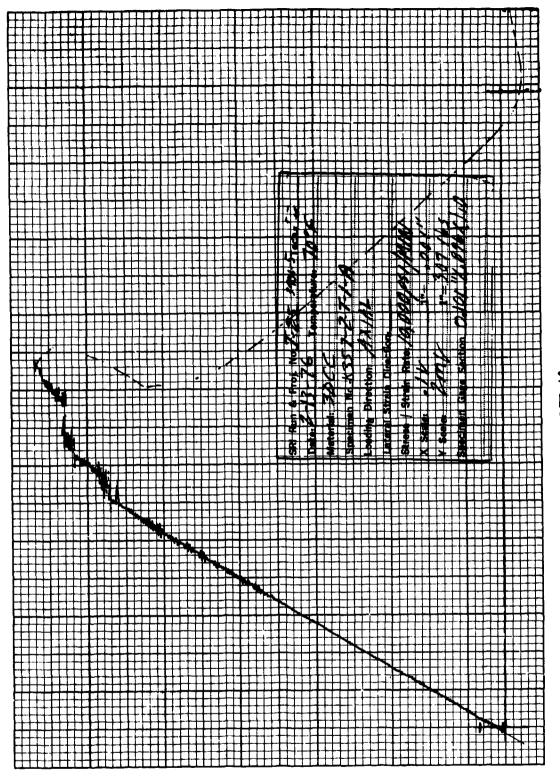


Preceding Page BLank - FILMES

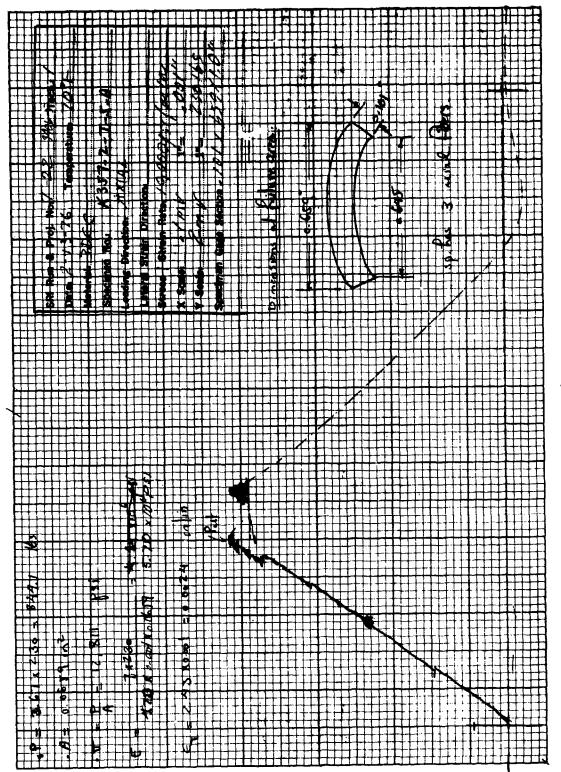
APPENDIX C2

Axial Tensile Results

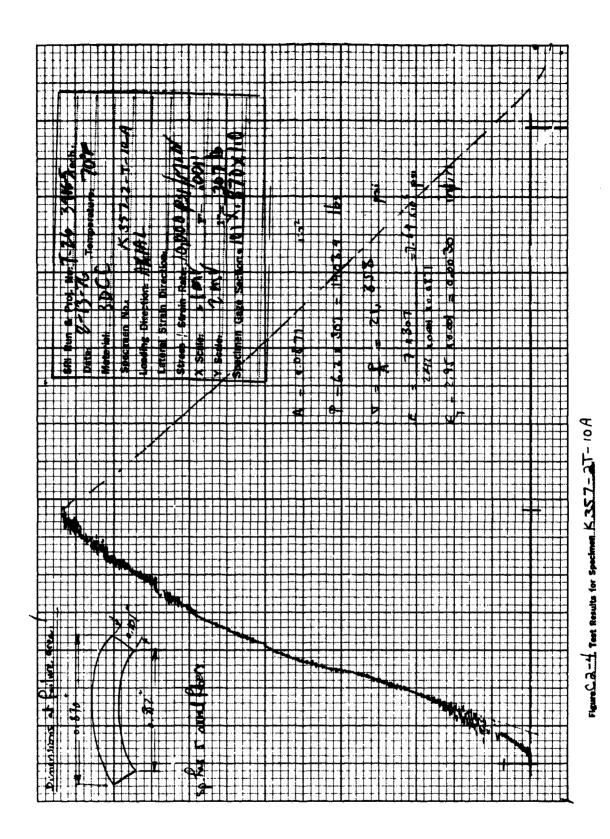




16.26.26 Test Results for Specimen K357-27-1A

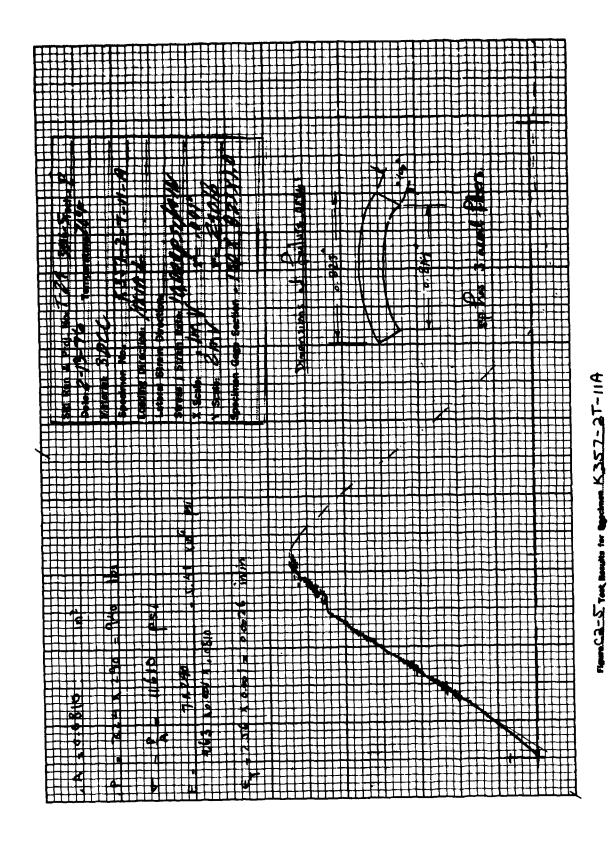


CA-3 Test Routes for Specimen, K.35.7-2.T-5A

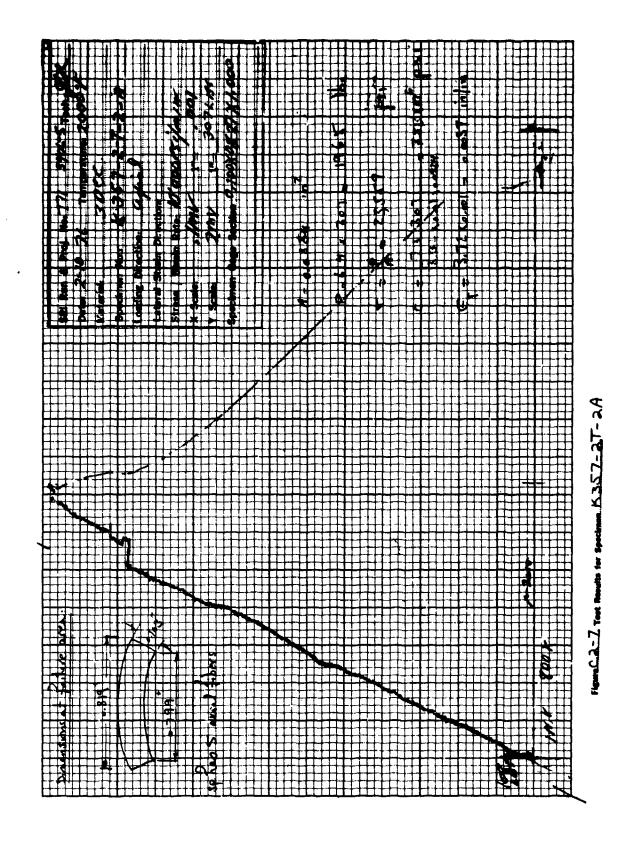


FT WITH LITT

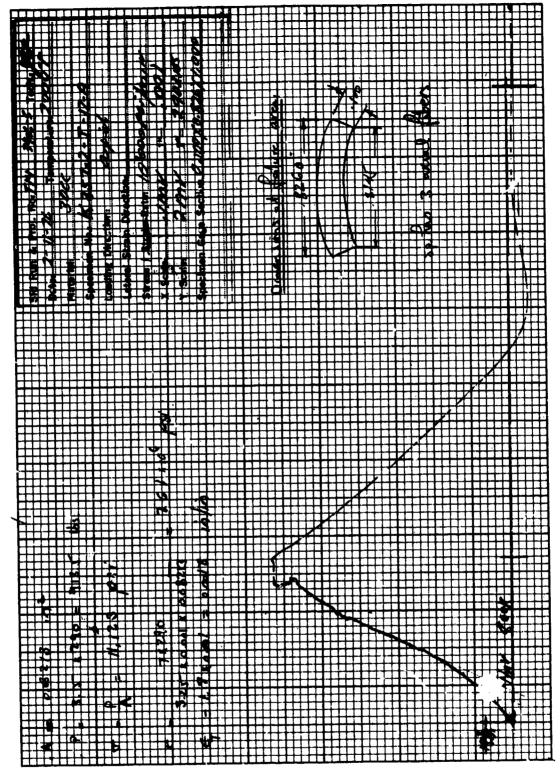
473



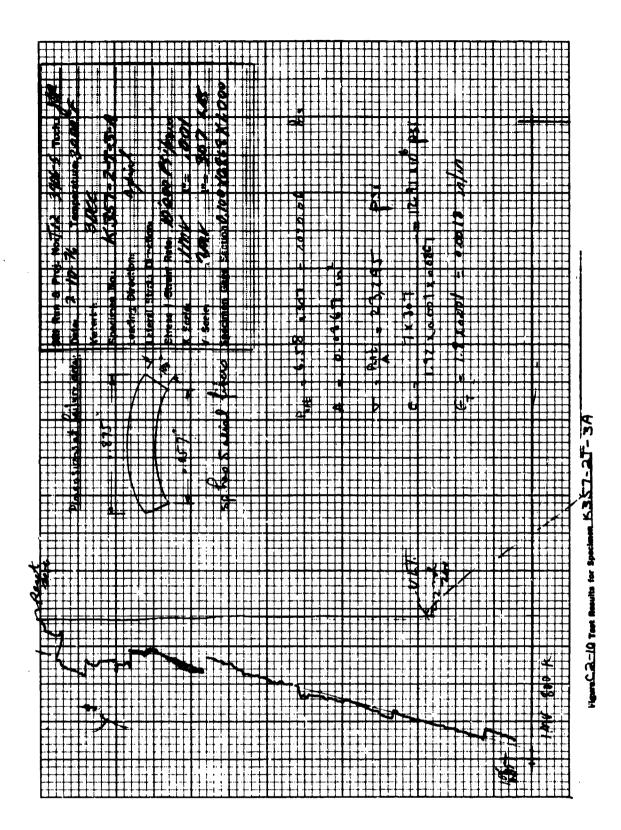
CA-La Tax marge for Specimen K3SZ-27-9A

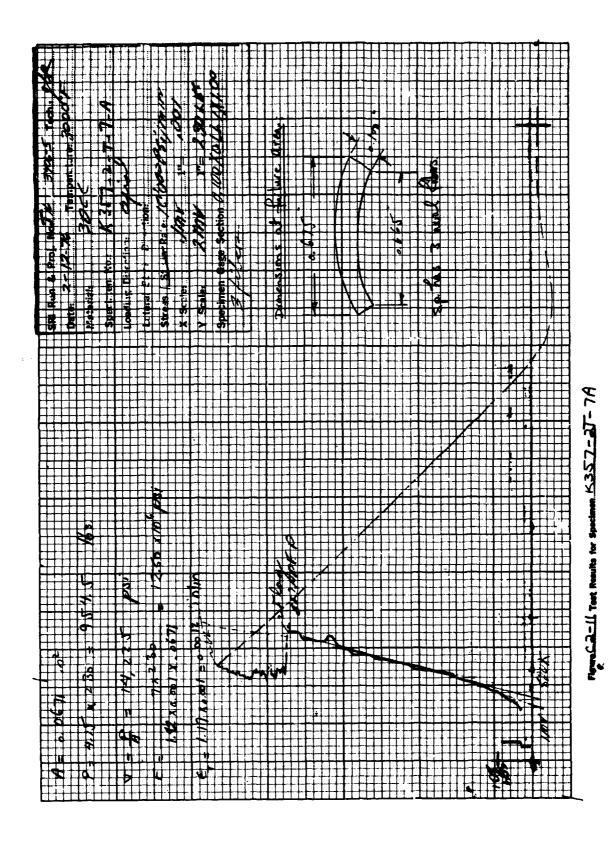


nc. 2. E Test Rooults for Specifical K35.7. ... 6.A.



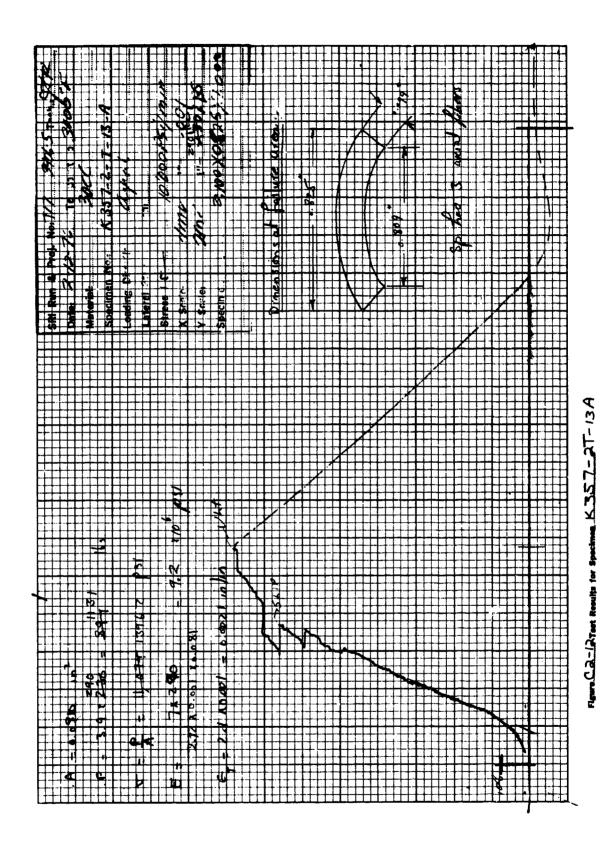
CA-1 True Boouts for Specimen K357-AT-12A

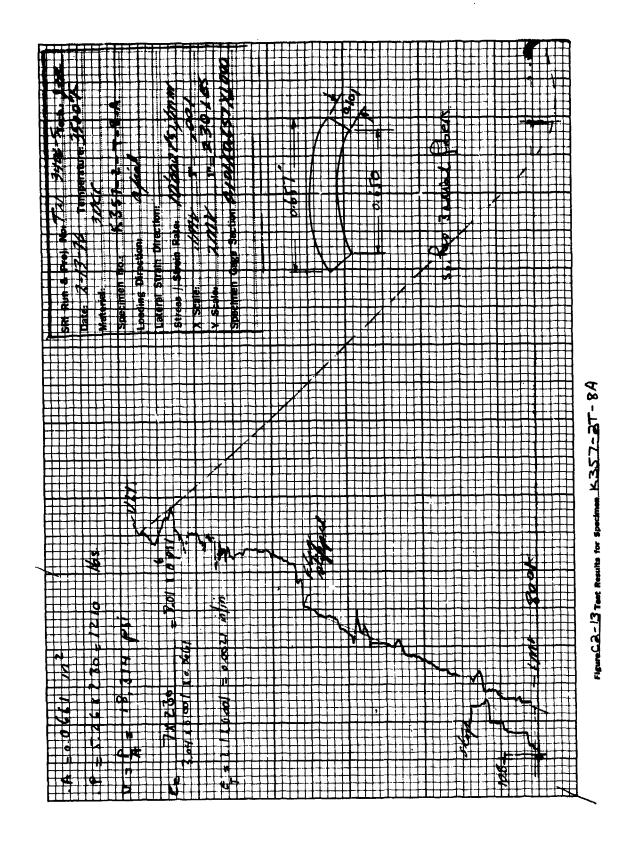


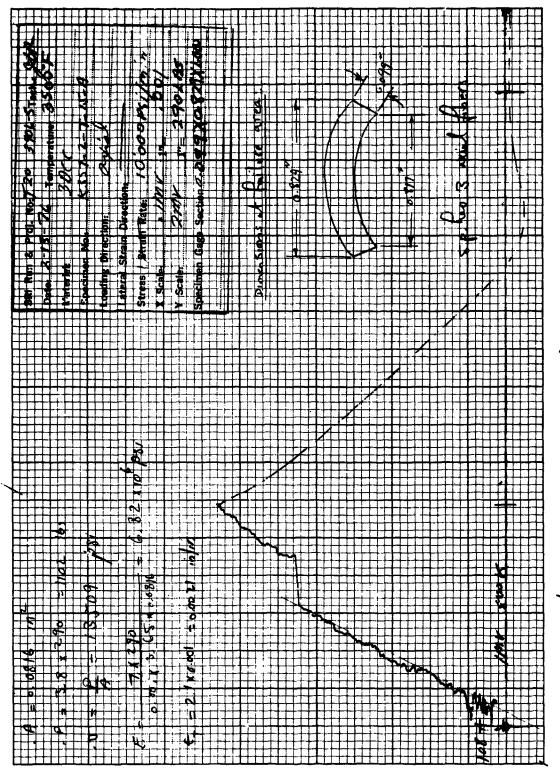


480

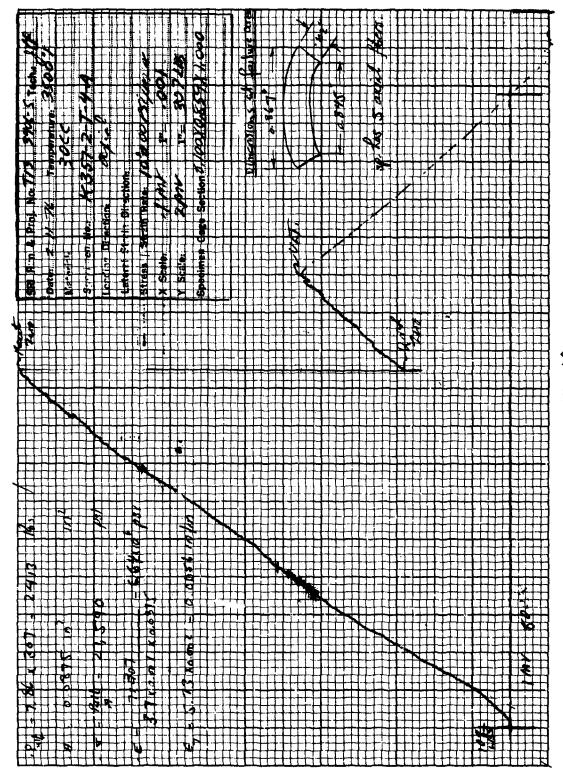
元十四世紀





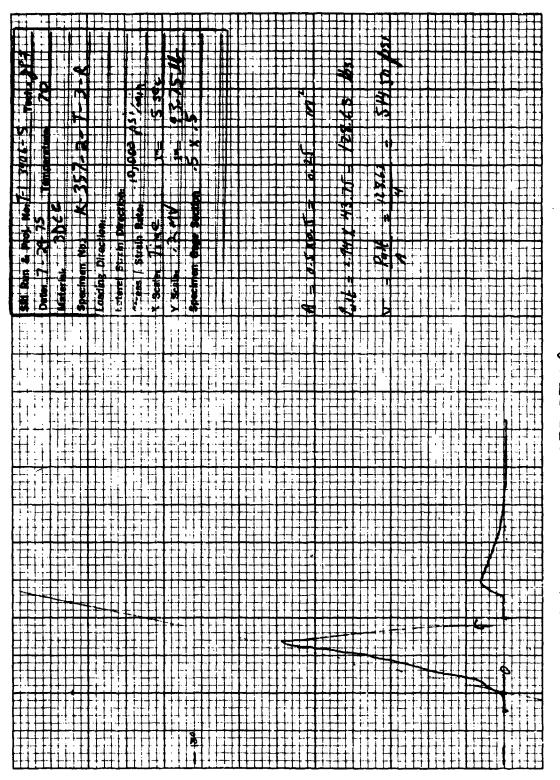


n. C.A. 1.4 Test Results for Specimen. K. 3.S. 7 - AT - 1.S. A



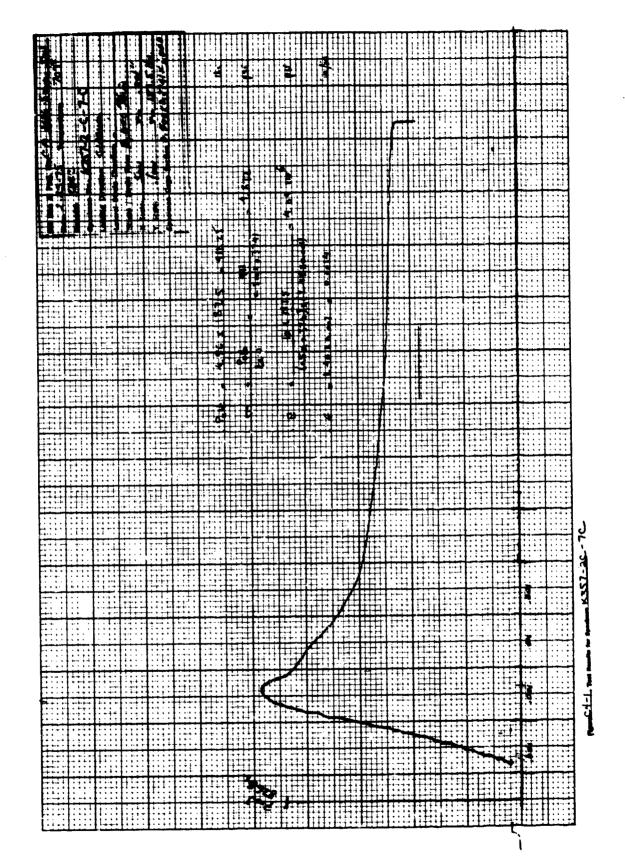
unCa-15 Test Results for Speckmen, K357-37-4A

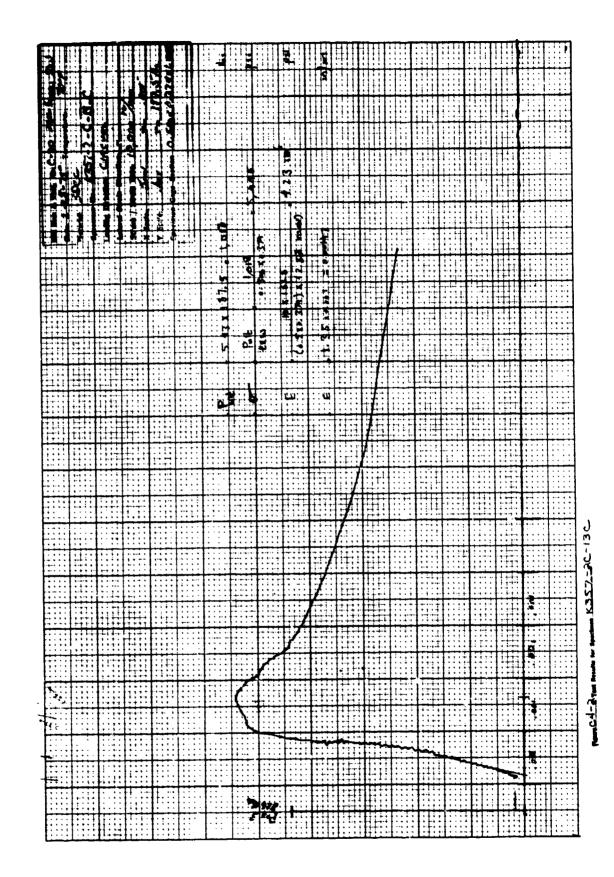
APPENDIX C3 Radial Tensile Results



are C.3-1 True for ults for Specimen K.35.7-27-3K

APPENDIX C4 Circumferential Compressive Results

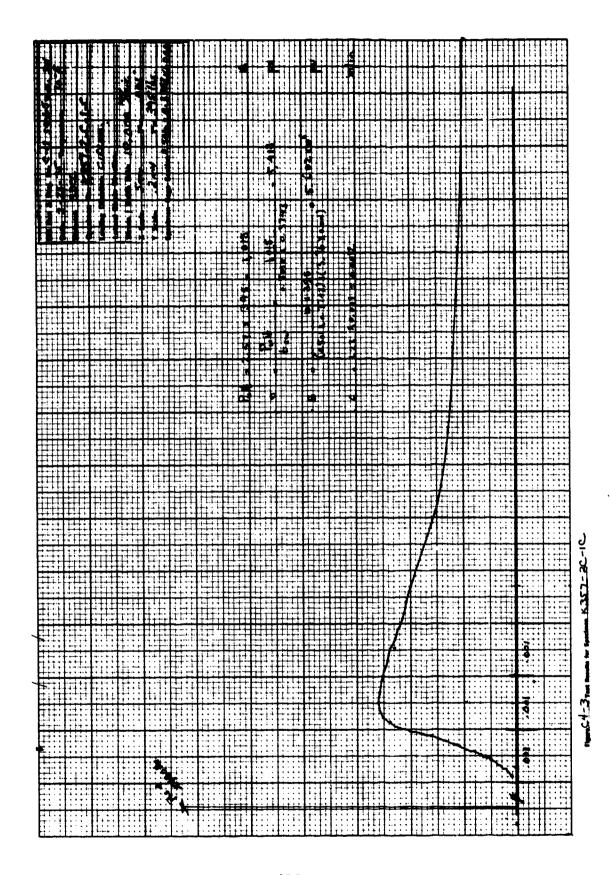


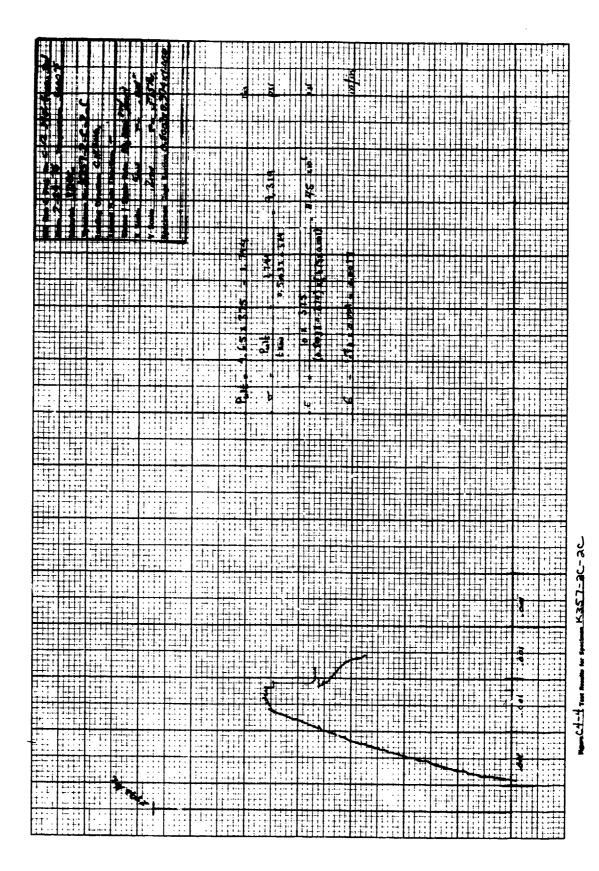


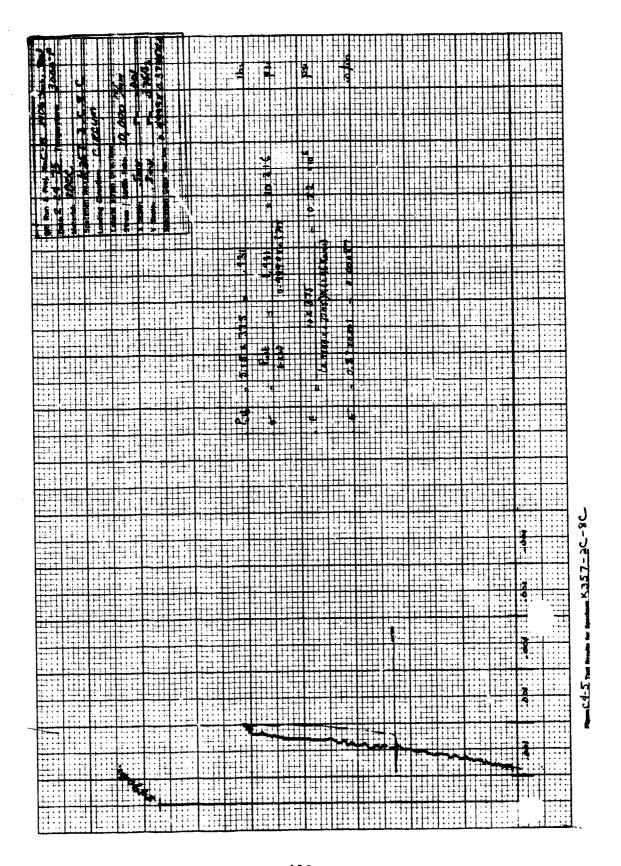
The same

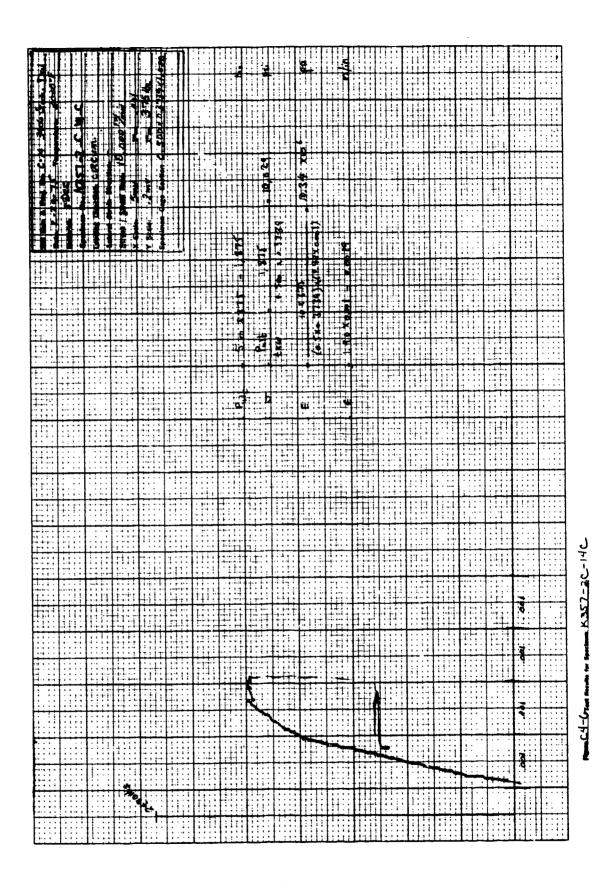
.....

489



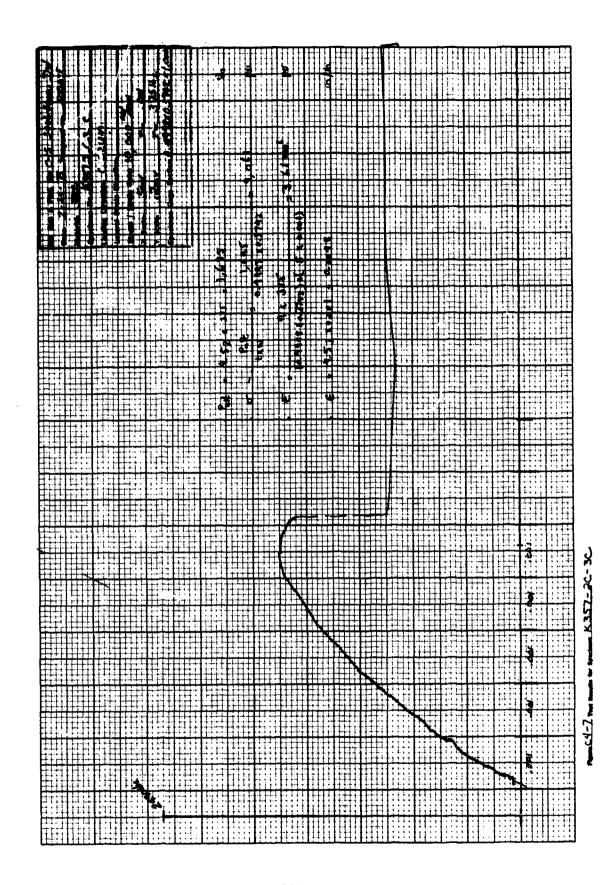


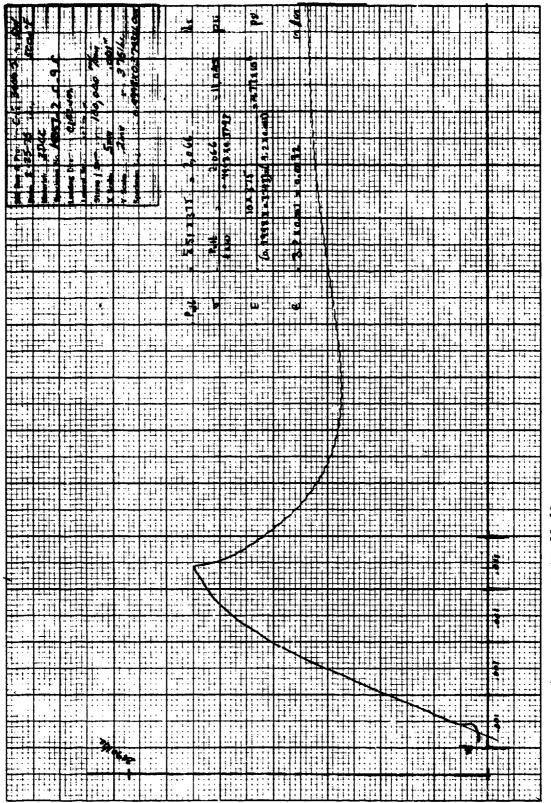




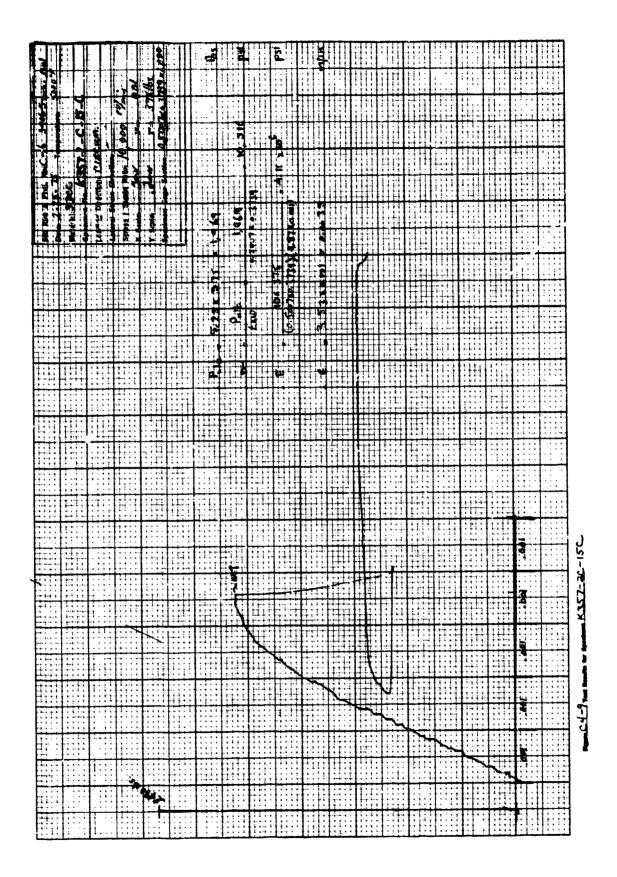
The second secon

493

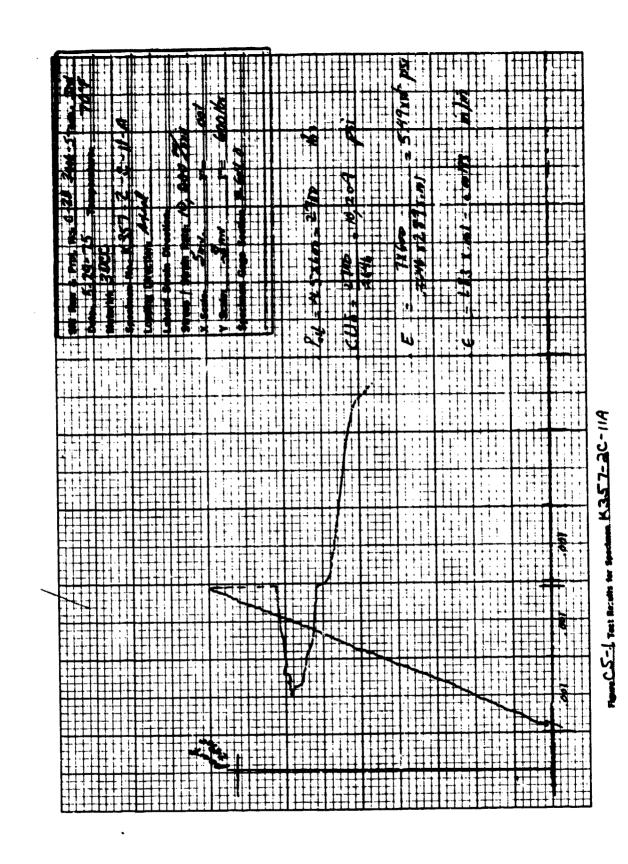


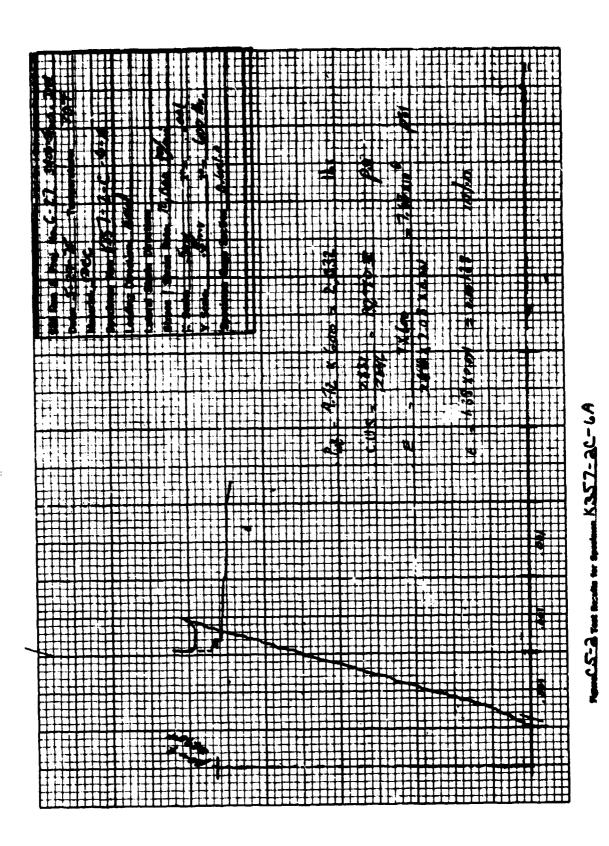


m.C.4.2 Test familie for Speciess. K.35.7.

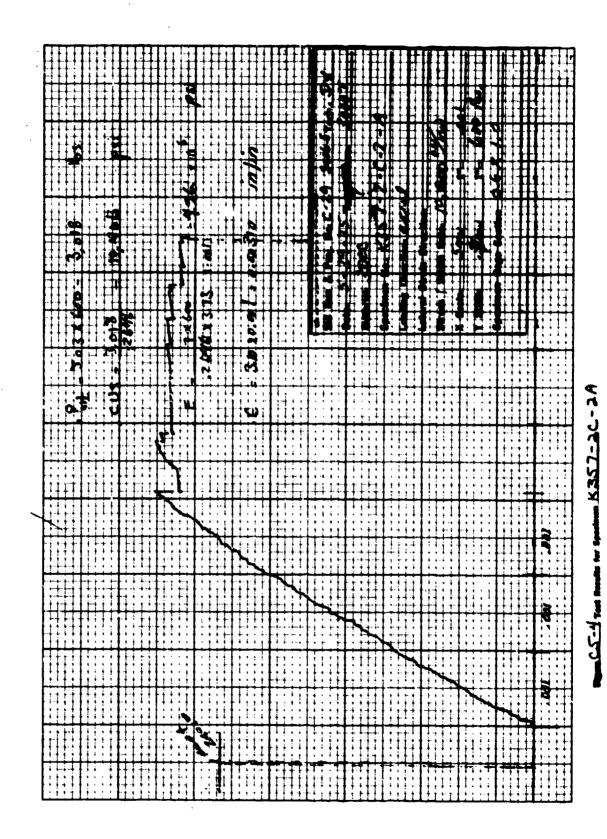


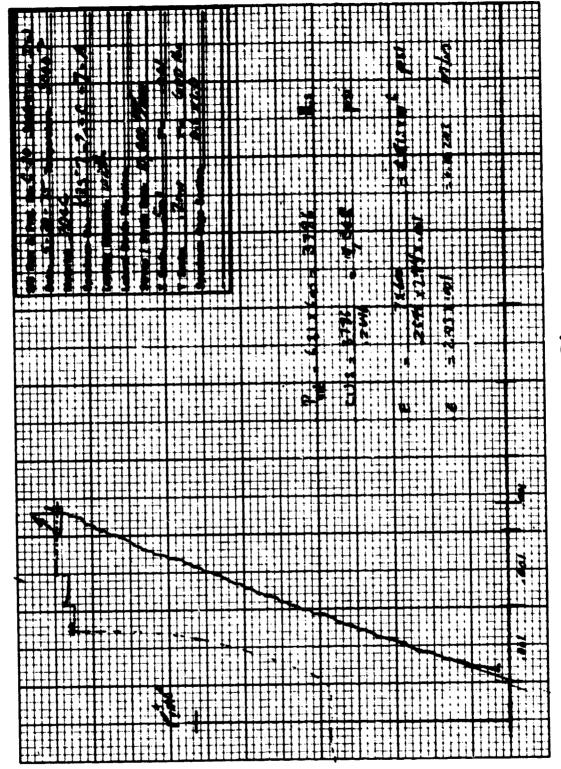
APPENDIX C5 Axial Compressive Results



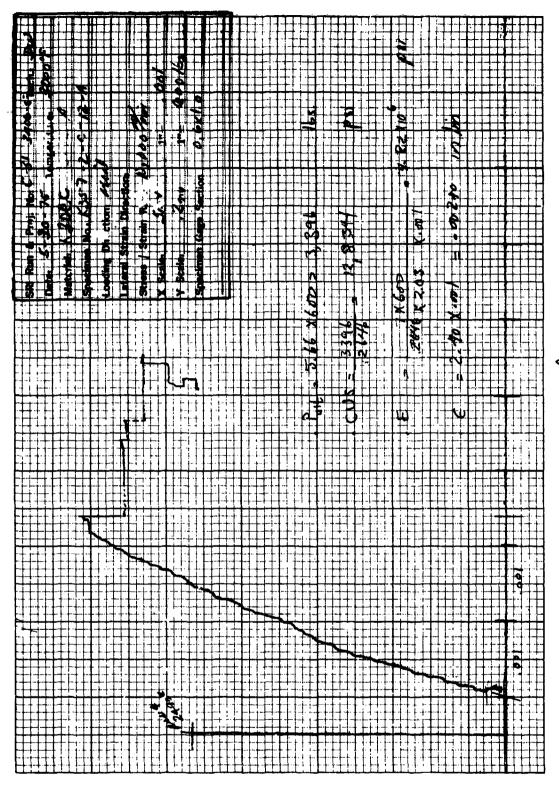


CS-3 700 Becato to Spectrum K357-2C-19

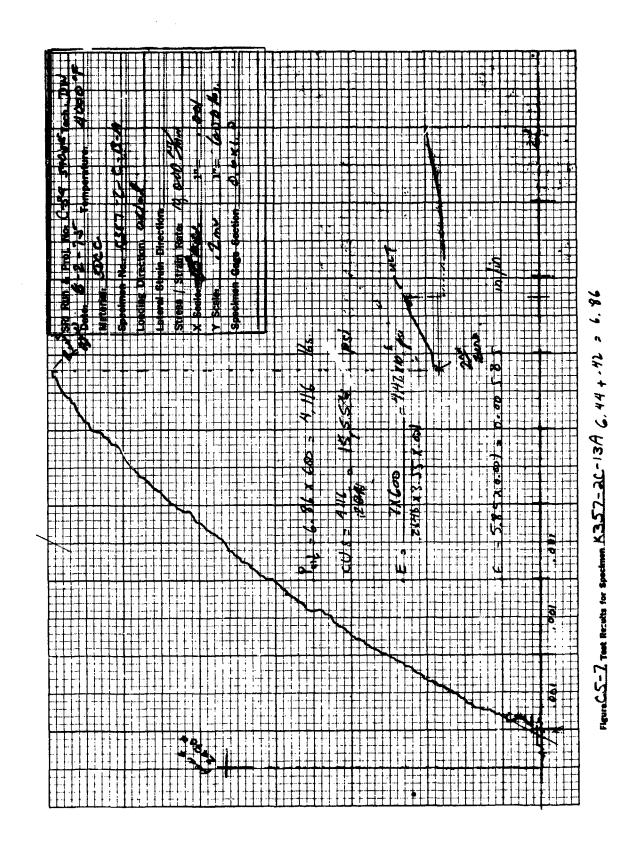


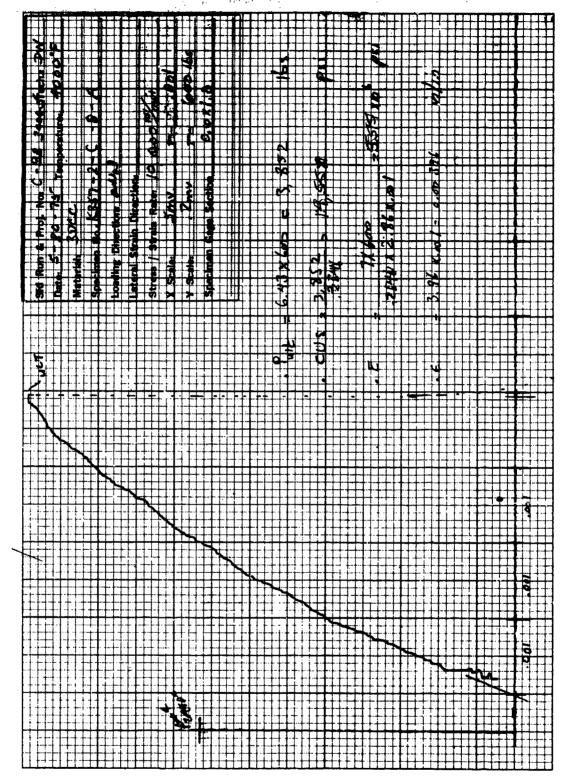


ACS-5 Tax Brids to Specimen K357-3C-74

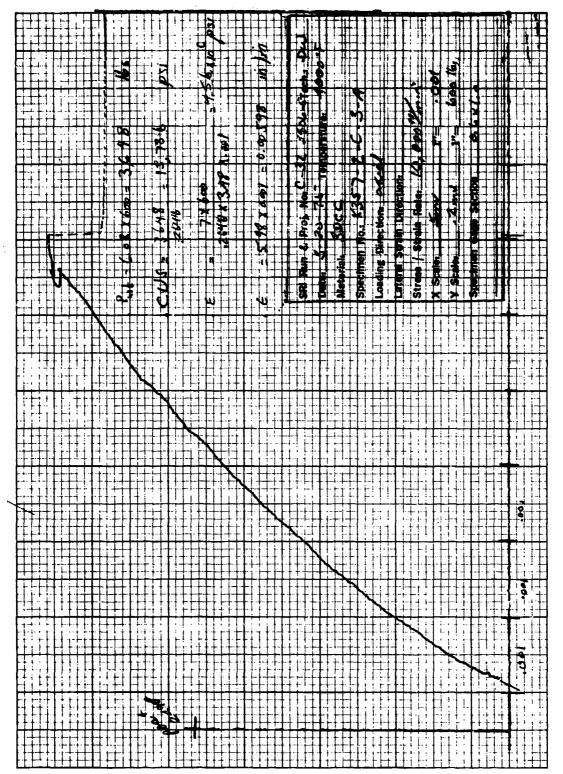


ACS-16 Teet Routs for Specimen K357-2C-12A





-CS-2 Tast Results for Spectmen K3S7-3C-84



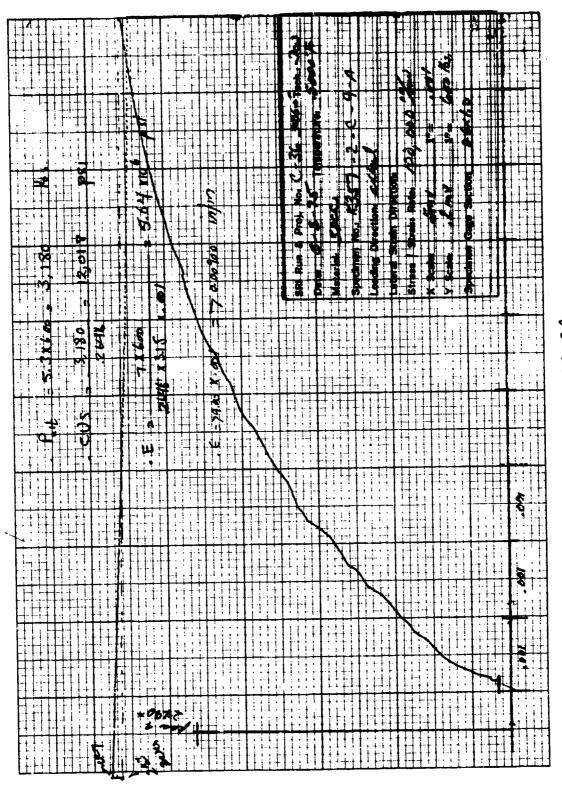
TOTAL SECTION OF THE PARTY OF T

Frame CS-1 Test Re-ults for Specimen K3S7-2C-3A

त्रा के अने के के के किया के किया के किया के किया है। जो के किया के किया के किया के किया के किया के किया के कि

C.S.-10 Tage Secults for Spectage K.352-2C - 4A

المحدد والأعلامية كوياب رئيس المعادات يسيد المشاه المالية المعادلة ويراه يقافها مأدع فيقطعه ويمقطع فيقافها الإنجاد



Man CS-11 Tage Rosulte for Spectmen K357-26-9A

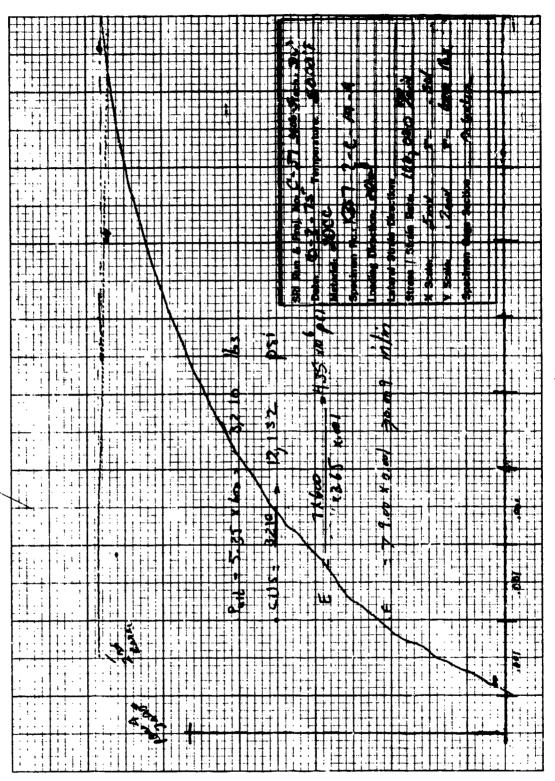
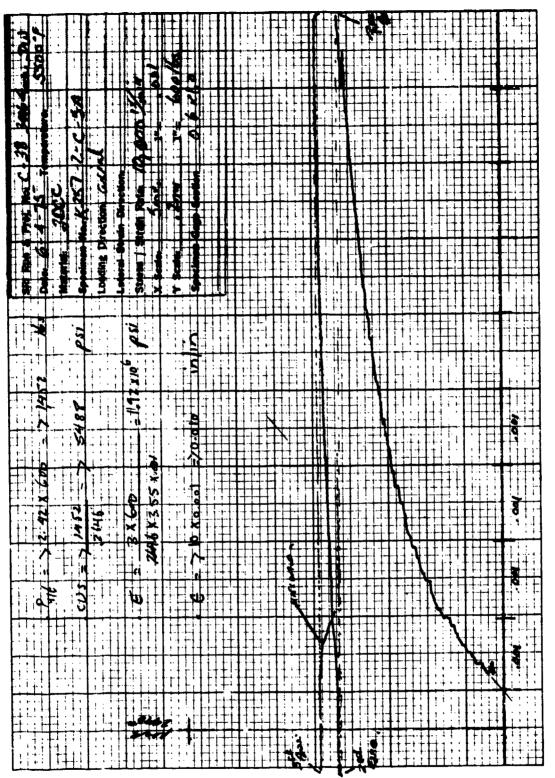
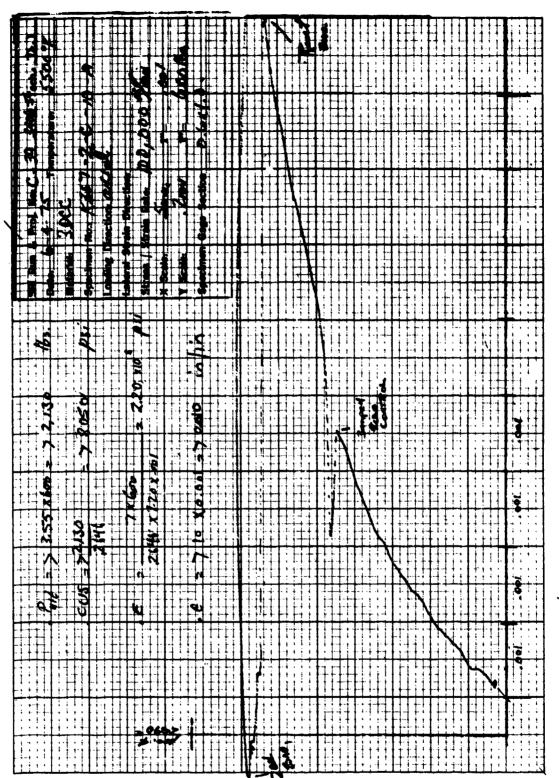


Figure CS-LATese Results for Spectmen. K357-2C-14A

्या है। इस स्वापना कार्या के के महिल्ला है। इस स्वापना कार्या के किए हैं। इस स्वापना कार्या के कार्या कर है।



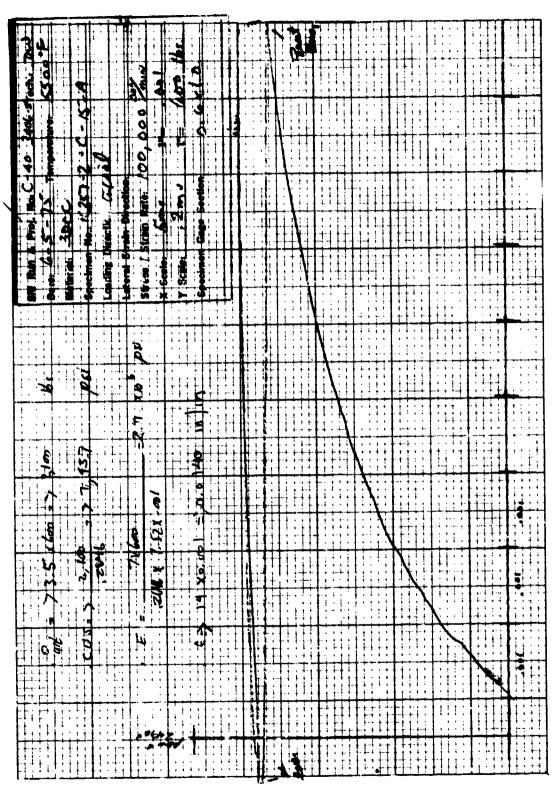
*CS-13 Tax Breaks for Section K357-3C-SA



The state of the s

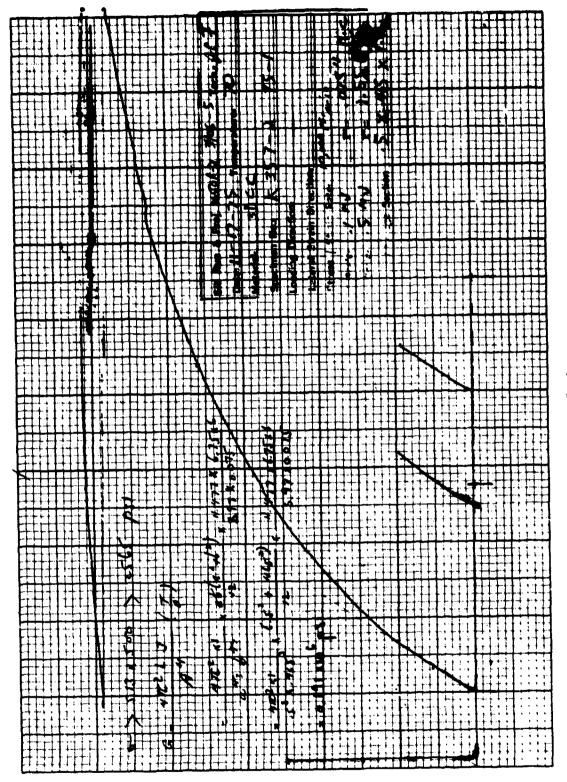
Figure CS-14 Tool Results for Specimen. K3S2-3C-10A

alle strategies in the strategies of the second second second second second second second second second second

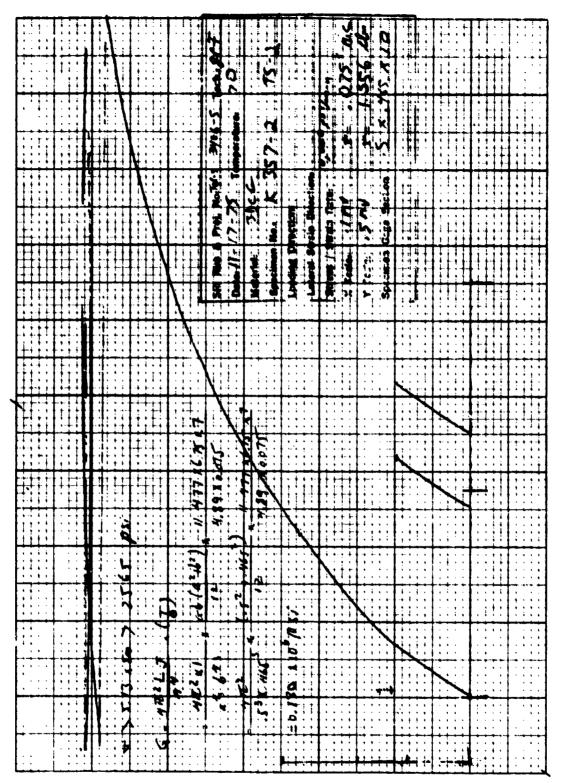


are CS-15 Taxe Resides for Spectmen K357-2C-15 A

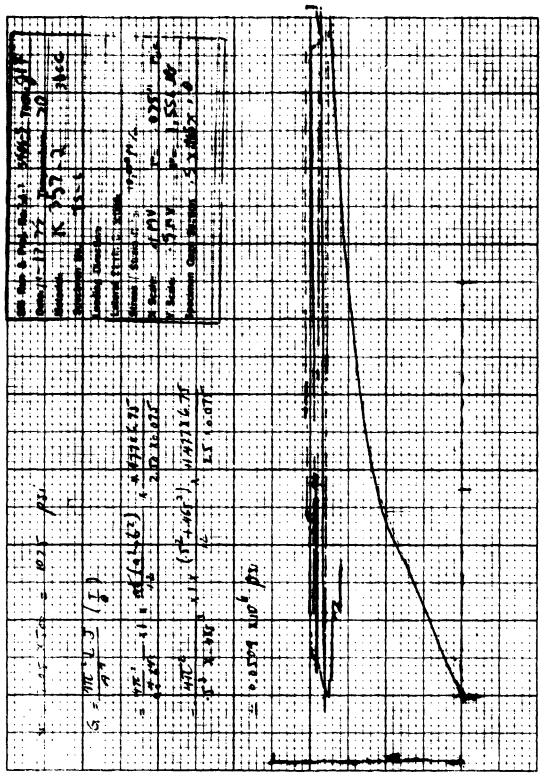
APPENDIX C6 Torsional Shear Results



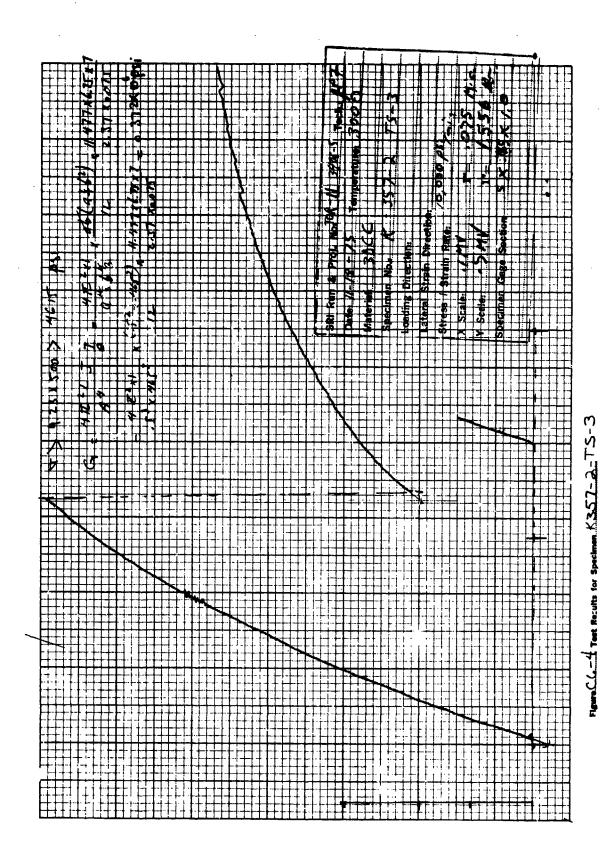
LL-1, Test Becels for Species, K.352-2-TS-1

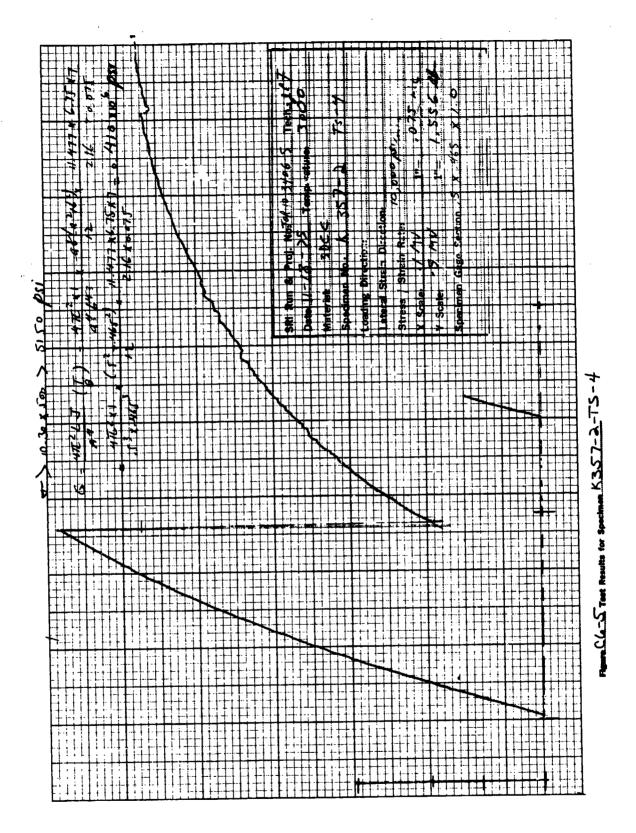


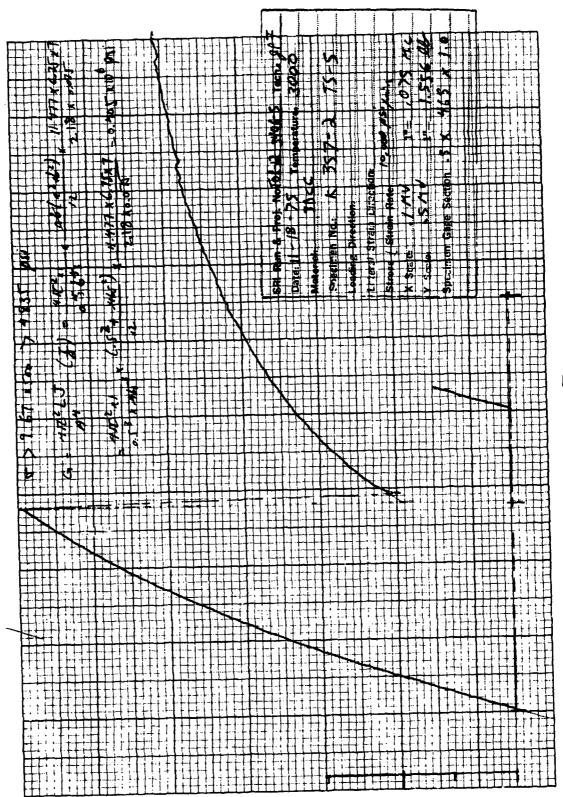
Hours Charles for the exection K357-2-75-2



m26-3 remain was K357-2-3 DCC







12-CL-C-T-2-T-3-T-3-T-3-T-3-T-3-5-5

DISTRIBUTION LIST

DEPARTMENT OF DEFENSE

Defense Advanced Research Project Agency ATTN: Strategic Tech. Office

Defense Communication Engineer Center ATTN: Code 720, John Worthington

Defense Communications Agency ATTN: Code 510, NMCSSC

Defense Documentation Center 12 cy ATTN: TC

Director

Defense Intelligence Agency

ATTN: DT-2, Weapons & Sys. Division

ATTN: Tony Dorr, (DIA-DT-2)
ATTN: DT-1C, Nuc. Eng. Branch
ATTN: DI-7D

Director

Defense Nuclear Agency

ATTN: DDST

ATTN: STSI, Archives

STTL, Tech. Library 3 cy ATTN:

ATTN: STSP ATTN: SPAS

SPSS ATTN:

ATTN: SPTD

Director of Defense Research & Engineering

Department of Defense

ATTN: George R. Barse

ATTN: DD/S&SS, John B. Walsh ATTN: DD/R&AT

ATTN: AD/DS

ATTN: AD/ET

ATTN: AD/ET, J. Persh

ATTN: S&SS (OS)

Commander

Field Command

Defense Nuclear Agency ATTN: FCTMD

ATTN: FCTMOT/LCDR Strode

FCPR

ATTN: FCTMOF

Chief

Test Construction Division, Field Command, DNA

ATTN: Joe LaComb

Director

Joint Strat, Target Planning Staff, JCS ATTN: JPTM

ATTN: JPTP

ATTN: JLTW-2

ATTN: JPST

Chief

Livermore Division, Field Command, DNA

Lawrence Livermore Laboratory

ATTN: FCPRL

DEPATIMENT OF DEFENSE (Continued)

OJCS/J-5

ATTN: J-5 Plans & Folicy R & D Division

Studies Analysis and Gaming Agency

Joint Chiefs of Staff ATTN: SDEB

DEPARTMENT OF THE ARMY

Director

BMD Advanced Tech. Center

Huntsville Office

ATTN: ATC-T, Melvin T. Capps

ATTN: Marcus Whitfield

ATTN: CRDABH-S, William C. Loomis

Program Manager

BMD Program Office

ATTN: DACS-BMT, John Shea

ATTN: DACS-BMZ

ATTN: Technology Division
ATTN: DACS-BMT, Clifford E. McLain
ATTN: DACS-BMZ-D, Julian Davidson

Commander

BMD System Command

ATTN: BDMSSC-TEB, R. Simpson

ATTN: BDMSC-TEN, Noah J. Hurst

Deputy Chief of Staff for Research Dev. & Acq.

Department of the Army
ATTN: NCB Division

Deputy Chief of Staff for Ops. & Plans

Department of the Army

ATTN: Director of Nuc. Plans & Policy

Commander

Harry Diamond Laboratories

ATTN: DRXDO-NP, Francis N. Wimenitz

ATTN: DRXDO-RC, Robert B. Oswald, Jr. ATTN: DRXDO-NP, Louis J. Belliveau

ATTN: DRXDO-RBH, James H. Gwaltney

Commender

Picatinny Arsenai

ATTN: SARPA-FR-E, Louis Avrami

SARPA-ND-C-T, Donald Miller ATTN:

ATTN: Al Loeb

ATTN: F. Cotton

ATTN: SMUPA-MD, Henry Opat

Director

TRASANA

ATTN: R. E. DeKinder, Jr.

Director

US Army Ballistic Research Labs.

ATTN: DRXBR-X, Julius J. Meszaros

ATTN: DRXBR-TL-IR, J. H. Keerer ATTN: DRXRD-BVL, William J. Schuman, Jr.

ATTN: DRXBR-TB, J. T. Frasier
ATTN: Robert E. Eichelberger

ATTN: Richard Vitali

DEPARTMENT OF THE NAVY (Continued) DEPARTMENT OF THE ARMY (Continued) Commanding Officer Commander Naval Weapons Evaluation Facility US Army Mat. & Mechanics Research Center ATTN: Peter Hughes ATTN: DRXMR-HH, John F. Dignam ATTN: Lawrence R. Oliver Commander US Army Materiel Development & Readiness Command Director Strategic Systems Project Office ATTN: DRCDE-D, Lawrence Flynn Navy Department ATTN: NSP-272 Commander ATTN: NSP-273 US Army Missile Command ATTN: DRS-RKP, W. B. Thomas ATTN: Troy Smith DEPARTMENT OF THE AIR FORCE ATTN: DRSMI-RRR, Bud Gibson
ATTN: DRSMI-XS, Chief Scientist
ATTN: DRCPM-PE-EA, Wallace O. Wagner Commandant AF Flight Dynamics Laboratory, AFSC
ATTN: FXG Commander AF Geophysics Laboratory, AFSC US Army Nuclear Agency ATTN: Chan Touart ATTN: COL DeVerill ATTN: ATCA-NAW AF Materials Laboratory, AFSC ATTN: MAJ J. Vecke ATTN: LPH, Gordon Griffith ATTN: MONA-SA ATTN: MBC, Donald L. °chmidt ATTN: MBE, George v ...chmict ATTN: Bill Kessle: ATTN: MONA-WE ATTN: CDC-NVA ATTN: MAS Chief ATTN: T. Nicholas US Army Research Office ATTN: LTM ATTN: Technical Library AF Rocket Propulsion Laboratory, AFSC DEPARTMENT OF THE NAVY ATTN: RTSN, G. A. Beale Chief of Naval Material AF Weapons Laboratory, AFSC Navy Department ATTN: Dr. Minge ATTN: DYS, Lt E. J. Burns ATTN: MAT 0323, Irving Jaffe ATTN: Al Sharp Chief of Naval Operations ATTN: SAB Navy Department ATTN: DYT ATTN: Robert A. Blaise ATTN: DYV ATTN: Code 604C3, Robert Piacesi ATTN: OP 62 ATTN: ALO, Maj Lawrence T. James ATTN: SUL 2 cy ATTN: OP 981 2 cy ATTN: NTO ATTN: Tech. Review Chief of Naval Research Navy Department ATTN: Code 464, Thomas P. Quinn ATTN: Col Earnest F. Dukes, Jr. Director Headquarters Naval Research Laboratory ATTN: Code 5180, Mario A. Persechino ATTN: Code 2600, Tech. Lib. ATTN: Code 7770, Gerald Cooperstein Air Force Systems Command ATTN: SOSS ATTN: XRTO Commander Commander Arnold Engineering Development Center Naval Sea Systems Command ATTN: XOA Navy Department ATTN: ORD-0333A ATTN: 0333A, Marlin A. Kinna Commander ATTN: Code 0351 4 cy ATTN: EWFS, D. Ward

Commander

Naval Surface Weapons Center ATTN: Code 2302, Leo F. Gowen

ATTN: Code WA-501, Navy Nuc. Programs Off.

ATTN: Code 241, Joseph Petes ATTN: Code 322, Victor C. Dawson

ATTN: Code 323, W. Carson Lyons

Commander

Foreign Technology Division, AFSC ATTN: PDBG ATTN: TDFBD, J. D. Pumphrey

ATTN: TDPTN

NEPARTMENT OF THE AIR FORCE (Continued)	DEPARTMENT OF DEFENSE CONTRACTORS
Hg USAF/RD	Acurex Corporation
ATTN: David S. Hyman	ATTN: J. Courtney
ATTN: RDOSM	ATTN: C. Nardo
ATTN: RDQ	ATTN: J. Huntington
ATTN: RDQSM	ATTN: Robert M. Kendall
ATTN: RDPM	(11 IIII HODOLE III HOROLE
ATTN: RD	Aeronautical Research Assoc. of Princeton, Inc
Alln: ND	ATTN: Coleman Donaldson
U. UCAP/VO	Alin. Coleman bondigaon
Hq USAF/XO ATTN: XOOSS	Aerospace Corporation
Alla: A0055	ATTN: Richard Crolius, A2-RM1027
UMBO / DV	ATTN: R. Allen
SAMSO/DY	ATTN: J. McClelland
ATTN: DYS	ATTN: R. Strickler
CANCO (NO)	ATTN: W. Barry
SANSO/MN	ATTN: R. Mortensen
ATTN: MNNR	ATTN: W. Mann
cauco/Ro	WIIN: M' GHUL
SAMSO/RS	Anniable Commission Tax
ATTN: RST	Analytic Services, Inc.
ATTN: RSSE	ATTN: Jack Selig
ATTN: RSS	ADO Processoral
	ARO, Incorporated
Commander In Chief	ATTN: John C. Adams
Strategic Air Command	
ATTN: XPFS	AVCO Research & Systems Group
ATTN: XOBM	ATTN: Doc. Control
ATTN: DOXT	ATTN: John E. Stevens, J100
ATTN: NRI ATTN: XPQM	ATTN: S. Skemp, J200
	ATTN: George J. Davis
	ATTN: J. Patrick
ENERGY RESEARCH & DEVELOPMENT ADMINISTRATION	ATTN: William G. Reinecke, K100
	ATTN: George Weber, J230
Division of Military Application	ATTN: John Gilmore, J400
US Energy Research & Development Admin.	
ATTN: Doc. Control for Research & Dev. Branch	Battelle Memorial Institute
	ATTN: Merwyn R. Vanderlind
University of California	ATTN: E. Unger
Lawrence Livermore Laboratory	ATTN: Richard Castle
ATTN: Larry W. Woodruff, L-96	ATTN: W. Pleifer
ATTN: C. Joseph Taylor, L-92	
ATTN: Joseph B. Knox, L-216	The Boeing Company
ATTN: Joseph E. Keller, Jr., L-125	ATTN: Robert Dyrdahl
ATTN: G. Staihle, L-24	ATTN: William Crist
	ATTN: Brian Lempriere
Los Alamos Scientific Laboratory	ATTN: Ed York
ATTN: Doc. Control for T. Talley	ATTN: Robert Holmes
ATTN: Doc. Control for Richard A. Gentry	
ATTN: Doc. Control for John McQueen	The Boeing Company
ATTN: Doc. Control for Donald Kerr	ATTN: T. Swaney
ATTN: Doc. Control for R. S. Thurston	
ATTN: Doc. Control for J. W. Taylor	Brown Engineering Company, Inc.
	ATTN: Ronald Patrick
Sandia Laboratories	
Livermore Laboratory	California Research & Technology, Inc.
ATTN: Raymond Ng	ATTN: Ken Kreyenhagen
ATTN: Doc. Control for C. S. Hoyle	
ATTN: Doc. Control for T. Gold	Calspan Corporation
ATTN: Doc. Control for 8131 H. F. Norris, Jr.	ATTN: M. S. Holden
	ATTN: Romeo A. Deliberis
Sandia Laboratories	ATTN: M, G. Dunn
ATTN: Doc. Control for Walter Herrmann	
ATTN: Doc. Control for M. L. Merritt	University of Dayton
ATTN: Doc. Control for R. R. Boade	ATTN: Hallock F. Swift
ATTN: Doc. Control for Thomas B. Cook	ATTN: D. Gerdiman
ATTN: Doc. Control for D. McCloskey	
ATTN: Doc. Control for B. Caskey	Effects Technology, Inc.
ATTN: Doc. Control for Albert Chabai	ATTN: Robert Wengler
ATTN: Doc. Control for A. W. Synier	ATTN: Richard Parise

・ 「「「「「「」」」というでは、「「」」というでは、「「」」というでは、「「」」というでは、「「」」というできます。「「」」というできます。「「」」というできます。「「」」というできます。「「」」という

DEPARTMENT OF DEFENSE CONTRACTORS (Continued)

Ford Aerospace & Communications Operations ATTN: P. Spangler

Gard, Incorporated ATTN: Marion J. Balcerzak ATTN: W. F. Byrne

General Dynamics Corp. Fort Worth Division ATTN: R. Shemensky

「「一」のでは、「一」のでは、「一」のできる。

General Electric Company Space Division Valley Forge Space Center ATTN: C. Kyriss ATTN: A. Martellucci ATTN: B. M. MaGuire ATTN: Phillip Cline AiTN: Carl Anderson ATTN: Daniel Edelman ATTN: G. Harrison

General Electric Company TEMPO-Center for Advanced Studies ATTN: DASIAC

ATTN: B. Gambill General Research Corporation

ATTN: John Ise, Jr. ATTN: T. Stathacopoulos ATTN: Robert E. Rosenthal

Institute for Defense Analyses ATTN: IDA Librarian, Ruth S. Smith ATTN: Joel Bengston

ION Physics Corporation
ATTN: Robert D. Evans

Kaman AviDyne Division of Kaman Sciences Corp. ATTN: Norman P. Hobbs ATTN: E. S. Criscione ATTN: Ray Reutinick

Kaman Sciences Corporation ATTN: John R. Hoffman ATTN: Frank H. Shelton ATTN: Lonald C. Sachs ATTN: John Keith ATTN: Thomas Meagher ATTN: R. Keefe

LFE Corporation Environmental Analysis Lab. Division ATTN: Marcel Nathans

Lockheed Missiles & Space Company, Inc. ATTN: Art Thomas, Dept. 85-85 ATTN: Arthur Collins, Dept. 81-14 ATTN: L. D. Hull ATTN: Charles M. Lee ATTN: Gerald T. Chrusciel

Lockheed Missiles and Space Company ATTN: T. R. Fortune

Lockheed Missiles and Space Company ATIN: F. G. Borgardt ATTN: Raymond R. Capiaux

DEPARTMENT OF DEFENSE CONTRACTORS (Continued)

Martin Marietta Aerospace Orlando Division ATTN: Joyce Legare, MR-328 ATTN: William A. Gray, MP-61 ATTN: Gene Aiello ATTN: H. Rosenthal ATTN: G. Fotieo ATTN: James M. Potts, MP-61 ATTN: Laird Kinnaird

McDonnell Douglas Corporation ATTN: J. Kirby ATTN: J. F. Garibotti ATTN: Ken Kratch ATTN: R. J. Reck ATTN: Robert W. Halprin ATTN: L. Cohen ATTN: H. Hurwicz

McDonnell Douglas Corporation ATTN: Jean McGrew

National Academy of Sciences ATTN: National Materials Advisory Board for Donald G. Groves

National Materials Advisory Board for Edward R. Dyer

Northrop Corporation ATTN: Don Hicks

Pacific-Sierra Research Corp. ATTN: Gary Lang

Physical Sciences, Inc. ATTN: M. S. Finson

Physics International Company ATTN: Doc. Control for James Shea

Prototype Development Associates, Inc.

ATTN: John Slaughter ATTN: John McDonald

R & b Associates ATTN: Albert L. Latter ATTN: Cyrus P. Knowles ATTN: Harold L. Brode ATTN: Jerry Carpenter ATTN: F. A. Field

The Rand Corporation ATTN: R. Robert Rapp

Raytheon Company ATTN: Library

Science Applications, Inc. ATTN: R. Fisher ATTN: Dwane Hove ATTN: John Warner ATTN: G, Ray

Science Applications, Inc. ATTN: Lyle Dunbar ATTN: Carl Swain

Science Applications, Incorporated ATTN: William R. Seebaugh ATTN: William M. Layson

DEPARTMENT OF DEFENSE CONTRACTORS (Continued)

Southern Research Institute ATTN: C. D. Pears ATTN: John R. Koenig

Standford Research Institute ATTN: Philip J. Dolan ATTN: D. L. Huestis ATTN: OAI ATTN: Herbert E. Lindberg ATTN: Donald Curran ATTN: George R. Abrahamson

Stanford Research Institute ATTN: W. B. Reuland ATTN: Harold Carey

Systems, Science and Software, Inc. ATTN: G. A. Gurtman ATTN: Russell E. Duff

DEPARTMENT OF DEFENSE CONTRACTORS (Continued)

Terra Tek, Inc.
ATTN: Sidney Green

TRW Systems Group

ATTN: D. H. Baer, R1-2136

ATTN: R. K. Plebuch, R1-2078

ATTN: W. W. Wood

ATTN: Thomas G. Williams

ATTN: Peter Brandt, E1-2006

2 cy ATTN: I. E. Alber, R1-1008

ATTN: Peter K. Dai, R1/2170

TRW Systems Group
San Bernarding Operations
ATTN: '. Blankenship
ATTN: William Polich ATTN: L. Berger ATTN: Earl W. Allen, 520/141 ATTN: E. Y. Wong, 527/712